MINERALOGY OF DUST EMISSIONS FROM THE BODELE DEPRESSION

By

ROSEMARY ASSUNTA MILLHAM

Bachelor of Science
State University of New York at New Paltz
New Paltz, NY
1983

Master of Science in Education
State University of New York at New Paltz
New Paltz, NY
1987

Submitted to the Faculty of
the Graduate College of the
Oklahoma State University
in partial fulfillment of
the requirements for
the Degree of
DOCTOR OF PHILOSOPHY
July, 2007

MINERALOGY OF DUST EMISSIONS FROM THE

BODELE DEPRESSION

Dissertation Approved:

Steven Marks

_____

Dissertation Adviser

Caroline Beller

_____

Steve Stadler

_____

Jack Vitek

_____

A. Gordon Emslie

_____

Dean of Graduate College

ACKNOWLEDGEMENTS

This dissertation is dedicated to the memory of Yoram Kaufman,
a dedicated scientist, and good friend.
Thank you for believing in me.

It is with sincere thoughts and attitudes that I acknowledge the roles that Yoram Kaufman, Ilan Koren, and Vanderlei Martins have played in the development of my dissertation topic that was based on a need in the scientific community as essential to understanding climate, climate change, and climate modeling as the weather is to understanding climate. Through their dogged belief in my abilities, patience in the explanation of the difficult to explain, and the trust they placed on me in my own abilities as a geologist, Yoram, Ilan, and Vanderlei pushed the envelope of my resolve and dedication to complete the task.

To Steve Marks and Jack Vitek, to whom I owe the deepest gratitude for their unfailing support, advice, and direction, I say thank you for your valued trust in my work ethics, dedication, and abilities.

To my family, especially to my adult children, Jennifer and Matthew, I am amazed and truly blessed to know how much faith you have in me to accomplish something I thought was unreachable. To my husband, Bobby Boy, thanks for all of the meals and doggie walks that allowed me to work uninterrupted for days at a time when I needed the time to follow through on an idea, concept, or theory. You are truly one-of-a-kind.

TABLE OF CONTENTS

Chapter Page

LIST OF TABLES

LIST OF FIGURES

Figure Page

CHAPTER I

INTRODUCTION

In 1934, after an extensive drought occurred in the Great Plains of the United States, huge plumes of dust flowed over the land heading to the eastern states along the path of the westerly winds. Known as the Dust Bowl, the Great Plains became a wasteland as topsoil eroded eastward because soil management practices and farming techniques were not suited to the topography of the land or extended drought conditions. Aeolian processes (transport of sediment by the force of winds) transformed the former farms into useless land. These processes have occurred before human interference. An example of past aeolian processes in America is the Quaternary silt depositions in the Loess Hills in Iowa.

Early geologists assumed loess deposits were either fluvial (deposited by a river) or lacustrine (formed in a lake) in origin. Craton scientists now know that loess deposits are aeolian (deposited by the wind). During the last Ice Age, glaciers advanced down into the mid-continent of North America, grinding underlying rock into fine powder-like sediment called "glacial flour”. As temperatures warmed, the glaciers melted and enormous amounts of water and sediment rushed down the Missouri River valley system. The sediments were deposited on flood plains downstream, creating huge mud flats. During the winter, the melt waters would recede leaving the mud flats exposed. As they dried, fine-grained

mud material called silt was deflated and entrained in the atmosphere by prevailing westerly winds and were redeposited over broad areas. The heavier, coarser, silt was deposited closest to the Missouri River flood plain source, forming sharp, high bluffs on the western margin of the Loess Hills (USGS, 2005). Finer light silt, deposited farther east, created gently sloping hills on the eastern margin. This process repeated for thousands of years, building layer upon layer until the loess reached thicknesses of 60 feet or more and became the dominant feature of the terrain. Differential rates of deposition, hence, occurred between the Great Plains and the Loess Hills of Iowa.

How this transport of mineral dust entrained in the atmosphere affected climate and climate change during this period will be difficult to unravel, just as it is difficult today to understand the impact mineral dust has on climate and climate change.

Identifying the mineralogy of atmospheric mineral dust emitted from the Bodele Depression, centrally located at 17° N Latitude and 18° E Longitude, in northern Chad in central northern Africa, is of significant interest to atmospheric scientists. Research hypothesizes that approximately 50 percent of the total Sahara atmospheric mineral dust transported to, and deposited in, the Amazon River basin is emitted from a single source: the Bodele Depression (Figure 1) (Koren, et al., 2006, Prospero, 1996 and 1999).

The role of atmospheric mineral dust in the climate system includes atmospheric photochemistry (Bian and Zender, 2003), stratospheric water vapor (Sherwood, 2002), condensation nuclei and ice nuclei (Lohman, 2002), the radiative budget (Myhre and Stordal, 2001; Kaufman, et al., 2001 and 2002), and nutrient

Figure 1. Bodele Depression, Chad (Tchad), in Africa
Source: www.wec-int.org

Note: The Bodele Depression is situated within 16°-18° N Latitude by 16° -18° E Longitude.

transport to oceans and forests (Prospero, 1996; Grini, et al., 2005). Modeling studies have attempted to quantify the global production and transport of atmospheric mineral dust (Tegan and Fung, 1994; Claquin, 1999; Ginoux, et al., 2001; Zender, et al., 2003a) with some significant success.

Mineralogy of the atmospheric mineral dust plays an important role in the overall effect of mineral dust in the climate system. The absorption and reflective properties of these minerals, hygroscopic characteristics, and the condensation nuclei and cloud type capabilities, assist in estimating the affect that atmospheric mineral dusts have on climate.

Statement of the Problem

To understand and accurately model the affects that atmospheric aerosols have on climate and climate change, information on aerosol size, shape, composition, and distribution must be well understood. Atmospheric mineral dust can constitute up to ~50 percent of the total volume of atmospheric aerosols in a given column of air (Andreae, 1986), making them a significant target for identification and interpretation. Difficulties in precisely pinpointing source areas for atmospheric mineral dust make it difficult to identify source mineral composition. The Bodele Depression is a significant known source of atmospheric mineral dust with geological and geomorphological histories insufficient for mineral identification. Analyses of in situ aerosol and bulk samples are necessary for accurate mineral identification, and hence, properties and characteristics necessary for understanding the effects mineral dust have on climate and climate change.

Purpose of the Study

This study focuses on the identification of the mineral dust emitted from the Bodele Depression in north-central Africa in the Sahara (Figure 1), known as the single most dusty place on Earth (Koren, et. al., 2006; Tegan, et al., 2006; Todd, et al., 2005; Washington, et al., 2005 and 2006). The purpose of mineral identification is to better understand the affects that the mineral dust, emitted from the Bodele Depression, has on climate and climate change relative to radiative forcing, cloud properties, and the suppression of precipitation. Understanding the affects of these minerals will make modeling parameters for climate change more accurate, therefore, more predictable. Knowledge about the mineralogy of dust emissions allows scientists to accurately predict the results of internal and external mixing during dust transport, dust interactions with other natural and anthropogenic aerosols, hygroscopic characteristics, and the impact on cloud properties.

Significance of the Study

The Bodele Depression in central northern Africa is the single most abundant source of global atmospheric mineral dust (Tegen, et al., 2006, Koren, et. al., 2006, Todd, et. al., 2005). Transported across the Sahara from east to west as dictated by the prevailing trade winds, it is estimated that ~50 percent of the Saharan dust reaching the Amazon River basin during winter months in the Northern Hemisphere originates in the Bodele (Koren, et al., 2006).

Identification of the mineralogy associated with the dust emissions from the Bodele Depression will provide critical information necessary to assess the affects

the dust has on climate and climate change relative to reflective and/or absorption responses to sunlight, effects on atmospheric temperature profiles, the role the mineral dust exhibits as condensation nuclei, and the impact on the water cycle through changes in cloud cover, cloud properties, and precipitation. Understanding the mineralogy of the Bodele Depression will provide information necessary for modeling and predicting the effects of atmospheric mineral dust on global climate and climate change.

Additionally, current research provides conflicting mineralogy results. The BodEx 2005 experiment group analysis of bulk samples from the Bodele indicates diatomaceous Earth as the primary material comprising the sediments entrained as atmospheric mineral dust from the Bodele (Todd, et al., 2006). My geological and laboratory analyses do not support this hypothesis.

Research Questions

The following questions are the focus of this study:

1. Where does the material emitted from the Bodele Depression originate?
2. What geological or geomorphological history of the region affects the mineral composition of the dust emissions from the Bodele?
3. Are the mineralogies of the Bodele bulk and aerosol samples within expected parameters for the regions geological history?
4. Do the BodEX samples provide the necessary information to determine the identification of the minerals emitted from the Bodele Depression in general?

Definition of Terms

Definitions and descriptions are derived from the 2001 Intergovernmental Panel on Climate Change (IPCC), derived from IPCC reports in 1992, 1994, 1995, 1996, 1997, and 2000, unless otherwise specified.

Aerosols - A collection of airborne solid or liquid particles, with a typical size between 0.01 μm and 10 μm and residing in the atmosphere for at least several hours. Aerosols may be of either natural or anthropogenic origin. Aerosols may influence climate in two ways: directly through scattering and absorbing radiation, and indirectly through acting as condensation nuclei for cloud formation or modifying the optical properties and lifetime of clouds. The term has also come to be associated, erroneously, with the propellant used in “aerosol sprays”.

Afforestation - Planting of new forests on lands that historically have not contained forests.

Albedo - The fraction of solar radiation reflected by a surface or object, often expressed as a percentage. Snow covered surfaces have a high albedo; the albedo of soils ranges from high to low; vegetation covered surfaces and oceans have a low albedo. The Earth’s albedo varies mainly through varying cloudiness, snow, ice, and leaf area and land cover changes.

Altimetry - A technique for the measurement of the elevation of the sea, land, or ice surface. For example, the height of the sea surface (with respect to the centre of the Earth or, more conventionally, with respect to a standard “ellipsoid of revolution”) can be measured from space by current state-of-the-art radar altimetry

with centrimetric precision. Altimetry has the advantage of being a measurement relative to a geocentric reference frame, rather than relative to land level as for a tide gauge, and of affording quasi-global coverage.

Anthropogenic - Resulting from or produced by human activities.

Atmosphere - The gaseous envelope surrounding the Earth. The dry atmosphere consists almost entirely of nitrogen (78.1% volume mixing ratio) and oxygen (20.9% volume mixing ratio), together with a number of trace gases, such as argon (0.93% volume mixing ratio), helium, and radiatively active greenhouse gases such as carbon dioxide (0.035% volume mixing ratio), and ozone. Additionally, the atmosphere contains water vapor; amount is highly variable but typically 1% volume mixing ratio. The atmosphere also contains clouds and aerosols.

Autotrophic Respiration - Respiration by photosynthetic organisms (plants).

Biomass - The total mass of living organisms in a given area or volume; recently dead plant material is often included as dead biomass

Biosphere (terrestrial and marine) - The part of the Earth system comprising all ecosystems and living organisms, in the atmosphere, on land (terrestrial biosphere), or in the oceans (marine biosphere), including derived dead organic matter, such as litter, soil organic matter, and oceanic detritus.

Black Carbon - Operationally defined species based on measurement of light absorption and chemical reactivity and/or thermal stability; consists of soot, charcoal, and/or possible light-absorbing refractory organic matter.

Burden - The total mass of a gaseous substance of concern in the atmosphere.

Carbonaceous Aerosol - Aerosol consisting predominantly of organic substances and various forms of black carbon.

Carbon Cycle - The term used to describe the flow of carbon (in various forms, e.g. as carbon dioxide) through the atmosphere, ocean, terrestrial biosphere, and lithosphere.

Carbon Dioxide (CO2) Fertilization - The enhancement of the growth of plants because of increased atmospheric CO2 concentration. Depending on their mechanism of photosynthesis, certain types of plants are more sensitive to changes in atmospheric CO2 concentration. In particular, C3 plants generally show a larger response to CO2 than C4 plants.

Charcoal - Material resulting from charring of biomass, usually retaining some of the microscopic texture typical of plant tissues; chemically it consists mainly of carbon with a disturbed graphitic structure, with lesser amounts of oxygen and hydrogen. See: black carbon; Soot particles. (Source: Charlson and Heintzenberg, 1995, p. 402.)

Climate - Climate in a narrow sense is usually defined as the "average weather", or more rigorously, as the statistical description in terms of the mean and variability of relevant quantities over a period ranging from months to thousands or millions of years. The classical period is 30 years, as defined by the World Meteorological Organization (WMO). These quantities are most often surface variables such as temperature, precipitation, and wind. Climate in a wider sense is the state, including a statistical description, of the climate system.

Climate Change - Climate change refers to a statistically significant variation in either the mean state of the climate or in its variability, persisting for an extended period (typically decades or longer). Climate change may be due to natural internal processes or external forcings, or to persistent anthropogenic changes in the composition of the atmosphere or in land use. Note that the framework Convention on Climate Change (UNFCCC), in its Article 1, defines “climate change” as: “a change of climate which is attributed directly or indirectly to human activity that alters the composition of the global atmosphere and which is in addition to natural climate variability observed over comparable time periods.” The UNFCCC thus makes a distinction between “climate change” attributable to human activities altering the atmospheric composition, and “climate variability” attributable to natural causes.

Climate Feedback - An interaction mechanism between processes in the climate system is called a climate feedback, when the result of an initial process triggers changes in a second process that in turn influences the initial one. A positive feedback intensifies the original process, and a negative feedback reduces it.

Climate Model (hierarchy) - A numerical representation of the climate system based on the physical, chemical, and biological properties of its components, their interactions and feedback processes, and accounting for all or some of its known properties. The climate system can be represented by models of varying complexity, i.e. for any one component or combination of components a *hierarchy* of models can be identified, differing in such aspects as the number of spatial dimensions, the extent to which physical, chemical or biological processes are

explicitly represented, or the level at which empirical parametrizations are involved. Coupled atmosphere/ocean/sea-ice General Circulation Models (AOGCMs) provides a comprehensive representation of the climate system. There is an evolution towards more complex models with active chemistry and biology. Climate models are applied, as a research tool, to study and simulate the climate, but also for operational purposes, including monthly, seasonal, and interannual climate predictions.

Climate Prediction - A climate prediction or climate forecast is the result of an attempt to produce a most likely description or estimate of the actual evolution of the climate in the future, e.g. at seasonal, interannual or long-term time scales.

Climate Projection - A projection of the response of the climate system to emission or concentration scenarios of greenhouse gases and aerosols, or radiative forcing scenarios, often based upon simulations by climate models. Climate projections are distinguished from climate predictions in order to emphasize that climate projections depend upon the emission/concentration/ radiative forcing scenario used, which are based on assumptions, concerning, e.g., future socio-economic and technological developments, that may or may not be realized, and are therefore subject to substantial uncertainty.

Climate Scenario - A plausible and often simplified representation of the future climate, based on an internally consistent set of climatological relationships, that has been constructed for explicit use in investigating the potential consequences of anthropogenic climate change, often serving as input to impact models. Climate projections often serve as the raw material for constructing climate scenarios, but climate scenarios usually require additional information such as about the observed

current climate. A *climate change scenario* is the difference between a climate scenario and the current climate.

Climate Sensitivity - In IPCC Reports, *equilibrium climate sensitivity* refers to the equilibrium change in global mean surface temperature following a doubling of the atmospheric (equivalent) CO2 concentration. More generally, equilibrium climate sensitivity refers to the equilibrium change in surface air temperature following a unit change in radiative forcing (°C/Wm-2). In practice, the evaluation of the equilibrium climate sensitivity requires very long simulations with Coupled General Circulation Models (Climate model). The *effective climate sensitivity* is a related measure that circumvents this requirement. It is evaluated from model output for evolving non-equilibrium conditions. It is a measure of the strengths of the feedbacks at a particular time and may vary with forcing history and climate state.

Climate System - The climate system is the highly complex system consisting of five major components: the atmosphere, the hydrosphere, the cryosphere, the land surface and the biosphere, and the interactions between them. The climate system evolves in time under the influence of its own internal dynamics and because of external forcings such as volcanic eruptions, solar variations and human-induced forcings such as the changing composition of the atmosphere and land-use change.

Climate Variability - Climate variability refers to variations in the mean state and other statistics (such as standard deviations, the occurrence of extremes, etc.) of the climate on all temporal and spatial scales beyond that of individual weather events. Variability may be due to natural internal processes within the climate system (*internal variability*), or to variations in natural or anthropogenic external forcing.

Cloud Condensation Nuclei - Airborne particles that serve as an initial site for the condensation of liquid water and which can lead to the formation of cloud droplets.

Cooling Degree-days - The integral over a day of the temperature above 18°C (e.g. a day with an average temperature of 20°C counts as 2 cooling degree days).

Cryosphere - The component of the climate system consisting of all snow, ice, and permafrost on and beneath the surface of the Earth and ocean.

C3 Plants - Plants that produce a three-carbon compound during photosynthesis; including most trees and agricultural crops such as rice, wheat, soybeans, potatoes, and vegetables.

C4 Plants - Plants that produce a four-carbon compound during photosynthesis; mainly of tropical origin, including grasses and the agriculturally important crop; maize, sugar cane, millet and sorghum.

Deforestation - Conversion of forest to non-forest. For a discussion of the term forest and related terms such as afforestation, reforestation, and deforestation.

Desertification - Land degradation in arid, semi-arid, and dry sub-humid areas resulting from various factors, including climatic variations and human activities. Further, the UNCCD (The United Nations Convention to Combat Desertification) defines land degradation as a reduction or loss, in arid, semi-arid, and dry sub-humid areas, of the biological or economic productivity and complexity of rain-fed cropland, irrigated cropland, or range, pasture, forest, and woodlands resulting from land uses or from a process or combination of processes, including processes arising from human activities and habitation patterns, such as: (i) soil

erosion caused by wind and/or water; (ii) deterioration of the physical, chemical and biological or economic properties of soil; and (iii) long-term loss of natural vegetation.

Detection and Attribution - Climate varies continually on all time scales. *Detection* of climate change is the process of demonstrating that climate has changed in some defined statistical sense, without providing a reason for that change. *Attribution* of causes of climate change is the process of establishing the most likely causes for the detected change with some defined level of confidence.

Diurnal Temperature Range - The difference between the maximum and minimum temperature during a day.

El Niño-Southern Oscillation (ENSO) - El Niño, in its original sense, is a warm water current, which periodically flows along the coast of Ecuador and Peru, disrupting the local fishery. This oceanic event is associated with a fluctuation of the intertropical surface pressure pattern and circulation in the Indian and Pacific oceans, called the Southern Oscillation. This coupled atmosphere-ocean phenomenon is collectively known as El Niño-Southern Oscillation, or ENSO. During an El Niño event, the prevailing trade winds weaken and the equatorial countercurrent strengthens, causing warm surface waters in the Indonesian area to flow eastward to overlie the cold waters of the Peru Current. This event has great impact on the wind, sea surface temperature, and precipitation patterns in the tropical Pacific. It has climatic effects throughout the Pacific region and in many other parts of the world. The opposite of an El Niño event is called *La Niña.*

Emission Scenario - A plausible representation of the future development of emissions of substances that are potentially radiatively active (e.g. greenhouse gases, aerosols), based on a coherent and internally consistent set of assumptions about driving forces (such as demographic and socio-economic development, technological change) and their key relationships.

Energy Balance - Averaged over the globe and over longer time periods, the energy budget of the climate system must be in balance. Because the climate system derives all its energy from the Sun, this balance implies that, globally, the amount of incoming solar radiation must on average be equal to the sum of the outgoing reflected solar radiation and the outgoing infrared radiation emitted by the climate system. A perturbation of this global radiation balance, be it human induced or natural, is called radiative forcing.

Equilibrium and Transient Climate Experiment - An *equilibrium climate experiment* is an experiment in which a climate model is allowed to fully adjust to a change in radiative forcing. Such experiments provide information on the difference between the initial and final states of the model, but not on the time-dependent response. If the forcing is allowed to evolve gradually according to a prescribed emission scenario, the time dependent response of a climate model may be analyzed. Such an experiment is called a *transient climate experiment.*

Equivalent CO2 (carbon dioxide) - The concentration of CO2 that would cause the same amount of radiative forcing as a given mixture of CO2 and other greenhouse gases.

Flux Adjustment - To avoid the problem of coupled atmosphere-ocean general circulation models drifting into some unrealistic climate state, adjustment terms can be applied to the atmosphere/ocean fluxes of heat and moisture (and sometimes the surface stresses resulting from the effect of the wind on the ocean surface) before these fluxes are imposed on the model ocean and atmosphere. Because these adjustments are pre-computed and therefore independent of the coupled model integration, they are uncorrelated to the anomalies, which develop during the integration.

Fossil CO2 (carbon dioxide) Emissions - Emissions of CO2 resulting from the combustion of fuels from fossil carbon deposits such as oil, gas, and coal.

General Circulation - The large-scale motions of the atmosphere and the ocean as a consequence of differential heating on a rotating Earth, aiming to restore the energy balance of the system through transport of heat and momentum.

General Circulation Model (GCM) - See Climate model.

Global Surface Temperature - The global surface temperature is the area-weighted global average of (i) the sea-surface temperature over the oceans (i.e. the subsurface bulk temperature in the first few meters of the ocean), and (ii) the surface-air temperature over land at 1.5 m above the ground.

Global Warming Potential (GWP) - An index, describing the radiative characteristics of well mixed greenhouse gases, that represents the combined effect of the differing times these gases remain in the atmosphere and their relative effectiveness in absorbing outgoing infrared radiation.

Greenhouse Effect - Greenhouse gases effectively absorb infrared radiation, emitted by the Earth's surface, by the atmosphere itself due to the same gases, and by clouds. Atmospheric radiation is emitted to all sides, including downward to the Earth's surface. Thus, greenhouse gases trap heat within the surface-troposphere system. This is called the *natural greenhouse effect.* Atmospheric radiation is strongly coupled to the temperature of the level at which it is emitted. In the troposphere, the temperature generally decreases with height. Effectively, infrared radiation emitted to space originates from an altitude with a temperature of, on average, -19°C, in balance with the net incoming solar radiation, whereas the Earth's surface is kept at a much higher temperature of, on average, +14°C. An increase in the concentration of greenhouse gases leads to an increased infrared opacity of the atmosphere, and therefore to an effective radiation into space from a higher altitude at a lower temperature. This causes a radiative forcing, an imbalance that can only be compensated for by an increase of the temperature of the surface-troposphere system. This is the *enhanced greenhouse effect.*

Greenhouse Gas - Greenhouse gases are those gaseous constituents of the atmosphere, both natural and anthropogenic, that absorb and emit radiation at specific wavelengths within the spectrum of infrared radiation emitted by the Earth's surface, the atmosphere and clouds. This property causes the greenhouse effect. Water vapor (H2O), carbon dioxide (CO2), nitrous oxide (N2O), methane, (CH4) and ozone (O3) are the primary greenhouse gases in the Earth's atmosphere. Moreover, there are a number of entirely human-made greenhouse gases in the atmosphere, such as the halocarbons and other chlorine and bromine containing

substances, dealt with under the Montreal Protocol. Beside CO2, N2O and CH4, the Kyoto Protocol deals with the greenhouse gases sulfur hexafluoride (SF6), hydro fluorocarbons (HFCs) and perfluorocarbons (PFCs).

Indirect Aerosol Effect - Aerosols may lead to an indirect radiative forcing of the climate system through acting as condensation nuclei or modifying the optical properties and lifetime of clouds. Two indirect effects are distinguished:

First indirect effect: A radiative forcing induced by an increase in anthropogenic aerosols, which cause an initial increase in droplet concentration and a decrease in droplet size for fixed liquid water content, leading to an increase of cloud albedo. This effect is also known as the *Twomey effect*. This is sometimes referred to as the *cloud albedo effect*. However, this is highly misleading since the second indirect effect also alters cloud albedo.

Second indirect effect: A radiative forcing induced by an increase in anthropogenic aerosols, which cause a decrease in droplet size, reducing the precipitation efficiency, thereby modifying the liquid water content, cloud thickness, and cloud life time. This effect is also known as the *cloud lifetime effect* or *Albrecht effect*.

Industrial Revolution - A period of rapid industrial growth with far-reaching social and economic consequences, beginning in England during the second half of the eighteenth century and spreading to Europe and later to other countries including the United States. The invention of the steam engine was an important trigger of this development. The industrial revolution marks the beginning of a strong increase in the use of fossil fuels and emission of, in particular, fossil carbon dioxide. In this

Report the terms pre-industrial and industrial refer, somewhat arbitrarily, to the periods before and after 1750, respectively.

Infrared Radiation - Radiation emitted by the earth's surface, the atmosphere, and the clouds. It is also known as terrestrial or long-wave radiation. Infrared radiation has a distinctive range of wavelengths ("spectrum") longer than the wavelength of the red color in the visible part of the spectrum. The spectrum of infrared radiation is practically distinct from that of solar or short wave radiation because of the difference in temperature between the Sun and the Earth-atmosphere system.

Integrated Assessment - A method of analysis that combines results and models from the physical, biological, economic and social sciences, and the interactions between these components, in a consistent framework, to evaluate the status and the consequences of environmental change and the policy responses to it.

Internal Variability - See Climate variability.

Inverse Modeling - A mathematical procedure by which the input to a model is estimated from the observed outcome, rather than *vice versa*. It is, for instance, used to estimate the location and strength of sources and sinks of CO2 from measurements of the distribution of the CO2 concentration in the atmosphere, given models of the global carbon cycle and for computing atmospheric transport.

Land Use - The total of arrangements, activities, and inputs undertaken in a certain land cover type (a set of human actions). The social and economic purposes for which land is managed (e.g., grazing, timber extraction, and conservation).

Land-Use Change - A change in the use or management of land by humans, which may lead to a change in land cover. Land cover and land-use change may have an impact on the albedo, evapotranspiration, sources and sinks of greenhouse gases, or other properties of the climate system and may thus have an impact on climate, locally or globally. See also: the IPCC Report on Land Use, Land-Use Change, and Forestry.

La Niña - El Niño-Southern Oscillation.

Lifetime - Lifetime is a general term used for various time-scales characterizing the rate of processes affecting the concentration of trace gases. The following lifetimes may be distinguished: *Turnover time* (T) is the ratio of the mass M of a reservoir (e.g., a gaseous compound in the atmosphere) and the total rate of removal S from the reservoir: T = M/S. For each removal, process separate turnover times can be defined. In soil carbon biology, this is referred to as *Mean Residence Time (MRT). Adjustment time* or *response time* (Ta) is the time-scale characterizing the decay of an instantaneous pulse input into the reservoir. The term *adjustment time* is also used to characterize the adjustment of the mass of a reservoir following a step change in the source strength. *Half-life* or *decay constant* is used to quantify a first-order exponential decay process. See: Response time, for a different definition pertinent to climate variations. The term *lifetime* is sometimes used, for simplicity, as a surrogate for *adjustment time.* In simple cases, where the global removal of the compound is directly proportional to the total mass of the reservoir, the adjustment time equals the turnover time: T = Ta. An example is CFC- 11, which is removed from the atmosphere only by photochemical processes in the stratosphere. In more

complicated cases, where several reservoirs are involved or where the removal is not proportional to the total mass, the equality T = Ta no longer holds. °Carbon dioxide (CO2) is an extreme example. Its turnover time is only about 4 years because of the rapid exchange between atmosphere and the ocean and terrestrial biota. However, a large part of that CO2 is returned to the atmosphere within a few years. Thus, the adjustment time of CO2 in the atmosphere is actually determined by the rate of removal of carbon from the surface layer of the oceans into its deeper layers. Although an approximate value of 100 years may be given for the adjustment time of CO2 in the atmosphere, the actual adjustment is faster initially and slower later on. In the case of methane (CH4) the adjustment time is different from the turnover time, because the removal is mainly through a chemical reaction with the hydroxyl radical OH, the concentration of which itself depends on the CH4 concentration. Therefore, the CH4 removal S is not proportional to its total mass M.

Lithosphere - The upper layer of the solid Earth, both continental and oceanic, which comprises all crustal rocks and the cold, mainly elastic, part of the uppermost mantle. Volcanic activity, although part of the lithosphere, is not considered as part of the climate system, but acts as an external forcing factor.

Mole Fraction - Mole fraction, or *mixing ratio*, is the ratio of the number of moles of a constituent in a given volume to the total number of moles of all constituents in that volume. It is usually reported for dry air. Typical values for long-lived greenhouse gases are in the order of £gmol/mol (parts per million: ppm), nmol/mol (parts per billion: ppb), and fmol/mol (parts per trillion: ppt). Mole fraction differs from *volume mixing ratio*, often expressed in ppmv etc., by the

corrections for non-ideality of gases. This correction is significant relative to measurement precision for many greenhouse gases. (Source: Schwartz and Warneck, 1995).

Net Biome Production (NBP) - Net gain or loss of carbon from a region. NBP is equal to the Net Ecosystem Production minus the carbon lost due to a disturbance, e.g. a forest fire or a forest harvest.

Net Ecosystem Production (NEP) - Net gain or loss of carbon from an ecosystem. NEP is equal to the Net Primary Production minus the carbon lost through heterotrophic respiration.

Net Primary Production (NPP) - The increase in plant biomass or carbon of a unit of a landscape. NPP is equal to the Gross Primary Production minus carbon lost through autotrophic respiration.

Nitrogen fertilization - Enhancement of plant growth through the addition of nitrogen compounds. In IPCC Reports, this typically refers to fertilisation from anthropogenic sources of nitrogen such as human-made fertilisers and nitrogen oxides released from burning fossil fuels.

Non-linearity - A process is called “non-linear” when there is no simple proportional relation between cause and effect. The climate system contains many such non-linear processes, resulting in a system with a potentially very complex behavior. Such complexity may lead to rapid climate change.

North Atlantic Oscillation (NAO) - The North Atlantic Oscillation consists of opposing variations of barometric pressure near Iceland and near the Azores. On average, a westerly current, between the Icelandic low-pressure area and the Azores

high-pressure area, carries cyclones with their associated frontal systems towards Europe. However, the pressure difference between Iceland and the Azores fluctuates on time-scales of days to decades, and can be reversed at times.

Organic Aerosol - Aerosol particles consisting predominantly of organic compounds, mainly C, H, O, and lesser amounts of other elements. (Source: Charlson and Heintzenberg, 1995, p. 405).

Parameterization - In climate models, this term refers to the technique of representing processes, that cannot be explicitly resolved at the spatial or temporal resolution of the model (sub-grid scale processes), by relationships between the area or time averaged effect of such sub-grid scale processes and the larger scale flow.

Patterns of Climate Variability - Natural variability of the climate system, in particular on seasonal and longer time-scales, predominantly occurs in preferred spatial patterns, through the dynamical non-linear characteristics of the atmospheric circulation and through interactions with the land and ocean surfaces. Such spatial patterns are also called “regimes” or “modes”. Examples are the °north Atlantic Oscillation (NAO), the Pacific-North American pattern (PNA), the El Niño-Southern Oscillation (ENSO), and the Antarctic Oscillation (AO).

Precursors - Atmospheric compounds which themselves are not greenhouse gases or aerosols, but which have an effect on greenhouse gas or aerosol concentrations by taking part in physical or chemical processes regulating their production or destruction rates.

Projection (generic) - A projection is a potential future evolution of a quantity or set of quantities, often computed with the aid of a model. Projections are

distinguished from *predictions* in order to emphasize that projections involve assumptions concerning, e.g., future socioeconomic and technological developments that may or may not be realized, and are therefore subject to substantial uncertainty.

Proxy - A proxy climate indicator is a local record that is interpreted, using physical and biophysical principles, to represent some combination of climate-related variations back in time. Climate related data derived in this way are referred to as proxy data. Examples of proxies are: tree ring records, characteristics of corals, and various data derived from ice cores.

Radiative Forcing - Radiative forcing is the change in the net vertical irradiance (expressed in Watts per square meter: Wm-2) at the tropopause due to an internal change or a change in the external forcing of the climate system, such as, for example, a change in the concentration of carbon dioxide or the output of the Sun. Usually radiative forcing is computed after allowing for stratospheric temperatures to readjust to radiative equilibrium, but with all tropospheric properties held fixed at their unperturbed values. Radiative forcing is called *instantaneous* if no change in stratospheric temperature is accounted for.

Radiative Forcing Scenario - A plausible representation of the future development of radiative forcing associated, for example, with changes in atmospheric composition or land-use change, or with external factors such as variations in solar activity. Radiative forcing scenarios can be used as input into simplified climate models to compute climate projections.

Rapid Climate Change - The non-linearity of the climate system may lead to rapid climate change, sometimes called *abrupt events* or even *surprises*. Some abrupt

events may be imaginable, such as a dramatic reorganization of the thermohaline circulation, rapid deglaciation, or massive melting of permafrost leading to fast changes in the carbon cycle. Others may be truly unexpected, as a consequence of a strong, rapidly changing, forcing of a nonlinear system.

Regimes – Preferred: patterns of climate variability.

Reservoir - A component of the climate system, other than the atmosphere, which has the capacity to store, accumulate or release a substance of concern, e.g. carbon, a greenhouse gas or a precursor. Oceans, soils, and forests are examples of reservoirs of carbon. *Pool* is an equivalent term (note that the definition of pool often includes the atmosphere). The absolute quantity of substance of concerns, held within a reservoir at a specified time, is called the *stock*.

Response Time - The response time or *adjustment time* is the time needed for the climate system or its components to re-equilibrate to a new state, following a forcing resulting from external and internal processes or feedbacks. It is very different for various components of the climate system. The response time of the troposphere is relatively short, from days to weeks, whereas the stratosphere comes into equilibrium on a time-scale of typically a few months. Due to their large heat capacity, the oceans have a much longer response time, typically decades, but up to centuries or millennia. The response time of the strongly coupled surface-troposphere system is, therefore, slow compared to that of the stratosphere, and mainly determined by the oceans. The biosphere may respond fast, e.g. to droughts, but also very slowly to imposed changes.

Scenario (generic) - A plausible and often simplified description of how the future may develop, based on a coherent and internally consistent set of assumptions about driving forces and key relationships. Scenarios may be derived from projections, but are often based on additional information from other sources, sometimes combined with a "narrative storyline".

Sink - Any process, activity, or mechanism, which removes a greenhouse gas, an aerosol, or a precursor of a greenhouse gas or aerosol from the atmosphere.

Soil moisture - Water stored in or at the land surface and available for evaporation.

Solar Radiation - Radiation emitted by the Sun. It is also referred to as short-wave radiation. Solar radiation has a distinctive range of wavelengths (spectrum) determined by the temperature of the Sun.

Soot Particles - Particles formed during the quenching of gases at the outer edge of flames of organic vapors, consisting predominantly of carbon, with lesser amounts of oxygen and hydrogen present as carboxyl and phenolic groups and exhibiting an imperfect graphitic structure. (Source: Charlson and Heintzenberg, 1995, p. 406.)

Source - Any process, activity, or mechanism, which releases a greenhouse gas, an aerosol, or a precursor of a greenhouse gas or aerosol into the atmosphere.

Spatial and Temporal Scales - Climate may vary on a large range of spatial and temporal scales. Spatial scales may range from local (less than 100,000 km2), through regional (100,000 to 10 million km2) to continental (10 to 100 million km2). Temporal scales range from seasonal to geological (hundreds of millions of years).

Transient Climate Response - The globally averaged surface air temperature increase, averaged over a 20 year period, centered at the time of CO2 doubling, i.e., at year 70 in a 1% per year compound CO2 increase experiment with a global coupled climate model.

Troposphere - The lowest part of the atmosphere from the surface to about 10 km in altitude in mid-latitudes (ranging from 9 km in high latitudes to 16 km in the tropics on average) where clouds and "weather" phenomena occur. In the troposphere temperatures generally decrease with height.

Uncertainty - An expression of the degree to which a value (e.g. the future state of the climate system) is unknown. Uncertainty can result from lack of information or from disagreement about what is known or even knowable. It may have many types of sources, from quantifiable errors in the data to ambiguously defined concept or terminology, or uncertain projections of human behavior. Uncertainty can therefore be represented by quantitative measures (e.g. a range of values calculated by various models) or by qualitative statements (e.g., reflecting the judgment of a team of experts).

Uptake - The addition of a substance of concern to a reservoir. The uptake of carbon containing substances, in particular carbon dioxide, is often called (carbon) sequestration.

Scope of Study

The scope of this study involves the identification of the four in situ bulk samples and four in situ aerosol samples collected from the Bodele Depression during the BodEX experiment in February of 2005. The available French geological survey maps and the geological/geomorphological histories of the region will aid these analyses. Through analysis of samples and correlations with known mineralogies, maps, and histories, the Bodele Depression minerals have been identified.

The BodEX (Bodele Experiment) 2005 team is composed of a group of academic scientists from the University of London and Cambridge University, England. The experiment was the first conducted in situ at the Bodele Depression. The team of scientists, an interdisciplinary study group funded by the Gilchrist Educational Trust and the Royal Geographical Society, collected samples of bulk material at the surface of the Bodele, and in aerosol filters 3 meters above the surface. Aerosol and bulk samples, collected by the BodEX team, were derived from four locations centered at 17° N Latitude and 18° E Longitude.

Limitations

The limitations to this study involve the limited number of samples obtained from the Bodele depression, US government limitations on the distribution of maps of the region of study over the past two years, and the inability to account for the percentage of carbon within the mineral samples because of the carbon filters used with the Scanning Electron Microscope. Significant civil unrest in Sudan and Chad

has made travel to the region impossible for many US nationals. Any maps of the Sudan, Libya, and Chad regions relative to topography and mineral deposits have become unavailable to US citizens. This ruling, according to the Omni Maps Corporation, the sole provider for such maps, was passed by the US government in the fall of 2005.

Additional samples from the Bodele Depression are unavailable at this time because of visitation restrictions. The Bodele is reached through the country of Sudan where civil unrest makes visitation visas impossible to obtain (for US citizens).

The carbon filters used for adhering the powdered samples onto the heads for the Scanning Electron Microscope (SEM) are part of the chemical analyses for the SEM data. It is impossible to determine the quantity of carbon that is part of the samples, and the quantity of carbon caused by the filters.

Assumptions

It is easy to assume that the in situ bulk and aerosol samples provided to me by the BodEX 2005 team are representative of the entire Bodele depression region, and hence, are the primary source of dust emissions from the surface of the Bodele. That is, however, an assumption, and further samples from the region should provide support for the findings in this report, or prove the need for further research. It is unclear whether the samples were representative of the scope of the Bodele Depression, or restricted to a smaller area along the fringes of the depression, or near the center.

Additionally, it is easy to assume that the general mineralogy of the region would fall into the standardized mineralogy of arid regions with associated geological histories of periodic wet and arid conditions over time, say the Holocene to the present. This assumption could prove a disadvantage to accuracy in identification of the Bodele Depression mineralogy.

Finally, the extensive knowledge available related to the development of Mega-Lake Chad post-Holocene, as a freshwater lake with thriving diatoms, could lead to the assumption that the Bodele Depression materials are primarily diatomaceous Earth. MODIS images from the TERRA and AQUA satellites demonstrate the highly reflective characteristics of the Bodele and the dust emissions. Although the reflective characteristics support the predominance of diatomaceous Earth in the Bodele, chemical analyses, d-spacing values, and visual images are needed to support this hypothesis.

CHAPTER II

REVIEW OF LITERATURE

Introduction

The Sahara is the single most productive source of aeolian (wind-driven) soil dust (Swap. et al., 1996; Giles, 2005; Prospero, et al., 2003; Washington, et al., 2003). Studies show that ~50 percent of all aeolian material supplied to the oceans of the world and ~ 40 million tons of mineral dust deposits to the Amazon River Basin (Koren, et al., 2006; Tegan, et al., 2006; Todd, et al., 2005; Washington, et al., 2005 and 2006), Central America, and parts of southern North America and Caribbean each year. The generation of mineral dust emissions of this magnitude illustrates the importance of understanding the geomorphological processes of aeolian saltation, deflation, and the entrainment of atmospheric mineral dust (Goudie, and Middleton, 2001, Colarco, et al., 2003).

Wind blown particles move in three modes: creep, saltation (Figure 2), and suspension (Bagnold, 1941; Bagnold, 1954). When wind velocities reach ~ 4.5 m/s a rolling "creep' action can occur. Stronger winds can cause creep in pebble-sized particles.

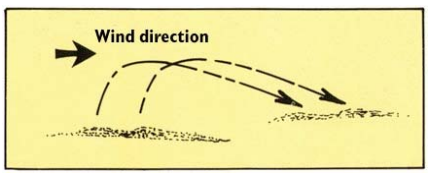

Figure 2. Saltation of Sediments
Source: USGS at http://pubs.usgs.gov/gip/deserts/eolian/

Saltation occurs when particles are lifted off the surface and 'jump' a few centimeters downwind but no more than ~ one centimeter from the surface. This process accounts for 75-80 percent of sediment transport in arid regions. The saltation process is responsible for sending additional sediment into transport as the force from particles falling back to Earth is transferred to other particles, causing them to become airborne. Particles of clay and silt (Figure 3) have the ability to be lifted above the zone of saltation to be carried in suspension thousands of meters into the air. These suspended (entrained) particles can be transported hundreds of kilometers downwind (Colarco, et al., 2003, Englestaedter, et al., 2005, Prospero, 1999; Chiapello, et al., 2005; Evan, et al., 2006; Gangoiti, et al., 2006, Kubilay, et al., 2000; Moulin, et al., 1997).

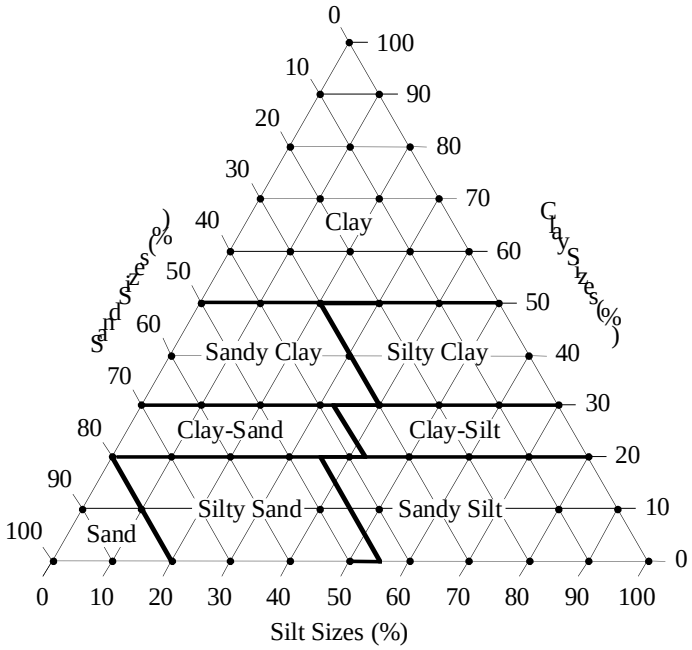

Figure 3. Particle Size Classification
Source: U.S. Engineering Department, Civil, at
http://www.civil.usyd.edu.au/courses/civl2410/classification.doc

Most aeolian deflation zones are composed of desert pavement, a sheet like surface of rock fragments that remains after wind and water have removed the fine particles. Almost half of the desert surfaces of the Earth are stony deflation zones. The rock mantle in desert pavements protects the underlying material from deflation zones (United States Geological Survey (USGS), 1997; Tarbuck and Lutgens, 1993).

A dark, shiny stain called desert varnish, or rock varnish, is often found on the surface of desert rocks that have been exposed at the surface for a long time. Manganese, iron oxides, hydroxides, and clay minerals form most varnishes and provide the shine (USGS, 1997; Tarbuck and Lutgens, 1993).

Wind-driven grains of sand abrade landforms. The abrading by particles carried in the wind creates grooves or small depressions. Ventifacts are rocks that have been cut, and sometimes polished, by the abrasive action of wind. Deflation basins, called blowouts, are hollows formed by the removal of particles by the wind. Blowouts are generally small, but may be up to several kilometers in diameter. Sculpted landforms, called yardangs, are up to tens of meters high and kilometers long and are landforms streamlined by desert winds (Figure 4).

Windblown sediment is deposited downwind from the source area. Particle size and wind velocity determines the distance a particular particle is transported (Grini and Zender, 2004; Grini, et al., 2005; Prospero, et al., 2002; Todd, et al., 2005; Prospero, et al., 1999; Prospero, 1996; Washington, et al., 2005 and 2006; Zender, et al., 2003a and 2003b). Particles >10 μm will be deposited closer to the source region than particles < 10μm. As particles are deposited, they can create landform deposits

characteristic of desert regions, called dunes. Dune deposits occur in a variety of shapes and sizes (Figure 5).

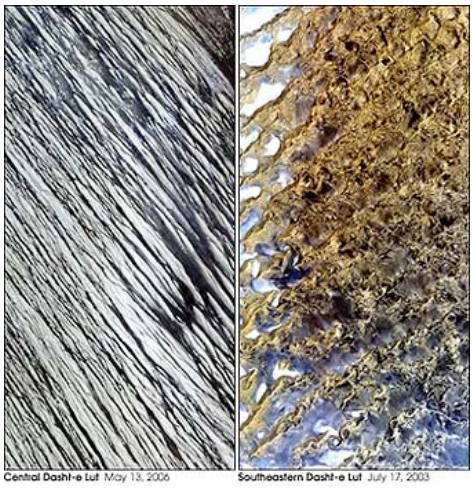

Figure 4. Yardang Linear Features
Source: NASA satellite image at http://eosdata.gsfc.nasa.gov/geomorphology/

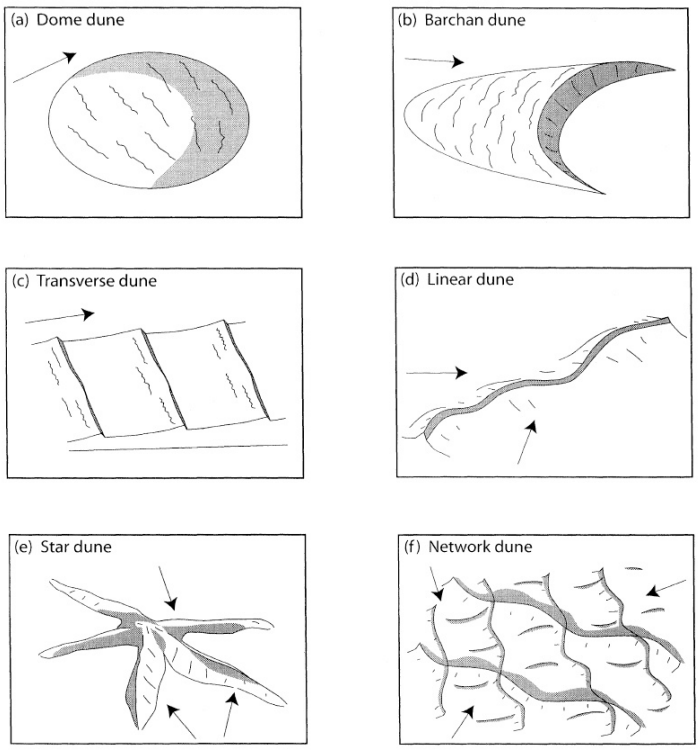

Figure 5. Dune Types
Source: McKee, 1979, Cooke, et al., 1993

The mechanics of deposition in the formation of dunes has three primary modes (Hunter, 1977); migration of wind ripples, fallout from suspension of saltating particles (these particles are suspended ~ one centimeter above the ground), and avalanching on the lee slope of the dune. The sediments are predominately quartz and feldspars of sand-sized grains that are not suspended, nor entrained, as atmospheric dust. The initiation, development, and equilibrium morphology of dunes are determined by changes in the sediment transport rates spaciotemporally, resulting in erosion or deposition (Lancaster, 1995; Bagnold, 1954). The kinematics of sediment transport requires that the mass or volume of sediment be conserved (Middleton & Southard, 1984).

For a specific area of the surface of a dune, a decrease in local sediment transport rates with increased distance results in an influx of sediment to the area will exceed the outflux, leading to sediment storage and an increase in the local bed elevation by deposition of sediments (Lancaster, 1995; Bagnold, 1954). Conversely, increased sediment transport rates with distance result in sediment outflux exceeding the influx that leads to removal of sediment materials, lowering the local bed elevation through the erosion of sediments (Lancaster, 1995). The relationships are expressed in terms of the sediment continuity equation:

$$dh/dt = -dq_{\varsigma}/dx$$

where h is the local bed elevation, q_{ς} is the local volumetric sediment transport rate in the direction x, and t is time (Lancaster, 1995). Therefore, spatial changes in sand transport rates are a fundamental control of dune morphology.

Several factors affect particle movement. At ground level, the roughness of the surface is a controlling factor for wind erosion (USGS, 1997; Tarbuck and Lutgens, 1993. Vegetation (Tegan, et al., 2002), boulders, and buildings increase the frictional roughness of the surface and reduce wind velocity. In regions where vegetation, rock outcrops, or buildings do not exist, wind erosion is more prevalent. Additionally, the size of the particle has a significant affect on the threshold for particle saltation, deflation, and entrainment. Particle sizes <10μm are the particles likely to be transported greater distances. For example, dust emissions from the Bodele Depression (Figure 6) range in particle size from <1μm to >20μm, but particles >10μm settle to the surface rapidly (Todd, et al., 2005; Washington and Todd, 2005: Zender, et al., 2003a) southwest of the Bodele. Concurrently, the trade winds and low-level jet continue to loft particles <10μm into the upper troposphere (Koren, et al., 2006; Tegen and Fung, 1994; Washington, et al., 2006, Zender, et al., 2003a). Third, the amount of moisture received in a given arid region affects saltation and the aggregation of soil particles affecting the ability of a given wind velocity to loft particles of any size. Arid regions with rainfall < 100mm per year do tend to be the dustiest places on Earth.

The power of wind to erode surface particles is controlled primarily by two factors: wind velocity and surface roughness. Erosive force increases exponentially with increases in wind velocity. Wind velocity controls equate to the formula $E = V^3 rho$, where E is erosivity, V is velocity and rho is air density. The erosivity of wind is an exponential function of wind velocity. If the wind velocity, for example, doubles, the wind is eight times more erodible or, if it triples, the wind is 27 times

more erodible (Pidwirny, 2006). This is evident in satellite images of arid regions like the Bodele Depression where wind velocities increase dramatically as they are funneled through a natural gap between two mountain ranges, causing high sustained winds that carry ~240± 80 Tg of mineral dust out of the Bodele each year (Kaufman, et al., 2005; Koren, et al., 2006).

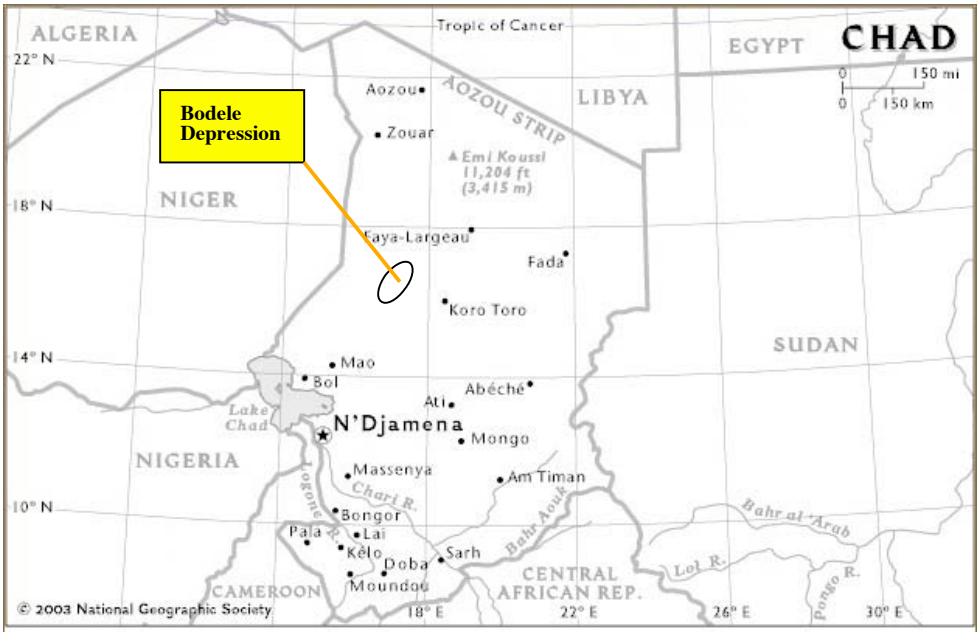

Figure 6. Bodele Depression, Chad
Source: National Geographic Society; modified to illustrate location of the Bodele

The roughness of the surface plays an important role, at ground level, in controlling wind erosion. Boulders, buildings, trees, shrubs, and small plants, such grasses, can increase the frictional roughness of the surface, and reduce wind velocity. For example, there is little wind erosion in heavily vegetated areas, and wind velocity decreases exponentially near the ground. The grain size of soil particles is directly related to its ability to be saltated, deflated, and entrained (Alfaro, et al., 1998; Carlson and Prospero, 1997; Grini, et al., 2005; Koren and

Kaufman, 2004). The threshold velocity of a particle is related to the square root of the particle size. The smaller the particle, the lower the terminal falling velocity, hence, the more likely the particle will become entrained (Figure 7).

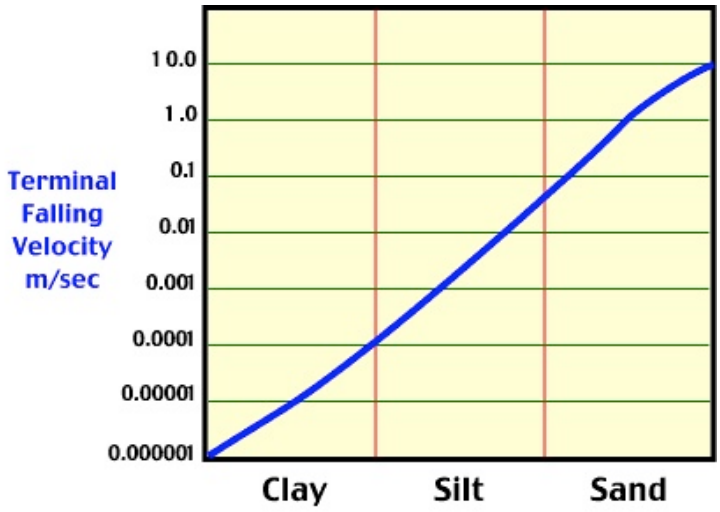

Figure 7. Particle Size Suspension and Wind Velocity
Source: http://www.physicalgeography.net/fundamentals/10ah.html

North African trade wind patterns are defined primarily by latitudinal location (Figure 8) and are modified, intensified, and changed through low-level jets (a region of relatively strong winds in the lower part of the atmosphere), jet streams, moisture content and other weather, and climate factors. Additionally, diurnal variations occur as warm air descends after sunrise, increasing the air pressure variations and thus, increasing wind velocity (N'Tchayi, et al., 1996). Seasonal variations also occur as low level jets migrate northward and southward, strengthening during drier periods (Washington, et al., 2006).

The low level jet of the Bodele Depression may be responsible for increased emissions of dust (Washington, et al., 2006; Tegan, et al., 2006), and may have

contributed to the formation of the depression during the post-Holocene. Currently, the Bodele Depression is affected by northeast trades winds all year, but are affected by increased dry, hot, Harmattan winds (Figure 9) during the winter months. These Harmattan winds converge with the warm moist Atlantic monsoon air masses from the south where they meet and mix over hundreds of kilometers. Harmattan winds normally override the monsoons carrying ~50± 15Tg of mineral dust to the Amazon River Basin each winter in the Northern Hemisphere from November to April (Koren, et al., 2006; Kaufman, et al., 2005).

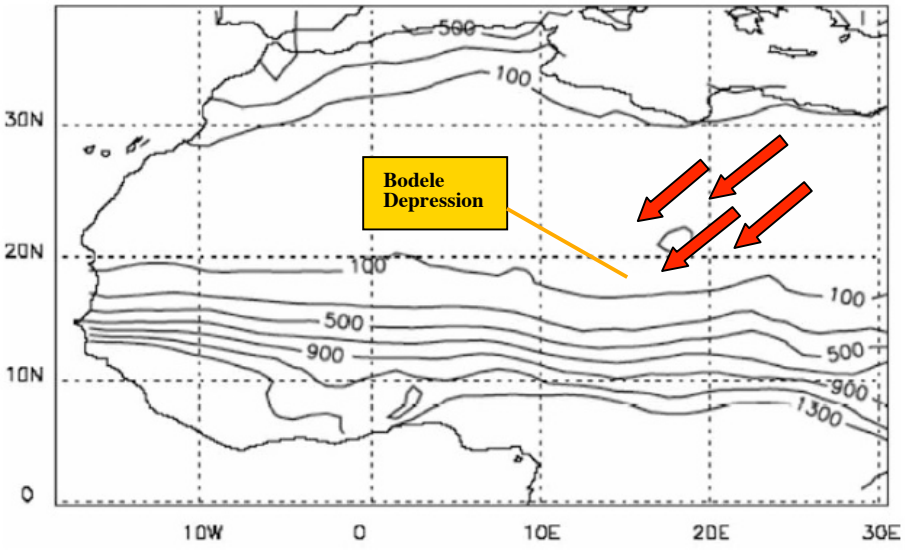

Figure 8. Trade Wind Patterns of Northern Africa, with the Sahara general wind direction indicated by red arrows
Source: From the dataset of New, et al., 2000

Brooks, et al., (2005) determined that the monsoon rain belts had shifted N-S and S-N during the early Holocene (~ 6,000-10,000 years before present). These shifts in the Sahara boundaries northward and southward over time changed the

climate latitudinally causing increased rainfall at latitudes not currently receiving significant rainfall (rainfall in an area < 100mm is considered arid). Additionally, the shifts in monsoonal rain belts have been correlated with glacial cycles, of which 17 have occurred over the past 1.6 million years. This indicates that the shifting boundary of the southern edge of the Sahara has caused changes in climate over time as rainfall increased and decreased in a given area depending on the location of the monsoonal shift (Brooks, et al., 2005). In fact, studies of fossil dunes (Talbot, 1982) have been located ~5° south of the present mobile dunes.

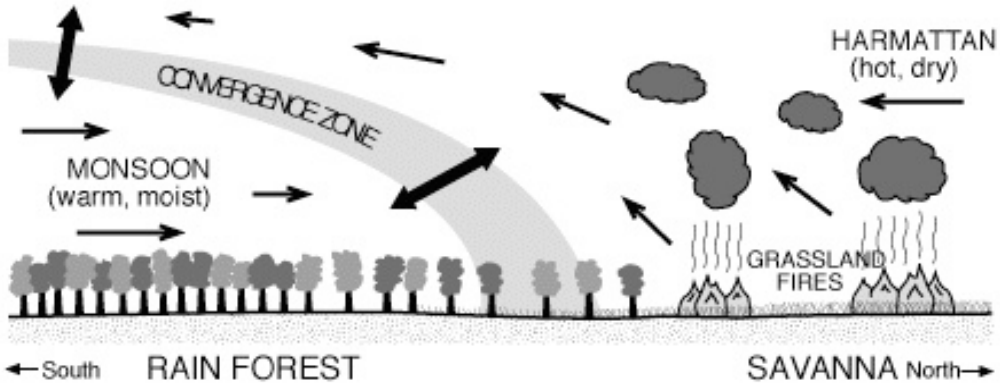

Figure 9. Harmattan Wind Diagram
Source: Bob Henson, UCAR communications

Once sediments are lofted by winds, they can become entrained. Entrained sediments, usually between 0.5μm and 10μm in size, are sustained in the upper atmosphere and then considered aerosols by atmospheric scientists. These mineral dust aerosols may constitute up to ~50 percent of known aerosols in the upper atmosphere.

Research on the effects of aerosols on climate and climate change has increased over the past two decades. Identification of aerosol sources and the spatial

and temporal distribution in the troposphere (Swap, et al., 1996) are of major interest to scientists. Studies strongly suggest these factors affect global climate through

direct and indirect radiative forcing in the atmosphere by effecting temperature profiles (Kaufman, et al., 2002; Broecker, 2002; Myhre, et al., 2003; Facchini, et al., 1999; Kaufman, et al., 2001; Dubovik, et al., 2003; Hansen, et al., 1997; Charlson, et al., 1992; Duce, 1995). Complicating issues, the role as condensation nuclei (CNN), affects on water vapor through changes in cloud cover, cloud properties, and cloud precipitation, and interactions with other aerosols during transport are poorly understood and make modeling the effects of aerosols on climate difficult (Kaufman, et al., 2002; Novakov and Corrigan, 1996; Clarke, 1992; Chuang, et al., 2002; Feingold, et al., 1999a).

Additionally, the size, shape, distribution, and composition of atmospheric aerosols may adversely affect climate (Kaufman, et al., 2002; Zender, et al., 2003a and 2003b; Alfaro, et al., 1998; Dubovik, et al., 2006, Gong, et al., 1998), and understandings of these parameters are limited for use in modeling climate. Of the major atmospheric aerosols, sea salt, black carbon, ash, and mineral dust, atmospheric mineral dust is the least understood, and may have the most impact on climate. Difficulties in precisely pinpointing source areas for atmospheric mineral dust makes it difficult to identify source regions for dust emissions, hence mineral composition identification is problematic. This study, therefore, focuses on identification of the mineral dust emitted from the Bodele in north- central Africa, in

the Sahara, known as the single dustiest place on Earth (Koren, et al., 2006; Tegan, et al., 2006; Todd, et al., 2005; Washington, et al., 2005 and 2006).

Of great importance, and little understood in the field of atmospheric sciences, are the tiny particles suspended in the atmosphere responsible for providing the "seeds" upon which water vapor condenses to form clouds (CNN). These aerosols are emitted into the atmosphere naturally and through human endeavors (anthropogenic). The source of these aerosols often dictate the type of environmental responses they undergo in the atmosphere, as well as the impact they exert on the meteorological processes in a local, regional or global environment.

At the forefront of current atmospheric aerosol research are studies being conducted to better understand the structure, size and distribution, and reflectivity of aerosols, which is essentially determined by their source region (Zender, 2006). Research into source regions (Flores, et al., 2006; Prospero, et al., 2002; Tegan and Fung, 1994) has resulted in a much more complex parameterization of definable impacts on portions of the climate processes than originally thought necessary, and instead of answering a multitude of climate questions, the knowledge of aerosol sources and the impact on climate change has created more unanswered questions with few sustainable answers.

To confuse the climate issue further, anthropogenic aerosols, far less understood than natural aerosols, are becoming more profuse as human activities continue to produce aerosols in quantities high enough to imbalance the energy budget of the Earth system (Novakov, et al., 1996; Martins, et al., 1998), possibly

effecting overall climate change. In particular, assessing the effect of anthropogenic aerosols on aerosol/cloud interactions is sufficiently uncertain (Intergovernmental Panel on Climate Change (IPCC), 1996) and creates considerable ambiguity concerning the overall effect of anthropogenic aerosols on direct and indirect climate forcings.

Because clouds play a major role in governing many aspects of global climate, studies involving cloud development, sustainability, interactions, radiative properties, type, and distribution are crucial to understanding how aerosols affect cloud properties and precipitation. The global distribution of cloud cover in the atmosphere at any given time is averaged to approximately 50 percent (Figure 10). Clouds regulate the amount of incoming solar radiation (ISR) that reaches the surface of Earth, the quantity reflected back into space, how much is absorbed in the atmosphere, how and where warmth is distributed around the globe, and how much heat escapes the surface and atmosphere to be lost back into space. Understanding aerosol impact on cloud formation and interactions are necessary in understanding aerosol effect on global climate.

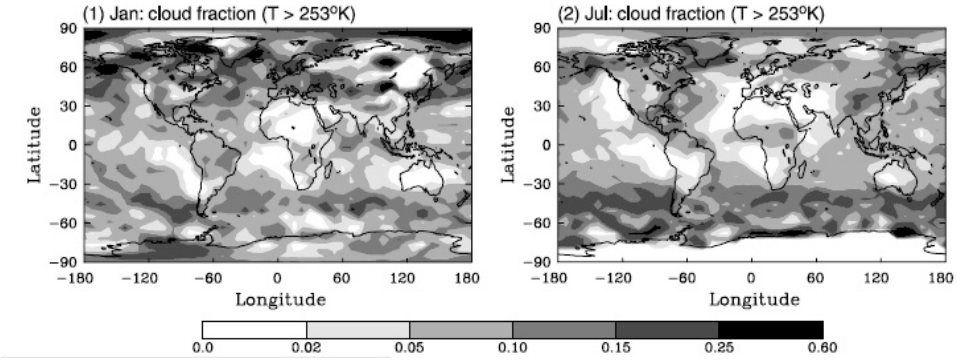

Figure 10. Model Simulated Column Averages of Cloud Fraction for Clouds with T>253°K
Source: Chuang, et al., 2002

Aerosols in General

Aerosols are defined as submicron particles suspended in the atmosphere upon which it is possible for water vapor to condense and form clouds. Through this normal process, latent heat energy is given off as the water vapor changes phase from a gas to a liquid, or a solid in the case of ice crystals (i.e. cirrus cloud formation at higher altitudes). This heat energy warms the air around it and creates unequal heating in a dynamic system known as cloud formation, subsequent disbursement, and possible precipitation. This scenario can be seen on any given day since 50 percent of the atmosphere contains some clouds at all times. Some types of clouds rarely produce precipitation (i.e. the cirrus clouds) and other do produce precipitation, (stratocumulus clouds), hence, it would appear that weather prediction, and the prediction of climate patterns would be a simple matter (Lu, et al., 2006). Contrary to this assumption, scientists found a multitude of factors determining that not all aerosols act as cloud condensation nuclei (CCN) equally.

Remotely sensed data collected with satellite tools (i.e. TOMS, MODIS, MISR) show various types, sizes, distributions, and sources of atmospheric aerosols and how some of these aerosols respond to atmospheric conditions and processes very differently from one another giving rise to the belief that these aerosols may be affecting the global climate system. Based on this evidence and indicators on direct and indirect climate forcing to be discussed later, aerosol studies have intensified dramatically. From an estimated seven to ten research papers a year in the early 1970's to over 100 per year by the year 2000 (Kaufmann, Y., et al., 2004), scientists

around the globe are taking a closer look at the “seeds” of cloud formation in order to better understand global climate change.

The two aerosol sources are natural and anthropogenic. They are submicron in size, and will act as cloud condensation nuclei (CNN) when atmospheric conditions allow water vapor to cool and release latent heat energy. Under normal conditions, this process allows heat energy to warm the surrounding atmosphere while increasing the likelihood for further moisture to be condensed, as warm air holds more moisture. This is a dynamic system, and changes in the system are tumultuous given the constant changes in air temperature, air pressure, wind speeds, updrafts and downdrafts, evaporation, condensing, transport, and distribution over broad regions in short periods of time.

Natural aerosols are produced through Earth processes. Winds pick up dust and send it aloft in the troposphere to be carried as far away as thousands of miles from the source region. Volcanoes spew ash and dust particles know to circle the Earth in less than three days. Pollens, ash from forest fires, and a multitude of other natural aerosols are approximately the submicron size necessary to form cloud droplets that are the most likely to produce clouds could eventually produce precipitation within the region of formation. Additionally, these aerosols have reflective properties based on the constituent properties of the aerosol source, and when all of the weather and climate processes are in place, create a global radiative energy balance necessary for a normative Earth environment.

Anthropogenic aerosol sources are varied and produce smaller particle sizes and diverse composition aerosols with properties and reflectance capabilities unlike

natural aerosols. Since the Industrial Revolution, anthropogenic aerosols have continued to increase in number and significance relative to the affect they have on global climate change. Major contributing sources for anthropogenic aerosols include fossil fuel and biomass burning, agricultural practices, and changes in land management and use. The most significant properties and characteristics of these aerosols related to the affect imposed on climate are the radiative effects and single scattering albedo (Hansen, et al., 1997), accumulation mode (hydroscopic level) (Jones, et al., 1994), and the first and second direct forcing, as well as indirect effects on global climate change (Penner, et al., 1999a, 1994b).

A difficult task is the concept of point-sourcing aerosols. To define aerosol sources, it is important to note that many species of aerosols are not directly emitted into the atmosphere, but are products formed in the atmosphere through mechanical and chemical processes imposed upon gaseous precursors (e.g., sulphates and secondary organics) in the production of anthropogenic aerosols. Sourcing for natural aerosols is usually a product of simple meteorological or solid Earth processes (sea salt spray, dust, and volcanic eruptions) (Levin, et al., 2005). In addition, refractive indexes (RI) vary widely for aerosols because RI depends on particle size, composition, and distribution spatially and temporally (Sassen, et al., 2003). These properties also influence aerosol atmospheric lifetimes and radiative effects. To complicate research further, many aerosol species combine to form mixed particles with optical properties and atmospheric lifetimes different from those of their components (Table 1).

Table 1. Annual Aerosol Source Strength

	Northern Hemisphere	Southern Hemisphere	Global[a]	Range	Source
NO_x (as TgN/yr)	32	9	41		(see also Chapter 4).
Fossil fuel (1985)	20	1.1	21		Benkovitz *et al.* (1996)
Aircraft (1992)	0.54	0.04	0.58	0.4-0.9	Penner *et al.* (1999b); Daggett *et al.* (1999)
Biomass burning (ca. 1990)	3.3	3.1	6.4	2-12	Liousse *et al.* (1996); Atherton (1996)
Soils (ca. 1990)	3.5	2.0	5.5	3-12	Yienger and Levy (1995)
Agricultural soils			2.2	0-4	Yienger and Levy (1995)
Natural soils			3.2	3-8	Yienger and Levy (1995)
Lightning	4.4	2.6	7.0	2-12	Price *et al.* (1997); Lawrence *et al.* (1995)
NH_3 (as TgN/yr)	41	13	54	40-70	Bouwman *et al.* (1997)
Domestic animals (1990)	18	4.1	21.6	10-30	Bouwman *et al.* (1997)
Agriculture (1990)	12	1.1	12.6	6-18	Bouwman *et al.* (1997)
Human (1990)	2.3	0.3	2.6	1.3-3.9	Bouwman *et al.* (1997)
Biomass burning (1990)	3.5	2.2	5.7	3-8	Bouwman *et al.* (1997)
Fossil fuel and industry (1990)	0.29	0.01	0.3	0.1-0.5	Bouwman *et al.* (1997)
Natural soils (1990)	1.4	1.1	2.4	1-10	Bouwman *et al.* (1997)
Wild animals (1990)	0.10	0.02	0.1	0-1	Bouwman *et al.* (1997)
Oceans	3.6	4.5	8.2	3-16	Bouwman *et al.* (1997)
SO_2 (as TgS/yr)	76	12	88	67-130	
Fossil fuel and industry (1985)	68	8	76	60-100	Benkovitz *et al.* (1996)
Aircraft (1992)	0.06	0.004	0.06	0.03-1.0	Penner *et al.* (1998a); *Penner et al.* (1999b); Fahey *et al.* (1999)
Biomass burning (ca. 1990)	1.2	1.0	2.2	1-6	Spiro *et al.* (1992)
Volcanoes	6.3	3.0	9.3	6-20	Andres and Kasgnoc (1998) (incl. H_2S)
DMS or H_2S (as TgS/yr)	11.6	13.4	25.0	12-42	
Oceans	11	13	24	13-36	Kettle and Andreae (2000)
Land biota and soils	0.6	0.4	1.0	0.4-5.6	Bates *et al.* (1992); Andreae and Jaeschke (1992)
Volatile organic emissions (as TgC/yr)	171	65	236	100-560	
Anthropogenic (1985)	104	5	109	60-160	Piccot *et al.* (1992)
Terpenes (1990)	67	60	127	40-400	Guenther *et al.* (1995)

Source: IPCC compilation, 2001

Finally, the formation of clouds affects aerosols as well. The clouds can scavenge aerosols by adding mass through liquid phase chemistry, and through the formation of new aerosol particles in and near clouds. These chemical reactions are dynamic and tend to occur in seconds in tumultuous events. The new aerosol cloud droplets will have characteristics and properties again, very different from their component parts (Penner, et al., 1999a, 1994b).

Modern aerosol sourcing has made substantial progress in the last three years. Today we have better inventories of precursor gas emission for many species (including DMS and SO2; Table 1).

Additionally, the scientific emphasis is on spaciotemporally resolved source and distribution fields. Mathematical conversion methods are better-understood and explicit representation of number/size and mass/size distributions (Tegan, et al., 2006; Zender, 2006) as well as the specification of optical and hydration properties in models have seen progress. In the future, real data analysis and modeling will deviate little and modeling will become a normal method for climate prediction and global climate change (Ginoux, et al., 2003).

Primary and Secondary Sources of Aerosols

Soils dust is a major contributor to atmospheric aerosols. It is especially responsible for aerosol attributes such as optical thickness and aerosol loading in the sub-tropics and tropical regions of the globe. It is estimated that between 1,000 and 5,000 Mt/year (Table 2) of dust become atmospheric aerosols (Duce, et al., 1995) with a high spatial and temporal variability. These soils dust originate in deserts, dry lakebeds, semi-arid desert fringes, and dry regions disturbed by human activity.

Most of the dust aerosols are produced in the Northern Hemisphere (NH), therefore, studies concerning global climate issues normally separate the NH from the SH when releasing results. These soils aerosols are up drafted through the deflation process where surface wind speeds exceed the threshold velocity of a particle size/mass ratio. It is a function of surface roughness, grain size, and soil

moisture. Upwards of 50 percent of these dusts are considered anthropogenic in origin (Tegan and Fung, 1995), but that may be disputable. Until recently, it was believed that most aerosol dust was due to natural processes. Today scientists are still undecided about the quantity of atmospheric mineral dust produced through natural processes, and how much is anthropogenic (Ginoux, et al., 2003).

Confusing this issue are normal climate anomalies. Examples are sited in classic El Niño cycles when Saharan dust quantities deposited in the Caribbean have increased substantially (Prospero and Ness, 1996), and in North American oscillations (La Niña) the dust export is to the Mediterranean and North America (Moulin, et al., 1997).

Table 2. Primary Particle Emissions

	Northern Hemisphere	Southern Hemisphere	Global	Low	High	Source
Carbonaceous aerosols						
Organic Matter (0-2 μm)						
Biomass burning	28	26	54	45	80	Liousse *et al.* (1996), Scholes and Andreae (2000)
Fossil fuel	28	0.4	28	10	30	Cook *et al.* (1999), Penner *et al.* (1993)
Biogenic (>1 μm)	-	-	56	0	90	Penner (1995)
Black Carbon (0-2 μm)						
Biomass burning	2.9	2.7	5.7	5	9	Liousse *et al.* (1996); Scholes and Andreae (2000)
Fossil fuel	6.5	0.1	6.6	6	8	Cooke *et al.* (1999); Penner *et al.* (1993)
Aircraft	0.005	0.0004	0.006			
Industrial Dust, etc. (>1 μm)			100	40	130	Wolf and Hidy (1997); Andreae (1995) Gong *et al.* (1998)
Sea Salt						
d< 1 μm	23	31	54	18	100	
d=1-16 μm	1,420	1,870	3,290	1,000	6,000	
Total	1,440	1,900	3,340	1,000	6,000	
Mineral (Soil) Dust[b]						
d< 1 μm	90	17	110	-	-	
d=1-2 μm	240	50	290	-	-	
d=2-20 μm	1,470	282	1,750	-	-	
Total	1,800	349	2,150	1,000	3,000	

Source: Duce, 1995

Note: for the year 2000 (Tg/year).

As seen in the primary particle emission table (Table 2), soils dust quantities can be significantly high, and produce large numbers of particles for distribution over very broad regions, sometimes thousands of miles.

Once the dust is airborne, its lifetime in the atmosphere is dependent on particle size. Larger particles (greater than a micron) are the first to sort out (be deposited), while the smaller particles (sub-micron size) could stay up for several days to 2-3 weeks before being deposited out of the system, or becoming cloud condensation nuclei and leaving the atmospheric system through precipitation (Figure 11). Figure 11 illustrates the quantity of mineral dust emitted globally, and the excessively high concentrations of dust emitted from the Sahara. Mineral dust emissions exceed all other aerosol sources in global production, but constitute a relatively small area of landmass by comparison.

Sea salt is the most common primary aerosol. The physical processes that force emissions of sea salt into the atmosphere are the bursting of entrained air bubbles as whitecaps form on the surface of the ocean. These whitecaps are driven by wind speed at the surface; therefore, the quantities of sea salt dispersion are directly related to wind speed (Levin, et al., 2005). The sea salt aerosols are the dominant and most efficient cloud condensation nuclei. They are able to absorb water quickly to form water droplets for cloud formation, and have dominant light scatter efficiency. It is estimated that there is a particle of sea salt for every liter of air. These giant salt particles (submicron in size, they are still giant aerosols) modify stratocumulus cloud drizzle and cloud albedo significantly (Feingold, et al., 1999).

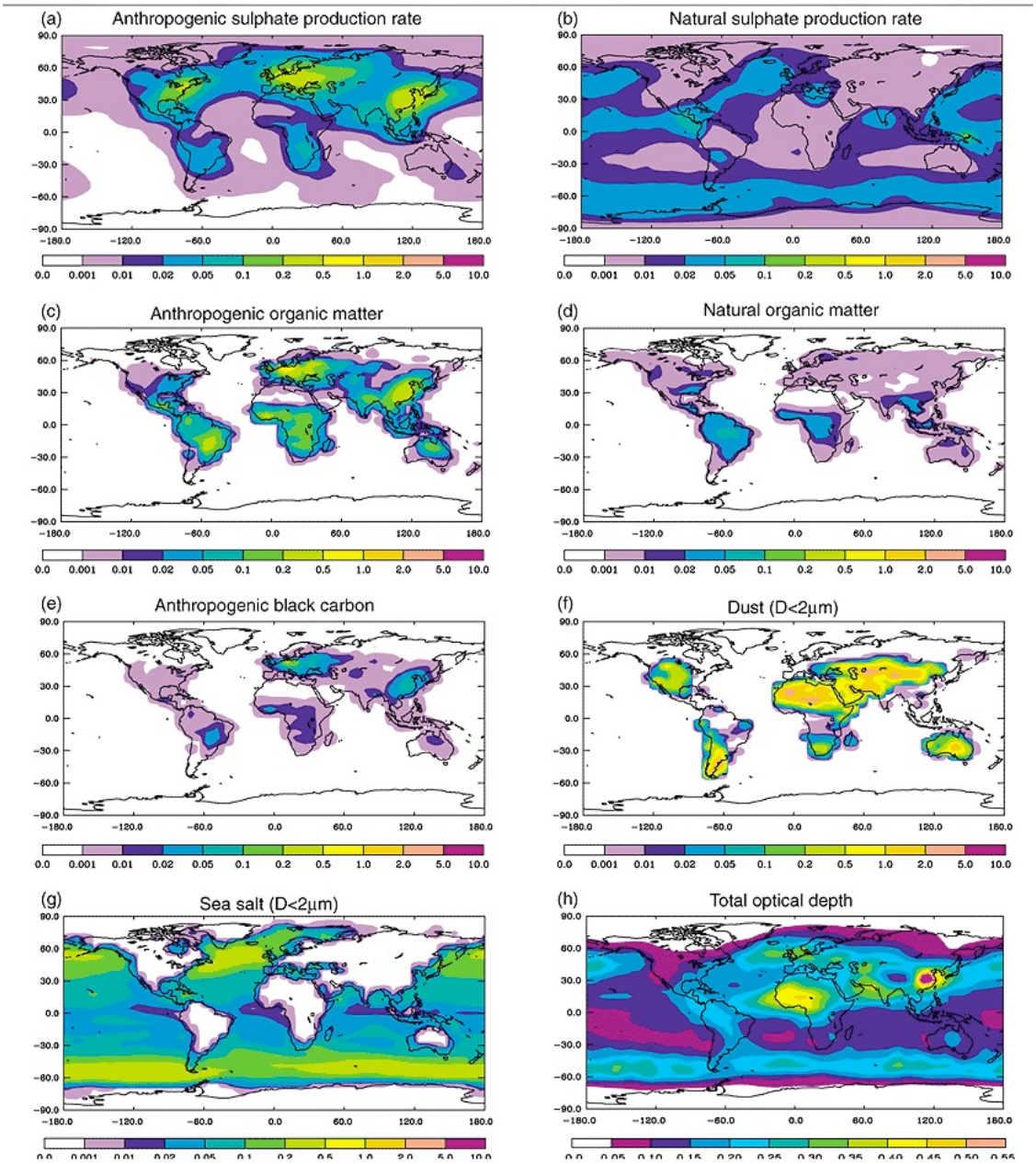

Figure 11. Annual Average Aerosol Source Strength
Source: IPCC, 2001

The sizes of sea salt aerosols range between 0.05-10.0 μm, with atmospheric lifetimes of a few days to about two weeks. With these disparities, analysis of emission and distribution needs a size-resolved model (Gong, et al., 1998). The total estimate of these aerosols in the atmosphere, based on a modern model, is close to

3,300 Tg/yr (Gong, et al., 1998) and appears to be in line with previous studies that put the figure at 1,000-3,000 Tg/yr (Erickson and Duce, 1988), or the average of 5,900 Tg/yr (Tegan, et al., 1997). A newer model would need to be somewhere between the modern and older values to be effective (Figures 12 and 13).

Industrial dust is the primary anthropogenic aerosol. It is estimated that between 100 Tg/yr (Andrea, 1995) and 200 Tg/yr (Wolf and Hidy, 1997) of industrial aerosols are distributed every year. They are derived from sources widely monitored and regulated and include aerosols from fossil fuel burning (coal, gasoline, etc.), cement manufacture, metallurgy and waste incinerators. These aerosols are not considered factors in the global climate model because their impact is minimal on a global scale (Figure 14). There is serious discussion among atmospheric scientists that suggest this may not be the case. Until further research is conducted and conclusions are reached, these aerosols will not be discussed again in this paper.

Carbonaceous aerosols, organics and black carbons (hydrocarbons), make up a large fraction of anthropogenic aerosols. They are highly variable in size and distribution, as well as in their scattering efficiency and cloud condensation nuclei availability. They originate, primarily, from biomass burning, whether natural or anthropogenic. Other sources for these aerosols include fossil fuel burning, and atmospheric oxidation of biogenic and anthropogenic volatile organic compounds (VOC; Organic chemical compounds that have a high enough vapor pressure under normal conditions to vaporize and enter the atmosphere).

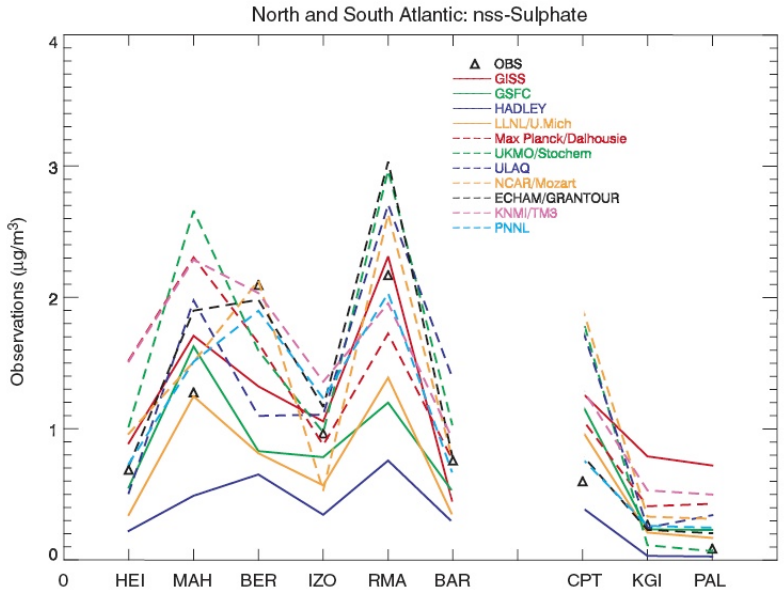

Figure 12. Observed and Model-Predicted Annual Average Sulphate Concentrations
Source: Data provided by D, Savoie and J. Prospero, University of Miami.

Note: Non-Sea Salt Sulphate (in µg m-3) at a series of stations in the North and South Atlantic.

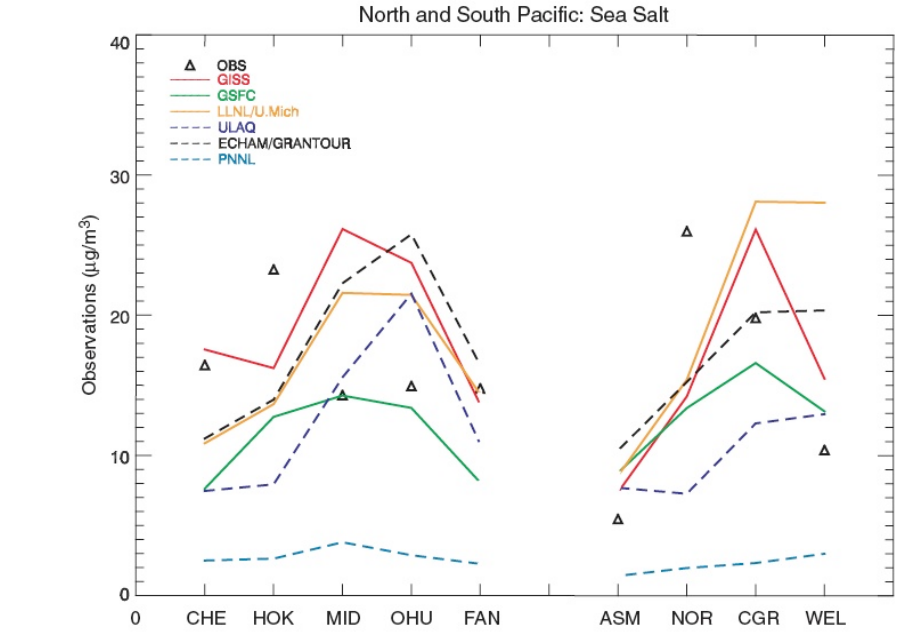

Figure 13. Observed and Mode-Predicted Annual Average Concentrations of Sea Salt.
Source: Data provided by D, Savoie and J. Prospero, University of Miami.

Note: Sulphate (in µg m-3) at a series of stations in the North and South Atlantic.

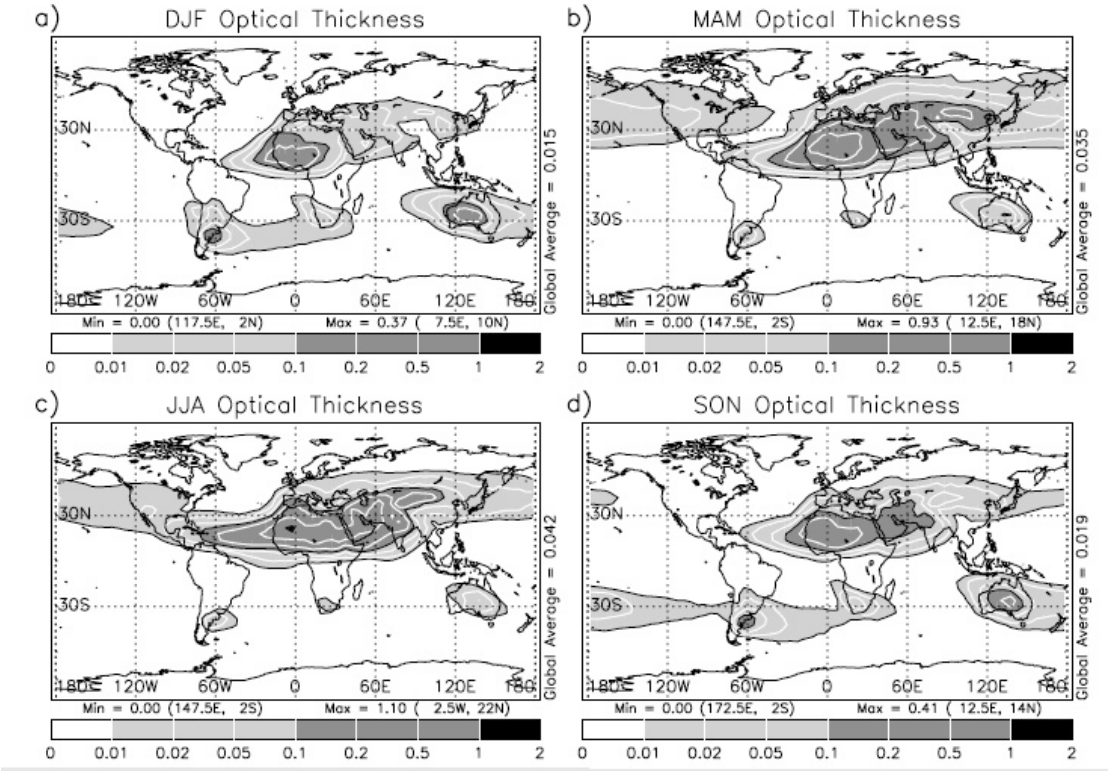

Figure 14. Simulated Surface Mass Concentrations of Dust Particles
Source: Miller, et al., 2006

Note: With (a) d< 2μm and (b) 2<d<20 μm. Bracketed values are global average A and maximum M.

Estimations for emissions of these aerosols are approximately 45-80 Tg/yr for biomass burning black carbons, and 10-30 Tg/yr for fossil fuel burning (Liousse, et al., 1996). Organics are the largest component of biomass burning (Andrea, 1998), scatter as much light as sulfates do (Hegg, et al., 1997), tend to concentrate in the upper atmosphere (Rivera and Carpio, 1996), and make excellent cloud condensation nuclei (Saxena, et al., 1995).

Atmospheric oxidation of biogenic hydrocarbons will yield hydrocarbons. This process produces compounds of low volatility that readily form aerosols. This is a gas to particle conversion, and is considered a secondary organic aerosol (SOA).

The size of the aerosol produced is still submicron. Studies in isolated smog chambers provided data with a VOC emissions rate of some 300-500 Tg/yr that provided global aerosol production from biogenic precursors at 30-270 Tg/yr (Andreae and Crutzen, 1997). These studies are contradicted by further studies indicating that knowledge of biomes, plant type and emissions of monterpenes, or ORVOC, on a global scale can produce accurate inferred results (Griffin, et al., 1999).

Aerosol production yields, however, also depend on oxidation mechanisms, according to some experiments. In general, oxidation by O_3 or NO_3 yields more aerosols than the oxidation of OH (Hoffman, et al., 1997). The only regions where O_3 or NO_3 are predominant are where pollution is in evidence on a global scale, therefore, most oxidation of this type occurs through OH reaction.

Aerosol Light Scattering Efficiency

The complexities surrounding the understanding of radiative properties of anthropogenic aerosols has led to studies of their effect on radiative forcing, which is believed to impact global climate change. To provide accurate data and prediction, properties relevant to radiative forcing need to be considered and understood. Composition, size, and distribution of aerosols are the suspect properties related to both direct and indirect radiative forcing, and knowledge of four quantities as a function of λ is necessary to translate aerosol burden into optical depths and then radiative perturbance. This is due, primarily, to the limitations of measurement vertically in a column of given air, as satellites are able to give us τ (tao) at the

uppermost surface of the cloud, and ground instruments the bottom (τι) layer. These quantities are mass light-scattering efficiency (asp), functional dependency of light-scattering relative to relative humidity (RH), the single-scattering albedo of the aerosol (ωo), and the asymmetry parameter, g (Charlston, et al., 1992; Penner, et al., 1994) (Figure 15).

Atmospheric mineral dust identification is critical for determining the hygroscopicity of the aerosols as they are transported over long distances mixing internally and externally with other aerosols, and interacting with water vapor and solar radiation. Of the four quantities, light scattering is measurable, or can be calculated, from aerosol studies on size and composition allowing for "closure studies" to compare different measurements for consistency. For example, derived optical depth comparison with directly measured or inferred optical depths of aerosols using sun photometers or satellite radiometers are being used to determine light scattering efficiency quantities at specific locals (Clarke, et al., 1996; Hegg, et al., 1991). This does not take into account aerosols in accumulation mode (the ability to hydrate). Aerosols in accumulation mode with dry diameters between 0.01 and 1 μm are most important because they can hydrate to 0.1 and 2.0 μm increasing the mass extinction rate of efficiency the greatest (Schwartz, 1996), increasing light scattering efficiency within the cloud, and reduce the amount of light scattered back into the atmosphere.

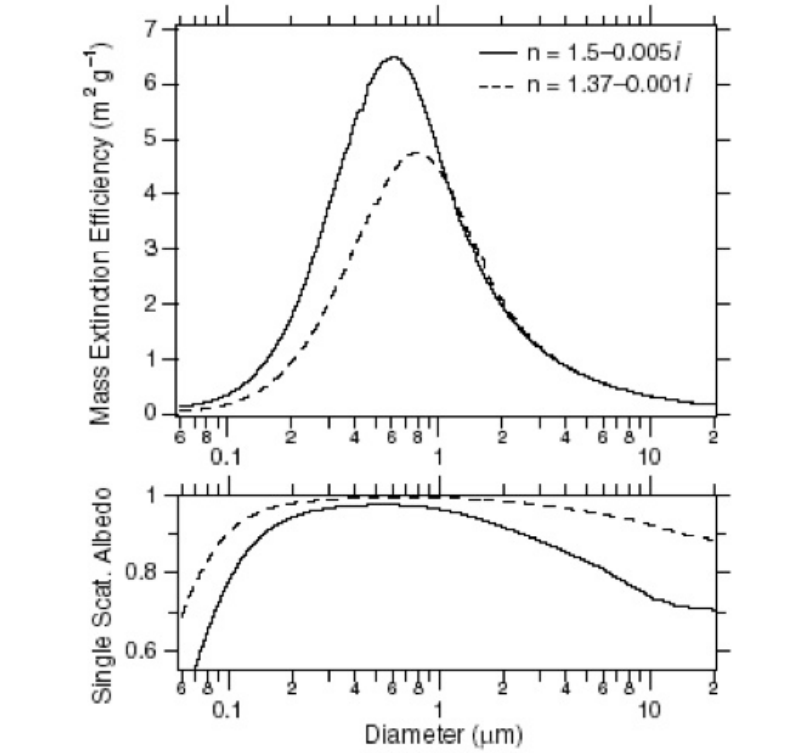

Figure 15. Extinction Efficiency (per unit aerosol mass) and Single Scattering Albedo (ωo)
Source: Andreae, et al., 2005

Note: The calculations are integrated over a typical solar spectrum rather than using a single wavelength. Aerosols with a diameter of between 0.1 and 2μm scatter the most light per unit mass. Coarse mode aerosols (i.e. those larger than accumulation mode) have a smaller single scattering albedo even if they are made of the same material (i.e. refractive index) as accumulation mode aerosols. If the refractive index 1.37-0.001i is viewed as that of a hydrated aerosol, then the curve represents the wet extinction efficiency. The dry extinction efficiency would be larger and shifted to slightly smaller diameters.

These accumulation mode aerosols, hence, have high light scattering efficiency. In addition, they tend to have a longer atmospheric lifespan (up to 5-7 days) and produce the majority of cloud condensation nuclei for a given region due to the aerosol hydration capabilities. In this respect, anthropogenic aerosol perturbances, (i.e. sulfur emissions) have a large climate impact when they produce, or affect, accumulation mode aerosols (Jones et al., 1994) The hydrated aerosols,

therefore, in a size range between 0.1-2.0 μm, increase mass extinction while increasing scatter efficiency within the cloud (Figure 16) and a have direct effect on climate forcing.

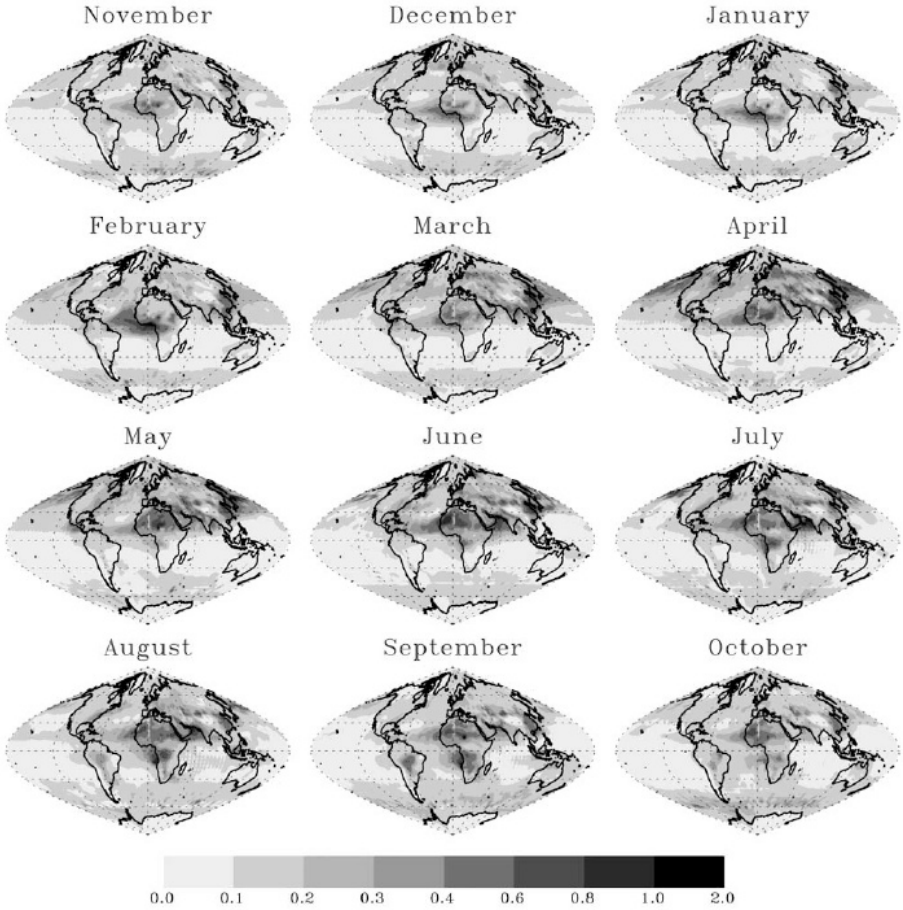

Figure 16. Aerosol Optical Depth
Source: Yu, et al., 2003

The relative humidity in a given volume of air (parcel) is going to affect the functional dependency of light scattering within the cloud, f (RH) dependent upon the aerosol present at a given time. However, uncertainties exist in measurements of most anthropogenic aerosols, and calculations on quantities and effect are limited to known parameters. When measuring scattering efficiency in a saturated parcel of air,

the function of RH is calculated with known accumulation modes of identified aerosols (Jones, et al., 1994).

Depending on the source aerosol, the direct radiative effect of the aerosol can be sensitive to single scattering albedo, or ωo (the ratio of scattering efficiency to total light extinction (scattering + absorption); Mainly defined for small-particle scattering of electromagnetic waves). For example, a change in ωo 0.9 to 0.8 (Figure 17) can change the sign of the direct effect of depending on the albedo of the underlying surface, and the aerosol altitude (Hansen, et al., 1997). Since it is very difficult to measure ωo accurately, some anthropogenic aerosols can be "weeded" out of the samples simply by separating them out from other aerosols using filters. Black Carbon aerosols, which are very high absorbers of solar radiation, (Figure 17) are one such aerosol that can be separated in this manner. In addition to filtering black carbons out of the "mix", this measure can also provide data on light extinction (that light absorbed directly by black carbons) and light scattering, through measuring the difference between extinction and scatter. This is difficult in that absorption is often the difference between two very large numbers, so careful calibration of tools is necessary to obtain accurate readings (Dubovik, et al., 1998). In addition, retrieving ωo data from satellites is inaccurate therefore, well-calibrated Sun photometers are used at ground stations and in aircraft, and their data is compared to direct Sun extinction measurements (Dubovik, et al., 1998).

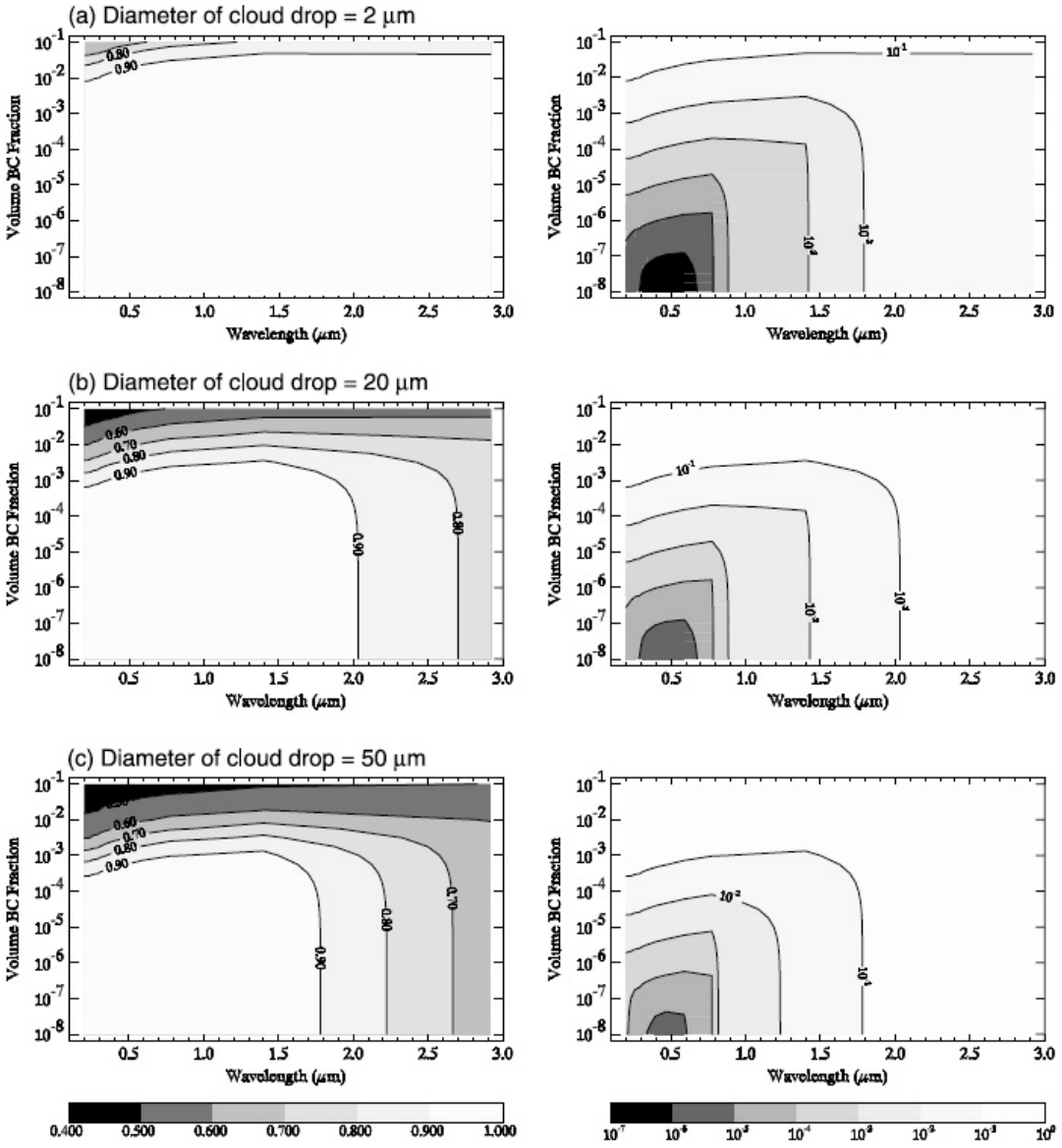

Figure 17. Variations of Single Scattering Albedo
Source: Chuang, et al., 2002

Note: Single scattering albedo (left panel) and co-albedo (right panel) of cloud drops as a function of volume black carbon fraction and wavelength.

When considering specific aerosol species, light scattering efficiencies vary greatly for various reasons. Dust sizes, for example, have a range of 1-20μm (Table

2), therefore, the refractive indexes vary. Minerals mixed internally or in aggregates (Tegan and Lacis, 1996; Sokolik and Toon, 1996) will produce a wide range of light scattering efficiencies. Scientists derive a volume median diameter between 2-4μm to determine the average, or use the Saharan dust radiative indices to estimate global dust radiative forcing (Tegan, 1996). In this manner, they can adjust for differences in the size/distribution ratio. Findings indicate that the model has a scattering albedo of less than 1, resulting in small forcings due to particle cancellation of solar and thermal forcing, as well as a plus and minus forcing over geographic regions (Tegan and Lacis, 1996). However, different radiative indices from different regions, as well as regional albedo differences at the surface, lead to a large uncertainty in "top of the atmosphere" (tao) atmospheric dust forcings (Sokolik and Toon, 1996). This is primarily due to initial aerosol light scattering at the cloud top. This creates a very bright image, and scattering is difficult to measure.

It is also difficult to determine the light scattering albedo for black carbons with any accuracy. These aerosols absorb solar radiation, reduce energy reaching the surface of the Earth, and are considered the first direct forcing effect on the radiation budget, know as the Twomey Effect (Figure 18). There is no accurate method to separate the black carbons from other organic carbon aerosols with efficiency. Some thermal methods are used to measure the amount of carbon evolved from a filter sample as a function of temperature. The problems here are due to errors from pyrolysis of organics, or the interference from other species of aerosols (Reid, et al., 1998; Martins, et al., 1998). Another method uses light absorption of aerosols on a filter measured in transmission or reflectance, but calibrations for converting this

change to black carbon is not universally accepted in the science community, and is often not applicable (Liousse, et al., 1993). Therefore, it is very difficult to identify the source strength of light absorbing aerosols (Figures 19 and 20).

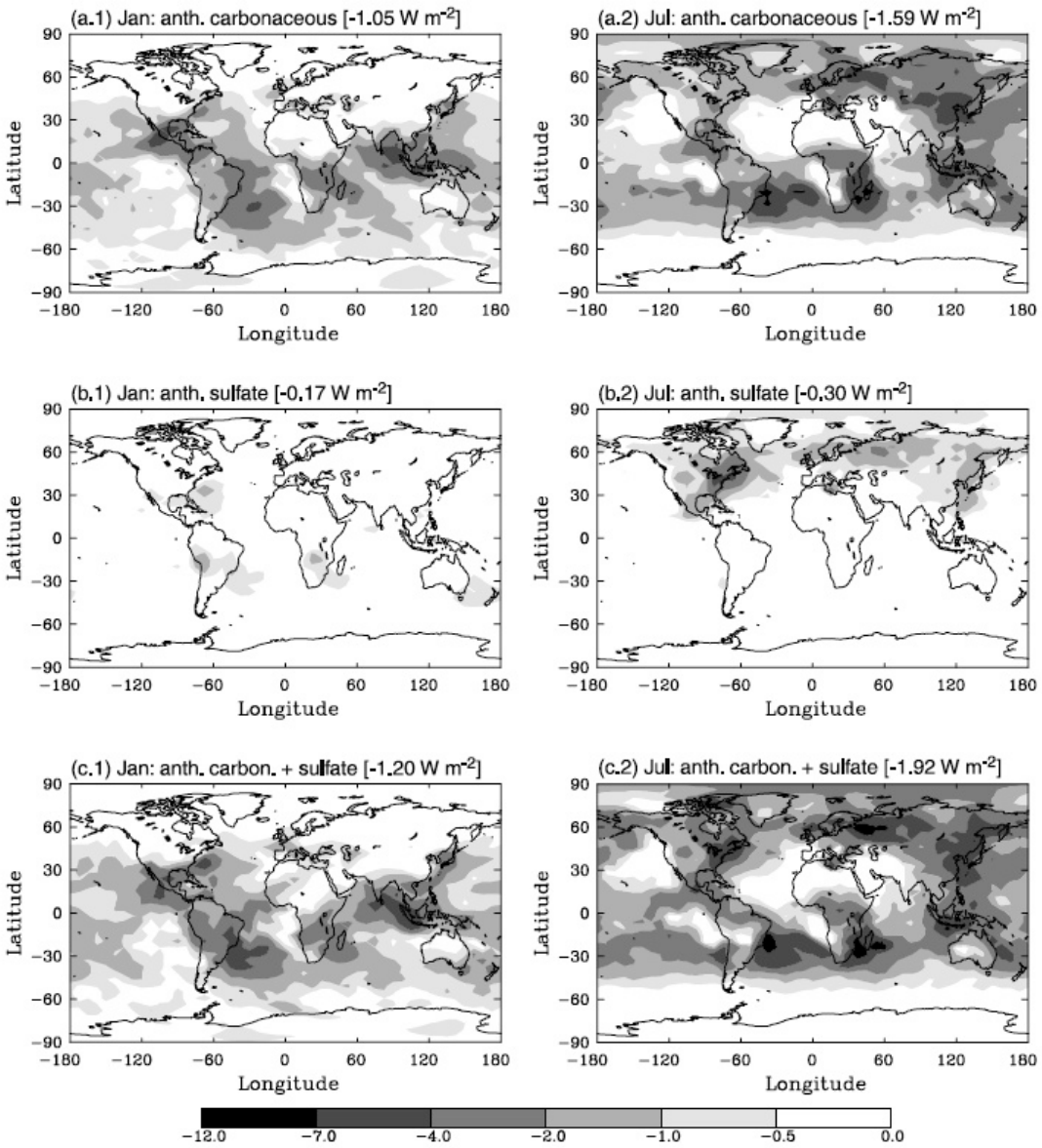

Figure 18. Monthly Averages of Simulated First Direct Forcings
Source: Chuang, et al., 2002

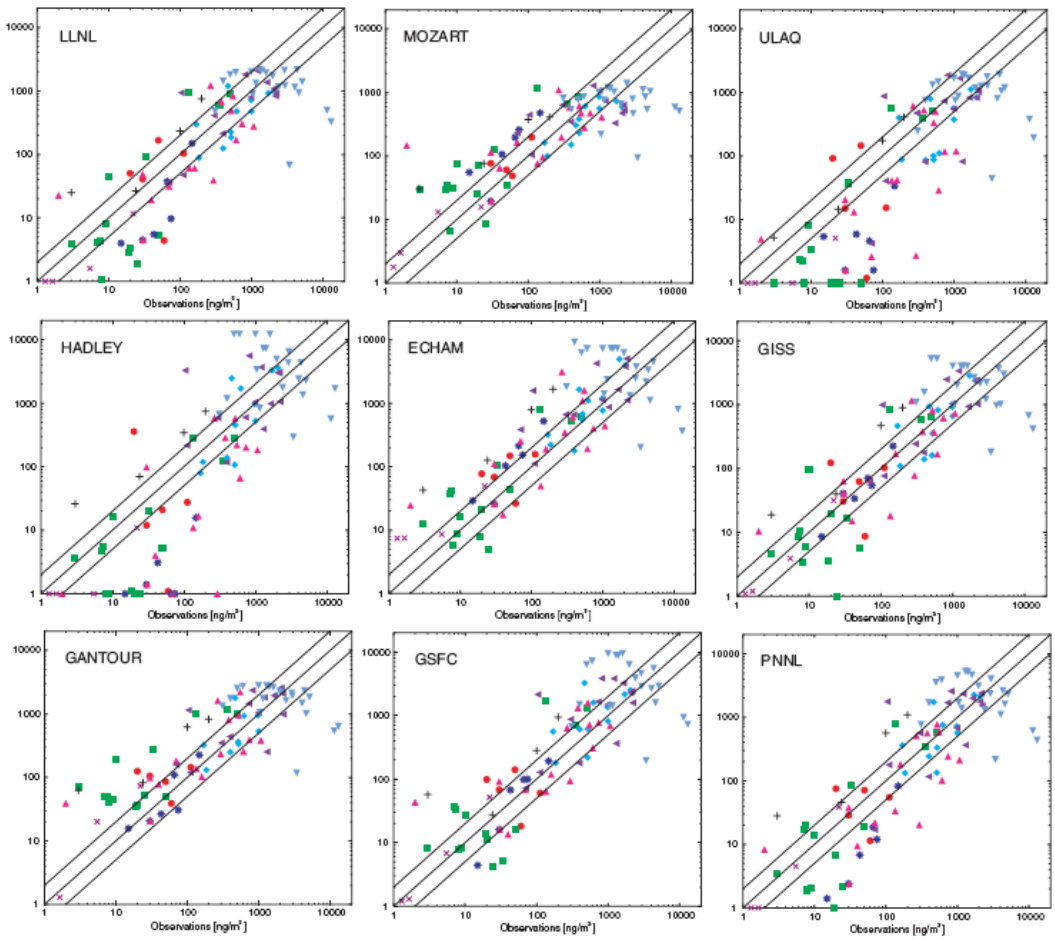

Figure 19. Observed and Simulated Concentrations of Black Carbon
Source: Yu, et al., 2003

Another analytical problem is the difficulty in making valid measurements of various organic compounds species due to large artifacts produced by absorption of organics from the gas phase onto the aerosol collection media, or the evaporation of volatile organics (Appel, et al., 1983). The magnitude of these aerosols could be comparable to organic compounds in unpolluted regions and still have the same results. New methods to derive differences between aerosol types in the organic species use diffusion denuders to remove gas phase impactors with relatively inert surfaces and organics (Eatough, et al., 1996). Another modern method uses thermal

low-pressure drop adsorption analysis to improve accuracy of corrections from back-up filters (Novakov, et al., 1997). The direct effect of light absorption characteristics of some carbon species (i.e. soot and tarry substances), that are non-absorbing black carbon constituents, may have an affect on the magnitude of the direct effect on models making them less than accurate (Hansen, et al., 1997).

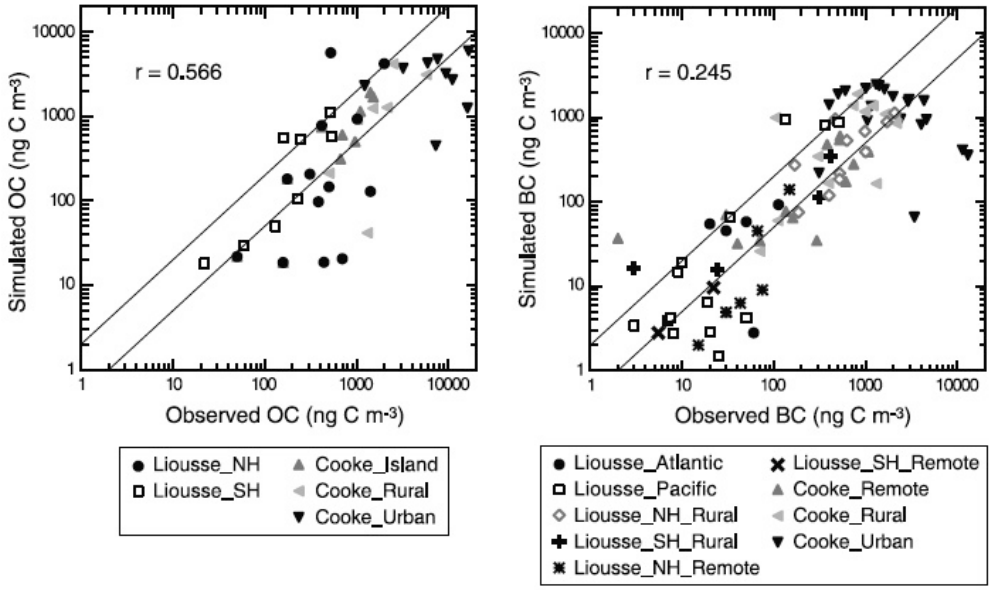

Figure 20. Observed and Simulated Organic Carbon
Source: Chuang, et al., 2002

Other factors effecting refractive properties involve the volatile organic compounds, or VOCs (Organic chemical compounds that have a high enough vapor pressure under normal conditions to vaporize and enter the atmosphere). The condensation of organic compounds onto aerosols is a function of the vapor pressure of the various molecules present, the ambient temperature, and the presence of other organics that can absorb products from gas-phase hydrocarbon oxidation

(Odum, et al., 1996; Hoffman, et al., 1997; Griffin, et al., 1999). These are difficult to measure because of the inability to separate out the individual components of the aerosols before condensation. When combining these volatile organic compounds (VOC) aerosols with appropriate transport and reaction mechanisms in a global climate transport model, the hydrocarbon emissions yield estimated ranges of biogenetically derived secondary organic aerosols (SOA) of between 13-24 Tg/yr (Griffin, et al., 1999) and 8-40 Tg/yr (Penner, et al., 1999). These studies are based on various hydrocarbons (terpenes; C10H12 and C5H8) found in biomass burning (Guenther, et al., 1995), for a total source strength ~14 Tg/yr (Table 2). Secondary organic aerosols are formed from precursor VOC under oxidation. It has been estimated that SOA contribute up to 70 percent of organic aerosols in a given smog event.

In addition, although the precursors of these aerosols are natural in origin, the aerosol yield on oxidation mechanisms implies that aerosol production from biogenic emissions may be influenced by human activity such as the anthropogenic emission of Nox (the generic term for a group of highly reactive gases, all of which contain nitrogen and oxygen in varying amounts). This has caused an increase in O_3 and NO_3, resulting in a three-four-fold increase in biogenic aerosol production since pre-industrial times (Kanakidou, et al., 2000). For example, recent studies in Amazonia confirm low aerosol yields and little production of new particles from VOC oxidation under unpolluted conditions. Projections on industrial growth for this region in the tropics could change these yields given the vast amount of VOC in the

humid tropics, and projected increases in anthropogenic aerosols, hence, the production of SOA (Artaxo, et al., 1998).

The reverse of this scenario is conditions where anthropogenic aerosols can be oxidized to form organic particulate matter. These are normally aromatic and characterized by increased chemical stability resulting from the delocalization of electrons in a ring system (benzene) containing multiple conjugated double bonds. Typically 30g of organic particulate matter is required to 1 Kg aromatic compound oxidized under urban conditions (Odum, et al., 1996), therefore its impact to stabilize is negligible.

It is estimated that the global measure for VOC is 109± 27 Tg/yr, and that 60 percent is attributed to the burning of fossil fuel and 40 percent to biomass burning. Emissions of aromatic VOC amounts to about 19± 5 Tg/yr of which 12± 3 Tg/yr is attributed to fossil fuels. Thus, there is a very small source strength for aromatic aerosols overall, with an average of ~0.6 Tg/yr.

Aerosols and Cloud Formation

Clouds form as condensation nuclei (small particles in the atmosphere, typically < 10μm, upon which water coalesces to form cloud droplets) allow water to condense upon the surface of the aerosol particle. Factors controlling these cloud condensation nuclei (CCN) include the effectiveness of an aerosol particle to become a CCN. Effectiveness depends upon the size of the particle and its response to water. Aerosols are hygroscopic, hydrophilic, or hydrophobic. Hydrophobic aerosols will not activate in cloud under any circumstances, hydrophilic are water-insoluble, but

have hydrophilic sites that allow particles to wet and activate under supersaturated conditions, and hygroscopic contain some water-soluble component and will activate at lower saturations given sufficient time to achieve critical radius. Water-soluble aerosols include sulfates, NaCl, and other water-soluble salts. These are common in the atmosphere (Hudson and Da, 1996), and are well understood.

The ability to understand organic aerosols and their solubility, hence, CCN ability, is not good. Without a clearer understanding of the role these aerosols play in the formation of CCN, there will continue to be a large degree of uncertainty for global scale modeling of cloud nucleation. Organic species of aerosols that are soluble can be high relative to sulfates (Zappoli, et al., 1999) and may be important sources of CCN in some circumstances (Novakov and Penner, 1993; Rivera-Carpio, et al., 1996). For example, organic aerosols from biomass burning are primarily organic and act as CCN, but the CCN activity may be due to co-resident inorganic components (Novakov and Corrigan, 1996). Studies conducted over biomass burning in Amazonia found products of terpene oxidation, which serve as CCN (Leaitch, et al., 1999). Additionally, it was found that particles from pinene oxidation absorbed some of the water at an RH of ~84 percent (Virkkula, et al., 1999), while under lower RH percent rate pinene oxidation products remained unsaturated. Even volatile organic acids may contribute to CCN formation over large areas of biomass burning (Yu, 2000), and broad areas of organic “films” can be responsible for large uptakes of water at low RH.

Other factors include the solubility of oxygenated organic species that tend to decrease with increased carbon numbers (Saxena and Hildemann, 1996). Studies

show (Shulman, et al., 1996), however, that cloud activation of organic species with low solubility may be delayed 1-3 seconds to account for dissolution time needed (Shantz, et al., 1999). In addition, mixing of sea salts or acids with organics lowers solubility and may lead to a reduction of critical supersaturation for activation of cloud formation (Corrigan and Novakov, 1999) especially if the organics reduce surface tension (Shulman, et al., 1996) as demonstrated in natural cloud water (Facchini, et al., 1999). Thick coatings of too high a molecular weight organic (tetracosane or lauric acid) can reduce hygroscopic growth factors for NaCl aerosol particles (Hansson, et al., 1998), Further studies suggest, however, that this is a rare occurrence and of little importance at this time (Shulman, et al., 1996).

Another critical component of the atmosphere to be considered are the inorganic, highly soluble gases, such as HNO_3, that can dissolve into a growing solution droplet before activation in cloud (Kulmula, et al., 1993; Laaksonen, et al., 1998). The result is the increase in droplet number, tempered by the enhancement of condensation rate that contributes to a slight reduction in cloud supersaturation. Understanding the affect of enhancement and the reduction of supersaturation will depend on proper evaluations on the mixing ratio of such gases relative to CCN solute concentrations.

Additionally, there are the sulfates to factor in to overall cloud droplet formation in the atmosphere. The in-cloud oxidation of SO_2 needs to be factored for the development of the CCN spectrum because current models indicate that the fraction of secondary sulfate due to oxidation of SO_2 in cloud can range from 60-80 percent (Table 3). Although it does not affect model sulfur budgets, it has significant

consequences for the magnitude of predicted indirect forcing (Chuang et al., 1997; Zhang et al., 1999). Large scale models need to represent several factors related to CCN in order to assess indirect climate forcing effects accurately. These models need to capture size and distribution of the mass of water-soluble species, the degree of solubility of represented species, and the amount of mixing of individual species within a give size fraction.

The most critical species are the sulfates, organics, sea salts, and nitrates. In order to understand the direct and indirect forcings on climate on a global scale, there is a need to understand the numerous variables to create an accurate model based on size distribution and composition, solubility, and radiative effects of clouds.

The general methods for relating change in number density (Nd) to aerosol concentrations are empirical relationships directly connecting some aerosol quantity to Nd. Under this approach, there are two empirical treatments.

Table 3. Aerosol Sulfates Precursors

Model	Sulphur source Tg S/yr	Precursor deposition %	Gas phase oxidation %	Aqueous oxidation %	SO_2 burden Tg S	$\tau(SO_2)$ days	Sulphate dry deposition %	Sulphate wet deposition %	SO_4^{2-} burden Tg S	$\tau(SO_4^{2-})$ days	P days
A	94.5	47	8	45	0.30	1.1	16	84	0.77	5.0	2.9
B	122.8	49	5	46	0.20	0.6	27	73	0.80	4.6	2.3
C	100.7	49	17	34	0.43	1.5	13	87	0.63	4.4	2.2
D	80.4	44	16	39	0.56	2.6	20	80	0.73	5.7	3.3
E	106.0	54	6	40	0.36	1.2	11	89	0.55	4.1	1.9
F	90.0	18	18	64	0.61	2.4	22	78	0.96	4.7	3.8
G	82.5	33	12	56	0.40	1.9	7	93	0.57	3.8	2.5
H	95.7	45	13	42	0.54	2.4	18	82	1.03	7.2	3.9
I	125.6	47	9	44	0.63	2.0	16	84	0.74	3.6	2.2
J	90.0	24	15	59	0.60	2.3	25	75	1.10	5.3	4.5
K	92.5	56	15	27	0.43	1.8	13	87	0.63	5.8	2.5
Average	98.2	42	12	45	0.46	1.8	17	83	0.77	4.9	2.9
Standard deviation	14.7	12	5	11	0.14	0.6	6	6	0.19	1.0	0.8

Model/Reference: A MOGUNTIA/Langner and Rodhe, 1991; B: IMAGES/Pham *et al.*, 1996; C: ECHAM3/Feichter *et al.*, 1996; D: Harvard-GISS / Koch *et al.*, 1999; E: CCM1-GRANTOUR/Chuang *et al.*, 1997; F:ECHAM4/Roelofs *et al.*, 1998; G: CCM3/Barth *et al.*, 2000 and Rasch *et al.*, 2000a; H: CCC/Lohmann *et al.*, 1999a.; I: Iversen *et al.*, 2000; J: Lelieveld *et al.*, 1997; K: GOCART/Chin *et al.*, 2000.

Source: See model explanation below the figure.

The first is based on relationships between number density (Nd) and the number concentration of aerosol particles, (Na), (Jones, et al., 1994), above a certain size. This works for particles that serve as nuclei for cloud droplets (Figure 21) in stratiform clouds, but becomes ambiguous for cumuliform cloud types because the activation of particles smaller than the threshold for Na (Isaac, et al.,1991; Gilliani et al.,1995). This approach uses observations of Nd and CCN versus particulate, or cloud water sulphates, to devise relationships between Nd and particulate sulfate. It circumvents the assumption required in deriving aerosol concentration numbers (Na) from sulfate mass by using sulfates as a surrogate for Nd specifically accounting for other particulate species. This works as long as relationships are used that take into account the potential regional and seasonal differences in the chemical mixture of the aerosols (VanDingenen, et al., 1995; Menon and Saxena, 1998). For example, the empirical relationships derived for regions with high sulfate loading caused by industry may not be appropriate for biomass aerosols.

Relating Nd to particle mass concentrations and mean volume diameter in accumulation mode aerosols is a newer empirical approach based on the mass scavenging efficiencies of accumulation mode aerosols by stratiform clouds (CCN size good for this) (Glantz and Noone, 2000). It is important, however, to be aware of the effects of any attempt to average scales (Gultepe and Isaac, 1997), because figures need to be carefully calibrated and data driven through accurate measurements.

Advantages for empirical methods in modeling are that they account for the effects of Nd that are associated with cloud dynamics in an “average” sense, since

updraft velocity variations are the main reason for large scatter in observations from which empirical relationships are derived (Leaitch et al., 1996; Feingold et al., 1999). These models average the updraft velocities as well.

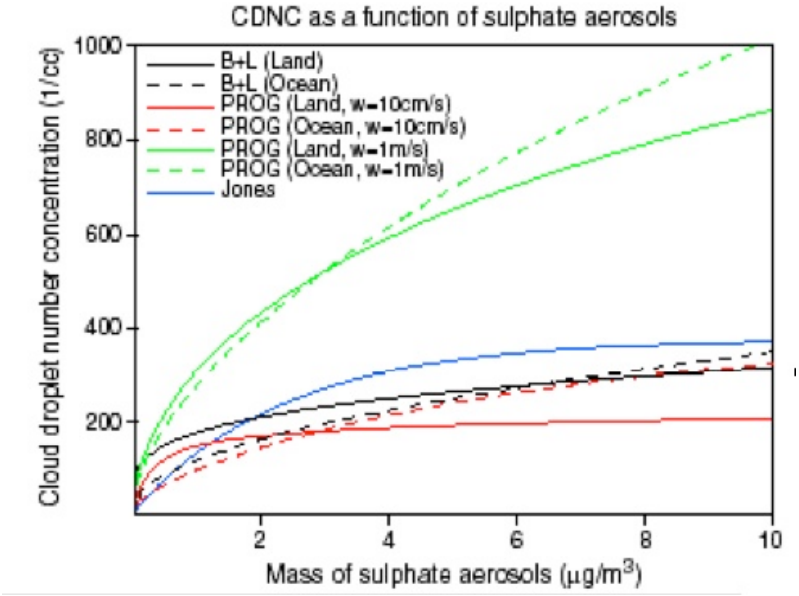

Figure 21. Sulphate Aerosols
Source: Penner, et al., 2005

Note: Droplet concentrations as a function of sulphate concentrations for three different treatments: the empirical treatment of Jones, et al., (1994b), the empirical treatment of Boucher and Lohmann, (1995), and the mechanistic treatment of Chuang and Penner, (1995).

The second method used to relate Nd changes to changes in aerosol concentrations is based on the prediction parameterization of cloud droplet formation processes (Abdul-Razza and Ghan, 2000). This approach requires a form of representation of CCN activity of the particles, and a representation of the dynamic and thermodynamic properties of clouds. Some of the aerosol properties necessary to describe the CCN spectrum need to be assumed in order to apply the model (Figure 12). The two approaches are ~close at about 180 overland, and 585 over water.

CCN droplet number concentrations can be non-linear, even in a heterogeneous cloud mix. For example, high concentrations of sea salt particles in the presence of lower sulfate concentrations lead to an increase in cloud droplet concentration number (Nd) and higher updraft speeds. Conversely, the Nd is lowered by high sea salt concentrations if sulfate concentrations are higher and updraft speeds weaken (O'Dowd, et al., 1999).

Atmospheric Mineral Dust

The role of atmospheric mineral dust in the climate system includes atmospheric photochemistry (Bian and Zender, 2003), stratospheric water vapor (Sherwood, 2002), condensation nuclei and ice nuclei (Lohman, 2002), the radiative budget (Myhre and Stordal, 2001), and nutrient transport to oceans and forests (Prospero, 1996; Grini, et al., 2005; Fung, et al., 2000). Modeling studies have attempted to quantify the global production and transport of atmospheric mineral dust (Tegan and Fung, 1994; Claquin, 1999; Ginoux, et al., 2001; Zender, et al., 2003a) with some significant success.

Mineralogy of the atmospheric mineral dust plays an important role in the overall effect of mineral dust in the climate system. The absorption and reflective properties of these minerals, the hygroscopic characteristics, and the condensation nuclei and cloud type capabilities assist in estimating the affect atmospheric mineral dusts have on climate (Kaufman, et al., 2001 and 2002; Chuang, et al., 2002; Penner, et al., 1999a).

Research estimates that ~50 percent of the global production of tropospheric aerosol particles consists of mineral dust originating from the deserts and their borders (Andreae et al, 1986; Prospero, 1999). Unlike other tropospheric aerosol species, mineral dust particles are lofted rapidly to high altitudes by very high winds occurring over limited regions with very fine-grained soils (Falkovich, 2001). Recent studies by Prospero, et al., (2002) identify the 'hot spots' of dust emission as regions of topographical lows where flooding has occurred in the past 2 million years, allowing for alluvial dust particles available for erosion. These dust emissions involve physical processes controlled by meteorological parameters and soils surface features (Prospero, 1999). Ginoux, et al. (2001) discovered that the timing of dust events, signified by aerosol optical depth (AOD) measurements in the atmosphere at downwind positions, are largely independent of the timing of dust emissions from western Africa. This suggests that, in some cases, there is a persistent reservoir of suspended dust particles over Africa, and that timing downwind events is more strongly tied to transport dynamics of dust than to any chosen dust model available today.

Satellite observations (i.e. MODIS tool on TERRA and AQUA) illustrate that although mineral dust originates from specific source areas around the globe, it can be transported long distances and influence various natural atmospheric processes such as climate and atmospheric chemistry. By reflecting and absorbing sunlight, mineral dust can have a direct effect on climate by changing the temperature profile of the atmosphere (Kaufman, 2002). The dust can affect climate indirectly by modifying cloud properties and characteristics, and the development of precipitation

(Levin, 2005). Mineral dust mixes with other aerosols as it is transported downwind of the source region (Arimoto, 2001). Mixing of different aerosol populations, whether internally or externally, can influence the radiative effects (Seinfeld, et al., 2004); adjust atmospheric chemistry and particle size, shape, and distribution (Arimoto, 2001), and change cloud properties and the event of precipitation (Kaufman, 2002).

Atmospheric mineral dust can also affect global biochemical processes. It was found to be a major source of micronutrients controlling ocean vegetation (Bergametti, 1998), and is thought to be a significant source of nutrient replenishment in the soils of the Amazon River Basin (Prospero, 1996; Koren et al., 2006; Mahowald, et al., 2005; Tegan and Fung, 1994; Zender, et al., 2003). Studies conducted by Koren, et al., (2006), suggest that 240 ± 80 Tg of atmospheric mineral dust is emitted from Africa to the Atlantic coast of Africa annually between 20° and 30° North Latitude. Of that total, 120 ± 40 Tg is deposited in the Atlantic Ocean. ~30 Tg are transported to northern Africa and Europe, ~70 Tg reach the Caribbean in summer months and some ~50 Tg reach the Amazon River Basin in winter. Of the ~50 Tg of dust deposited in the Amazon River Basin during the winter months of the Northern Hemisphere, 50 percent is emitted from a single source in the Sahara, the Bodele Depression (Koren, et al., 2006; Kaufman, et al., 2005; Tegan, et al., 2006; Todd, et al., 2005; Washington, et al., 2005 and 2006).

Atmospheric mineral dust plays an important role in climate that scientists do not entirely understand at this time. The complexities of meteorological processes, diverse source regions of mineral dust, compositional parameters of dust emitted,

and the physical and chemical properties and characteristics of dust emissions make modeling the affects of dust emissions on climate, climate change, and global climate modeling a difficult task. Understandings about the size, shape, distribution, and composition of mineral dust is required if modeling climate change is to be successful.

Geological and Geomorphological Considerations

The importance of understanding the geological history and geomorphology of the region affecting the Bodele Depression deposits is essential for identification of source points on the surface of the Earth, and for in situ measurements to identify mineralogy. The geological history of the Bodele Depression and surrounding region is as complex and diverse as is its position in the northern African continent. The Bodele is positioned in a region known as the complex 'Sahara Metacraton'.

While the Earth processes known as plate tectonics were shifting lithospheric plates about the surface of the planet, causing collisions and break-up among and between plates (Figure 22), weathering and erosion, volcanic activity, and crustal upheaval were continuing uninterrupted. Bits and pieces of former 'continental' plates were pulled off, sheared, destroyed, recrystallized, or weathered and eroded, as tectonic activities shifted because of changing forces within the Earth (Abdelsalam, et al., 2000, Abdelsalam, et al., 1991). The African continent was the center of the 'Greater Gondwana' (Stern, 94) or Pannotia (Dalziel, 1997) by the end of the Pre-Cambrian, and constituted Achaean cratons and Neo-Proterozoic orogenic belts (Figure 23).

However, the tract of land in northern Africa containing the Bodele region is very different from the continental crust formed so many years ago. It is not truly cratonic in nature, and differs from all other regions of northern African continental crust in that it is definitively separate from the rest of the continent in form and history. This tract of crust is dominated by medium-high grade gneissic and migmatitic terranes, occupying the region surrounded by the Arabian-Nubian shield in the east, the Tuareg shield to the west, the Congo shield to the south, and the Phanerozoic cover of the northern continental margin in southern Egypt and Libya (Abdelsalam, et al., 1991). It was not a craton or orogenic belt in the classical sense (Bates and Jackson, 1980) during the Neo-Proterozoic time as are the remaining crustal regions of the African continent (Abdelsalam, et al., 2001).

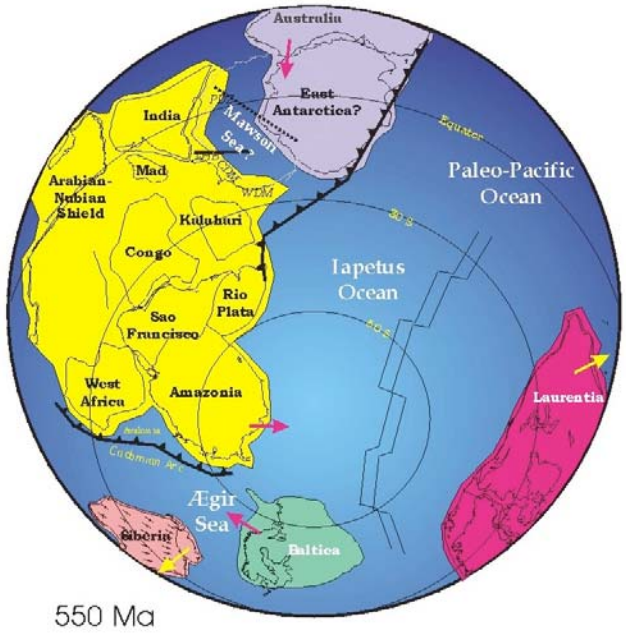

Figure 22. Gondwana
Source: http://www.clas.ufl.edu/ via Wikipedia

Geochronological and isotopic data (Pegram, et al., 1976; Harris, et al., 1984; Toteu, et al., 1987; Schandelmeir, et al., 1988; Key, et al., 1989; Stern and Dawoud, 1991; Stern, et al., 1994) provide indications that this crust is heterogeneous, and in direct contrast with Juvenile Arabian-Nubian shield of Neo-Proterozoic age and with the Achaean continental crust of the Congo craton to the south. It is a pre-Paleozoic continental crust overlain with Neo-Proterozoic tectonic events, with some isolated Neo-Proterozoic juvenile material interspersed. These data show, then, that a craton existed before Neo-Proterozoic orogenic events, and was subsequently decratonized (a significantly altered craton) during the Neo-Proterozoic (Black and Liégeois, 1993).

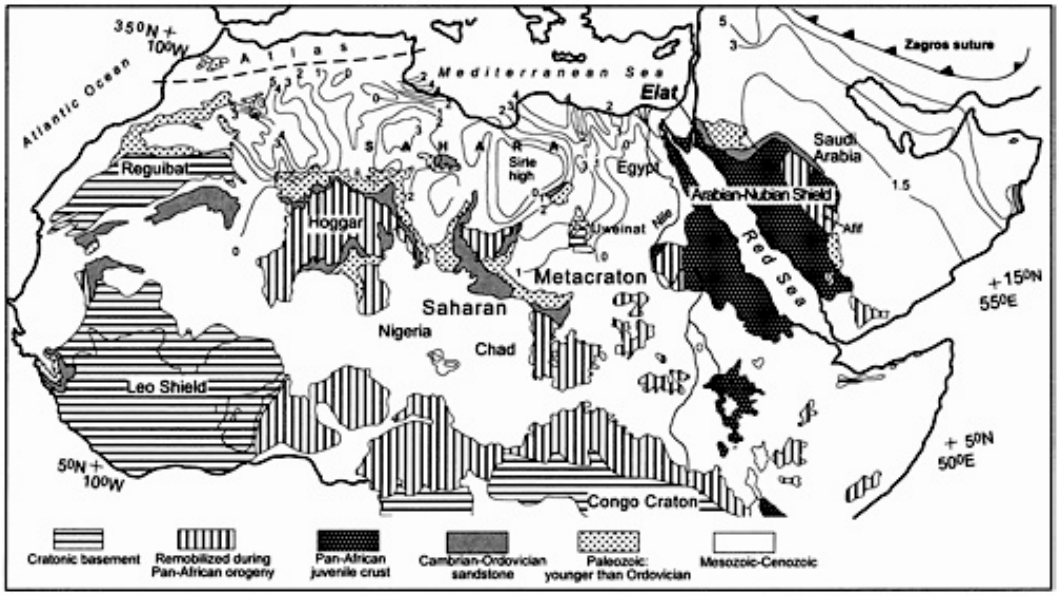

Figure 23. Saharan Metacraton
Source: Abdelsalam, 2001

The geochronological and isotopic data indicates that a cohesive continental crust existed in the region prior to the Neo-Proterozoic orogenics that caused tectonic

events that produced rifting and subsequent ocean basins, and that these ocean basins were then closed resulting in blocks of continent crust collisions (Ghuma and Rogers, 1978; Pinna, et al., 1994; Stern, et al., 1994; Nzenti, 1998).

The crust that constitutes the Tibesti and Ennedi, therefore, the country of Chad, and the region northeast of the Bodele depression, hence the entire Bodele region of study, is a tract of continental crust comprised of a melange of exotic terranes assembled during Neo-Proterozoic times (Küster and Liégeois, 2001). Because of the difficulty in identifying the geological boundaries of the region relative to surrounding cratons, and its complex nature as a melange, this part of northern Africa earned the name 'Central Saharan Ghost Craton' ((Black and Liégeois, 1993), but it was never considered stable enough to be considered a craton.

Abdelsalam, et al., (2001) suggests the region be renamed 'Saharan Metacraton' with the knowledge that a craton is a stable unit of a continent having experienced only slight deformation along passive margins, and a 'metacraton' possibly (the term and its definition have yet to be accepted internationally) as one that is recrystallized, deformed, and/or demonstrates activity along passive margins, or, a 'decratonized' craton.

This 'Saharan Metacraton' (Figure 23 and Figure 24), a melange of complex materials formed during the early processes shaping the Earth tectonically, is overlain with Cretaceous and younger rocks that remain un-deformed and un-metamorphosed, with Pre-Cambrian rocks exposed as uplifted massifs such as the Tibesti, Air, Bayuda, Darfur, Uweinat, Kordofan, Nubian Desert, and Nuba mountains (Abdelsalam, et al., 1995). The lithology of the Cretaceous and younger

rocks are dominated by medium-high grade gneisses, metasediments, and migmatites, with outcrops of low-grade volcano-sedimentary rocks and some granulites. Magmatic intrusions by Neo-Proterozoic granitoids occurred from 750-550 Ma. Research data include Rb/Sr and U/Pb dating of detrital zircons that data some to most of the medium-high grade gneisses at the age of the Neo-Proterozoic time of tectonic activity, with some involvement of Paleo-Proterozoic and possible Archean continental crust involved (Abdelsalam, et al., 2001). The low-grade volcano-sedimentary rocks are found within the medium-high grade gneissic terranes, and are attributed to outcrops detached from the Arabian-Nubian shield (Vail, 1983, 1985), or due to the opening and closing of an ocean-forming type event (possibly the Red sea) east of the region (Schandelmeir, et al., 1990; Harms, et al., 1994).

Structural trends within the 'Saharan Metacraton' (Figure 24) include the ENE to WSW trends, or 'Zalingei Folded Zone' (Vail 1976; Schandelmeir, et al., 1987), and the N-S trends that include the Tibesti of the study region. The ENE-WSW trend was considered pre-Neo-Proterozoic (Grant, 1978), but was later found to contain zircon ages ~630-620 Ma from the granitoids deformed by the structures. Küster and Liégeois (2001) interpreted them as inherited structures from early Neo-Paleozoic terrane collisions.

The Tibesti are N-S trending structures in the form of fold and thrust belts (Ghuma and Rogers, 1978; Schandelmeir, et. al., 1990), caused from the opening and closing of oceanic basins. Abdelsalam, et al., (2001) offer that the folds and thrust belts are caused by the lateral extension stresses due to E-W directed crustal

shortening coupled with collisional forces between the 'Saharan Metacraton' and the Arabian-Nubian shield. Küster, D., Liégeois, (2001) consider some of the N-S trending faults as post-collisional deformation directly related to ENE-WSW directional collisions resulting in significant horizontal movement between terranes.

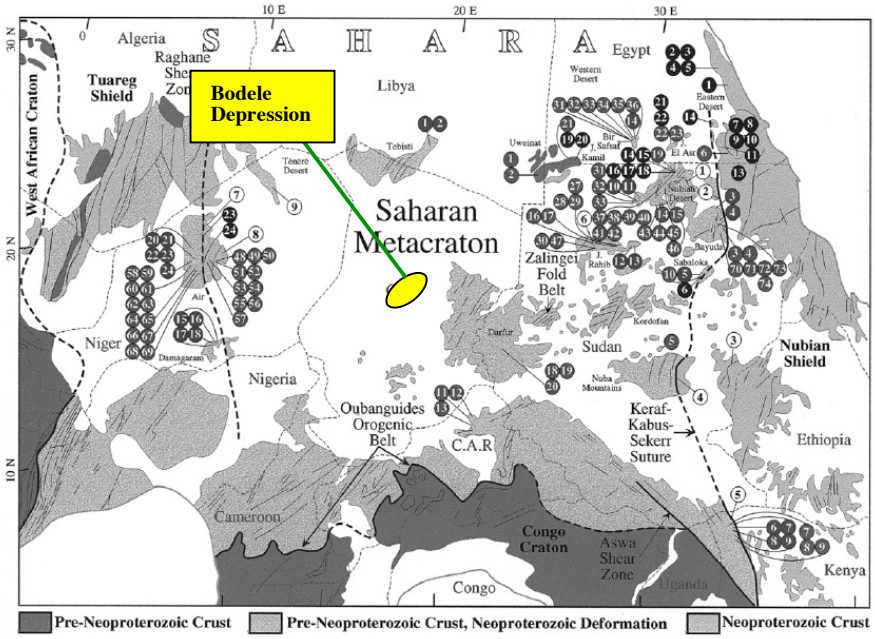

Figure 24. Area of Study on the Metacraton
Source: Abdelsalam, et al., 2001, modified to illustrate location of the Bodele Depression

A general summary of events is described in the Abdelsalam, et al., (2001) scenario that explains the assemblage of the metacraton through a combination of processes. Crustal thickening and lithospheric delamination (Brown and Philipps, 2000) occurred as the metacraton was subjected to collisional forces along at least two of the passive margins. This triggered extension accompanied by horizontal movement along shear zones, followed by high-temperature metamorphism and the

generation of magma. This process can explain the dismembering and create localized Neo-Proterozoic juvenile terranes within the metacraton.

The Bodele Depression is centrally located within this 'Saharan Metacraton' (Figure 24) in the structural zone of the ENE-WSW folded/faulted region at ~18° N latitude by ~19°E longitude, just southwest of the gap that separates the Tibesti and Ennedi Mountains. To understand the composition of the mineral dust emitted by the Bodele, however, knowledge about the mineralogy of the region affecting the material in the Bodele needs to be understood. Therefore, the Lake Chad Basin (Figure 25), the Tibesti, and the southeastern Libyan section of the Sahara are included in the following discussion on the regional geology.

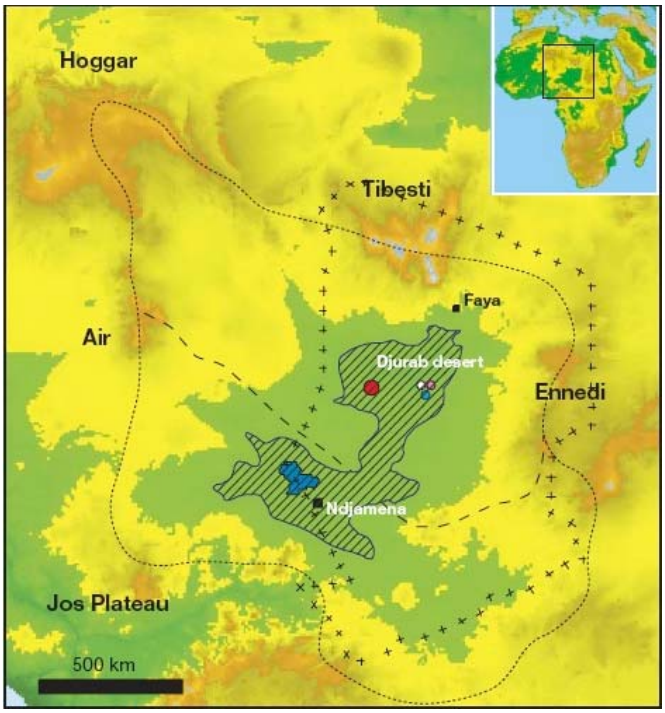

Figure 25. Lake Chad Basin Map
Source: Vignaud, et al., 2002

Note: The boundaries of the ancient Lake Chad basin are shown as a dotted line (with northern and southern sub-basins divided by a dashed line). The inferred maximum extension of the Holocene 'Lake Mega Chad' is hatched in black; the small blue area within it corresponds to present-day Lake Chad. Red circle, the Toros-Menalla hominid site (TM 266); white circle, the Kossom-Bougoudi area; pink circle, Kolle´ area; blue circle, Koro-Toro area. Colors represent altitude: green, 280–430 m; yellow to grey, 430–850 m; brown, 850–2,000 m; grey-blue patches in Tibesti area, about 2,000–3,400m.

The Chad basin has been forming since the Cretaceous Period on a section of the Precambrian African Shield, or 'Saharan Metacraton', as the result of extensional tectonic forces. Evidence of crystalline rock is found under the more recent deposits.

Researchers believe that the ancient sea (Brooks, et al., 2005), Mega-Chad, had the most significant influence on the formation of the Chad basin because the basins of the sea and the lake overlap in some areas. The sea itself was over 600 ft (180 m) deep in most regions and covered over 154,400 square miles (441,584 square km) of central African land before draining into the Atlantic Ocean via the Benue River. The floor of the Chad basin intersects with the ancient Mega-Chad basin in the northeastern portion of Lake Chad at the lowest point of the lake called the Djourab Depression.

The structural history of the Lake Chad Basin (Figure 25) is as complex as the metacraton discussed previously, and identified by lineaments derived from a number of positive Bouguer gravity anomalies (Avbovbo, et al., 1986). It is tectonically active basin with structural features extending NW into the Air Plateau, and SW toward the Benue Rift (Burke, 1976; Ajayi and Ajakaiye, 1981) that is a failed arm of a triple-junction (Figure 25). Current streams (the Logone, Chari, and Kamadogu) and earlier rivers are controlled by the structural features created, in part, by tectonic forces (Durand, 1982).

Inside the Lake Chad Basin is the Quaternary Chad formation composed of argillaceous (fine-grained) sequences with arenaceous (coarse-grained) horizons. Its sedimentary history dates to the early Paleozoic when sediments were deposited on the stable 'metacraton' of the Saharan platform. The platform (Saharan Metacraton)

itself is 1000-8000m thick and includes the lithologies discussed earlier, the repeated tectonic deformations, subsidence, and subsequent formation of three distinct sedimentary basins, one of which is the Lake Chad Basin. The Chad formation is the youngest of the Lake Chad Basin structures containing aquifers that are intrinsically connected to modern Lake Chad. Upper, middle, and lower aquifers exist in the SW portion of the basin, with the upper aquifer composed of fine-grained sediment ~30 m thick and hydraulically connected to Lake Chad (Carinouze, 1983; Isiorho and Matisoff, 1990) and is separated from the middle aquifer by ~ 100m of clay-rich sediment. The importance of these aquifers to the Bodele is that scientists believe that a portion of the lake waters, with no other apparent outsource, actually leach away to the Bodele. If true, the moisture content in the Bodele sediment can have an effect on saltation and deflation of the mineral dust emitted from the Bodele.

The Chad formation is overlain by aeolian deposits of sands, and fluvial, deltaic, and lacustrine deposits ~1-6m thick. Fluvial deposits are located along stream valleys composed of two units of silty clay sediments; old alluvium and young alluvium (Hammond and Abdou, 1982), with some areas of overlying sediment ~1-1.5m thick.

Extending northward from the Lake Chad Basin, Phanerozoic sedimentary basins, and platform type sequences, along the northern edge of Gondwana, store huge amounts of siliclastic rocks (Figure 24). In northern Africa, the siliclastics fill a number of basins up to 3-4 Km deep (Petters, 1991).

The portion of the Sahara indicated for the study of the Bodele Depression mineral dust emissions is composed of an exotic melange of pre-Neo-Proterozoic

materials of gneissic, migmatitic, and volcano-sedimentary nature, with magmatic intrusions and subsequent sedimentary basin deposits of siliclastics up to 3-4 km thick. Therefore, the mineral composition of the material affecting the Bodele region and dust emissions are expected to contain continental crust materials including all sedimentary basin type deposits (sandstones, siltstones, clays, etc.), some erratic occurrences of trace elements or minerals from volcanic activity, and weathered, eroded, and deposited materials from exposed gneisses and migmatitic materials.

The Bodele Depression

Identifying the mineralogy of atmospheric mineral dust emitted from the Bodele Depression in northeastern Chad in central northern Africa is of significant interest to atmospheric scientists. Research hypothesizes that approximately 50 percent of the total Sahara atmospheric mineral dust transported to, and deposited in, the Amazon River basin is emitted from a single source: the Bodele (Koren, et al., 2006; Prospero et al., 2002; Reid, et al., 2003; Kaufman et al., 2005) (Figure 26).

Methods used by scientists to calculate quantities of emissions and depositions include the use of images and data derived from the MODIS tool aboard the NASA TERRA and AQUA satellites. The satellites descend in a polar orbit at ~ 10:30 and 1:30 GMT respectively, every day. Scientists tracked dust emissions uplifted from the Bodele Depression and transported to the Atlantic Ocean to determine the speed of a dust parcel by calculating the difference in parcel movement from the TERRA descent to the AQUA descent. Other tools used by the scientists to calculate quantity and transport of dust emissions included MISR on

TERRA. Scientists calculate the optical properties of dust plumes derived from the MISR tool on the satellite. Each MISR pixel is measured from nine different angles, enabling the use of directional variability of the dust to retrieve optical parameters over bright surfaces. The dust flux was calculated by converting MISR optical thickness into dust mass.

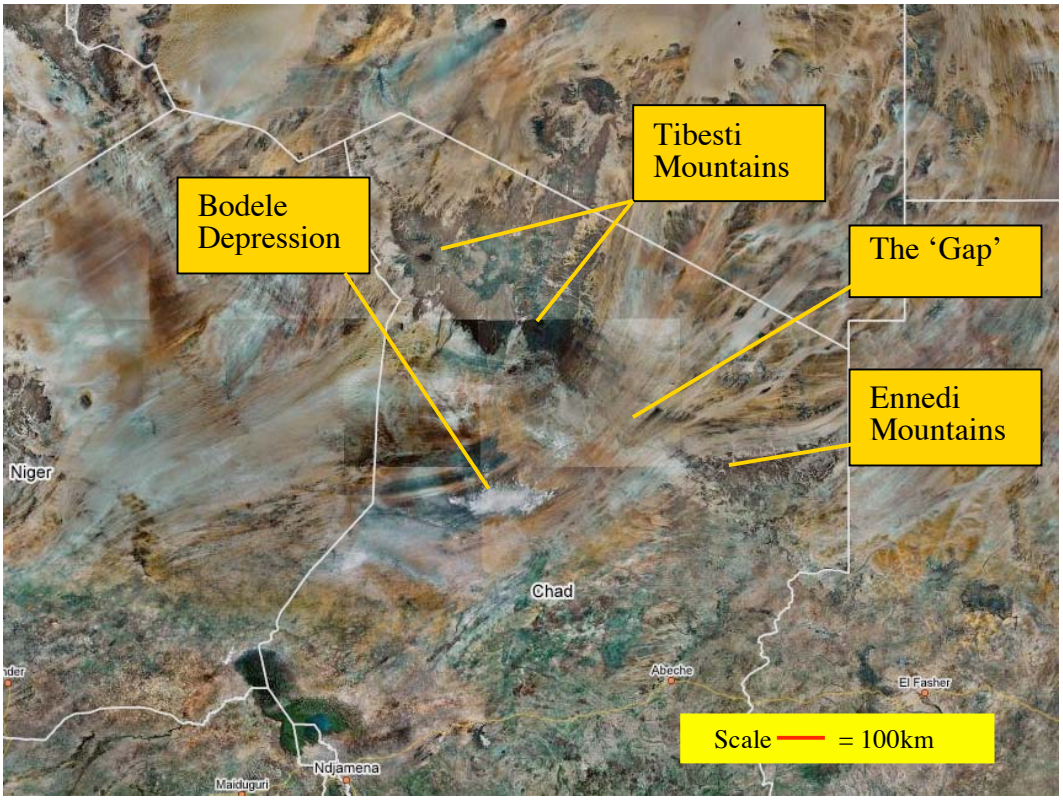

Figure 26. Map of Chad with Bodele Depression in Central Africa
Source: Visual Earth, modified to indicate position of the Bodele Depression
Satellite resolution is 1km per pixel

Note: The Tibesti and Ennedi Mountains, and the 'gap' modifying wind velocity in the region.

The Bodele Depression in central northern Africa is the single most abundant source of global atmospheric mineral dust (Koren, et al., 2006; Tegan, et al., 2006;

Todd, et al., 2005; Washington, et al., 2005, 2006). Transported across the Sahara from east to west as dictated by the prevailing trade winds, it is estimated that ~50 percent of the Saharan dust reaching the Amazon River basin during winter months originates in the Bodele (Koren, et al., 2006; Chiapello and Prospero, 2004). Significant is that the Bodele is ~0.5 percent the size of the Amazon River Basin and ~ 0.2 percent of the area known as the Sahara.

Identification of the mineralogy of the Bodele dust, based on the geology of the regions known as the Tibesti and Ennedi, and the geological history of the Bodele, including mega-Lake Chad, will provide important information significant to climate modeling, estimated impact on the climate system, and the significance of these minerals for oceans and forests (Prospero, 1996; Chiapello and Prospero, 2004; Fung, et al., 2000).

The Bodele depression is a dry remnant of Mega-Lake Chad (Drake, N., 2006). The lake existed in the post-glacial Pleistocene expanding and retreating as climate fluxes occurred during the last vestiges of the glaciers. The Mega-lake was a freshwater system extending from 11° to 18° N. latitude (Vignaud, et al., 2002) covering portions of present day Cameroon, Nigeria, Niger, Sudan, the Central African Republic, and most of Chad (Figure 27: interpretations of mega-Lake Chad to topographical and political maps from the French Geological Survey). The lake formed and remained in place from ~13,000 years to ~ 6-8,000 years ago.

Diatoms appear to have flourished in this inland freshwater lake and are apparent in ground and aerosol samples of the area. No conclusive evidence exists, however, that diatoms constitute the majority of the materials found in the Bodele.

Identification of the predominant minerals of the Bodele is necessary for understanding the impact Bodele mineral dust may have on climate.

The mega-lake had expanded and shrunk with changes in climate over the past 13,000 years. At its largest, around 4000 BC, the lake is estimated to have covered an area of 400,000 square kilometers. Lake sediment analysis indicates dry periods around 8500 BC, 5500 BC, 2000 BC, and 100 BC (Brooks, et al., 2005). It was one of the largest lakes in the world when surveyed by Europeans in 1823. Since 1823, it has shrunk considerably. The changes in the lake over the past 33 years are more dramatic. The present-day Lake Chad is located in the far southwestern corner of the country (Figure 27).

Another consideration is that Lake Chad has no apparent outlet, and water from it appears to percolate northeast into the Soro and Bodele depressions. If this proves to be the case, periods of higher than average moisture could effect the saltation and lofting of minerals from the Bodele.

The region is unique in that the Bodele Depression and its subsequent depositional characteristics are defined by a number of factors. First, the Tibesti and Ennedi Mountains to the north and northeast of the Bodele are a complex system with a catastrophic past. Primarily Paleolithic and pre-Cambrian materials in general, this region was modified during crustal plate activity creating and closing ancient seas that eventually became the Atlantic. Crustal deformation and subsequent volcanic activity and hot spots in the Tibesti shaped the mountains as they appear today, but are the result of differential erosion of an anticline- synclinal system modified by volcanic activity. At first glance, the ridge of materials comprising the

Tibesti and Ennedi range appears to be the remnants of an enormous syncline. After careful study, the geomorphology and mineralogy of the region suggests that this is a syncline modified by volcanic activity, crustal deformation, and partial melting and recrystallization because of tectonic forces and subsequent differential weathering and erosion.

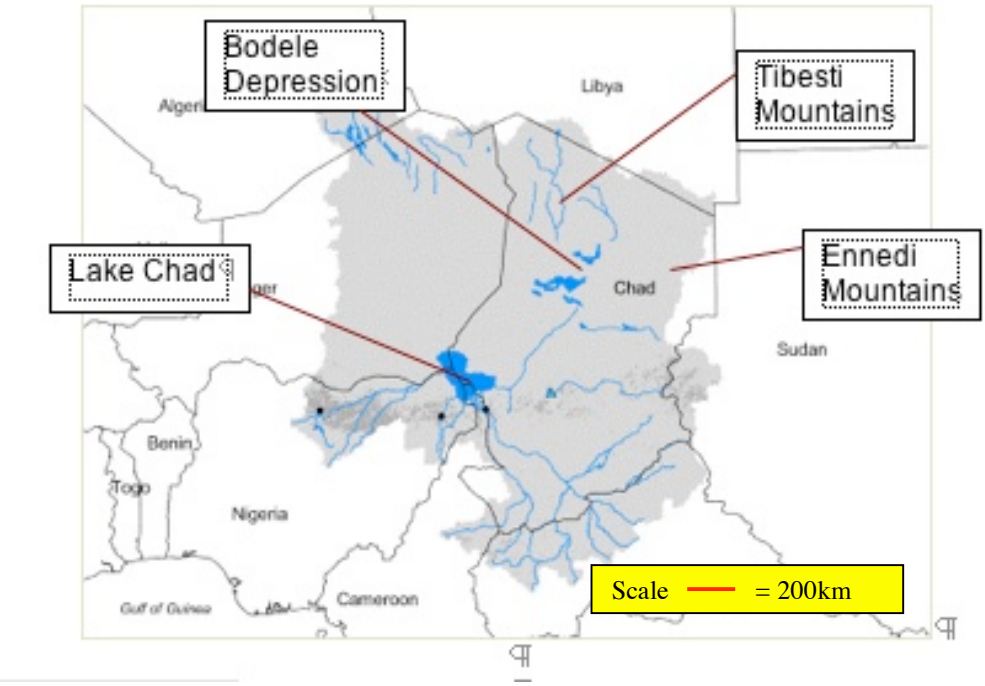

Figure 27. Mega-Lake Chad Regional Map and Locations
Source: Watersheds of the World at
http://www.iucn.org/themes/wani/eatlas/html/af1.html

Note: The gray area is the extent of the mega-Lake Chad.

Summary

As the single dustiest place on Earth (Koren, et al., 2006; Tegan, et al., 2006; Todd, et al., 2005; Washington, et al., 2005 and 2006), the Bodele and its atmospheric mineral dust emissions are of primary importance to the scientific study

of the affect dust have on climate and climate change. Identification of the minerals composing these dust emissions is critical for understanding their impact, and for developing successful models for climate change. The complex geological and geomorphological history of the Bodele Depression provides a view of the past, and a method to look at future identifications of the dust mineralogy. The key mineralogical data lies within the following concepts:

- Enormous amounts of Paleozoic sandstone sequences were deposited in northern Africa following an extended Neoproterozoic orogenic cycle culminating in the assemblage of Gondwana
- Use of U-Pb dating of detrital zircons to determine extent of depositions from Israel through northern present-day Africa. Aeolian processes dictate that knowledge of the extent of these depositions is needed to backward trace mineral supply to the Bodele. Gneisses, migmatics, volcanic sedimentary rocks, and traditional transgressive sea deposits.
- This sandstone forms the base of the widespread siliclastic section now exposed along the edges of the Arabian-Nubian shield located in northeastern Africa and Arabia.
- Pre-Neoproterozoic zircons lost PB possibly as a consequence of the
- Pan-African orogeny resetting the clock in the rocks at that time.
- Extensive deposits of alluvial sediments deposited in the metacraton since the beginning of the Holocene, along with subsequent flooding post-Holocene glaciation.

CHAPTER III

METHODOLOGY

The mineralogy of the atmospheric mineral dust from the Bodele Depression emitted into the system will be determined using French geological maps, traditional X-ray diffraction, Continuum X-Ray Diffraction and Fluorescence system analysis, and scanning electron microscope imaging and spectral analysis. The resulting data will be correlated to the geological history and mineralogical composition of the Tibesti/Ennedi Mountains and the Bodele to identify the composition of the atmospheric dust produced in the Bodele. These details can be incorporated in future research into models that assess climate change.

Procedures and Instrumentation

Using the in situ ground and aerosol samples provided by the British BodEx experiment team, the following research tools and methods would provide the data necessary to assess and identify the mineralogy of the Bodele atmospheric mineral dust. From these data, identification of elemental composition identification, atomic mass percentage and mass weight percentage analyses will be conducted to verify d-spacing and k-fluorescence results. The tools to be used include:

- Traditional X-ray diffractometer: The < 2 mm fraction of four in situ coarse dust samples will analyzed by X-ray diffraction (XRD) according to standard techniques. Oriented mounts to be analyzed in air-dried, ethylene glycol solvated (24 h) and heated (250 C, 1 h) states. Whole-powder specimens will be analyzed for bulk mineralogy by XRD analysis of randomly oriented (spray-dried) powders (Hillier, 1999). Mineral abundances to be quantified with an internal standard of ZnO (10% of XRD powder by mass) using the mineral intensity factor approach of Srodon et al (2001). All samples will be analyzed on a Siemens D-500 diffractometer and processed using Jade ® software (mdi.com).

- Scanning Electron Microscope: The primary performance specification for the FESEM is resolution. Point-to-point resolution is 1 nm at an accelerating voltage of 30 kV and 4 nm at 1.0 kV. This is achieved using an Schottky field-emission source, a beam booster that maintains high beam energy throughout the microscope column, an electromagnetic multi-hole beam aperture changer, and a magnetic field lens. The beam path is designed to prevent crossover of beam electrons. These features result in reduced chromatic aberration, improved beam brightness (even at low electron probe energies), and little beam energy spread. All of these features contribute to the microscope's excellent resolution. Spectral analysis will be randomly conducted for each of 50+ mini-samples obtained from four sample packages provided by the BodEx Experiment 2005 team, England.

- New concept Continuum X-Ray Diffraction and Fluorescence system: A new technology is being developed incorporating miniaturized CCD and XRD tools designed to conduct x-ray diffraction, x-ray fluorescence (Gendreau, et al., 2006), and optical imaging on non-powdered bulk samples providing mineral identification, elemental composition, and optical properties of a sample, combined with unique information about size and orientation of crystallites within a sample. This tool has produced the same type of information with aerosol filter samples with a good degree of accuracy. The specifics for the instrumentation at the present time (we are adjusting certain parametric measures and additional d-spacing and K-fluorescence values to cover higher and lower value than currently in use) are included in the appendix.

- Geological, topographical, and geomorphological maps of the area from the French and German Geological Societies will be used to study, analyze, and interpret the surface lithology and bedrock mineralogy, topographical features, and structural features.

Data Collection

The collection of data is based on results achieved from the traditional XRD, Scanning Electron Microscope images and chemical analyses, a new XRD XRF instrumentation (APPENDIX H), regional geomorphological history, and French geological survey maps. Samples used in the analyses were obtained from the BodEX (Bodele Experiment) 2005 study team composed of a group of academic scientists from the University of London and Cambridge University, England. The main collaborator

from BodEX, Martin Todd, is from the University College London. The BodEX study was the first conducted in situ at the Bodele Depression. The team of scientists, an interdisciplinary study group funded by the Gilchrist Educational Trust and the Royal Geographical Society, collected samples of bulk material at the surface of the Bodele, and in aerosol filters 3 meters above the surface. Samples for analysis were obtained from the BodEX team from England, with our main collaborator from BodEX, Martin Todd, from the University College London. The four primary samples were collected at four different locations between 17.1° North Latitude and 17.6° North Latitude, by 18.24° East Longitude by 18.15° East Longitude.

I labeled the four bulk sample packets NASA 1 through NASA 4 for the XRD analyses, and a series of A through D for the SEM analyses. Samples for the SEM, A-D, were sub-numbered for samplings within the samples. For example, sample A (number 1 for the XRD work) materials were randomly extracted from the sample packet for four individual sections of the SEM head used in the scans. This process, for samples A-D, produces 16 sample regions on the SEM head. The process was conducted twice, providing 32 samples on SEM heads from the four existing sample packets. Additionally, each sub-sample on the heads was randomly scanned for chemical analyses, and regions of interest were zoomed for a more specific analysis of particles of interest. General information for each of the sixteen sections on a specific head was recorded. Sample A, for example, produced a full image and random scan chemical analysis, and several zoomed-in images with chemical analyses. All conditions, assigned sample labels, and SEM manipulations were recorded. The process was repeated for all sections, A-D, on the SEM head.

The traditional X-Ray diffractometer sample analyses, NASA 1 through NASA 4, were prepared in typical powdered form in dry mount, with e-glycol, and with zinc oxide. The three separate preparations were necessary to validate findings in the traditional dry mount sample analyses. The zinc oxide samples, with zinc oxide at 10 percent, provided a baseline calibration, and the e-glycol additions in the third set of samples produced a separation in the layers of minerals for a more accurate d-spacing values and identification of the materials. NASA 1 through NASA 4 samples prepared with e-glycol, dry mount, and zinc oxide, provided 12 separate analyses; three for each NASA sample.

Data Analysis

The initial hypothesis from sample analyses is that the mineralogy of the Bodele Depression is more complex than the BodEx experiment team has concluded (diatomaceous Earth). A second hypothesis is that the Bodele mineralogy is strongly connected with weathering and erosion from the Tibesti with significant deposition during the Mega-Lake Chad period and post-Holocene. The source of the Tibesti sediment has influenced the deposits in the Bodele Depression for tens of millions of years, long before the Pleistocene and subsequent formation of the lake. Continual mixing of the Tibesti sediments with organic debris produced during the Mega-Lake Chad period would produce typical weathered granitic sediments with the freshwater diatoms seen in imaging analyses. Most of the sediments derived from granites should prove to be felsic in nature, with some materials mafic in origin because of past intrusive and extrusive hot spot activity in the western/southern Tibesti during the Cenozoic. Additionally, typical sedimentary processes produced typical sedimentary rocks northeast

of the Bodele that eventually weathered and eroded from the source. These materials would include particles of sand, clay, and silt particles composed of quartz and aluminum silicate minerals.

Possible outcomes for the mineralogy analyses include the complex mixture described above, possible feldspar derived sediment coatings on most of the in situ diatoms (hiding the true nature of the samples), or a better than 50% occurrence of diatoms, indicating that the sediments are indeed diatomaceous Earth. The geologic history of the region from the Paleozoic to the Holocene, support a complex mix hypothesis that is presented as the problem being addressed.

Additional outcomes might include further development of the new technology, the XRD XRF (Continuum X-Ray Diffraction and Fluorescence system, APPENDIX H), if the aerosol results continue to correlate with the bulk samples. The ability of the XRD XRF to capture the chemistry and produce XRD results comparable with the traditional XRD technology will assist in validating mineralogy of the Bodele.

Traditional SEM and XRD derived data will be analyzed and compared with the new XRD XRF instrument and the geological data for the region of study to identify the mineralogy of the Bodele Depression dust emitted into the atmosphere of the Earth System.

CHAPTER IV

FINDINGS AND ANALYSIS OF DATA

The samples used in the analyses of the Bodele mineral dust were obtained from the BodEX (Bodele Experiment) 2005 study team composed of a group of academic scientists from the University of London and Cambridge University, England. The main collaborator from BodEX, Martin Todd, is from the University College London. The BodEX study was the first conducted in situ at the Bodele Depression. The team of scientists, an interdisciplinary study group funded by the Gilchrist Educational Trust and the Royal Geographical Society, collected samples of bulk material at the surface of the Bodele, and in aerosol filters 3 meters above the surface. Samples for analysis were obtained from the BodEX team from England, with our main collaborator from BodEX, Martin Todd, from the University College London. The four primary in situ bulk and aerosol samples were collected at four different locations between 17.1° North Latitude and 17.6° North Latitude (~ 60 km distance), by 18.24° East Longitude by 18.15° East Longitude (~ 88 km distance), with three of the locations ~20 km apart, and one ~100m from the location of sample three.

The mineralogy of the Bodele Depression materials is predominately ferromagnesian silicates, aluminum silicates, and amorphous silica (Figure 28), with

some calcium carbonates, dolomite, and exotic elements such as titanium and cosmic silicon, mixed with 10-20 percent desiccated diatom structures.

CHEMICAL GROUP		ANIONIC SPECIES	EXAMPLES
OXIDES minerals		Oxygen, O^{-2}	Hematite, Fe_2O_3; Magnetite; Fe_3O_4
SULFIDE minerals		Sulfur, S^{-2}	Pyrite, FeS_2
CARBONATE minerals		Carbonate, CO_3^{-2}	Calcite, $CaCO_3$; Dolomite, $CaMg(CO_3)_2$
SILICATE minerals		Silicate, SiO_4^{-4}, "Tetrahedron"	
	STRUCTURAL SUBGROUPS OF THE SILICATES	Isolated SiO_4^{-4} Tetrahedra	Olivine, $(Mg,Fe)_2SiO_4$; Garnet, $(Fe,Mg,Ca)_3Al_2Si_3O_{12}$
		Single Chains of Tetrahedra, $Si_2O_6^{-4}$	Pyroxene, e.g., Augite, $Ca(Mg,Fe)Si_2O_6$
		Double Chains of Tetrahedra, $(Si,Al)_8O_{22}^{-12 \text{ to } -14}$	Amphibole, e.g., Hornblende, $NaCa_2(Mg,Fe,Al)_5(Si,Al)_8O_{22}(OH)_2$
		Sheets, $(Si,Al)_4O_{10}^{-4 \text{ to } -6}$	Micas (phyllosilicates), e.g., Muscovite, $KAl_2(AlSi_3)O_{10}(OH)_2$, Biotite, $K(Mg,Fe)_3(AlSi_3)O_{10}(OH)_2$, Chlorite, $(Mg,Fe)_6Si_4O_{10}(OH)_8$
		Framework, SiO_2 or $(Al,Si)O_2^{-.25 \text{ to } -.5}$	Quartz, SiO_2 Feldspars K-Feldspar, $K(AlSi_3)O_8$ Plagioclase, $(Na,Ca)(Al,Si)_4O_8$

Figure 28. Mineral Groups
Source: Appalachian State University at http://www.appstate.edu/~abbottrn/mnrl-id

X-ray Diffractometer and Scanning Electron Microscope chemical analyses indicate that the minerals from the Bodele Depression dust emissions are primarily from clay minerals.

The physical characteristics of clays, more so than the chemical and structural characteristics, define this group. The elements comprising clay minerals, however, are the result of weathering and desiccation of silicate minerals compounded by periodic flooding and drying in the region of deposition.

Clay minerals tend to form microscopic to sub microscopic crystals. They can absorb water or lose water from simple humidity changes. When mixed with limited amounts of water, clays become plastic and are able to be molded.

When water is absorbed, clays will often expand as the water fills the spaces between the stacked silicate layers. Because of the absorption of water, the specific gravity of clays is highly variable and is lowered with increased water content. The hardness of clays is difficult to determine because of the microscopic nature of the crystals, but actual hardness is usually between 2 – 3; many clays give a hardness of 1 in field tests.

Clays tend to form from weathering and secondary sedimentary processes with only a few examples of clays forming in primary igneous or metamorphic environments. Clays are rarely found separately and are usually mixed with other clays and with microscopic crystals of carbonates, feldspars, micas, and quartz.

Analysis of SEM Bulk Data

The SEM bulk data analysis (Appendix C) has produced a plethora of possible ferromagnesian and aluminum silicate mineralogies for the Bodele Depression materials, with small quantities of calcium carbonate, dolomite, and isolated exotic elements such as titanium and cosmic silicon. The chemical analyses of the data produced the following atomic % and weight % values for 44 separate scans of 36 filters prepared from the original four sample packets provided by the BodEX team (Table 4).

These values indicate secondary sedimentary processes over time with some recent primary sedimentary processes in the ferromagnesian materials. The smectite group of clays appears to predominate the materials. The general formula is (Ca, Na, H)(Al, Mg, Fe, Zn)2(Si, Al)4O10(OH)2 - xH2O, where x represents the variable

amount of water that members of this group could contain. The formula for talc, for example, is Mg3Si4O10(OH)2. The gibbsite layers of the kaolinite group can be replaced in this group by a similar layer that is analogous to the oxide brucite (Mg2(OH)4). The structure of this group is composed of **s**ilicate layers that sandwich a **g**ibbsite (or brucite) layer in between, in an **s-g-s** stacking sequence. The variable amounts of water molecules would lie between the **s-g-s** sandwiches.

Table 4. Atomic % and Weight % Bulk Sample Analyses

Element	Weight %	Atomic %
Oxygen	1967.32	2394.94
Silicon	1052.14	734.8
Aluminum	185.95	138.34
Sodium	32.55	28.94
Iron	207.78	74.51
Potassium	31.05	15.86
Calcium	159.52	80.58
Magnesium	42.85	34.73
Phosphorus	46.27	31.44
Sulfur	2.08	1.3
Chlorine	0.56	0.32
Fluorine	9.02	9.74
Titanium	25.75	11.74

Source: Author's research

The materials were deposited over periods of time when alternating flooding and drying periods occurred, especially after the last glacial period, post Holocene, when Mega-Lake Chad expanded and shrunk as climate undulated between wet and dry periods.

Additionally, data suggests between 2-10 percent of the materials in the Bodele emissions are the desiccated remains of diatoms, said to have thrived in the fresh waters of Mega-Lake Chad during the Holocene at the full extent of the perimeter of the lake. These data are visual SEM scan images (Appendix D) obtained during the chemical analyses of each of the prepared 36 bulk sample filters.

Elemental percent by weight measurements for silicate minerals, expected in a depositional environment such as the Bodele Depression, is listed in table 5. Comparison of these figures with table 6, established for the bulk samples from the Bodele BodEX team, illustrates that the Bodele samples are of similar nature, and that discounting the 2-10 percent diatomaceous debris in a given sample results in figures to support the elemental measurements from the SEM bulk data. Complete data sets for the SEM bulk data, the source for table 6, are found in Appendix C.

Table 5. Traditional Elemental Weight % Analyses for Crustal Materials of Earth

Element	Approximate Percentage by Weight
Oxygen (O)	46.6
Silicon (Si)	27.7
Aluminum (Al)	8.1
Iron (Fe)	5.0
Calcium (Ca)	3.6
Sodium (Na)	2.8
Potassium (K)	2.6
Magnesium (Mg)	2.1
All others	1.7
Total	100

Source: http://www.appstate.edu/~abbottrn/mnrl-id/

Note: This chart provides a crustal composition baseline for comparative analysis of the Bodele depression mineral samples.

The differences in element percent by weight in tables 5 and 6 are due primarily from the occasional elevated measurements of titanium, phosphorous, and the inclusion of desiccated diatoms in the samples. Even with these considerations, however, the samples are consistent with the expected values overall within a standard deviation of ~0.3 percent. The elevated calcium results from the abundance of Ca feldspar clays and the calcium carbonates found in the samples, while the repressed sodium and potassium levels are accounted for in the displacement by the CaCo3 and Ca feldspars. Additionally, if an average 6 percent of the total diatomaceous Earth is taken from the oxygen and silicon values to account for the 6 percent average desiccated diatoms, the elemental measurements in tables 5 and 6 become more typical of crustal percent element values.

Table 6. Actual SEM Bulk Data Chemical Analyses

Element	% By Weight
Oxygen	52%
Silicon	28%
Aluminum	5%
Sodium	.8%
Iron	5%
Potassium	.8%
Calcium	4.8%
Magnesium	1.1%
Other	2.5%

Source: Author's research

Further comparison of elemental contributions for clay mineralization are obtained using the standard matrix for clay minerals (Table 7) whereby weathered

silicate minerals from the simple ferromagnesians to the complex framework feldspars and quartz minerals are accounted for in the elemental analyses.

Table 7. Elemental Table of Clay Mineral Elements for Crustal Material on Earth

Mineral	Chemical Formula	Charge per unit cell		Layer Charge
		Tetrahedral	Octahedral	
		equivalents mole^{-1}		
Kaolinite	$Si_4Al_4O_{10}(OH)_8$	0	0	0
Montmorillonite	$Ca_{0.66}Si_8(Al_{3.34}Mg_{0.66})O_{20}(OH)_4$	0	-0.66	-0.66
Vermiculite	$Ca_{1.48}(Si_{7.12}Al_{0.88})(Al_{2.8}Mg_{0.6}Fe_{0.6})O_{20}(OH)_4$	-0.88	-0.60	-1.48
Muscovite	$K_2(Si_6Al_2)Al_4\ O_{20}(OH)_4$	-2.0	0	-2.0
Chlorite	$Mg_{0.6}Al_{3.8}(Si_{7.8}Al_{0.2})(Al_{3.6}Mg_{0.4})O_{20}(OH)_4$	-0.2	-0.4	-0.6

Source: Sposito, 1973

Analysis of SEM Aerosol Data

The SEM aerosol data (Appendix E) compares comparatively well with the SEM Bulk data (Table 8). Except for a drastic decrease in sodium, the data tends to support mineralization of the bulk samples. The aerosol particles are much smaller than the bulk samples, even after powdering for XRD and SEM analyses. Whereas the aerosol samples range from 300nm to <10 μm, the powdered bulk sample powdered particles range from ~10μm to 300μm indicating that some mineral particles with higher size ranges may be difficult to deflate, therefore increasing or decreasing the elemental amounts in aerosol samples to account for discrepancies. Additionally, the samples were obtained during the winter months when the Harmattan winds are strongest, and that could cause changes in the heterogeneity of the samples lofted into the atmosphere. The Harmattan winds is the name given to

the easterly trade winds of the region during the winter months, when the winds become drier and hotter, and increase in velocity diurnally.

Table 8. Atomic % and Weight % Aerosol Sample Analyses

Element	Weight %	Atomic %
Oxygen	611.99	670.44
Silicon	248.71	153.36
Aluminum	68.88	45.5
Sodium	0.94	0.83
Iron	43.51	14.58
Potassium	6.34	3.17
Calcium	49.34	24.46
Magnesium	25.75	19.98

Source: Author's research

The type and quantity of elemental distribution for aerosol compared to bulk samples is sufficiently similar to assume they are primarily of the same materials, especially since the aerosol samples were collected within the source region of the Bodele Depression (Table 9). The lack of continuity between particular elements, such as sodium measurements, likely represents an affect of wind deflation forces versus particle mass, or possible 'wetting' of particles not deflated. In either case, this accounts for the lack of sodium concentrations in the aerosol samples. Note the lack of diatom particles in the images (Appendix F), which averages 2-10 percent consistent with bulk sample data.

Table 9. Actual SEM Aerosol Data Chemical Analyses

Element	% By Weight
Oxygen	57.89%
Silicon	23.56%
Aluminum	6.52%
Sodium	.08%
Iron	4.1%
Potassium	6.34%
Calcium	4.6%
Magnesium	2.4%

Source: Author's research

Analysis of XRD Bulk Data

The traditional XRD data (Table 10) analyses indicate that the Bodele materials are primarily montmorillite (smectites), kaolinites, illite, halloysite, quartz, augite, and possible amorphous quartz. The NASA 1-4 samples are the four individual sample sites where the BodEX team collected the samples. The labels NASA 1 through NASA 4 were assigned arbitrarily to the four sample packets received from the BodEX team.

Table 10. Bodele Semi-Quantitative Mineral Analysis; Traditional XRD

	Quartz	Halloysite	Smectite	Dioct	Augite	Sum
NASA 4	3	18	18	44	19	58
NASA 1	4	25	21	74	nd	50

Source: Author's research

The sum column with percent composition of 58 percent for the NASA 4 sample indicates that ~40 percent of the remaining materials are amorphous, and, in conjunction with said clay minerals, are probably allophane and amorphous silica. With NASA1, the summation of dioct clay of ~74 percent indicates that the total for halloysite and smectite should equal 74 percent and results may indicate difficulties in crystal orientation with the XRD vectors with limited supplies of the sample. Additional runs preparing samples with spray dry methods should remove effects of crystal orientation preference and produce evidence that is more conclusive. Additional samples are obtainable through the BodEX team and will be run later for clarification. Results from the runs produced d-spacings, however, are indicative of the following clay minerals and other silicates (Figure 29); halloysite, smectite, kaolinite, illite, and some quartz.

Samples NASA 1-4 were prepared in dry mount for figure 20, resulting in a fairly consistent reading for high quantities of halloysite and smectites (montmorillonites) and illite with d-spacing indicator at 2.56 for illite, kaolinite d-spacings at 7.13 and 3.58, and smectites at 12.94. Because of the wide variations in cation exchange between clay mineral groups, d-spacings can vary considerably from sample to sample. Therefore, XRD data (Appendix G) was compared to the SEM chemical data analyses in identifying the clay minerals involved in the samples.

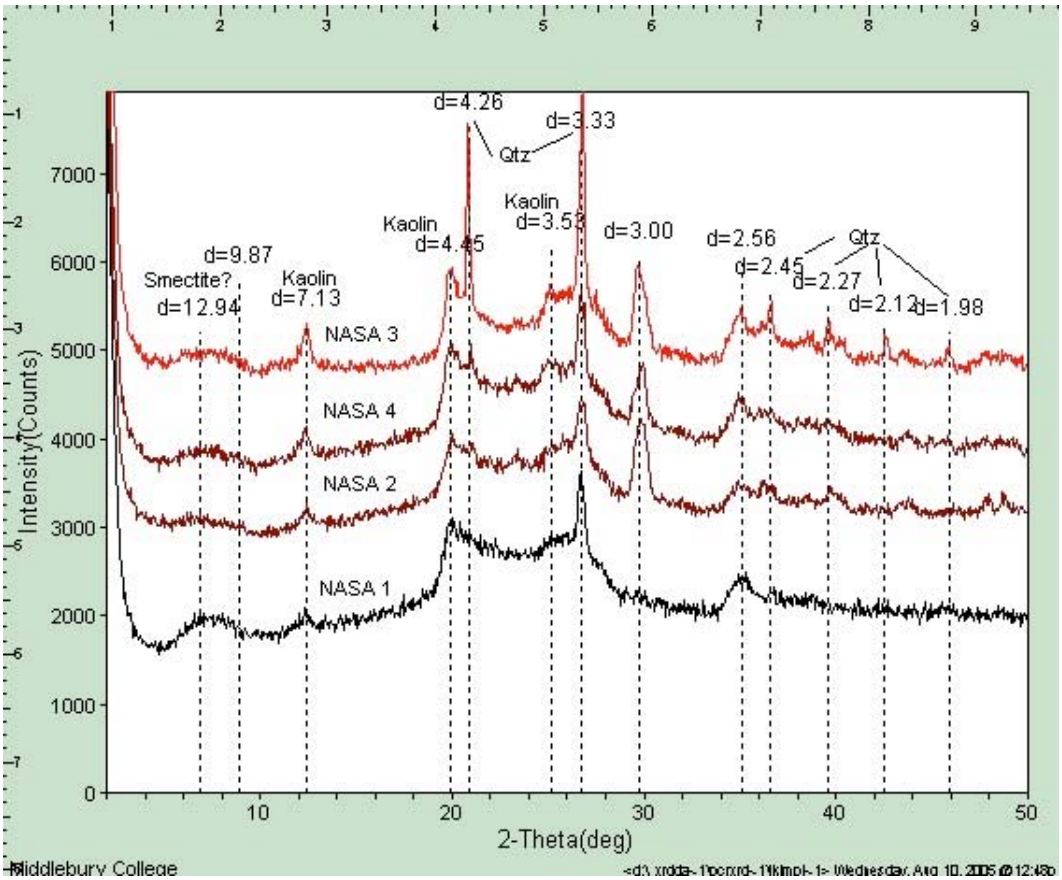

Figure 29. NASA 1-4 XRD Data
Source: Author's research

A second set of NASA 1-4 samples were prepared in ethylene glycol to separate particle layers, with similar results (Figure 30). Figure 30 illustrates the comparable d-spacings produced, with the added illite signatures not apparent in the dry mount samples. Additionally, a third set of slides was prepared with zinc oxide used as a baseline comparative distribution to enhance readings. In all three preparations with all four Bodele samples, the same results occur. Smectites (montmorillites), halloysite, kaolinite, illite, and some quartz are produced. Indicators exist for small amounts of augite or albite that also showed up in the SEM

chemical analyses from several samples. Hence, the SEM data supports the results from the XRD data.

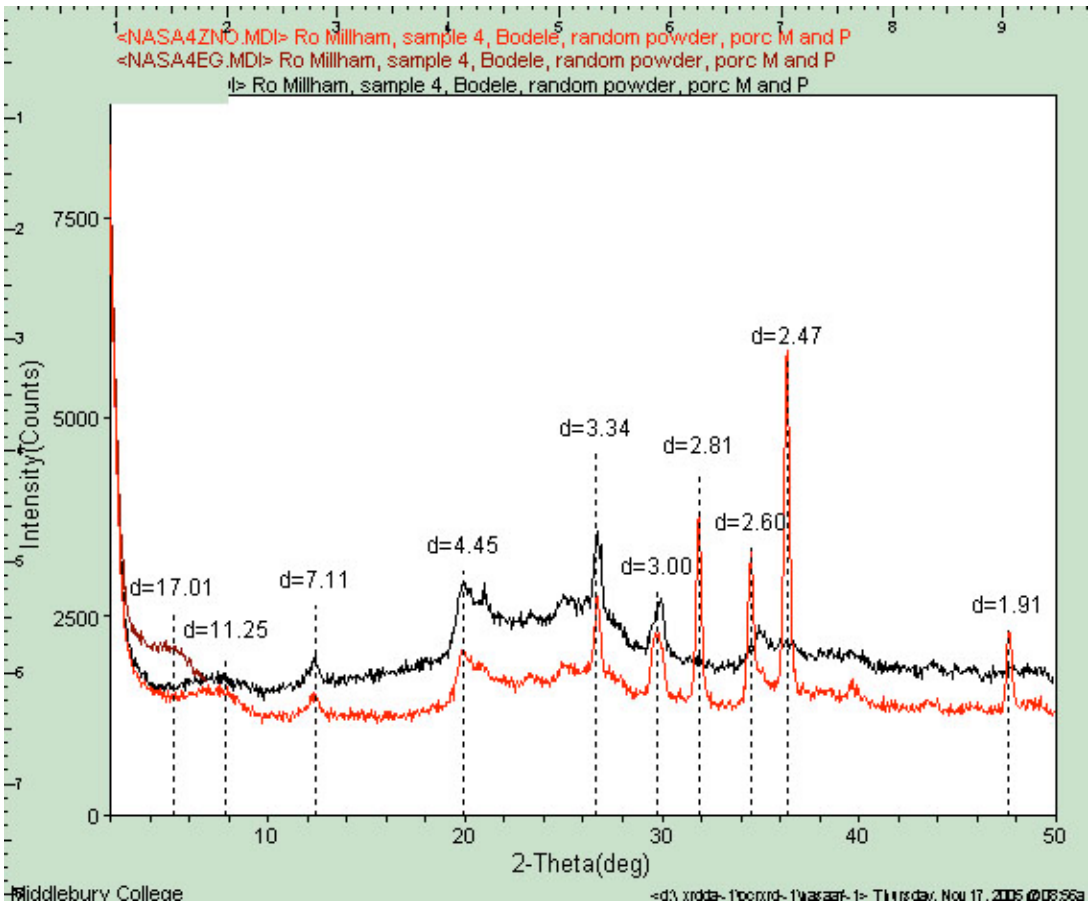

Figure 30. NASA 4 Sample E-glycol and Zinc Oxide Data
Source: Author's research

Analysis of XRD and XRD XRF Aerosol Data

Aerosol data for the Bodele samples produced the same results that the bulk samples produced. Although documentation is unavailable because of patent issues with our current XRD XRF (Appendix H), the following data were captured at a traditional XRD laboratory in Brazil.

- Aerosol Particles < 10mm were collected in Nuclepore filters. Gravimetry, scanning electron microscopy, and spectral absorption analyses were performed. Elemental composition and X-ray diffraction will be performed soon.

- Aerosol mass concentration varied from 75–10,000mg/m^3

- Aerosol spectral absorption efficiency was measured from 350-2500nm. Two main groups of particles were identified, both with strong absorption in the UV and visible but one with significantly stronger absorption in the near infrared than the second one. Aeronet absorption spectral dependence is consistent with the stronger absorption in the NIR.

- Preliminary distribution of particle sizes from the SEM shows similarities with Aeronet retrievals but significant difference in size range. SEM statistics show a direct correlation between the XRD and SEM samples compositions.

- Preliminary elemental composition measurements show predominant elements: Si, Al, K, Ca, and Cl. These are in agreement with bulk sample analyses in SEM data and XRD data (Figure 31).

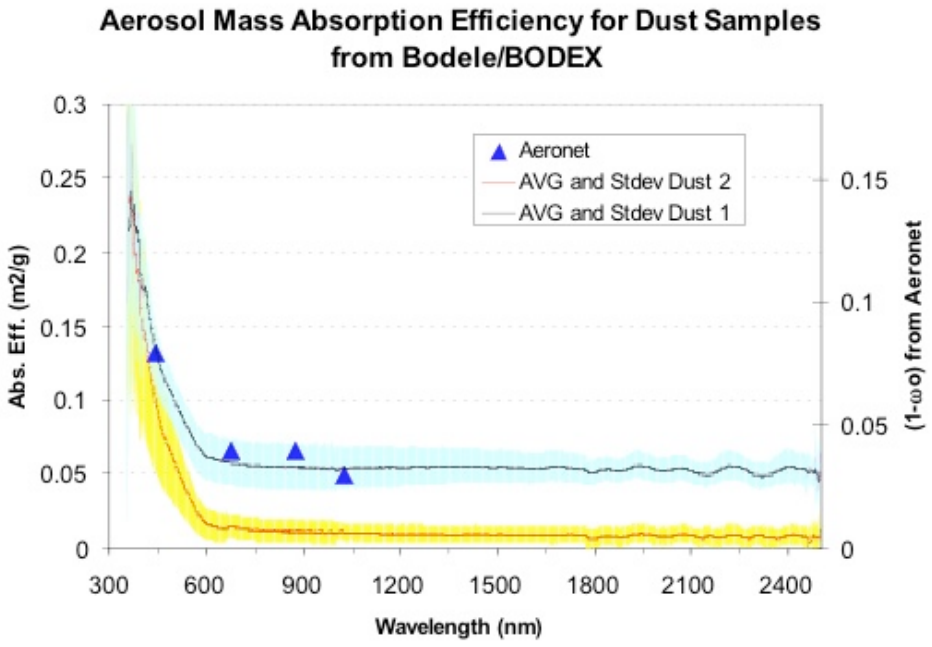

Figure 31. Aerosol XRD Data
Source: Vanderlei Martins, NASA GSFC, 2006

NASA-GSFC Filter Measurements from the BODEX experiment in Bodele/Chad produced the following data:

- Figures show the comparisons between imaginary refractive indices measured by aeronet and by the filter technique. Refractive index can be measured more directly than ωo with the filter technique.
- Aeronet error bars correspond to values reported by Oleg (2004), and are standard error bars for AERONET.
- Filter error bars correspond to the envelops of the density assumption (lower end corresponds to 1g/cm3 and the upper end to 2g/cm3).

This is illustrated in the following graph (Figure 32) by Vanderlei Martins (2006), and provides particle size distribution and refractive properties of the aerosol samples tested through the AERONET system.

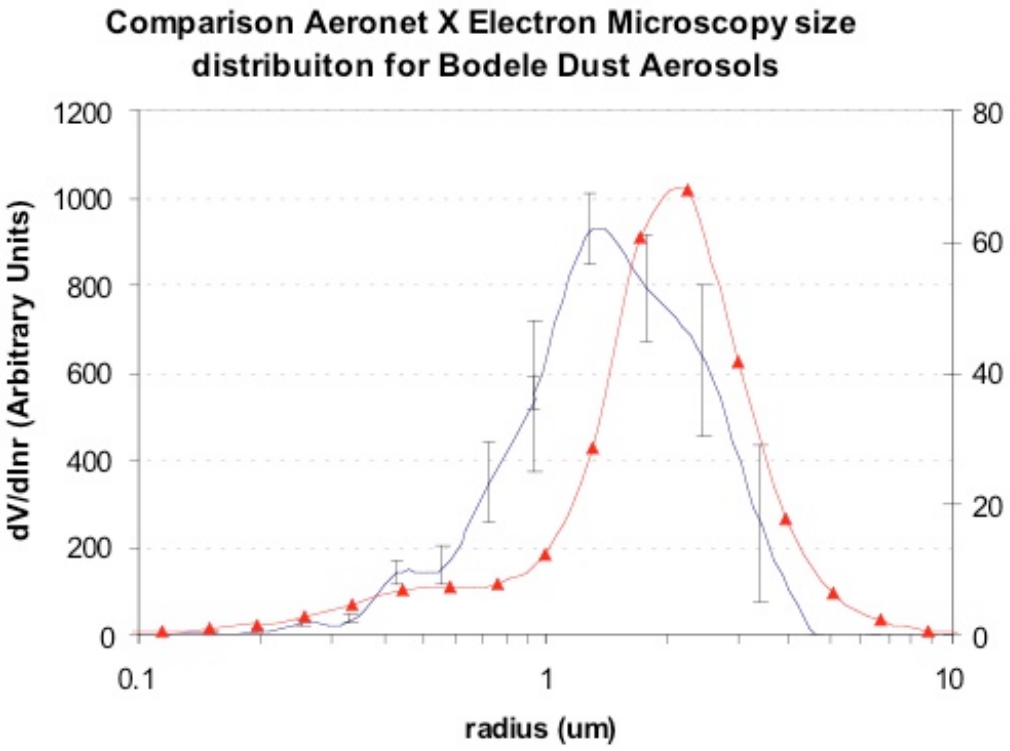

Figure 32. Aerosol Size Distribution for the Bodele
Source: Vanderlei Martins, NASA GSFC, 2006

In summary, the distribution of particle size and identification of mineral compositions using various techniques produced similar, if not exact, accurate results.

Additional data on elemental composition, gathered from the XRD XRF being developed for NASA at NASA's Goddard Space Flight Center, has provided elemental statistics supporting the XRD and SEM data. Patents pending limit what

can be shown here, however, the data are derived in k-fluorescence and d-spacing values comparable to all other data at this time. The quantity of elemental particles is not measured at this time. Hematite, not common in the Bodele samples, is illustrated in Figure 33. K-Fluorescence (provides elemental analyses of materials) values are indicated in the horizontal red scatters, and d-spacing values for crystal faces, hence, indices for mineral identification, are indicated in the vertical red scatters.

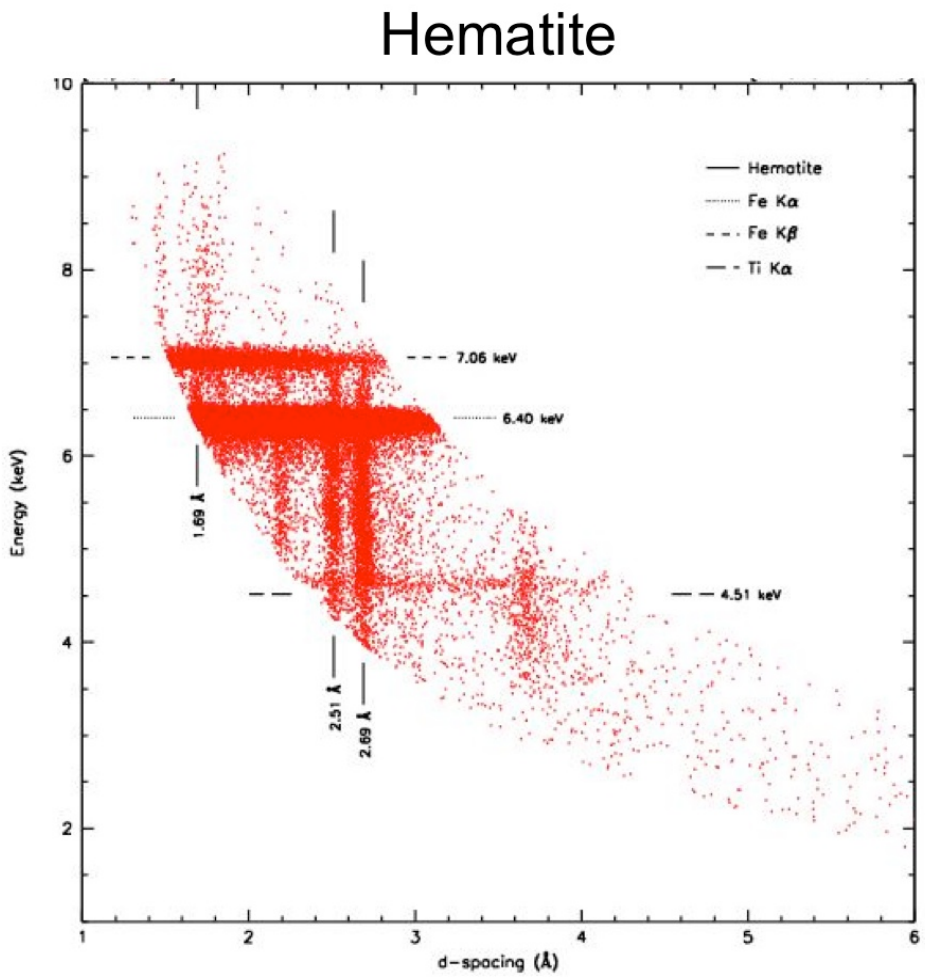

Figure 33. Aluminum Data from the XRD XRF Technology
Source: Keith Gendreau and Zaven Arzoumanian, NASA GSFC, 2006

Analysis of Geological Maps and History

The French geological maps and history for the region of study concurs with data results collected and with the extensive literature review conducted on the Bodele Depression, the Saharan Metacraton, and the Tibesti/Ennedi Mountains. All minerals found in the samples provided are expected to be found in the Bodele Depression with the exception of cosmic silicon (found in sample 3, filter 12) and a filter with 25.75% titanium, which is unexplainable at this time. The geological and geomorphological history of the region, especially in the climate changes experienced over the past 12,000 years that included cyclic flooding followed by long periods of drought conditions, support the minerals identified in the Bodele samples. Research indicates that arid regions that have been flooded in the past million years (Prospero, et al., 1999) tend to have sediment particles small enough to be deflated and entrained in the atmosphere.

Research Questions and Hypotheses

Research Question One

Where does the material emitted from the Bodele Depression originate?

The material emitted from the Bodele Depression is derived from weathered materials from the Saharan Metacraton and the Tibesti and Ennedi Mountains, sedimentary deposits deposited in the Mega-Lake Chad Basin during periods of wet conditions (lacustrine), alluvial deposition, wind-blown sediments from northeast of the Bodele in south-eastern Libya, and the desiccated remains of fresh water diatoms

that thrived in Mega-Lake Chad before it dried up. The sample material is composed of typical crustal minerals that have been weathered, are primary and secondary sediment deposits, and have been influenced by fluctuating wet and arid conditions in the Sahara over the past 12,000 years, or, the post-Holocene period.

Research Question Two

What geological and/or geomorphological history of the region affects the dust emissions from the Bodele?

Geomorphologically, the Bodele Depression is a remnant of Mega-lake Chad, once a freshwater lake, situated on the downwind side of a gap between two mountain ranges, the Tibesti and Ennedi. This gap acts as a funnel as the prevailing trade winds blow from the northeast through the gap, and into the Bodele. Wind speeds increase dramatically in the gap causing the Bodele particles to be deflated and, subsequently, entrained high up into the atmosphere very quickly. Once entrained, these particles are carried long distances to the Atlantic coast of Africa, with only the larger particles (>10μm) settling out either in or downwind of the Bodele. Of the 240± 80 Tg of dust emitted from the Bodele each year, scientists estimate that 120± 40 Tg is deposited in the Atlantic Ocean, and the remainder is deposited in the Caribbean (~70 Tg) in summer and the Amazon River Basin (~50 Tg) in winter (Koren, et al., 2006; Kaufman, et al., 2005).

The sediments contained in the Bodele Depression include material eroded from the granitic Tibesti and Ennedi mountains, recrystallized materials from the Sahara Metacraton, regressive/transgressive sea deposits from ancient coastal seas to

the northeast in Libya and Egypt, and the lacustrine sediments and diatom deposits in the lake basin. Millions of years of geological processes, including tectonic activity, volcanism, weathering and erosion, glacial cycles, and climate change, have contributed to the materials found in the Bodele.

Research Question Three

Are the mineralogies of the Bodele bulk and aerosol samples within expected parameters for the regions geological history, and are they similar?

The Bodele Depression samples, obtained from the BodEX team retrieved in February of 2005, exhibit mineralogies within the expected parameters of the geological history of the region of study. Typical crustal silicate minerals in the correct percentages of occurrence have been identified along calcium carbonates, dolomites, and iron oxides, and exotic rare occurrences of cosmic silicon and a single elevated measure of titanium. Considering the mineralogies of the region affecting the sediments in the Bodele, and the freshwater lake diatoms, the samples from the Bodele exhibit mineralogies expected for crustal materials associated with tectonic activity and volcanism.

Research Question Four

Do the BodEX samples provide the necessary information to determine the identification of the minerals emitted from the Bodele Depression in general?

The BodEX samples provide the necessary information to determine the mineral dust emitted from the Bodele. As stated previously, mineralization appears

to be consistent with expected crustal percent elemental compositions produced by typical crustal deposits of silicate minerals and sedimentary deposits expected for the region. These deposits, primarily clay mineral deposits and calcium carbonate, provide information on parent materials and climate change over time in the region of study, especially the wetting and drying of the region during shifts in climate post-Holocene.

The samples, however, were collected in a limited region of the Bodele Depression, and may not be representative of the depression as a whole. Questions regarding collection points, such as along the margins of the depression versus the extreme interior of the Bodele, cannot be answered at this time; hence, samples may represent specific marginal mineralogy (along the periphery) or may be representative of the entire Bodele.

Additionally, samples from the region surrounding the Bodele Depression, especially south-central Libya and the Tebesti/Ennedi, would be helpful for mineralogy verification and for comparative analysis of the Bodele samples. This would assist in determining primary and secondary sediment histories and mineralogy of the region.

CHAPTER V

SUMMARY, CONCLUSIONS, AND RECOMMENDATIONS

Summary

The dust emissions from the Bodele Depression are typical primary and secondary minerals derived from weathered and eroded crustal materials over millions of years. These sediments have been wetted during periods of humid climate conditions in the Sahara, followed by periods of arid climate conditions.

Additionally, the southern boundary of the Sahara has fluctuated regularly over time to produce tropical humid conditions for extended periods followed by drier conditions. For example, the southern boundary of the Sahara is located further north today than it has been in the past. As wet conditions prevailed, changes to sediments occurred as chemical activity altered and modified material in place. Drier conditions allowed for saltation and deflation to occur, causing dust storms to prevail in regions where vegetation is scarce or non-existent (Tegan, et al., 2002).

The Bodele Depression, located in the north-central Sahara, is emitting more dust than any other location on Earth. The geomorphology of the region dictates that the northeasterly trade winds blow through a gap between the Tibesti and Ennedi Mountains. The winds increase in velocity to the point whereby dust emissions

become intensified and carry up to ~240 Tg of dust from the Bodele to the Atlantic Ocean coast each year (Kaufman, et al., 2005; Koren, et al., 2006).

Analysis of the bulk and aerosol in situ samples from the Bodele Depression has provided data that supports the hypothesis that the mineralogy of the Bodele is typical for crustal sediments. Silicate minerals dominate the sample, primarily ferromagnesian and framework silicates, with percent elemental analyses corresponding with these minerals.

Conclusions

With the massive quantities of dust emitted from the Bodele each year, scientist need to understand the complex mineralogy of the materials in the Bodele to determine the effects these minerals have on climate and climate change over time. The optical properties, hygroscopic properties, and size, shape, composition, and distribution of dust in the atmosphere needs to be fully understood if the effect on climate and climate change is to be understood. Additionally, understanding the composition of these dusts, combined with a working knowledge of the reactions to sunlight, chemical abilities in interactions with other aerosols, and the affect on cloud properties and role as condensation nuclei, will provide information necessary for more accurate climate modeling.

The samples from the Bodele in situ aerosol and bulk ground materials produce the dust emissions occurring from the region ~40 percent (Kaufman, et al., 2005; Koren, et al., 2006) of the days in the winter months in the Northern Hemisphere. The results from literature review, X-Ray diffractometer data, SEM

data, geological survey maps, and CCD XRD data provided concrete identification of the Bodele minerals as typical crustal silicate minerals with small amounts of calcium carbonate, dolomite, silica, desiccated diatoms, and possible iron oxides. The silicate minerals are primarily ferromagnesian and framework silicates typical of low-lying depositional basins and the weathering processes occurring in alternating wet and dry periods. Clays minerals halloysite, kaolinite, and smectites (montmorillite) are the most common.

These data will positively affect climate modeling. Understanding the mineralogy will enable modelers to set parameters for reflective properties, hygroscopic characteristics, and chemical reactions as internal and external mixing of anthropogenic and other natural aerosols combine during transport. Accurate modeling of the effect atmospheric mineral dust has on climate will aid scientists in accurately projecting and predicting climate change and the causative agents.

Recommendations

Additional samples from the Bodele Depression, the Saharan Metacraton, and the Tibesti/Ennedi Mountains should be collected for conducting more analysis of the minerals that make up these structures. Additionally, the new XRD XRF should be used to further investigate the elemental analyses of all four samples currently with the NASA team.

Future samples from the Bodele Depression should be obtained from grid points or coordinate readings to ensure that the in situ samplings are completely representative of the region, and not isolated to a few meters or hundreds of meters

from the perimeter of the Bodele. Additionally, aerosol samplings should be obtained downwind of the Bodele to provide materials necessary for understanding internal and external mixing of Bodele materials in transport to the Atlantic Ocean, therefore, to better understand the dust emissions overall impact on climate and climate change.

BIBLIOGRAPHY

Abdelsalam, M.G., and Dawoud, A.S. (1991). The Kabus Ophiolitic Melange, Sudan, and its Bearing on the Western Boundary of the Nubian Shield. *Journal Geological Society*, London, 148, 83–92.

Abdelsalam, M.G., Stern, R.J., Abdel-Rahman, E.M., Elfaki, E.M., Elhur, B., and Ibrahim, F.M. (2000). Neoproterozoic Deformation in Sudan: The third cataract shear zone. *Journal African Earth Sciences,* 30, 2.

Abdelsalam, M.G., Liegeois J-P, and Stern, R.J. (2001). The Saharan Metacraton. *Journal of African Earth Sciences*, 34, 119-136.

Abdelsalam, M.G., Stern, R.J., Schandelmeier, H., & Sultan, M. (1995). Deformational History of the Keraf Zone in NE Sudan Revealed by Shuttle Imaging Radar. *Journal Geology*, 103, 475–491.

Abdul-Razzak, H. and Ghan, S. (2000). A Parameterization of Aerosol Activation 2: Multiple aerosol types. *Journal of Geophysical Research*, 105, 6837-6844.

Ajayi, C. I., and Ajakaiye, D. E. (1981). The Origin and Peculiarities of the Nigerian Benue Trough: Another look from recent gravity data obtained from middle Benue. *Tectonophysics*, 80, 285-303.

Alfaro, S., Ste'phane C., Gaudichet, A., Gomes, L., Maill'e, M. (1998). Mineral Aerosol Production By Wind Erosion: Aerosol particle sizes and binding energies. *Geophysical Research Letters*, 25, 7991–7994.

Andreae, M.O., and Crutzen, P. J. (1997). Atmospheric Aerosols: Biogeochemical sources and role in atmospheric chemistry. *Science,* 276, 1052-1056.

Andreae, M.O., Browell, E. V., Garstang, M., Gregory, G. L., Harriss, R. C., et al. (1998). Biomass-burning Emissions and Associated Haze Layers over Amazonia. *Journal of Geophysical Research*, 93, 1509-1527.

Andreae, M. O., Charlson, R. J., Bruynseels, F., Storms, H., et al., (1986). Internal mixtures of sea salt, silicates, and excess sulfate in marine aerosols. *Science,* 232, 1620-1623.

Appel, B. R., Tokiwa, Y., and Kothny, E. L. (1983). Sampling of the Carbonaceous Particles in the Atmosphere, II. *Atmospheric Environment*, 17, 1787-1796.

Arimoto, Richard (2001). Eolian Dust and Climate: Relationships to sources, tropospheric chemistry, transport, and deposition. *Earth Science Reviews*, 54, 1-3.

Artaxo, P., Swietlicki, E., Zhou, J., Hansson, H. C., Maenhaut, W., et al. (1998b). Aerosol Properties in the Central Amazon Basin during the Wet Season during the LBA/CLAIRE Experiment. *Journal of Geophysical Research*, 79, F155.

Avbovbo, A. A., Ayoola, E. O., and Osahon, G. A. (1986). Depositional and Structural Styles in Chad Basin of Northeast Nigeria. *American Association of Petrology*; Geololgy Bulletin, 70, 12, 1787-1798.

Bian, H., and Zender, C. S. (2003). Mineral Dust and Global Tropospheric Chemistry: Relative Roles of Photolysis and Heterogeneous Uptake. *Journal of Geophysical Research*, 108, D21, 4672.

Bishop, S. R., Momiji, H., Carretero-González, R., and Warren, A. (2002). Modelling Desert Dune Fields Based on Discrete Dynamics. *Discrete Dynamics in Nature and Society*, (Hindawi Publishing Corporation, New York, 7, 1, 7-17.

Black, R., and Liégeois, J. -P. (1993). Cratons, Mobile Belts, Alkaline Rocks, and Continental Lithospheric Mantle: The Pan-African testimony. *Journal of the Geological Society*, London, 150, 89–98.

Broecker, W. S. (2002). Dust: Climate's Rosetta Stone. *Proceedings of the American Philosophical Society*, 146, 1, 77-80.

Brooks, N., Chiapelle, I., Di Lernia, S., Drake, N., Legrand, M., Moulin, C., Prospero, J. M. (2005). The Climate-Environment-Society Nexus in the Sahara from Prehistoric Times to the Present Day. *The Journal of North African Studies*, 10, 3–4, 254-292.

Brown, C.D., and Philipps, R.J. (2000). Crust–Mantle Decoupling by Flexure of Continental Lithosphere. *Journal Geophysical Research*, 105, 13,221–13,237.

Burke, K. (1976). The Chad Basin: An Intra-continental Basin. *Tectonophysics*, 36, 192-206.

Carlson, T. N., and Prospero, J. M. (1972). The Large Scale Movement of Saharan Air Outbreaks over the Northern Equatorial Atlantic. *Journal of Applied Meteorology*, 11, 283–297.

Charlson, R.J., Schwartz, S. E. Hales, J. M., Cess, R. D., Coakley, J. A., Hansen, J. E., and Hofmann, D. J. (1992). Climate Forcing by Anthropogenic Aerosols. *Science*, 255, 423-430.

Chiapello, I., Moulin, C., and Propsero, J. M. (2005). Understanding the Long-term Variability of African Dust Transport Across the Atlantic As Recorded in Both Barbados Surface Concentrations and Large-scale Total Ozone Mapping Spectrometer (TOMS) Optical Thickness. *Journal of Geophysical Research*, 110, D18S10.

Chuang, C.C., Penner, J. E., Taylor, K. E., Grossman, A. A., and Walton, J. J. (1997). An Assessment of the Radiative Effects of Anthropogenic Sulphate. *Journal of Geophysical Research*, 102, 3761-3778.

Chuang, C. C., Penner, J., Prospero, J. M., et al. (2002). Cloud Susceptibility and the First Aerosol Indirect Forcing: Sensitivity to black carbon and aerosol concentrations. *Journal of Geophysical Research*, 107, D21, 4564.

Clarke, A.D. (1992). Atmospheric Nuclei in the Remote Free Troposphere. *Journal of Atmospheric Chemistry*, 14, 479-488.

Claquin, T., Schulz, M., and Balkanski, M. (1999). Modeling the Mineralogy of Atmospheric Dust Sources. *Journal of Geophysical Research*, 104, 22,243–22,256.

Colarco, P. R., Toon, O. B., and Holben, B. N. (2003). Saharan Dust Transport to the Caribbean during PRIDE 1: Influence of dust sources and removal mechanisms on the timing and magnitude of downwind aerosol optical depth events from simulations of in situ and remote sensing observations. *Journal of Geophysical Research*, 108, D19, 8589.

Colarco, P. R., Toon, O. B., Reid, J. S., et al. (2003). Saharan Dust Transport to the Caribbean during PRIDE 2: Transport, vertical profiles, and deposition in simulations of in situ and remote sensing observations. *Journal of Geophysical Research*, 108, D19, 8590.

Corrigan, C. E., and Novakov, T. (1999). Cloud condensation nucleus activity of organic compounds: a laboratory study. *Atmospheric Environment*, 33, 2661–2668.

Dalziel, I.W.D. (1997). Neoproterozoic-Paleozoic Geography and Tectonics: Review, hypothesis, and environmental speculation. *Geological Society America Bulletin*, 109, 16–42.

Drake, N., and Bristow, C. (2006). Shorelines in the Sahara: Geomorphological evidence for an enhanced monsoon from palaeolake Megachad. *Department of Geography*, King's College London, Strand, London, WC2R 2LS.

Dubovik, O., et al. (2003). Variability of Absorption and Optical Properties of Key Aerosol Types Observed in Worldwide Locations. *Journal of Atmospheric Sciences, American Meteorological Society*, 59, I 3, 590-608.

Dubivik, O., Sinyuk, A., Lapyonok, T., et al. (2006). Application of Spheroid Models to Account for Aerosol Particle Nonsphericity in Remote Sensing of Desert Dust. *Journal of Geophysical Research*, 111, D11208.

Dubovik O., Holben, B. N., Kaufman, Y. J., Yamasoe, M., Smirnov, A., et al. (1998). Single scattering albedo of smoke retrieved from the sky radiance and solar transmittance measured from ground. *Journal of Geophysical Research***,** 103, 31,903–31,923

Durand, J. R., Dufour, P., Verdeaux, F., and Zabi, S. (1982). Research and development: Some illustrations and prospects for Ivory Coast brackish waters. *Atlantica, Rio Grande*, 5, 2, 40.

Eatough, D.J., Eatough, D. A., Lewis, L., and Lewis, E. A. (1996). Fine Particulate Chemical Composition and Light Extinction at Canyon-lands National Park; Using organic particulate material concentrations obtained with a multi-system, multi-channel diffusion denuder sampler. *Journal of Geophysical Research*, 101, 19,515-19,531.

Engelstaedter, S., Tegen, I., and Washington, R. (2005). North African Dust Emissions and Transport. Institute for Tropospheric Research, Permoserstr. 15, 04318 Leipzig, Germany, *Earth Science Reviews, 79, I1-2, 73-100.*

Erickson III, D. J., and Duce, R. A. (1988). On the Global Flux of Atmospheric Sea Salt. *Journal of Geophysical Research*, 93, 14,079-14,088.

Evan, A. T., Heidinger, A. K., and Knippertz, P. (2006). Analysis of Winter Dust Activity off the Coast of West Africa Using a New 24-year Over-water Advanced Very High Resolution Radiometer Satellite Dust Climatology. *Journal of Geophysical Research*, 111, D12210.

Facchini, M.C., Mircea, M., Fuzzi, S., and Charlson, R. J. (1999). Cloud Albedo Enhancement by Surface-active Organic Solutes in Growing Droplets. *Nature*, 401, 257-259.

Falkovich, A., Ganor, E., Levin, Z., Formenti, P., and Rudich, Y. (2001). Chemical and Mineralogical Analysis of Individual Mineral Dust Particles. *Journal of Geophysical Research*, 106, n. D16, 18,029–18,036.

Feingold, G., Cotton, W. R., Kreidenweis, S. M., and Davis, J. T. (1999a). Impact of Giant Cloud Condensation Nuclei on Drizzle Formation in Marine Stratocumulus: Implications for cloud radiative properties. *Journal of Atmospheric Science*, 56, 4100-4117.

Flores, O., Claquin, T., and Schulz, M. (2006). Contributions to the Study of Atmospheric Dust Sources: A mineralogical approach. *Institute for Applied and Inorganic Chemistry*, University of Hamburg, Germany.

Fung, I., Meyn, S., Tegen, I., et al. (2000). Iron Supply and Demand in the Upper Ocean. *Journal of Geophysical Research*, 14, 1, 281–296.

Gangoiti, G., Alonso, L., Navazo, M., et al. (2006). North African Soil Dust and European Pollution Transport to America during the Warm Season: Hidden links shown by a passive tracer simulation. *Journal of Geophysical Research*, 111, D10109.

Gasse, F. (2005). Climate and Hydrological Changes in Tropical Africa during the Past Million Years. *CEREGE*, UMR 6635, BP 80, 13545 Aix-en-Provence cedex 04, France.

Ghuma, M.A., and Rogers, J.J.W. (1978). Geology, Geochemistry, and Tectonic Setting of the Ben Ghnema Batholith, Tibesti Massif, Southern Libya. *Geological Society America*, Bulletin 89, 1315–1358.

Giles, J. (2005). Climate Science: The Dustiest Place on Earth. *Nature*, 434, 816-819.

Gilliani, N., Schwartz, S. E., Leaitch, W. R., Strapp, J. W., and Isaac, G. A. (1995). Field Observations in Continental Stratiform Clouds: Partitioning of cloud droplets between droplets and non-activated interstitial aerosols. *Journal of Geophysical Research*, 100, 18,687-18,706.

Ginoux, P., Chin, M., Tegan, I., Prospero, J. M., Holben, B., Dubovik, O., Lin, S. (2001). Sources and Distributions of Dust Aerosols Simulated with the GOCART Model. *Journal of Geophysical Research*, 106, D17, 20,255-20,273.

Ginoux, P., and Torres, O. (2003). Empirical TOMS Index for Dust Aerosol: Applications to model validation and source characterization. *Journal of Geophysical Review*, 108, D17.

Glantz, P., and Noone, K. J. (2000). A Physically based Algorithm for Estimating the Relationship between Aerosol Mass to Cloud Droplet Number. *Tellus*, 52, 1216-1231.

Gong, S.L., Barrie, L. A., Blanchet, J. -P., and Spacek, L. (1998). Modeling Size-distributed Sea Salt Aerosols in the Atmosphere: An application using Canadian climate models. In: *Air Pollution Modeling and Its Applications XII*, Plenum Press, New York.

Goudie, A. S., and Middleton, N. J. (2001). Saharan Dust Storms: Nature and consequences. *Earth Science Reviews*, 56, 1, 179-204.

Grant, N.K. (1978). Structural Distinction between a Metasediemntary and an Underlying Basement in the 600 Ma old Pan-African Domain of Northwest Nigeria, West Africa. *Geological Society of America,* Bulletin 89, 50–58.

Griffin, R.J., Cocker III, D. R., Seinfeld, J. H., and Dabdub, D. (1999b). Estimate of Global Atmospheric Organic Aerosols from Oxidation of Biogenic Hydrocarbons. *Geophysical Research Letters*, 26, 2721-2724.

Grini, A., and Zender, C. S. (2004). Roles of Saltation, Sandblasting, and Wind Speed Variability on Mineral Dust Aerosol Size Distribution during the Puerto Rican Dust Experiment I (PRIDE). *Journal of Geophysical Research*, 107, doi: 10.1029.

Grini, A., Myhre, G., Zender, C. S., and Isaksen, I. S. A. (2005). Model Simulations of Dust Sources and Transport in the Global Atmosphere: Effects of soil erodibility and wind speed variability. *Journal of Geophysical Research*, 110, D02205.

Guenther, A., Hewitt, C., Erickson, D., Fall, R., et al. (1995). A Global Model of Natural Volatile Organic Compound Emissions. *Journal of Geophysical Research*, 100, 8873-8892.

Gultepe, I., and Isaac, G. A. (1997). Relationship between liquid water content and temperature based on aircraft observations and its applicability to GCMs (Global Climate Models). *Journal on Climate*, 10, 446-452.

Hansen, J.E., Sato, M., and Ruedy, R. (1997). Radiative Forcing and Climate Response. *Journal of Geophysical Research*, 102, 6831-6864.

Hansson, H.C., Rood, M. J., Koloutsou-vakakis, S., Hameri, K., Orsini, D., and Wiedensohler, A. (1998). NaCl Aerosol Particle Hygroscopicity Dependence on Mixing with Organic Compounds. *Journal of Atmospheric Chemistry*, 31, 321-346.

Harms, U., Darbyshire, D.P.F., Denkler, T., Hengst, M., and Schandelmeier, H. (1994). Evolution of the Neoproterozoic Delgo Sutures Zone and Crustal Growth in Sudan: Geochemical and radiogenic isotope constrains. *Geologische Rundschau*, 83, 591–603.

Harms, U., Schandelmeier, H., and Darbyshire, D.P.F. (1990). Pan-African Reworked Early/Middle Proterozoic Crust in NE Africa, W of the Nile: Sr and Nd Isotope Evidence. *Journal Geological Society*, London, 147, 859–872.

Harris, N.B.W., Hawkesworth, C.J., and Ries, A.C. (1984). Crustal Evolution in NE and E Africa from Model Nd Ages. *Nature*, 309, 773–776.

Haywood, J., Allen, R. P., Culverwell, I., et al. (2005). Can Desert Dust Explain the Outgoing Long-wave Radiation Anomaly over the Sahara During July 2003? *Journal of Geophysical Research*, 110, D05105.

Hegg, D.A., Radke, L.F., and Hobbs, P.V. (1991). Measurements of Aitken Nuclei and Cloud Condensation Nuclei in the Marine Atmosphere and their Relation to the DMS-Cloud-climate Hypothesis. *Journal of Geophysical Research*, 96, 18727-18733.

Hegg, D. A., Livingston, J., Hobbs, P. V., Novakov, T., and Russell, P. B. (1997). Chemical apportionment of aerosol column optical depth off the Mid-Atlantic coast of the United States. *Journal of Geophysical Research,* 102, n. D21, 25,293-25, 304.

Hoffmann, T., Odum, J. R., Bowman, F., Collins, D., Klockow, D., Flagan, R. C., and Seinfeld, J. H. (1997). Formation of Organic Aerosols from the Oxidation of Biogenic Hydrocarbons. *Journal of Atmospheric Chemistry*, 26, 189-222.

Hudson, J. G., and Da, X. (1996). Volatility and Size of Cloud Condensation Nuclei. *Journal of Geophysical Research,* 101, 4435–4442.

Hunter, R.E. (1977). Terminology of Cross-stratified Sedimentary Layers and Climbing-Ripple Structures. *Journal of Sedimentary Petrology*, 47, 697-706.

Isaac, G. A. (1991). Microphysical Characteristics of Canadian Atlantic Storms. *Atmospheric Research,* 26, 339-360.

Isiorho, S.A. (1985). The Significance of Lineaments Mapped from Remotely Sensed Images of the 1:250,000 Lau Sheet in the Benue Trough of Nigeria. *International Journal of Remote Sensing*, 6, 6, 911-918.

Isiorho, S. A., and Matisoff, T. O. (1990). Groundwater recharge from Lake Chad. *Limnology Oceanography,* 35, 4, 931-938.

Jickells, T. D., An, Z. S., Andersen, K. K., Baker, A. R., Bergametti, G., Brooks, N., Cao, J. J., et al. (2005). Global Iron Connections between Desert Dust, Ocean Biogeochemistry, and Climate. *Science*, 308, 5718, 67-71.

Kallos, G., Papadopoulos, A., et al. (2006). Transatlantic Saharan Dust Transport: Model simulation and results. *Journal of Geophysical Research*, 111, D09204.

Kanakidou, M., Tsigaridis, K., Dentener, F. J., and Crutzen, P. J. (2000). Human Activity Enhances the Formation of Organic Aerosols by Biogenic Hydrocarbon Oxidation. *Journal of Geophysical Research*, 1-5, 9243-9254.

Kaufman, Y. J., Tanr´e, D., Dubovik, O., Karnieli, A., and Remer, L. A. (2001). Absorption of Sunlight by Dust as Inferred from Satellite and Ground-based Remote Sensing. *Geophysical Research Letters*, 28, 1479–1482.

Kaufman, Y., Tanre', D., and Boucher, O. (2002). A Satellite View of Aerosols in the Climate System. *Nature*, 419, n. 6903, 215-223.

Kaufman, Y. J., Koren, I., Remer, L. A., Tanre, D., Ginoux, P., and Fan, S. (2005). Dust Transport and Deposition Observed from the Terra-Moderate Resolution Imaging Spectroradiometer (MODIS) Spacecraft over the Atlantic Ocean. *Journal of Geophysical Research*, 110, D10S12.

Key, R.M., Charsley, T.J., Hackman, T.J., Wilkinson, A.F., and Rundle, C.C. (1989). Superimposed Upper Proterozoic Collision Controlled Orogenies in the Mozambique Orogenic Belt of Kenya. *Precambrian Research*, 44, 197–225.

Koren, I., and Kaufman, Y. J. (2004). Direct Wind Measurements of Saharan Dust Events From Terra and Aqua Satellites. *Geophysical research Letters*, 31, L06122.

Koren, I., Kaufman, Y. K., Washington, R., Todd, M., Rudich, Y., Martins, J. V., and Rosenfeld, D. (2006). The Bodélé Depression: A Single Spot in the Sahara that Provides Most of the Mineral Dust to the Amazon Forest. *Environmental Research Letters*, 1, 14,005.

Kubilay, N., Nickovic, S., Moulin, C., and Dulac, F. (2000). An Illustration of the Transport and Deposition of Mineral Dust onto the Eastern Mediterranean. *Atmospheric Environment*, 93-130.

Kulmula, M., Laaksonen, A., Korhonen, P., Vesala, T., and Ahonen, T. (1993). The Effect of Atmospheric Nitric Acid Vapor on Cloud Condensation Nucleus Activation. *Journal of Geophysical Research*, 98, 22,949-22,958.

Küster, D., Liégeois, J-P. (2001). Sr, Nd Isotopes, and Geochemistry of the Bayuda Desert High-Grade Metamorphic Basement (Sudan): An early Pan-African oceanic convergent margin, not the edge of the East Saharan ghost craton. *Precambrian Research*, 109, 1-23.

Lafon, S., and Sokolik, I. (2006). Characterization of Iron Oxides in Mineral Dust Aerosols: Implications for light absorption. *Journal of Geophysical Research,* 111, D21207.

Laaksonen, A., Korhonen, P., Kulmala, M., and Charlson, R. J. (1998). Modification of the Kohler Equation to Include Soluble Trace Gases and Slightly Soluble Substances. *Journal of Atmospheric Science,* 55, 853-862.

Leaitch, W.R., Banic, C. M., Isaac, G. A., Couture, M. D., Liu, P. S. K., Gultepe, I., et al. (1996b). Physical and Chemical Observations in Marine Stratus during 1993 NARE: Factors controlling cloud droplet number concentrations. *Journal of Geophysical Research,* 101, 29,123-29,135.

Leaitch, W.R., Bottenheim, J. W., Biesenthal, T. A., Li, S-M., Liu, P. S. K., Asalian, K., Dryfhout-Clark, H., Hopper, F., and Brechtel, F. J. (1999). A Case Study of Gas-to-particle Conversion in an Eastern Canadian Forest. *Journal of Geophysical Research,* 104, 8095-8111.

Levin, Z., Teller, A., Ganor, E., and Yin, Y. (2005). On the Interactions of Mineral Dust, Sea-salt Particles, and Clouds: A measurement and modeling study from the Mediterranean Israeli Dust Experiment campaign. *Journal of Geophysical Research,* 110, D20202.

Liégeois, J-P., Latouche L., Navez J., and Black, R. (2000). Pan-African Collision, Collapse, and Escape Tectonics in the Tuareg shield: Relations with the East Saharan Ghost craton and the West African craton. 18th Colloquium of African Geology, Graz, Austria, *Journal of African Earth Science,* 30, 53–54.

Liousse, C., Cachier, H., and Jennings, S. G. (1993). Optical and Thermal Measurements of Black Carbon Aerosol Content in Different Environments: Variation of the specific attenuation cross-section, sigma (s). *Atmospheric Environment,* 27A, 1203-1211.

Liousse, C., Penner, J. E., Chuang, C., Walton, J. J., Eddleman, H., and Cachier, H. (1996). A Global Three-dimensional Model Study of Carbonaceous Aerosols. *Journal of Geophysical Research,* 101, 19,411-19,432.

Lohman, U. (2002). A Glaciation Indirect Effect Caused by Soot Aerosols. *Geophysical Research Letters,* 29, 4, 11-1-11-4.

Lu, M.-L., and Sienfeld, J. H. (2006). Effect of Aerosol Number Concentration on Cloud Droplet Dispersion: A large-eddy simulation study and implications for aerosol indirect forcing. *Journal of Geophysical Research,* 111, D02207.

Mahowald, N. M., Baker, A. R., Bergametti, G., Brooks, N., Due, R. A., Jickells, T. D., Kubilay, N., Prospero, J. M., and Tegen, I. (2005). The Atmospheric Global Dust Cycle and Iron Inputs to the Ocean. *Global Biogeochemical Cycles,* 19, GB4030.

Martins, J.V., Artaxo, P., Liousse, C., Reid, J. S., Hobbs, P. V., and Kaufman Y. J. (1998). Effects of Black Carbon Content, Particle Size, and Mixing on Light Absorption by Aerosols from Biomass Burning in Brazil. *Journal of Geophysical Research*, 103, 32,041-32,050.

McKee, E. D. (1979). Introduction to a Study of Global Land Seas. United States Government Printing Office, Washington, 1052, 1-19.

Menon, S., and Saxena, V. K. (1998). Role of Sulphates in Regional Cloud-climate Interactions. *Atmospheric Research*, 47-48, 299-315.

Middleton, G.V., and Southard, J.B. (1984). Mechanics of Sediment Movement: *Society of Economic Paleontologists and Mineralogists*, Short Course 3, 401.

Miller, R. L., Cakmur, R. V., Perlwicz, J., et al. (2006). Mineral Dust Aerosols in the NASA Goddard Institute for Space Sciences Model 'E Atmospheric General Circulation Model. *Journal of Geophysical Research*, 111, D06208.

Moulin, C., Lambert, C. E., Dulac, F., and Dayan, U. (1997) Atmospheric Dust on the Move; Control of atmospheric export of dust from North Africa by North Atlantic Oscillation. *Nature*, 387, 691-694.

Myhre, G., and Stordal, F. (2001). Global Sensitivity Experiments of the Radiative Forcing Due to Mineral Aerosols. *Journal of Geophysical Research*, 106, 18,193–18,204.

Myhre, G., Grini, A., Haywood, J., Stordal, F., Chatenet, B., Tanre', D., Sundet, J., and Isaksen, I. (2003). Modeling the Radiative Impact of Mineral Dust during the Saharan Dust Experiment (SHADE) Campaign. *Journal of Geophysical Research*, 108, 8579.

Novakov, T. and Penner, J. E. (1993). Large Contribution of Organic Aerosols to Cloud Condensation Nuclei Concentrations. *Nature*, 365, 823-826.

Novakov, T. and Corrigan, C. E. (1996). Cloud Condensation Nucleus Activity of the Organic Component of Biomass Smoke Particles. *Geophysical Research Letter*, 23, 2141-2144.

Novakov, T., Hegg, D. E., and Hobbs, P. E. (1997). Airborne Measurements of Carbonaceous Aerosols on the East Coast of the United States. *Journal of Geophysical Research*, 102, 30,023-30,030.

N'Tchayi Mbourou, G., Bertrand, M. G., J. and Nicholson, S. E. (1996). The Diurnal and Seasonal Cycles of Wind-Borne Dust over Africa North of the Equator. *Journal of Applied Meteorology*, 36, 868-882.

Nzenti, J.P. (1998). Neoproterozoic Alkaline Meta-igneous Rocks from the Pan-African North Equatorial Fold Belt (Yaounde, Cameroon): Biotites and magnetite-rich pyroxenites. *Journal African Earth Sciences,* 26, 37–47.

O'Dowd, C.D., Lowe, J. A., Smith, M. H., and Kaye, A. D. (1999). The Relative Importance of Nss-sulphate and Sea-salt Aerosol to the Marine CCN Population: An improved multi-component aerosol-cloud droplet parameterization. *Meteorological Society*, 125, 1295-1313.

Odum, J.R., Hoffmann, T., Bowman, F., Collins, D., Flagan, R. C., and Seinfeld, J. H. (1996). Gas/particle Partitioning and Secondary Organic Aerosol Yields. *Environmental Science Technology*, 30, 2580-2585.

Pegram, W.J., Register, J.K., Fullagar, P.D., Ghuma, M.A., and Rogers, J.J.W. (1976). Pan-African Ages from a Tibesti Massif Batholith, Southern Libya. *Earth and Planetary Scientific Letters*, 30, 123–128.

Perkins, S. (2001). Dust, the Thermostat: How Tiny Airborne Particles Manipulate Climate. *Science News*, 160, 13, 200.

Pinna, P., Calvez, J.Y., Abessolo, A., Angel, J.M., Mekoulou-Mekoulou, T., Mananga, G., and Vernhet, Y. (1994). Neoproterozoic Events in Tchollire area: Pan-African crustal growth and geodynamics in central northern Cameroon (Adamawa and North Provinces). *Journal African Earth Sciences*, 18, 347–353.

Petit, R. H., Legrand, M., Jankowiak, I., et al. (2005). Transport of Saharan Dust over the Caribbean Islands: Study of an event. *Journal of Geophysical Research*, 110, D18S09.

Petters, S. W. (1991). Sequence Stratigraphy Based on Microfacies Analysis. *Geologie en Mijnbouw*, 76, 3, 197-215.

Prospero, J. M. (1999). Long-range Transport of Mineral Dust in the Global Atmosphere: Impact of African dust on the environment of the southeastern United States Proc. *National Academy of Sciences, Colloquium paper*, USA, 96, 3396–3403.

Prospero, J. M., Ginoux, P., Torres, O., Nicholson, S. E., Gill, T. E. (2002). Environmental Characterization of Global Sources of Atmospheric Soil Dust Identified with the Nimbus 7 Total Ozone Mapping Spectrometer. *Reviews of Geophysics, American Geophysical Union*, 40, 1, 1002.

Reid, J.S., Hobbs, P. V., Liousse, C., Martins, J. V., Weiss, R. E., and Eck, T. F. (1998a). Comparisons of Techniques for Measuring Shortwave Absorption and Black Carbon Content of Aerosols from Biomass Burning in Brazil. *Journal of Geophysical Research*, 103, 32,031-32,040.

Reid, J. S., Kinney, J. E., Westphal, D. L., Holben, B. N., Welton, E. J., Tsay, S., Eleuterio, J. R., et al. (2003). Analysis of Measurements of Saharan Dust by Airborne and Ground-based Remote Sensing Methods during the Puerto Rico Dust Experiment (PRIDE). *Journal of Geophysical Research*, 108, D19, 8586.

Rivera-Carpio, C.A., Corrigan, C. E., Novakov, T., Penner, J. E., Rogers, C. F., and Chow, J. C. (1996). Derivation of Contributions of Sulphate and Carbonaceous Aerosols to Cloud Condensation Nuclei from Mass Size Distributions. *Journal of Geophysical Research*, 101, 19,483-19,493.

Sassen, K., DeMott, P. J., Prospero, J. M., and Poellot, M. R. (2003). Saharan Dust Storms and Indirect Aerosol Effects on Clouds: CRYSTAL-FACE results. *Geophysical Research Letters*, 30, 12, 1633.

Satheesh, S. K. (2002). Aerosol Radiative Forcing over Tropical Indian Ocean: Modulation by Sea-surface Winds. *Current Science*, 82, 3, 10.

Saxena, P., Hildemann, L. M., McMurry, P. H., and Seinfeld, J. H. (1995). Organics Alter Hygroscopic Behavior of Atmospheric Particles. *Journal of Geophysical Research*, 100, 18,755-18,770.

Saxena, P., and Hildemann, L. M. (1996). Water Soluble Organics in Atmospheric Particles: A critical review of the literature and application of thermodynamics to identify candidate compounds. *Journal of Atmospheric Chemistry*, 24, 57-109.

Sears, J. W., St. George, G. M., & Winne, C. (2004). Continental Rift Systems and Anorogenic Magmatism. University of Montana, Missoula MT 59812, USA, *Elsevier; Science Direct*, http://www.sciencedirect.com.

Schandelmeier, H., Darbyshire, D.P.F., Harms, U., and Richter, A. (1988). The East Saharan Craton: Evidence for pre-Pan-African crust in NE Africa W of the Nile. In: The Pan-African belts of NE Africa and adjacent areas. *Friedr Viewegand Sohn*, 69–94.

Schandelmeier, H., Richter, A., and Harms, U. (1987). Proterozoic Deformation of the East Sahara Craton in Southeast Libya, South Egypt, and North Sudan. *Tectonophysics*, 140, 233–246.

Schandelmeier, H., Richer, A., Harms, U., and Abdel-Rahman, E.M. (1990). Lithology and Structure of the Late Proterozoic Jebel Rahib Fold-and-Thrust Belt (SW Sudan). *Berliner Geowissen Abher*, 12, 1, 15–30.

Schandelmeier, H., Wipfler, E., Küster, D., Sultan, M., Becker, R., Stern, R.J., and Abdelsalam, M.G. (1994). Atmur-Delgo Suture: A Neoproterozoic oceanic basin extending into the interior of northeast Africa. *Geology*, 22, 563–566.

Schwartz, S. E. and Warneck, P. (1995). Units for Use in Atmospheric Chemistry. *Pure & Applied Chemistry*, 67, 1377-1406.

Seinfeld, J.H., Carmichael, G.R., Arimoto, R., Conant, W.C., Brechtel, F.J., Bates, T.S., Cahill, T.A., Clarke, A.D., et al. (2004). ACE-Asia: Regional Climatic and Atmospheric Chemical Effects of Asian Dust and Pollution. *Bulletin of the American Meteorological Society*, 85, 367-380.

Shantz, N., R. Leaitch, S.-M. Li, W. Hoppel, G. Frick, P. Caffrey, D. Hegg, S., et al. (1999). Controlled Studies and Field Measurements of Organic Cloud Condensation Nuclei. Paper Number A22B-11, *American Geophysical Union* Fall Meeting, San Francisco.

Schwartz, S. E. (1996). The Whitehouse Effect: Shortwave radiative forcing of climate by anthropogenic aerosols: An overview. *Journal of Aerosol Science,* 27, 359-383.

Sherwood, S. (2002). A Microphysical Connection among Biomass Burning, Cumulus Clouds, and Stratospheric Moisture. *Science,* 295, 1272-1275.

Shulman, M.L., Jacobson, M. C., Charlson, R. J., Synovec, R. E., and Young, T. E. (1996). Dissolution Behaviour and Surface Tension Effects of Organic Compounds in Nucleating Droplets. *Geophysical Research Letters*, 23, 277-280.

Sokolik, I.N., and Toon, O. B. (1996). Direct Radiative Forcing by Anthropogenic Airborne Mineral Aerosols. *Nature*, 381, 681-683.

Sposito, G. (1973). Volume Changes in Swelling Soils. *Soil Science, 115, 315-320.*

Stern, R.J. (1994). Arc Assembly and Continental Collision in the Neoproterozoic East African Orogeny: Implication for the consolidation of Gondwanaland. *Annual Reviews of Earth Planetary Sciences*, 22, 319–351.

Stern, R.J., and Dawoud, A.S. (1991). Late Precambrian (740 Ma) Charnockite, Enderbite, and Granite from Jebel Moya, Sudan: A link between the Mozambique Belt and the Arabian-Nubian Shield? *Journal Geology*, 99, 648–659.

Stern, R.J., Kröner, A., Reischmann, T., Bender, R., and Dawoud, A.S. (1994). Precambrian Basement Around Wadi Halfa: A new perspective on the evolution of the Central Saharan Ghost craton. *Geologische Rundschau*, 83, 564–577.

Swap, R., Ulanski, S., Cobbett, M., Garstag, M. (1996). Temporal and Spacial Characteristics of Saharan Dust. *Journal of Geophysical Research,* 101, 4205-4220.

Takemi, T., et al. (2006). Role of Boundary Layer and Cumulus Convection on Dust Emission and Transport over a Midlatitude Desert Area. *Journal of Geophysical Research*, 111, D11203.

Tegen, I., and Fung, I. (1994). Modeling of Mineral Dust in the Atmosphere: Sources, Transport, and Optical Thickness. *Journal of Geophysical Research, 99*, 22,897–22,914.

Tegen, I., and Fung, I. (1995). Contribution to the Atmospheric Mineral Aerosol Load from Land Surface Modification. *Journal of Geophysical Research*, 100, n. D9, 18,707-18,726.

Tegen, I., and Lacis, A. A. (1996). Modelling of Particle Size Distribution and its Influence on the Radiative Properties of Mineral Dust Aerosol. *Journal of Geophysical Research*, 101, 19,237-19,244.

Tegen, I., Hollrig, P., Chin, M., Fung, I., Jacob, D., and Penner, J. E. (1997). Contribution of Different Aerosol Species to the Global Aerosol Extinction Optical Thickness: Estimates from model results. *Journal of Geophysical Research*, 102, 23,895-23,915.

Tegen, I., Harrison, S., Kohfeld, K., Prentice, I., Coe, M., and Heimann, M. (2002). Impact of Vegetation and Preferential Source Areas on Global Dust Aerosol: Results from a model study. *Journal of Geophysical Research*, 107, 4576.

Tegen, I., Heinol, B., Todd, M., Helmert, J., Washington, R., and Dubovik, O. (2006). Modeling Soil Dust Aerosol in the Bodélé Depression during the BoDEx Campaign. *Copernicus GmbH on behalf of the European Geosciences Union*.

Todd, M. C., Washington, R., Martins, J. V., Dubovik, O., Lizcano, G., M'Bainaye, S., and Engelstaedter, S. (2005). Mineral Dust Emission from the Bodélé Depression, Northern Chad, During BodEx 2005. *Submitted to the Geophysical Union, publishing in process, 2006.*

Toteu, S.F., Michard, A., Bertrand, J.M., and Rocci, G. (1987). U/Pb Dating of Precambrian Rocks from the Northern Cameroon, Orogenic Evolution, and Chronology of the Pan-African Belt of Central Africa. *Precambrian Research*, 37, 71–87.

Vail, J.R. (1976). Outline of the Geochronology and Tectonic Units of the Basement Complex of Northeast Africa. *Proceedings Royal Society, London*, A 350, 127–141.

Vail, J.R. (1983). Pan-African crustal accretion in NE Africa. *Journal African Earth Sciences*, 1, 285–294.

Vail, J.R. (1985). Pan-African (Late Precambrian) Tectonic Terranes and Reconstruction of the Arabian-Nubian Shield. *Geology*, 13, 839–842.

Van Dingenen, R.V., Raes, F., and Jensen, N. R. (1995). Evidence for Anthropogenic Impact on Number Concentration and Sulphate Content of Cloud-processed Aerosol Particles over the North Atlantic. *Journal of Geophysical Research*, 100, 21,057-21,067.

Vignaud, P., Duringer, P., Mackaye, H. T., Likius, A., Blondel, C., et al. (2002). Geology and Palaeontology of the Upper Miocene Toros-Menalla Hominid Locality, Chad. *Nature*, 418, 152-155.

Virkkula, A., Dingenen, R. V., Raes, F., and Hjorth, J. (1999). Hygroscopic Properties of Aerosol Formed by Oxidation of Limonene, A-pinene, and B-pinene. *Journal of Geophysical Research*, 104, 3569-3579.

Washington, R., and Todd, M. C. (2005). Atmospheric Controls on Mineral Dust Emission from the Bodélé Depression, Chad: The role of the low level jet. *Geophysical Research Letters*, 32, L17701.

Washington, R., Todd, M. C., Engelstaedter, S., Mbainayel, S., and Mitchell, F. (2006). Dust and the Low-level Circulation over the Bodélé Depression, Chad: Observations from BoDEx 2005. *Journal of Geophysical Research*, 111, D03201.

Washington, R., Todd, M. C., Lizcano, G., Tegen, I., Flamant, C., Koren, I., Ginoux, P., et al. (2006). Links between Topography, Wind, Deflation, Lakes, and Dust: The case of the Bodélé Depression, Chad. *Geophysical Research Letters*, 33, L09401.

Wolf, M.E. and Hidy, G. M. (1997). Aerosols and Climate: Anthropogenic emissions and trends for 50 years. *Journal of Geophysical Research*, 102, 11113-11121.

Yu, S., (2000). Role of Organic Acids (formic, acetic, pyruvic and oxalic) in the Formation of Cloud Condensation Nuclei (CCN): A review. *Atmospheric Research*, 53, 185-217.

Yu, R. E., Kaufman, Y. J., Holben, B. N., Geogdzhayev, I. V., and Mishchenko, M. I. (2003). Annual Cycle of Global Distributions of Aerosol Optical Depth from Integration of MODIS Retrievals and GOCART Model Simulations. *Journal of Geophysical Research*, 108, D3, 4128.

Zappoli, S., Andracchio, A., Fuzzi, S., et al. (1999). Inorganic, Organic and Macromolecular Components of Fine Aerosol in Different Areas of Europe in Relation to their Water Solubility, *Atmospheric Environment*, 33(17), 2733–2743.

Zender, C., Newman, D., and Torres, O. (2003b). Spatial Heterogeneity in Aeolian Erodibility: Uniform, Topographic, Geomorphologic, and Hydrologic Hypotheses. *Journal of Geophysical Research*, 108, 4543.

Zender, C., and Newman, D. (2002). Simulated Global Atmospheric Dust Distribution: Sensitivity to Regional Topography, Geomorphology, and Hydrology. *University of California*, Irvine.

Zender, C. S., Bian, H., and Newman, D. (2003a). The Mineral Dust Entrainment and Deposition (DEAD) Model: Description and global dust distribution. *Journal of Geophysical Research*, 108, 4416.

Zender, C. (2006). Particle Size Distributions: Theory and Application to Aerosols, Clouds, and Soils. *University of California* at Irvine Department of Earth System Science, University of California Irvine, CA.

Zhang, Y., Kreidenweis, S. M., and Feingold, G. (1999). Stratocumulus Processing of Gases and Cloud Condensation Nuclei: Part II: Chemistry sensitivity analysis. *Journal of Geophysical Research*, 104, 16,061-16,080.

Books

Andreae, M. O. (1995). *Climatic effects of changing atmospheric aerosol levels.* World Survey of Climatology (editor, A. Henderson-Seller), pp. 341-392. (Also in Future Climates of the World 16, Elsevier**).**

Bagnold, R. (1954 ed; 1941 ed). *Physics of Wind Blown Sand and Desert Dunes.* Methuen, University of Michigan, 265 pp.

Bates, R.L., Jackson J.A. (1980). *Glossary of Geology*. American Geological Institute, Falls Church, VA, 751 pp.

Carinouze, J.P. (1983). *Hydrochemical Regulation of the Lake: In Lake Chad; ecology and productivity of a shallow tropical system*. Junk Publishers, Boston, 95-123.

Cooke, R. U., Warren, A., and Goudie, A. S. (1993). *Desert Geomorphology*. University College of London Press, 526 pp.

Duce, R. A. (1995). *In Aerosol Forcing of Climate*. Editors, Charlson, R. J. & Heintzenberg, J., John Wiley, New York, pp. 43-72.

Hammad, F.A., and Abdou, H.F. (1982). *Hydrogeology: In Lake Chad Hydrology* Literature Survey, Adeniyi, F. A., Ed., University of Maiduguri Press, Maiduguri, Nigeria.

Lancaster, N., (1995). *Geomorphology of Desert Dunes*. Routledge Press, New York, 290 pp.

Penner, J.E., C.A. Atherton, and T.E. Graedel, (1994b). Global Emissions and Models of Photochemically Active Compounds. In Global Atmospheric-Biospheric Chemistry, ed. R. Prinn, Plenum Publishing, New York, pp. 223-248.

Prospero, J. M. (1996). *The Atmospheric Transport of Particles to the Ocean, in Particle flux in the Ocean*. John Wiley & Sons Ltd., New York, pp. 19-52.

Prospero J. M. (1996). *Saharan Dust Transport over the North Atlantic Ocean and Mediterranean: An overview*. In: The Impact of Desert Dust across the Mediterranean. In: Guerzoni and Chester (Eds.), pp. 133-151.

Talbot, M. R., (1983*). Late Pleistocene Rainfall and Dune Building in the Sahel.* Paleoecology of Africa, 16, Rotterdam; Balkema, pp. 203-213.

Tarbuck, E. J., and Lutgens, K. (1993). *Earth Science,* seventh edition. Macmillan College Publishing Company, New York, 755 pp.

Reports and Fact Sheets

Kaufman, Y. J. (2005). Aerosols: More Than Meets the Eye, (2005). National Aeronautics and Space Administration. FS-2005-9-072-GSFC.

Jones, P.R., Charlson, R. J., and Rodhe, H. (1994a). *Aerosols.* Aerosols. In: Climate Change 1994: Radiative Forcing of Climate Change and an evaluation of the IPCC IS92a Emission Scenarios. A special Report of IPCC Working Groups I and III. Editors, Houghton J.T., L.G. Meira Filho, J. Bruce, Hoesung Lee, B.A. Callander, E. Haites, N. Harris, and K. Maskell, *Cambridge University Press*, Cambridge, UK, 131-162.

Duzgoren-Aydin, N. S. (2003). *Comparative Study of Weathering Signatures in Felsic Igneous Rocks of Hong Kong.* Department of Earth Sciences, The University of Hong Kong, Pokfulam Road, Hong Kong, Chemical Speciation and Bioavailability.

Bergametti, G. & Dulac, F. (1998). *International Global Atmospheric Chemistry.* (IGAC) IGAC Activities News Letter 11, 13-17.

Penner, J.E., Chuang, C. C., and Grant, K. (1999a and 1999b). *Climate Change and Radiative Forcing by Anthropogenic Aerosols: A review of research during the last five years*. Paper presented at the La Jolla International School of Science, The Institute for Advanced Physics Studies, La Jolla, CA.

Intergovernmental Panel on Climate Change (1996). *Second Assessment on Climate Change*. IPCC (Intergovernmental Panel on Climate Change), Cambridge University Press, New York, and http://www.ipcc.ch/pub/sa(E).PDF

Intergovernmental Panel on Climate Change (2001). *Radiative forcing of climate change, in: Climate Change 2001,* (2001). IPCC (Intergovernmental Panel on Climate Change), Cambridge Univ. Press, New York, Cambridge University Press.

Mounkaila, M., Herrmann, L., Gaiser, T., and Maurer, T. (2003). *Spectral and Mineralogical Properties of Potential Dust Sources on a Transect from Sahara to Sahel in Chad*. Paper presented at 2nd Workshop on Mineral Dust, Paris. Laboratory Interuniversity des System Atmosphere, Paris.

Websites

Aeolian Science (1997). United States Geological Survey at http://pubs.usgs.gov/gip/deserts/eolian/

Bob Henson, UCAR communications at http://www.ucar.edu/communications/quarterly/spring98/EXPRESSO.html

Geomorphology (1997). United States Geological Survey at http://pubs.usgs.gov/info/loess/

NASA at http://eosdata.gsfc.nasa.gov/geomorphology/

Physical Geography at http://www.physicalgeography.net/fundamentals/10ah.html

Pidwirny, M., (2006). *Fundamentals of Physical Geography*. Online book at http://www.physicalgeography.net/fundamentals/contents.html

U.S. Engineering Department, Civil
http://www.civil.usyd.edu.au/courses/civl2410/classification.doc

University of Texas Library website at http://www.lib.utexas.edu/maps/africa/chad_rel91.jpg

Watersheds of the World at http://www.iucn.org/themes/wani/eatlas/html/af1.html

APPENDIXES

APPENDIX A

MAPS OF AFRICA, CHAD, AND BODELE

Map of Africa with Country Labels

Map of Chad with Bodele Label

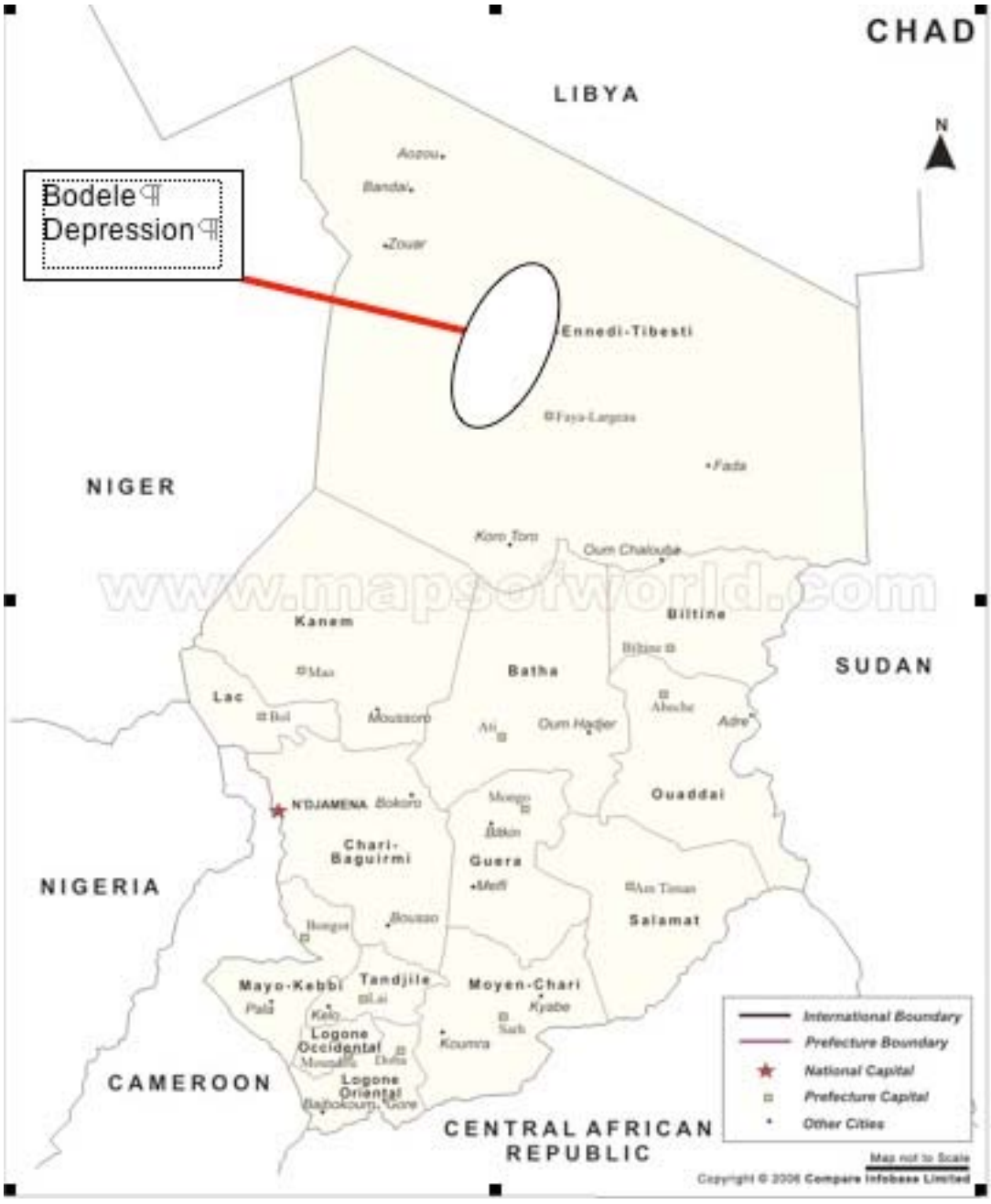

APPENDIX B

SATELLITE IMAGES OF THE BODELE

Bodele Depression Satellite Images Illustrating the Emissions: Note the year and day located in the upper left labeled MYD 21KM. A2005002. This notation means the year 2005 on the second day; hence, A2005002 is January 2, 2005.

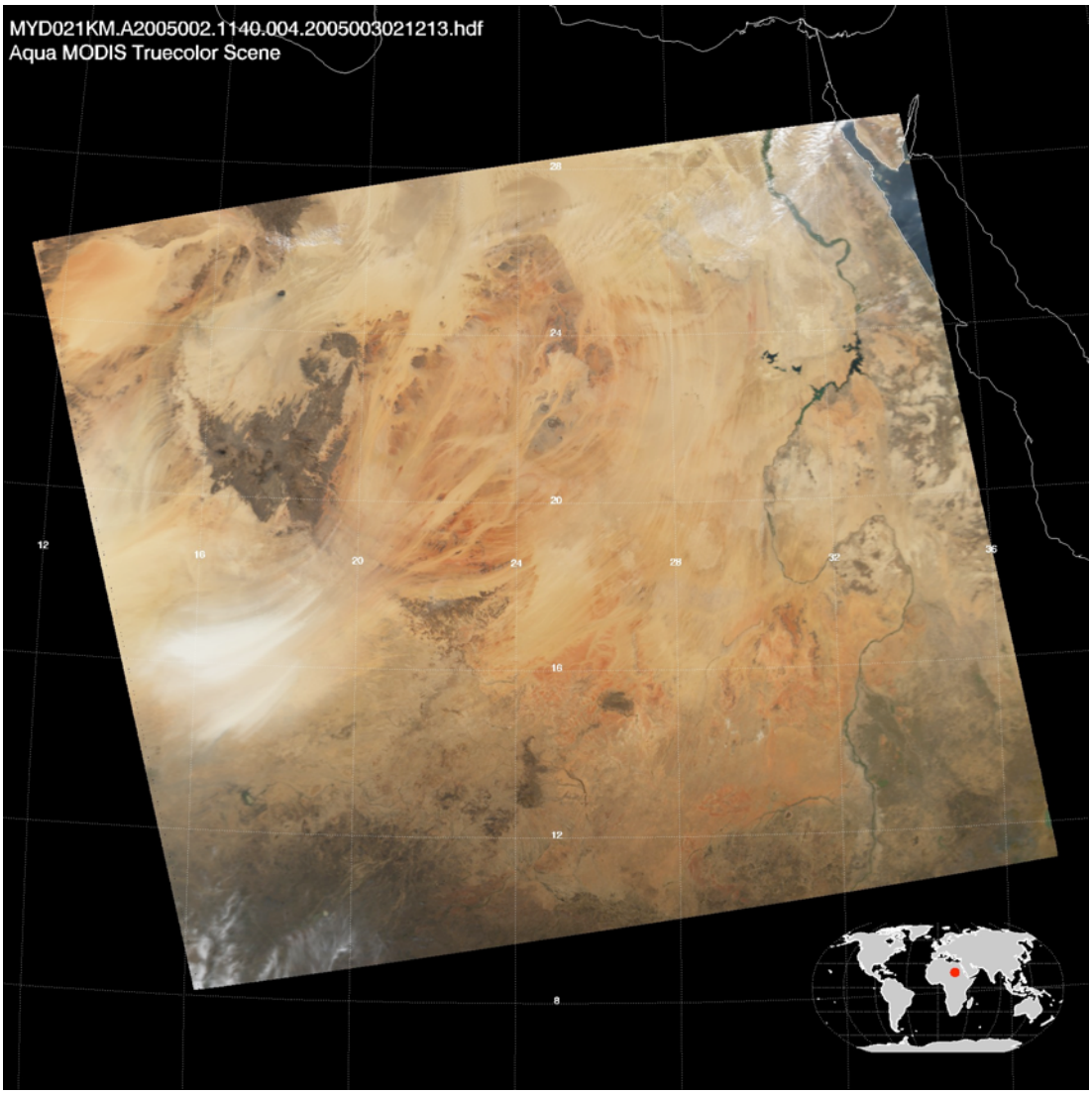

Note the white appearing swaths in the central left side of the satellite image. This is a typical dust emission from the Bodele in the winter months of the Northern Hemisphere. The Hamarttan winds cause increased activity in the Bodele during these months.

Note the date here is A2005021. This translates to January 21, 2005.

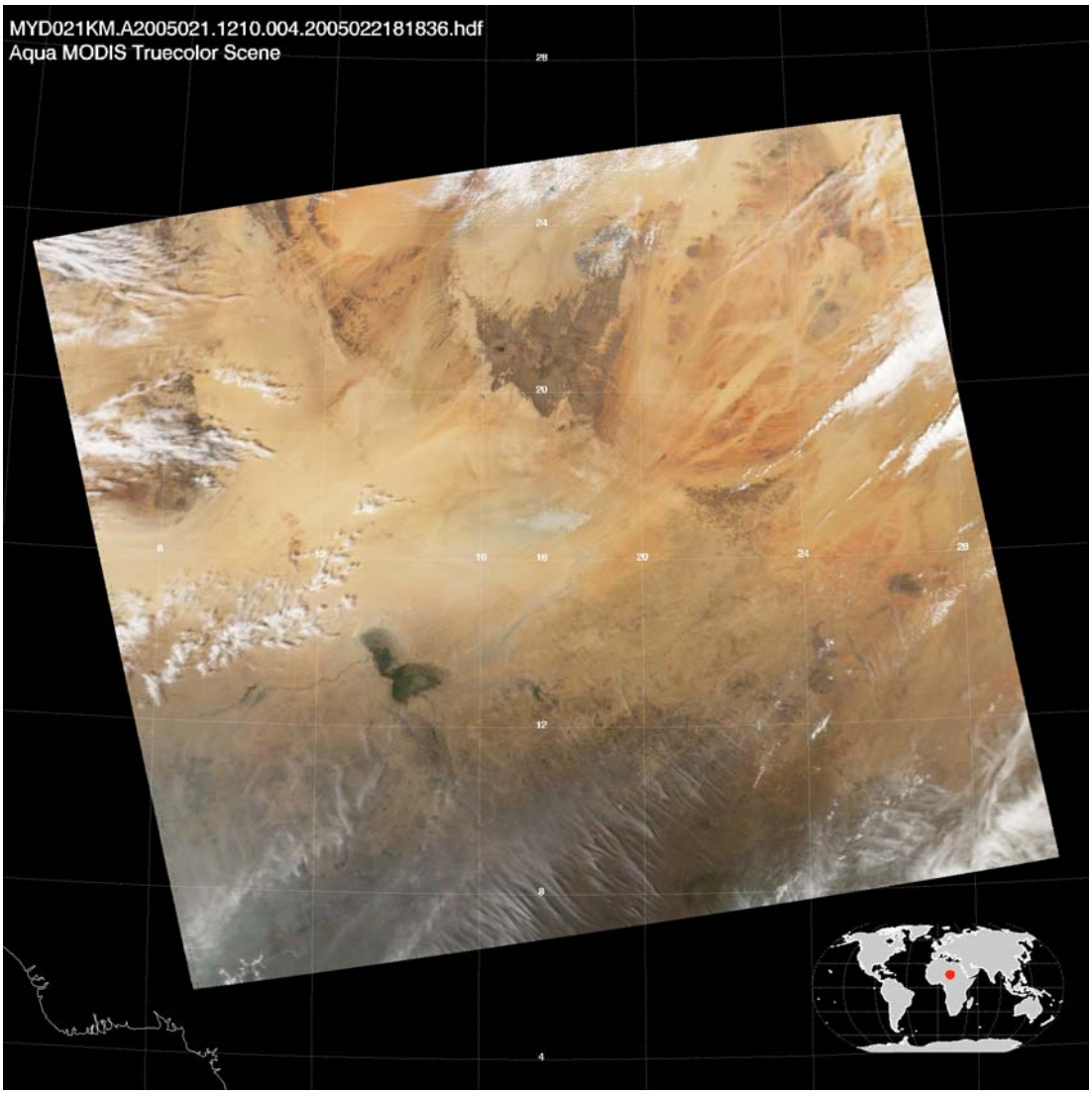

Note that this is an unusually quiet day for the Bodele in the winter months that normally see large dust emissions on most days because of the very hot, very dry Hamarttan Winds passing through the gap between the Tibesti and Ennedi Mountains.

Note the date is the 212th day of 2006. This translates to June 30, 2006.

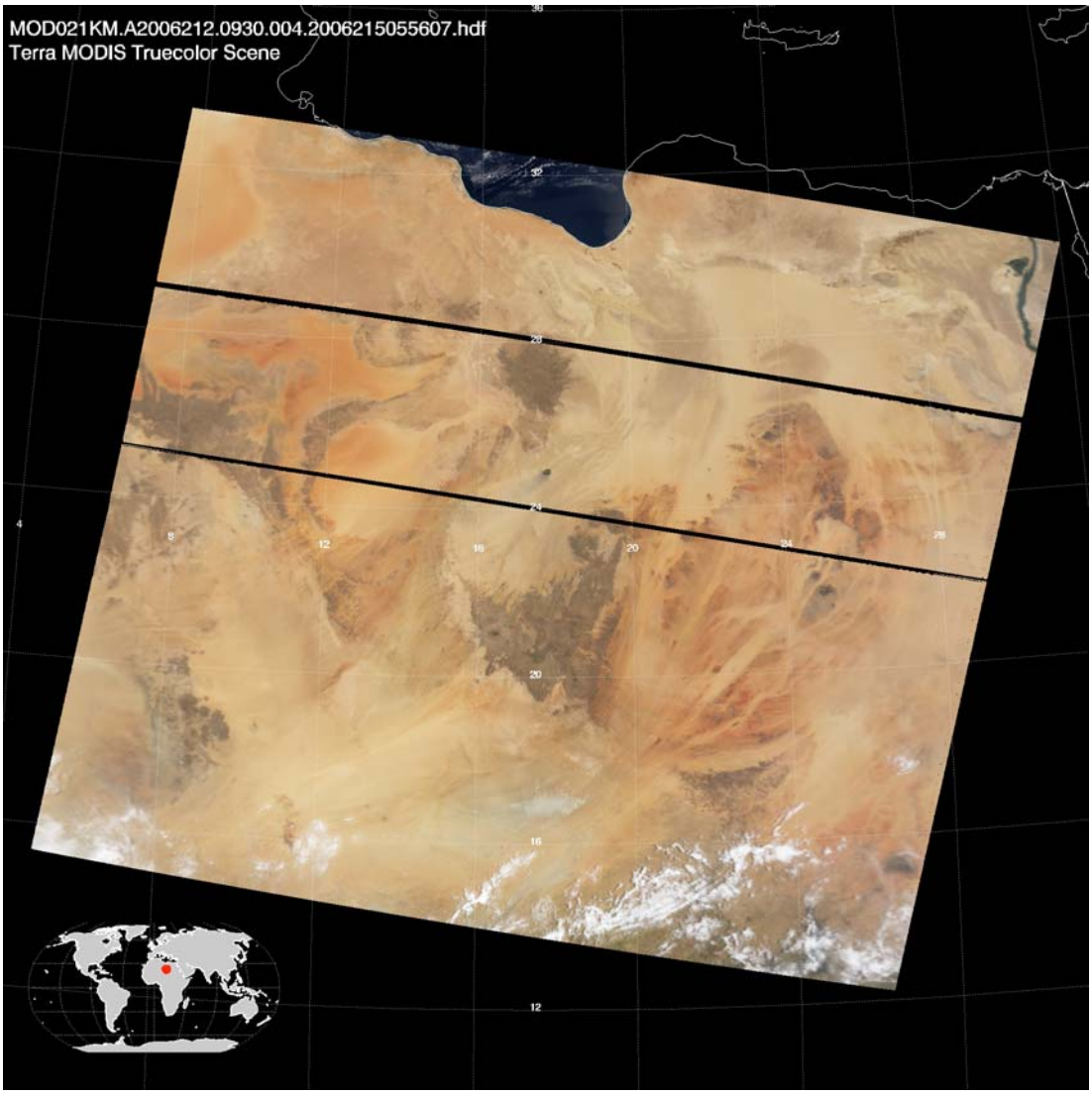

Note the inactivity of the Bodele on this day. Activity in the summer months produce more emissions, but the numbers of days of emission are about as numerous as the winter months, ~40%.

APPENDIX C

SEM DATA FOR BULK SAMPLES

Spectrum processing : 1A
Peak possibly omitted : 2.142 keV

Processing option : All elements analyzed (Normalised)
Number of iterations = 4

Standard :
C CaCO3 1-Jun-1999 12:00 AM
O SiO2 1-Jun-1999 12:00 AM
Al Al2O3 1-Jun-1999 12:00 AM
Si SiO2 1-Jun-1999 12:00 AM
Fe Fe 1-Jun-1999 12:00 AM

Element	Weight%	Atomic %
C K	39.04	50.71
O K	39.22	38.24
Al K	0.77	0.45
Si K	17.15	9.53
Fe L	3.82	1.07
Totals	100.00	

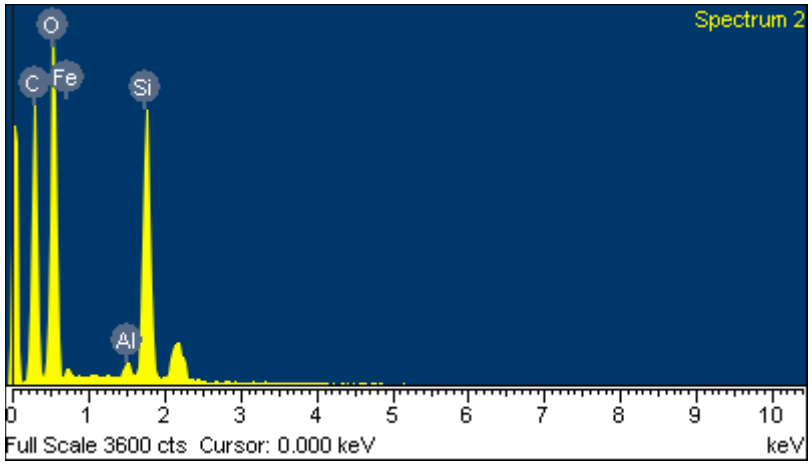

Comment: Sample 1A1: Silica and possible iron oxide.

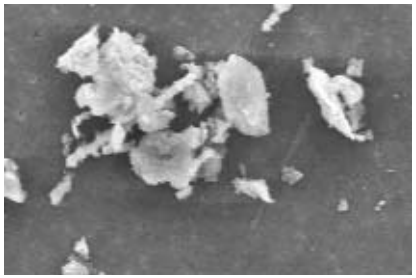

Spectrum processing :
Peak possibly omitted : 2.142 keV

Processing option : All elements analyzed (Normalised)
Number of iterations = 4

Standard :
C CaCO3 1-Jun-1999 12:00 AM
O SiO2 1-Jun-1999 12:00 AM
Al Al2O3 1-Jun-1999 12:00 AM
Si SiO2 1-Jun-1999 12:00 AM
Fe Fe 1-Jun-1999 12:00 AM

Element	Weight%	Atomic%
C K	39.04	50.71
O K	39.22	38.24
Al K	0.77	0.45
Si K	17.15	9.53
Fe L	3.82	1.07
Totals	100.00	

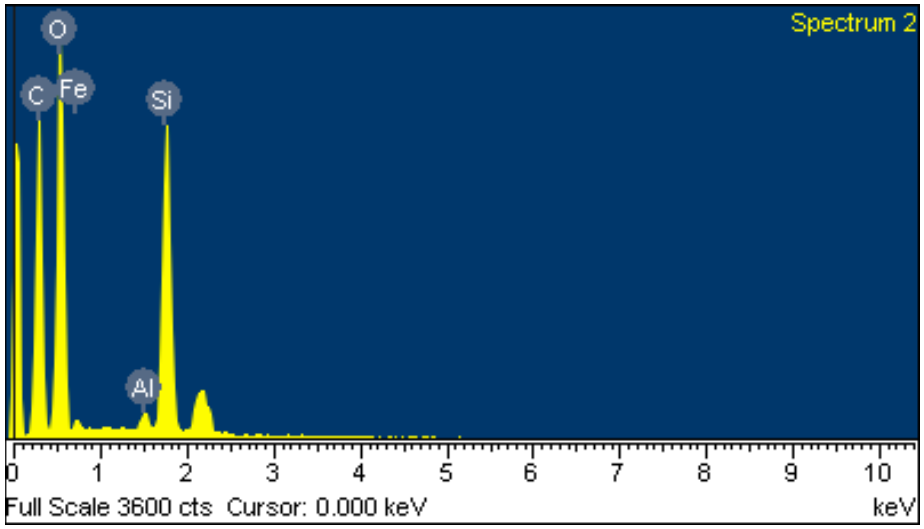

Comment: Sample 1A2 is predominately silica, SiO2, with trace iron particles. The diatom remains can be clearly seen. The carbon signature is from the filter housing the sample.

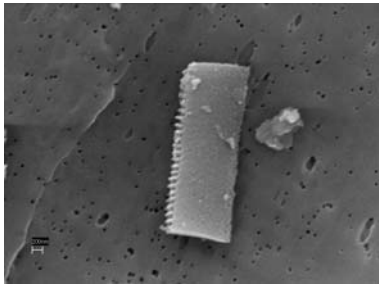

Bodele

22/06/2006 15:04:14

Spectrum processing :
No peaks omitted

Processing option : All elements analyzed (Normalised)
Number of iterations = 4

Standard :
C CaCO3 1-Jun-1999 12:00 AM
O SiO2 1-Jun-1999 12:00 AM
Al Al2O3 1-Jun-1999 12:00 AM
Si SiO2 1-Jun-1999 12:00 AM
Fe Fe 1-Jun-1999 12:00 AM
Au Au 1-Jun-1999 12:00 AM

Element	Weight%	Atomic%
C K	31.49	45.19
O K	38.46	41.42
Al K	0.94	0.60
Si K	18.42	11.30
Fe L	2.49	0.77
Au M	8.20	0.72
Totals	100.00	

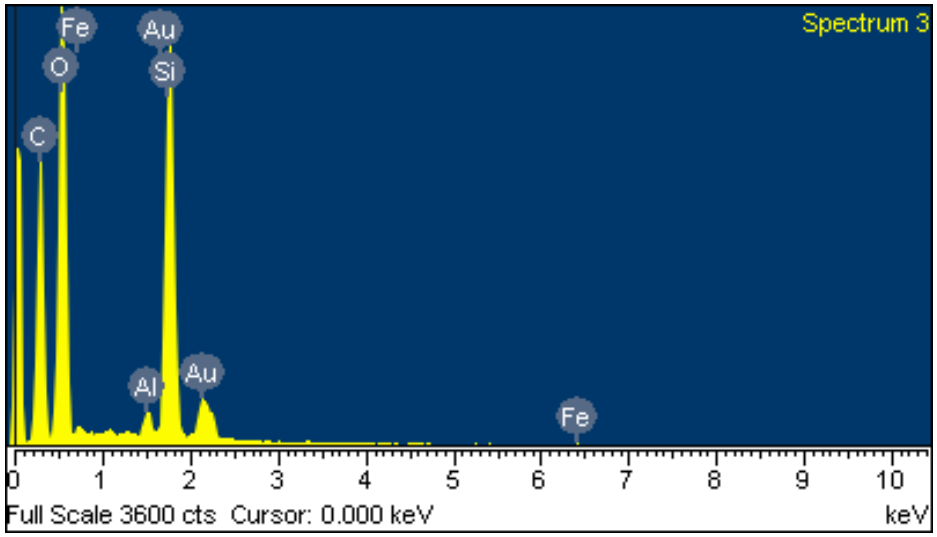

Comment: Sample 1A3: primarily silica, SiO2, with iron particles. The Gold is due to the spray for the SEM used for the SEM housing head, and most of the carbon is due to the filter.

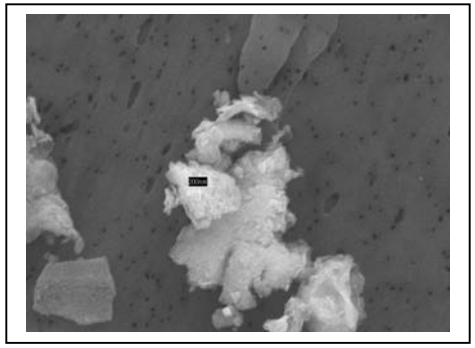

Bodele

22/06/2006 15:04:41

Spectrum processing :
Peaks possibly omitted : 0.720, 6.420 keV

Processing option : All elements analyzed (Normalised)
Number of iterations = 3

Standard :
C CaCO3 1-Jun-1999 12:00 AM
O SiO2 1-Jun-1999 12:00 AM
Al Al2O3 1-Jun-1999 12:00 AM
Si SiO2 1-Jun-1999 12:00 AM
Au Au 1-Jun-1999 12:00 AM

Element	Weight%	Atomic%
C K	53.93	66.20
O K	30.10	27.74
Al K	0.67	0.37
Si K	10.12	5.31
Au M	5.19	0.39
Totals	100.00	

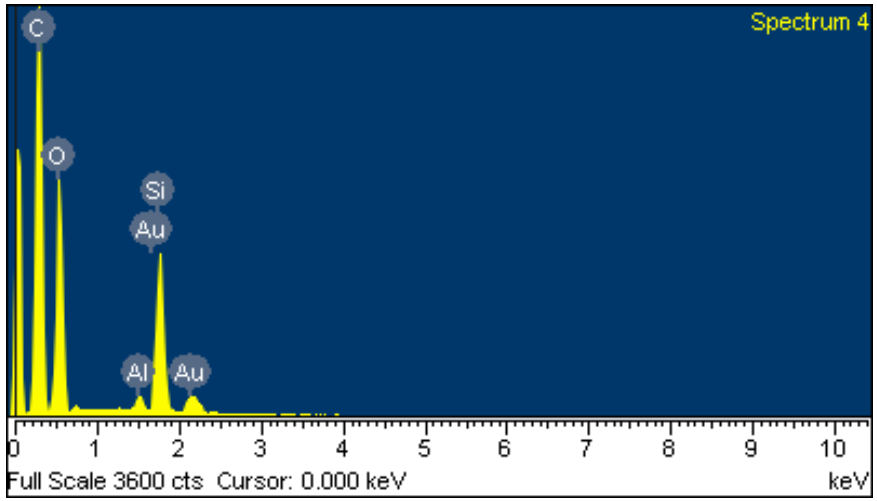

Comment: Sample 1A4: predominately SiO2 with residual Al. The gold is due to the setting spray for the SEM, and the carbon is due to the sample filter.

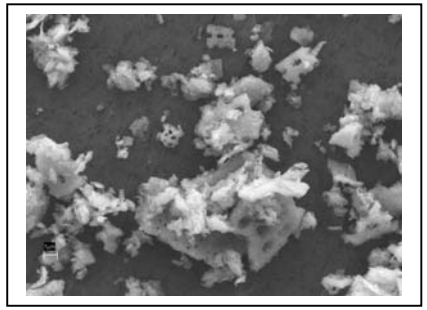

Bodele

22/06/2006 15:05:01

Spectrum processing :
No peaks omitted

Processing option : All elements analyzed (Normalised)
Number of iterations = 3

Standard :
C CaCO3 1-Jun-1999 12:00 AM
O SiO2 1-Jun-1999 12:00 AM
Si SiO2 1-Jun-1999 12:00 AM
Au Au 1-Jun-1999 12:00 AM

Element	Weight%	Atomic%
C K	9.96	16.22
O K	48.58	59.41
Si K	33.89	23.61
Au M	7.57	0.75
Totals	100.00	

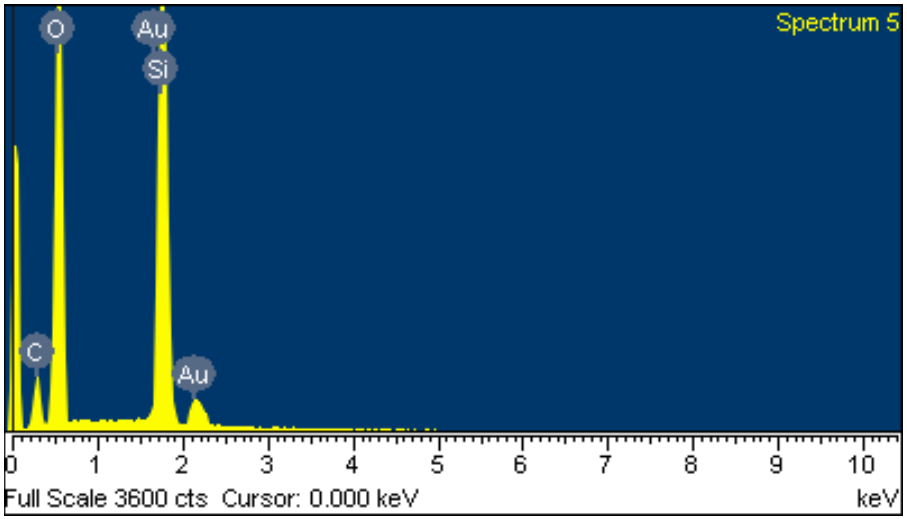

Comment: Sample 1B: predominately SiO2. The gold is due to the setting spray for the SEM, and the carbon is due to the sample filter.

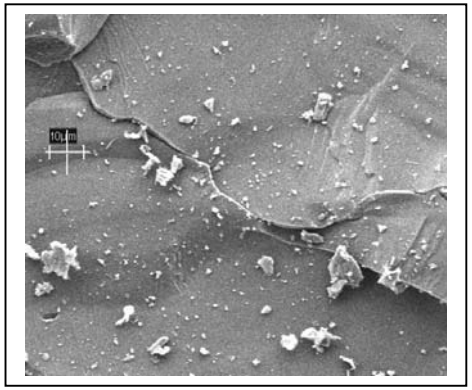

Bodele

22/06/2006 15:05:14

Spectrum processing :
Peak possibly omitted : 3.330 keV

Processing option : All elements analyzed (Normalised)
Number of iterations = 3

Standard :
C CaCO3 1-Jun-1999 12:00 AM
O SiO2 1-Jun-1999 12:00 AM
Na Albite 1-Jun-1999 12:00 AM
Al Al2O3 1-Jun-1999 12:00 AM
Si SiO2 1-Jun-1999 12:00 AM
Fe Fe 1-Jun-1999 12:00 AM
Au Au 1-Jun-1999 12:00 AM

Element	Weight%	Atomic%
C K	6.59	11.66
O K	45.81	60.88
Na K	0.55	0.51
Al K	1.35	1.06
Si K	30.84	23.35
Fe L	3.42	1.30
Au M	11.45	1.24
Totals	100.00	

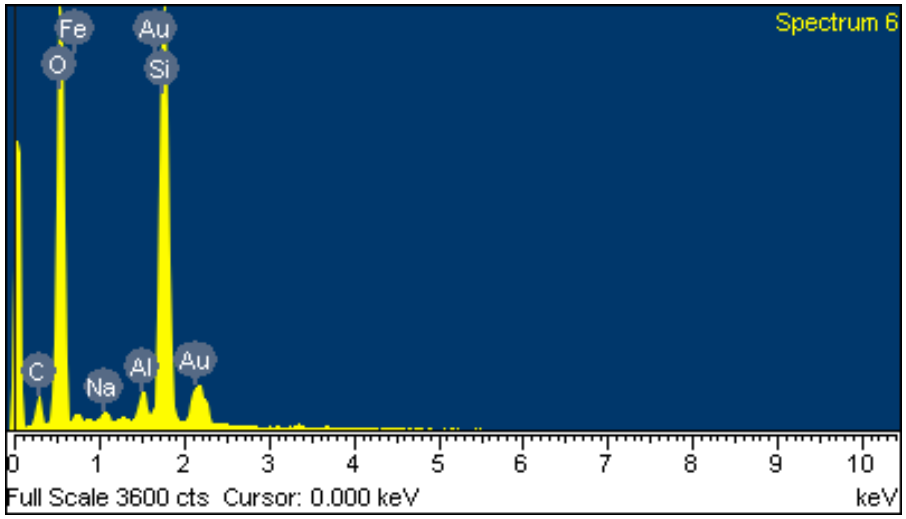

Comment: Sample 1C1: Clay minerals and silica (SiO2), possible hematite. The gold is due to the setting spray for the SEM, and the carbon is due to the sample filter.

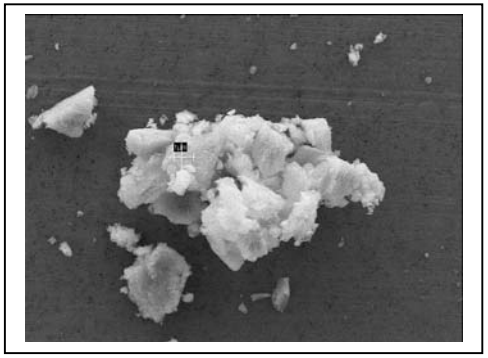

Bodele

22/06/2006 15:05:43

Spectrum processing :
No peaks omitted

Processing option : All elements analyzed (Normalised)
Number of iterations = 3

Standard :
C CaCO3 1-Jun-1999 12:00 AM
O SiO2 1-Jun-1999 12:00 AM
Na Albite 1-Jun-1999 12:00 AM
Al Al2O3 1-Jun-1999 12:00 AM
Si SiO2 1-Jun-1999 12:00 AM
P GaP 1-Jun-1999 12:00 AM
Ca Wollastonite 1-Jun-1999 12:00 AM
Fe Fe 1-Jun-1999 12:00 AM

Element	Weight%	Atomic%
C K	5.14	9.62
O K	42.52	59.73
Na K	1.20	1.17
Al K	0.88	0.73
Si K	3.68	2.94
P K	9.85	7.15
Ca K	24.45	13.71
Fe L	12.30	4.95
Totals	100.00	

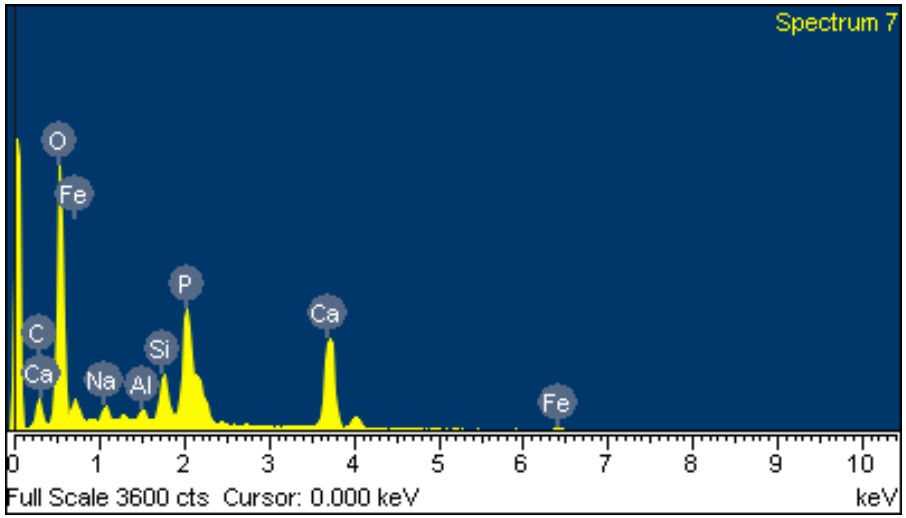

Comment: Sample 1C2: aluminum silicate clay minerals (probably feldspars), calcium carbonate, significant indications for hematite or illite with trace carbon from the sample filter.

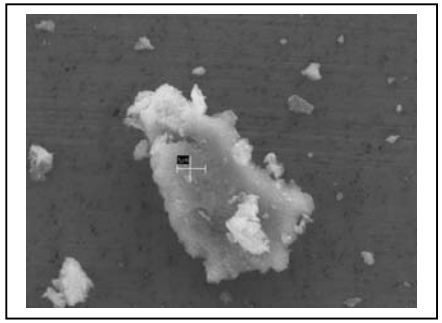

Bodele

22/06/2006 15:05:55

Spectrum processing :
Peak possibly omitted : 2.141 keV

Processing option : All elements analyzed (Normalised)
Number of iterations = 3
Standard :
C CaCO3 1-Jun-1999 12:00 AM
O SiO2 1-Jun-1999 12:00 AM
Na Albite 1-Jun-1999 12:00 AM
Mg MgO 1-Jun-1999 12:00 AM
Al Al2O3 1-Jun-1999 12:00 AM
Si SiO2 1-Jun-1999 12:00 AM
K MAD-10 Feldspar 1-Jun-1999 12:00 AM
Ca Wollastonite 1-Jun-1999 12:00 AM
Fe Fe 1-Jun-1999 12:00 AM

Element	Weight%	Atomic%
C K	6.23	10.20
O K	49.64	61.00
Na K	0.55	0.47
Mg K	0.47	0.38
Al K	4.41	3.22
Si K	31.21	21.85
K K	0.91	0.46
Ca K	0.87	0.43
Fe L	5.71	2.01
Totals	100.00	

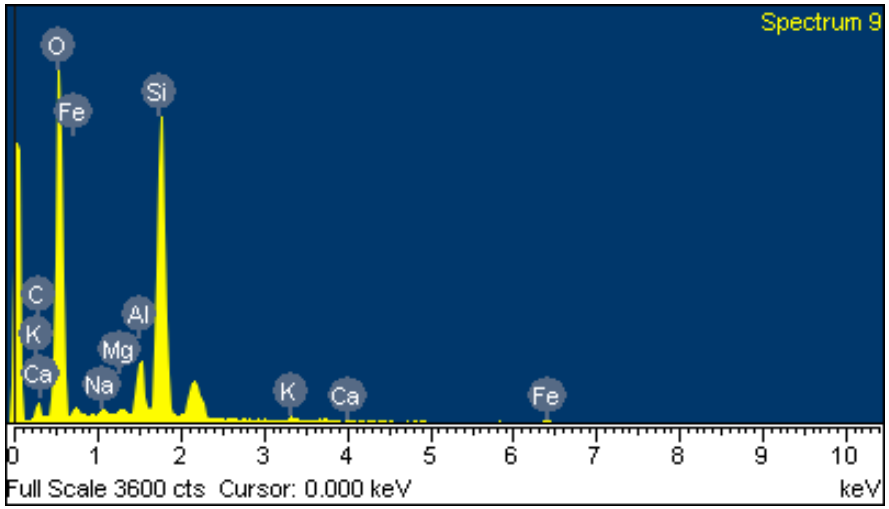

Comment: Sample 1D1 Bodele Random analysis: Ferromagnesium silicate material, portions of silica, and possible iron oxide.

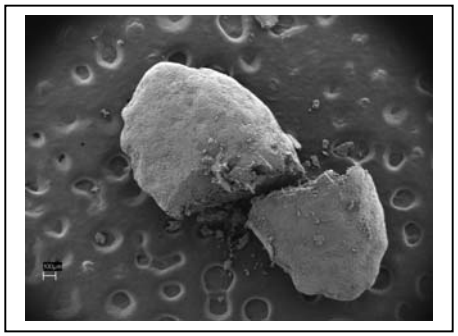

Spectrum processing :
Peaks possibly omitted : 2.149, 2.420 keV

Processing option : All elements analyzed (Normalised)
Number of iterations = 3

Standard :
O SiO2 1-Jun-1999 12:00 AM
Na Albite 1-Jun-1999 12:00 AM
Al Al2O3 1-Jun-1999 12:00 AM
Si SiO2 1-Jun-1999 12:00 AM
K MAD-10 Feldspar 1-Jun-1999 12:00 AM

Element	Weight%	Atomic%
O K	52.36	65.99
Na K	3.16	2.77
Al K	6.99	5.22
Si K	33.09	23.75
K K	4.41	2.27
Totals	100.00	

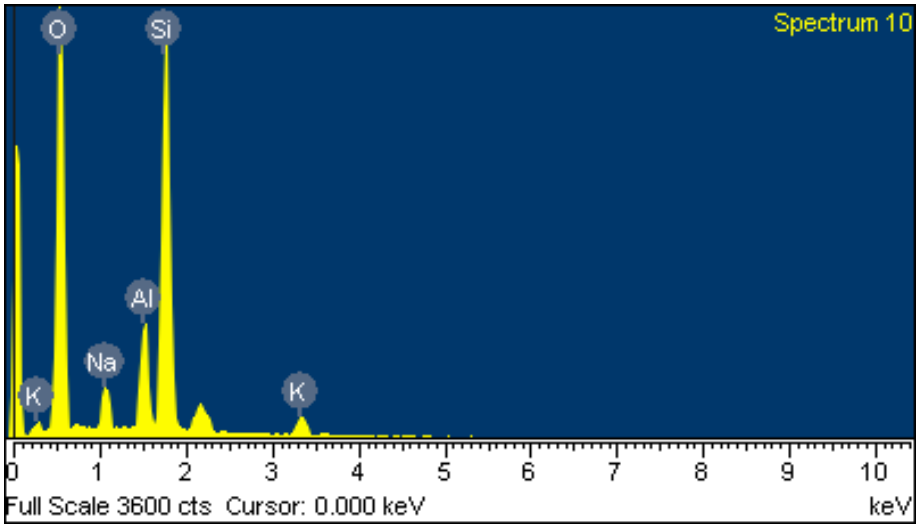

Comment: Dark particle Sample 2A3; dark material prior to powder; Aluminum silicate clay minerals, and silica.

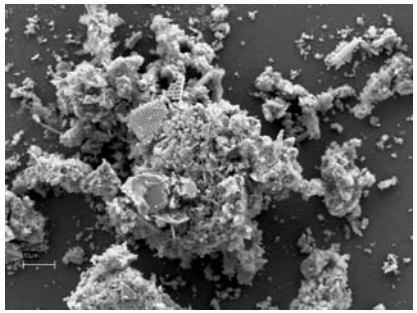

Spectrum processing :
No peaks omitted

Processing option : All elements analyzed (Normalised)
Number of iterations = 4

Standard :
C CaCO3 1-Jun-1999 12:00 AM
O SiO2 1-Jun-1999 12:00 AM
Al Al2O3 1-Jun-1999 12:00 AM
Si SiO2 1-Jun-1999 12:00 AM
Ca Wollastonite 1-Jun-1999 12:00 AM
Au Au 1-Jun-1999 12:00 AM

Element	Weight%	Atomic%
C K	40.73	53.18
O K	37.90	37.15
Al K	0.32	0.18
Si K	15.65	8.74
Ca K	1.01	0.39
Au M	4.40	0.35
Totals	100.00	

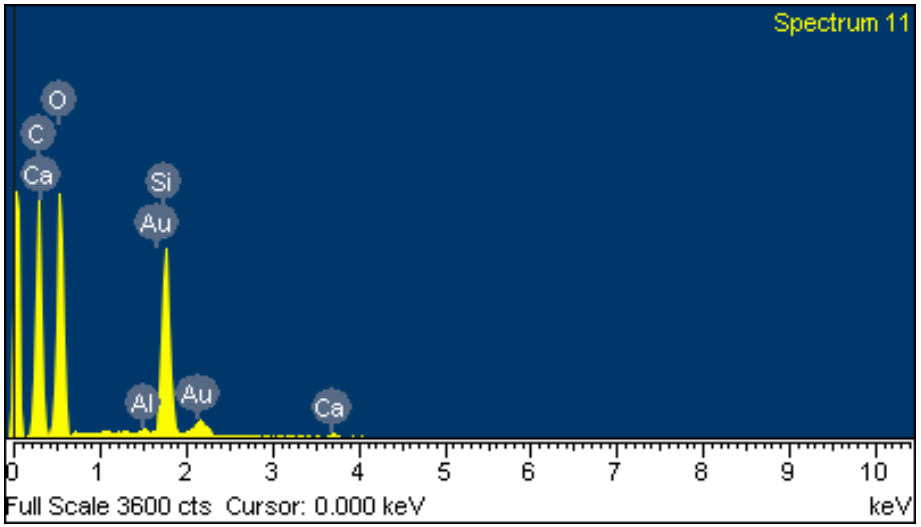

Comment: Sample 2A3; a section of diatom with possible carbonate and/or silicate mineral contamination. The gold signature is due to the spray adhesive used for SEM mounts.

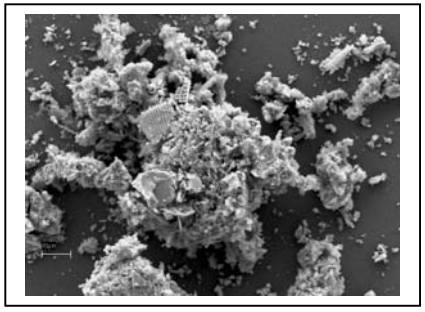

Bodele

22/06/2006 15:06:59

Spectrum processing :
Peaks possibly omitted : 2.146, 3.340 keV

Processing option : All elements analyzed (Normalised)
Number of iterations = 4

Standard :
C CaCO3 1-Jun-1999 12:00 AM
O SiO2 1-Jun-1999 12:00 AM
Al Al2O3 1-Jun-1999 12:00 AM
Si SiO2 1-Jun-1999 12:00 AM

Element	Weight%	Atomic%
C K	14.94	21.35
O K	57.71	61.91
Al K	0.64	0.41
Si K	26.72	16.33
Totals	100.00	

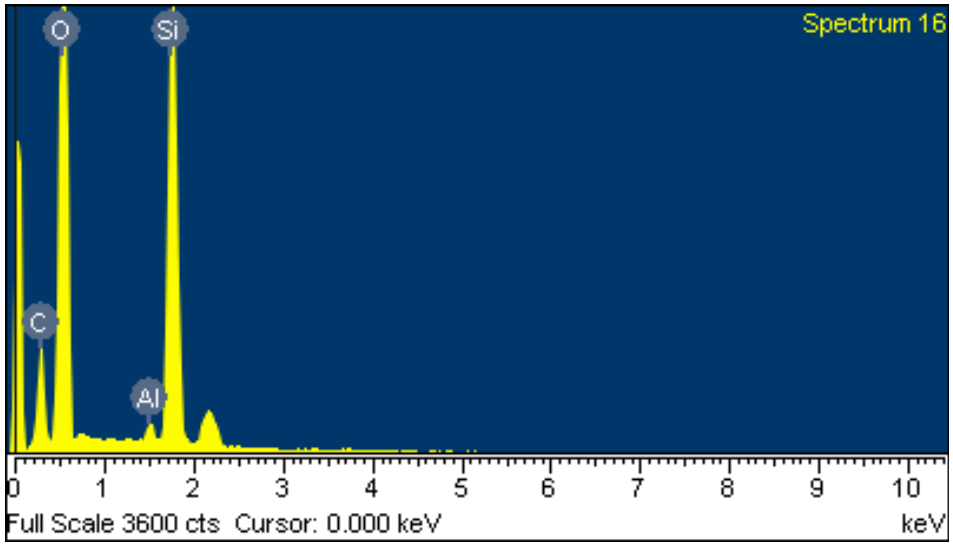

Comment: Sample 2C3 from diatom particle on the surface of an aluminum silicate.

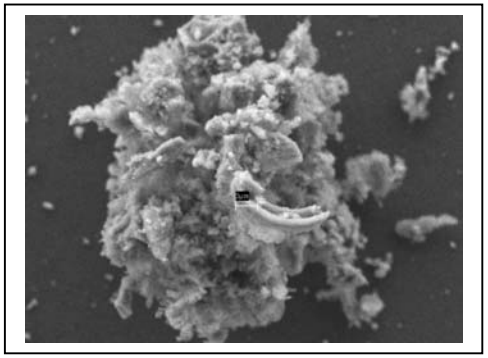

Bodele

22/06/2006 15:08:26

Spectrum processing :
Peak possibly omitted : 2.135 keV

Processing option : All elements analyzed (Normalised)
Number of iterations = 4

Standard :
C CaCO3 1-Jun-1999 12:00 AM
O SiO2 1-Jun-1999 12:00 AM
Mg MgO 1-Jun-1999 12:00 AM
Al Al2O3 1-Jun-1999 12:00 AM
Si SiO2 1-Jun-1999 12:00 AM
K MAD-10 Feldspar 1-Jun-1999 12:00 AM
Fe Fe 1-Jun-1999 12:00 AM
Cu Cu 1-Jun-1999 12:00 AM

Element	Weight%	Atomic%
C K	20.55	30.48
O K	42.15	46.93
Mg K	0.39	0.29
Al K	2.68	1.77
Si K	30.17	19.13
K K	0.76	0.35
Fe L	3.46	1.10
Cu L	-0.18	-0.05
Totals	100.00	

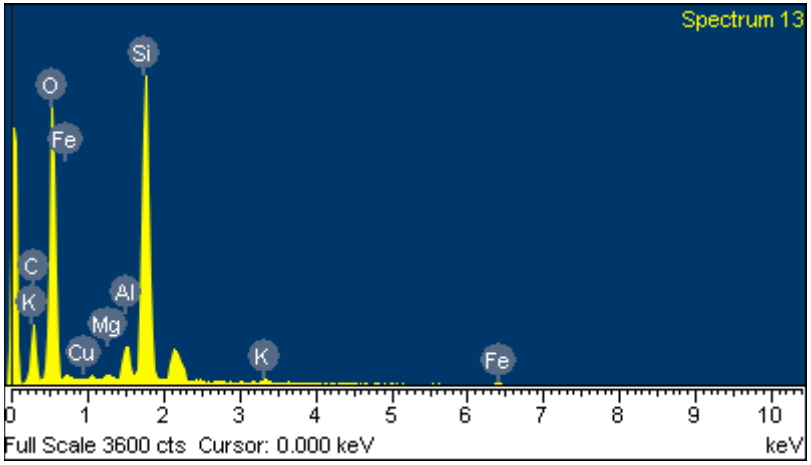

Comment: Sample 2B2: Ferromagnesium silicates and possible iron oxide. Questionable carbon reading, appears to be too high for filter alone.

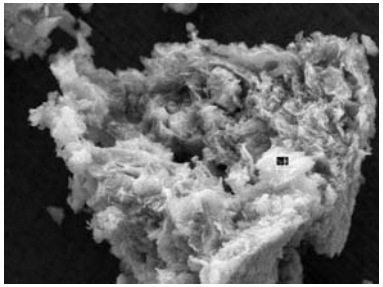

Spectrum processing :
Peak possibly omitted : 2.147 keV

Processing option : All elements analyzed (Normalised)
Number of iterations = 3

Standard :
C CaCO3 1-Jun-1999 12:00 AM
O SiO2 1-Jun-1999 12:00 AM
Si SiO2 1-Jun-1999 12:00 AM

Element	Weight%	Atomic%
C K	27.71	43.96
O K	13.64	16.25
Si K	58.65	39.79
Totals	100.00	

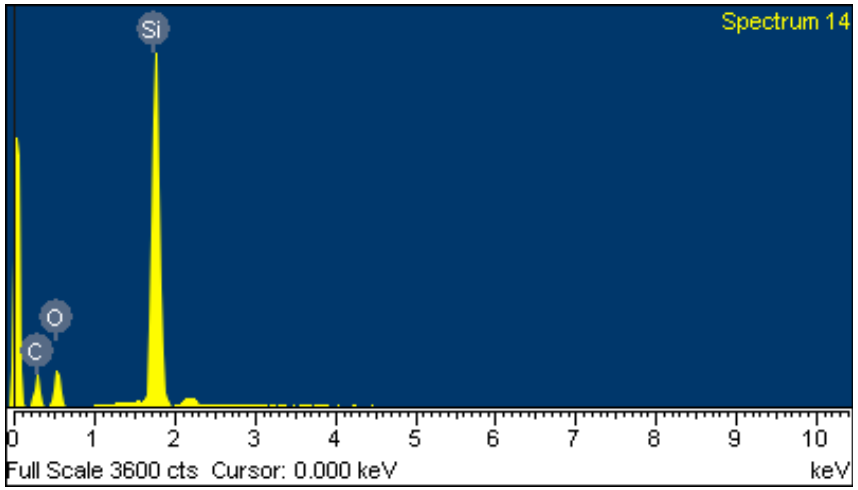

Comment: 2B3 sample, we believe, produced cosmic silicon with trace amounts of silica. Carbon is due to the sample filter.

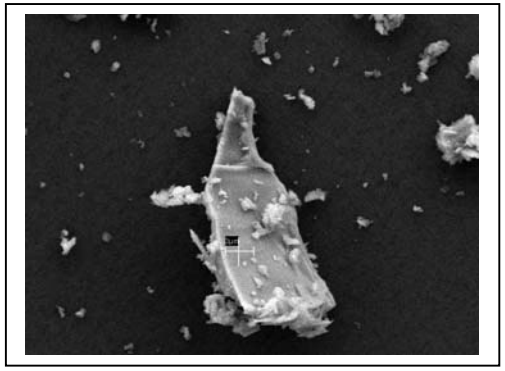

Spectrum processing :
No peaks omitted

Processing option : All elements analyzed (Normalised)
Number of iterations = 4

Standard :
C CaCO3 1-Jun-1999 12:00 AM
O SiO2 1-Jun-1999 12:00 AM
F MgF2 1-Jun-1999 12:00 AM
Na Albite 1-Jun-1999 12:00 AM
Si SiO2 1-Jun-1999 12:00 AM
P GaP 1-Jun-1999 12:00 AM
Ca Wollastonite 1-Jun-1999 12:00 AM

Element	Weight%	Atomic%
C K	35.93	50.13
O K	33.29	34.87
F K	1.82	1.61
Na K	0.72	0.52
Si K	0.67	0.40
P K	7.73	4.18
Ca K	19.83	8.29
Totals	100.00	

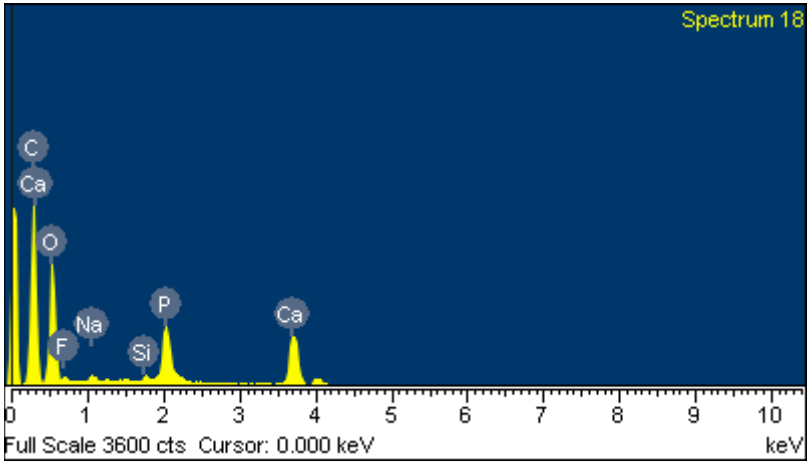

Comment: Calcium carbonate, the mineral apatite, and clay minerals (feldspars)

Spectrum processing :
Peak possibly omitted : 2.138 keV

Processing option : All elements analyzed (Normalised)
Number of iterations = 4

Standard :
C CaCO3 1-Jun-1999 12:00 AM
O SiO2 1-Jun-1999 12:00 AM
Na Albite 1-Jun-1999 12:00 AM
Mg MgO 1-Jun-1999 12:00 AM
Al Al2O3 1-Jun-1999 12:00 AM
Si SiO2 1-Jun-1999 12:00 AM
K MAD-10 Feldspar 1-Jun-1999 12:00 AM
Ca Wollastonite 1-Jun-1999 12:00 AM
Fe Fe 1-Jun-1999 12:00 AM

Element	Weight%	Atomic%
C K	45.40	57.65
O K	33.81	32.24
Na K	0.61	0.41
Mg K	0.62	0.39
Al K	2.42	1.37
Si K	11.24	6.10
K K	0.77	0.30
Ca K	1.32	0.50
Fe L	3.82	1.04
Totals	100.00	

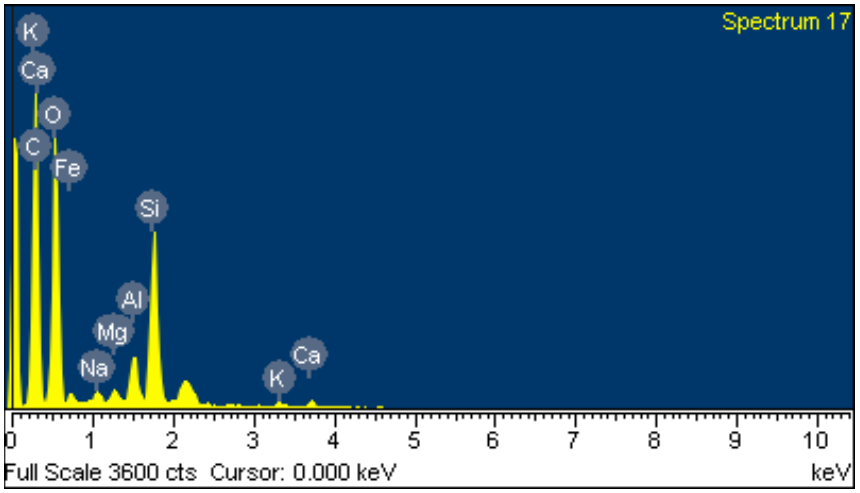

Comment: Sample 2C3: Ferromagnesium silicates, possible iron oxides. The high quantity of carbon is not accounted for by the sample filter alone.

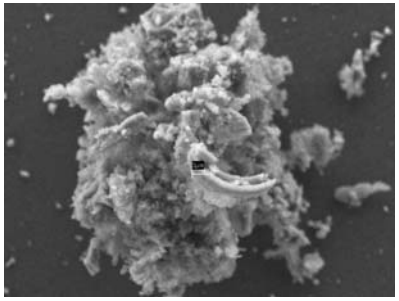

Spectrum processing :
No peaks omitted

Processing option : All elements analyzed (Normalised)
Number of iterations = 3

Standard :
C CaCO3 1-Jun-1999 12:00 AM
O SiO2 1-Jun-1999 12:00 AM
F MgF2 1-Jun-1999 12:00 AM
Na Albite 1-Jun-1999 12:00 AM
P GaP 1-Jun-1999 12:00 AM
Ca Wollastonite 1-Jun-1999 12:00 AM

Element	Weight%	Atomic%
C K	4.58	8.49
O K	40.53	56.44
F K	2.61	3.06
Na K	0.83	0.80
P K	15.96	11.48
Ca K	35.50	19.73
Totals	100.00	

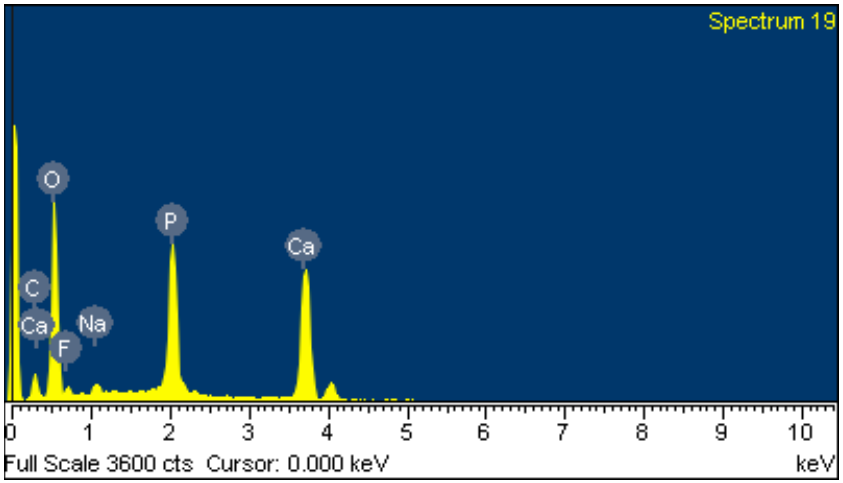

Comment: Sample 2C4; Indications are for the presence of Apatite mineral accounting for the F, and P, with small amounts of fluorite, and significant calcium carbonate.

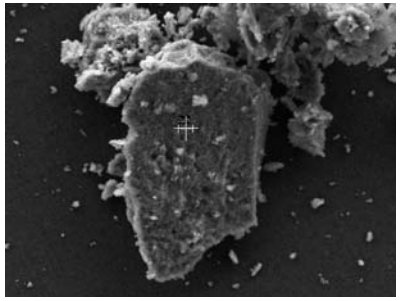

Spectrum processing :
Peak possibly omitted : 2.138 keV

Processing option : All elements analyzed (Normalised)
Number of iterations = 3

Standard :
O SiO2 1-Jun-1999 12:00 AM
Na Albite 1-Jun-1999 12:00 AM
Mg MgO 1-Jun-1999 12:00 AM
Al Al2O3 1-Jun-1999 12:00 AM
Si SiO2 1-Jun-1999 12:00 AM
K MAD-10 Feldspar 1-Jun-1999 12:00 AM
Fe Fe 1-Jun-1999 12:00 AM

Element	Weight%	Atomic%
O K	46.29	62.99
Na K	1.11	1.05
Mg K	1.44	1.29
Al K	7.38	5.96
Si K	29.25	22.67
K K	2.23	1.24
Fe L	12.30	4.80
Totals	100.00	

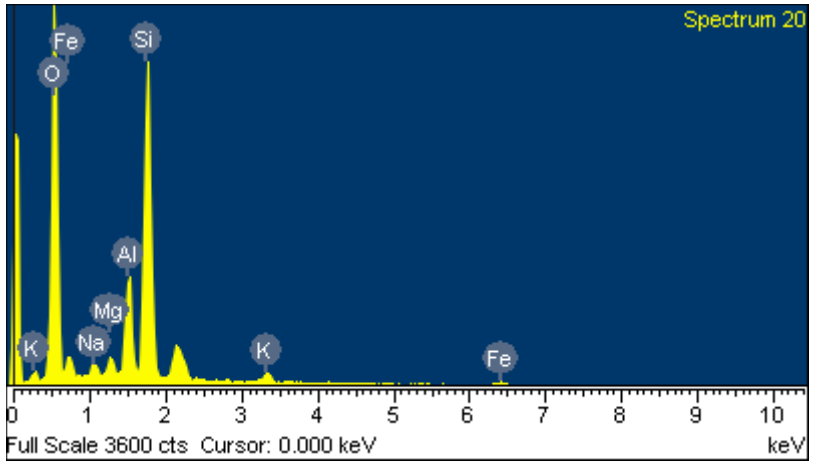

Comment: Randomized sampling sample 2D2; Ferromagnesium silicates and possible feldspar clay, iron oxides and silica.

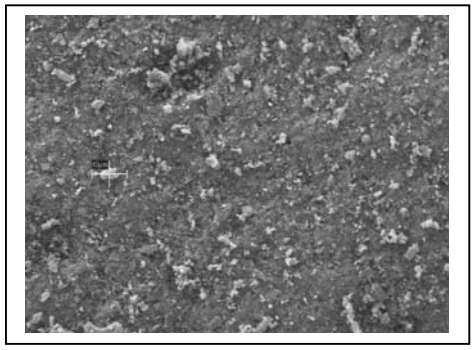

Spectrum processing :
No peaks omitted

Processing option : All elements analyzed (Normalised)
Number of iterations = 3

Standard :
O SiO2 1-Jun-1999 12:00 AM
Na Albite 1-Jun-1999 12:00 AM
Al Al2O3 1-Jun-1999 12:00 AM
Si SiO2 1-Jun-1999 12:00 AM
K MAD-10 Feldspar 1-Jun-1999 12:00 AM
Fe Fe 1-Jun-1999 12:00 AM
Au Au 1-Jun-1999 12:00 AM

Element	Weight%	Atomic%
O K	43.92	68.21
Na K	0.54	0.58
Al K	3.77	3.47
Si K	24.84	21.98
K K	0.86	0.55
Fe L	6.03	2.68
Au M	20.04	2.53
Totals	100.00	

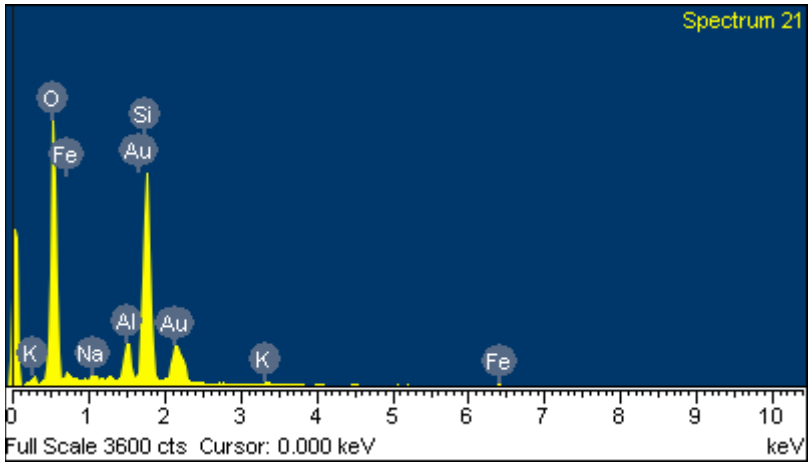

Comment: Sample 2D2: white particle; primarily Ferromagnesium silicate minerals with possible clay minerals and/or iron oxides with possible traces of silica.

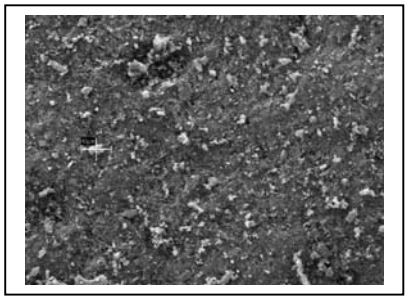

Spectrum processing :
Peak possibly omitted : 2.143 keV

Processing option : All elements analyzed (Normalised)
Number of iterations = 2

Standard :
C CaCO3 1-Jun-1999 12:00 AM
O SiO2 1-Jun-1999 12:00 AM
Na Albite 1-Jun-1999 12:00 AM
Mg MgO 1-Jun-1999 12:00 AM
Al Al2O3 1-Jun-1999 12:00 AM
Si SiO2 1-Jun-1999 12:00 AM
K MAD-10 Feldspar 1-Jun-1999 12:00 AM
Fe Fe 1-Jun-1999 12:00 AM

Element	Weight%	Atomic%
C K	4.07	7.01
O K	48.83	63.09
Na K	1.21	1.09
Mg K	0.99	0.84
Al K	5.93	4.55
Si K	24.16	17.78
K K	1.00	0.53
Fe L	13.80	5.11
Totals	100.00	

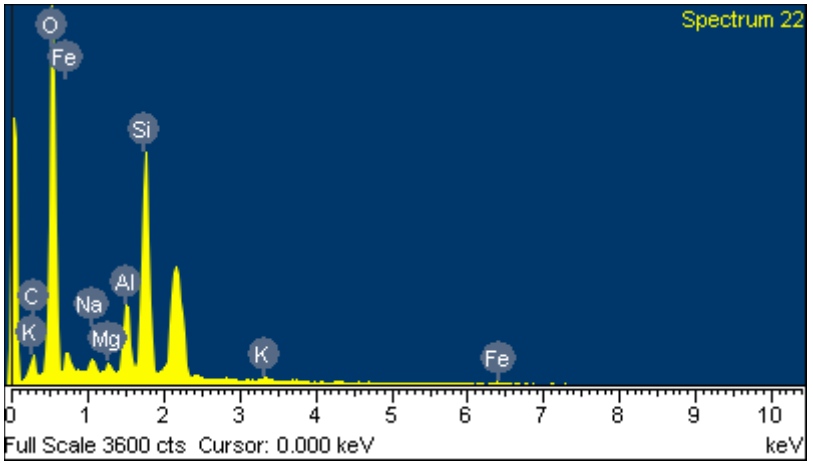

Comment: Sample 2D3: Ferromagnesium silicates, Aluminum silicates, clay minerals, possible iron oxide minerals and possible silica. Note carbon signature is due mainly to filter material.

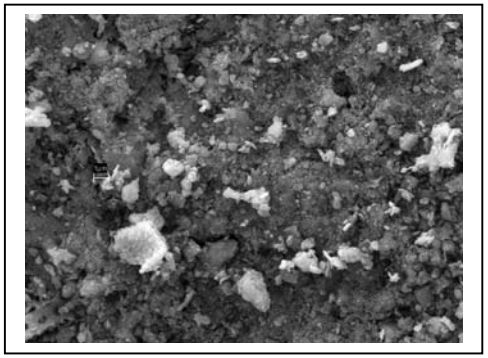

Spectrum processing :
Peak possibly omitted : 2.150 keV

Processing option : All elements analyzed (Normalised)
Number of iterations = 2

Standard :
C CaCO3 1-Jun-1999 12:00 AM
O SiO2 1-Jun-1999 12:00 AM
Na Albite 1-Jun-1999 12:00 AM
Mg MgO 1-Jun-1999 12:00 AM
Al Al2O3 1-Jun-1999 12:00 AM
Si SiO2 1-Jun-1999 12:00 AM
K MAD-10 Feldspar 1-Jun-1999 12:00 AM
Fe Fe 1-Jun-1999 12:00 AM

Element	Weight%	Atomic%
C K	4.66	7.80
O K	50.43	63.45
Na K	0.64	0.56
Mg K	1.29	1.07
Al K	8.41	6.27
Si K	23.14	16.59
K K	0.89	0.46
Fe L	10.53	3.79
Totals	100.00	

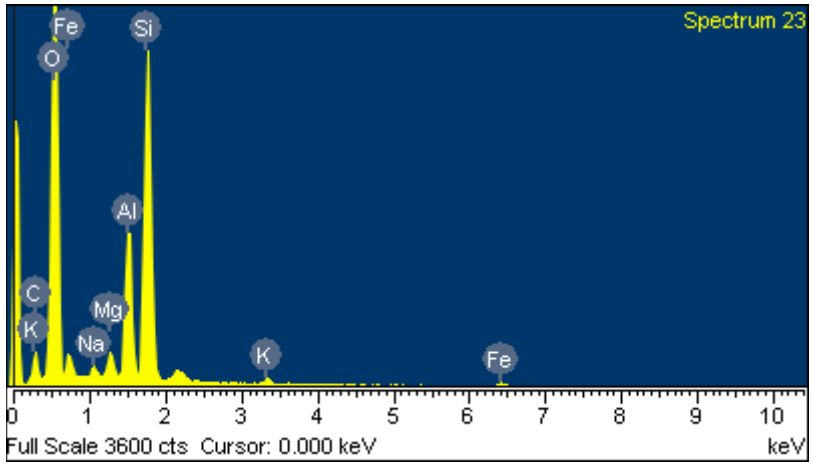

Comment: Sample 3A2: Ferromagnesium silicates, clay minerals, possible feldspars, possible iron oxides, with traces of silica.

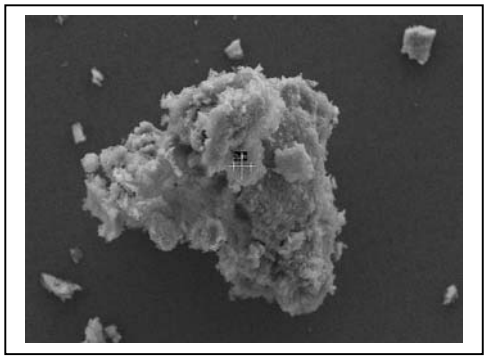

Spectrum processing :
No peaks omitted

Processing option : All elements analyzed (Normalised)
Number of iterations = 3

Standard :
C CaCO3 1-Jun-1999 12:00 AM
O SiO2 1-Jun-1999 12:00 AM
Na Albite 1-Jun-1999 12:00 AM
Mg MgO 1-Jun-1999 12:00 AM
Al Al2O3 1-Jun-1999 12:00 AM
Si SiO2 1-Jun-1999 12:00 AM
K MAD-10 Feldspar 1-Jun-1999 12:00 AM
Ca Wollastonite 1-Jun-1999 12:00 AM
Fe Fe 1-Jun-1999 12:00 AM

Element	Weight%	Atomic%
C K	2.61	4.35
O K	53.84	67.48
Na K	1.13	0.99
Mg K	2.03	1.68
Al K	6.02	4.48
Si K	23.66	16.89
K K	0.79	0.40
Ca K	1.25	0.62
Fe L	8.67	3.11
Totals	100.00	

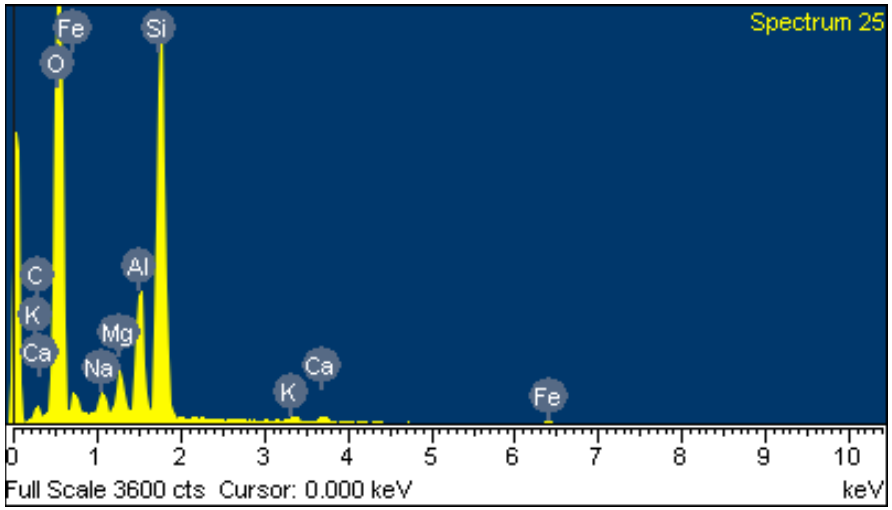

Comment: Sample 3B2: Ferromagnesium silicates, Al silicates (feldspars) clay minerals, possible iron oxides, and possible dolomite. The mineralization occurs consistently in the sample except for the region where the diatom particles can be seen in the image below.

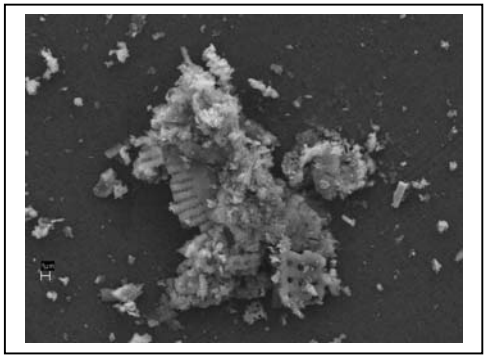

Spectrum processing :
Peaks possibly omitted : 2.154, 5.500 keV

Processing option : All elements analyzed (Normalised)
Number of iterations = 3

Standard :
C CaCO3 1-Jun-1999 12:00 AM
O SiO2 1-Jun-1999 12:00 AM
Al Al2O3 1-Jun-1999 12:00 AM
Si SiO2 1-Jun-1999 12:00 AM
Ti Ti 1-Jun-1999 12:00 AM

Element	Weight%	Atomic%
C K	1.57	2.86
O K	48.60	66.36
Al K	9.65	7.81
Si K	14.43	11.22
Ti K	25.75	11.74
Totals	100.00	

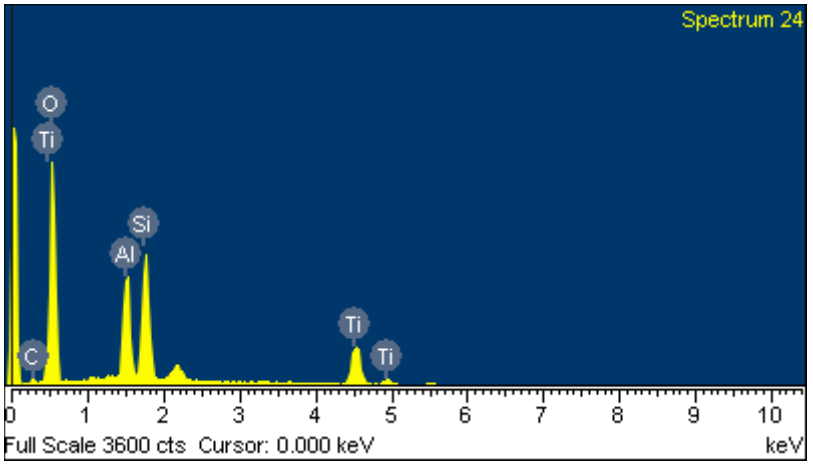

Comment: Sample 3B4 appear to contain all or most of the following minerals; silica, AlO2, TiO2, and possibly free titanium. There appears to be a large quantity of titanium in this particular sample, not seen in any of the others.

Spectrum processing :
Peak possibly omitted : 2.154 keV

Processing option : All elements analyzed (Normalised)
Number of iterations = 3

Standard :
C CaCO3 1-Jun-1999 12:00 AM
O SiO2 1-Jun-1999 12:00 AM
Mg MgO 1-Jun-1999 12:00 AM
Al Al2O3 1-Jun-1999 12:00 AM
Si SiO2 1-Jun-1999 12:00 AM
K MAD-10 Feldspar 1-Jun-1999 12:00 AM
Ca Wollastonite 1-Jun-1999 12:00 AM
Fe Fe 1-Jun-1999 12:00 AM

Element	Weight%	Atomic%
C K	43.10	56.91
O K	28.36	28.11
Mg K	1.47	0.96
Al K	5.44	3.20
Si K	14.94	8.44
K K	0.91	0.37
Ca K	3.38	1.34
Fe L	2.38	0.68
Totals	100.00	

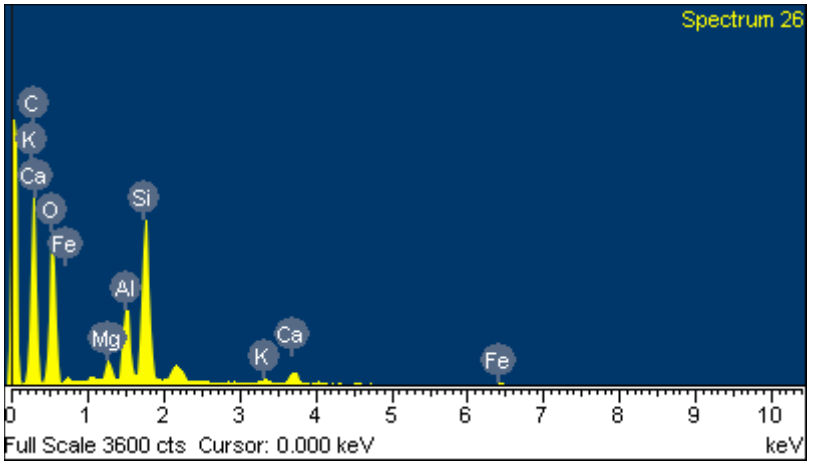

Comment: Sample 3C3: Ferromagnesium silicates, aluminum silicate clay minerals (feldspar), possible iron oxide.

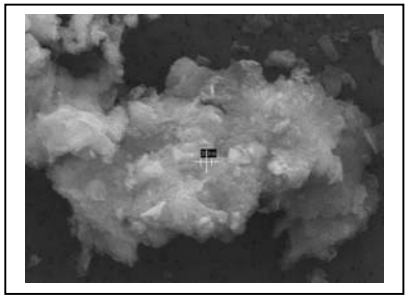

Spectrum processing :
Peak possibly omitted : 2.144 keV

Processing option : All elements analyzed (Normalised)
Number of iterations = 3

Standard :
C CaCO3 1-Jun-1999 12:00 AM
O SiO2 1-Jun-1999 12:00 AM
Na Albite 1-Jun-1999 12:00 AM
Mg MgO 1-Jun-1999 12:00 AM
Al Al2O3 1-Jun-1999 12:00 AM
Si SiO2 1-Jun-1999 12:00 AM
K MAD-10 Feldspar 1-Jun-1999 12:00 AM
Fe Fe 1-Jun-1999 12:00 AM

Element	Weight%	Atomic%
C K	0.43	0.75
O K	48.34	63.09
Na K	1.95	1.77
Mg K	2.96	2.54
Al K	8.93	6.91
Si K	28.84	21.44
K K	1.87	1.00
Fe L	6.69	2.50
Totals	100.00	

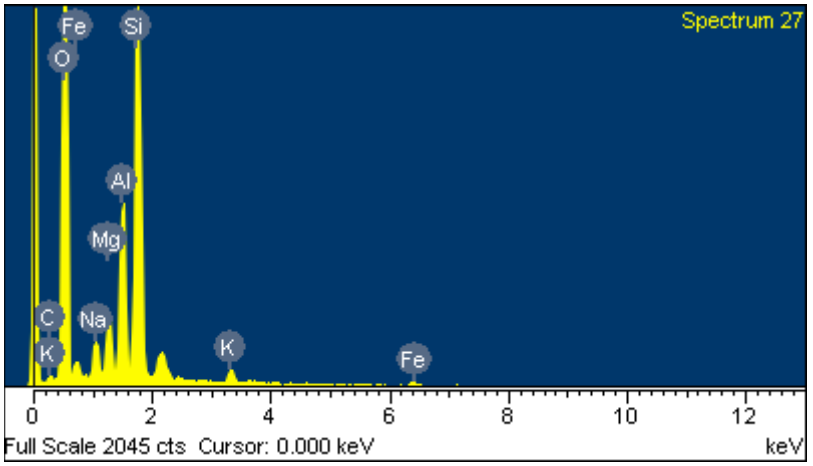

Comment: Sample 3D1: Ferromagnesium silicates, clay minerals, possible iron oxides, and possibly trace silica.

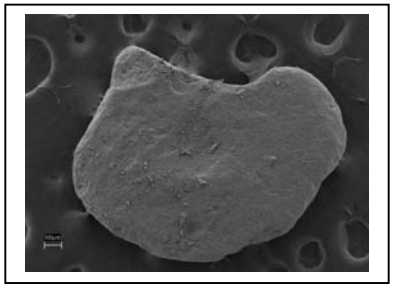

Spectrum processing :
Peak possibly omitted : 2.145 keV

Processing option : All elements analyzed (Normalised)
Number of iterations = 3

Standard :
C CaCO3 1-Jun-1999 12:00 AM
O SiO2 1-Jun-1999 12:00 AM
Na Albite 1-Jun-1999 12:00 AM
Mg MgO 1-Jun-1999 12:00 AM
Al Al2O3 1-Jun-1999 12:00 AM
Si SiO2 1-Jun-1999 12:00 AM
Ca Wollastonite 1-Jun-1999 12:00 AM

Element	Weight%	Atomic%
C K	9.56	14.77
O K	57.72	66.97
Na K	0.90	0.73
Mg K	0.77	0.59
Al K	2.24	1.54
Si K	10.44	6.90
Ca K	18.38	8.51
Totals	100.00	

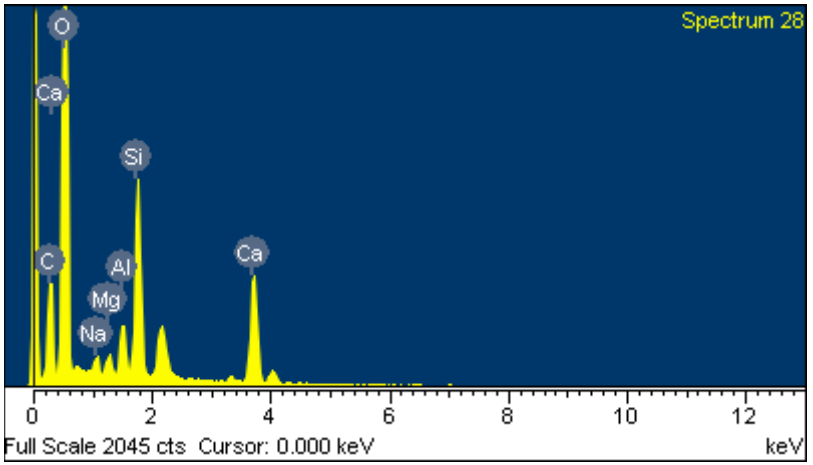

Comment: Sample 3D2: Ferromagnesium silicates, clay minerals and calcium carbonate with possible traces of silica.

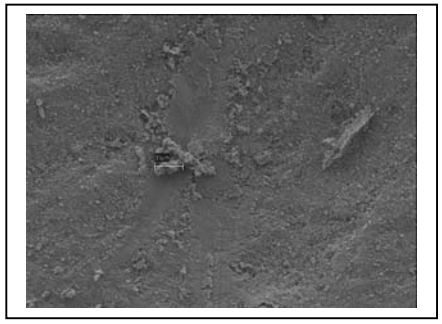

Spectrum processing :
Peak possibly omitted : 2.132 keV

Processing option : All elements analyzed (Normalised)
Number of iterations = 4

Standard :
C CaCO3 1-Jun-1999 12:00 AM
O SiO2 1-Jun-1999 12:00 AM
Al Al2O3 1-Jun-1999 12:00 AM
Si SiO2 1-Jun-1999 12:00 AM
K MAD-10 Feldspar 1-Jun-1999 12:00 AM
Fe Fe 1-Jun-1999 12:00 AM

Element	Weight%	Atomic%
C K	15.04	22.81
O K	48.66	55.41
Al K	2.67	1.80
Si K	27.53	17.86
K K	0.90	0.42
Fe L	5.20	1.70
Totals	100.00	

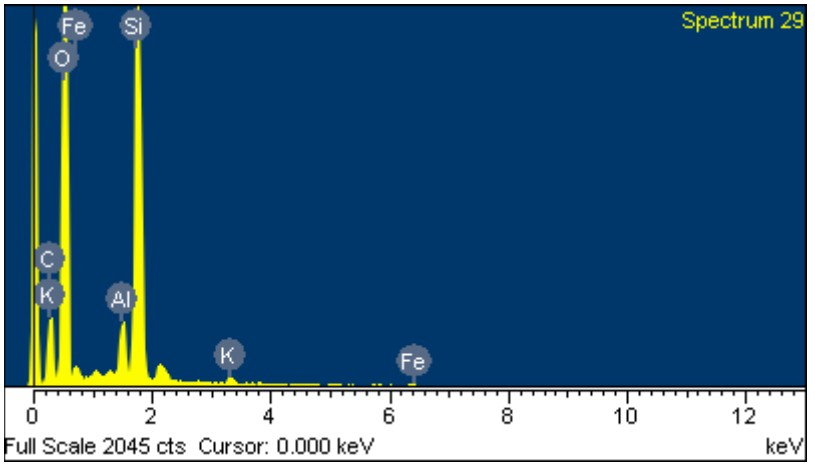

Comment: Sample 4A1: Clay minerals and silica

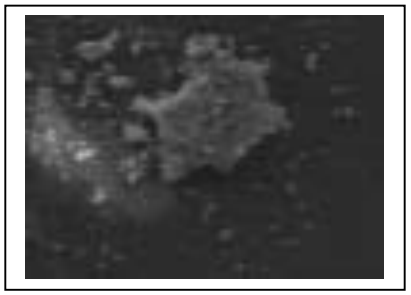

Spectrum processing :
Peak possibly omitted : 2.137 keV

Processing option : All elements analyzed (Normalised)
Number of iterations = 2

Standard :
C CaCO3 1-Jun-1999 12:00 AM
O SiO2 1-Jun-1999 12:00 AM
Na Albite 1-Jun-1999 12:00 AM
Mg MgO 1-Jun-1999 12:00 AM
Al Al2O3 1-Jun-1999 12:00 AM
Si SiO2 1-Jun-1999 12:00 AM
K MAD-10 Feldspar 1-Jun-1999 12:00 AM
Fe Fe 1-Jun-1999 12:00 AM

Element	Weight%	Atomic%
C K	1.94	3.29
O K	49.48	62.97
Na K	0.81	0.72
Mg K	1.03	0.86
Al K	5.91	4.46
Si K	35.19	25.51
K K	0.83	0.43
Fe L	4.83	1.76
Totals	100.00	

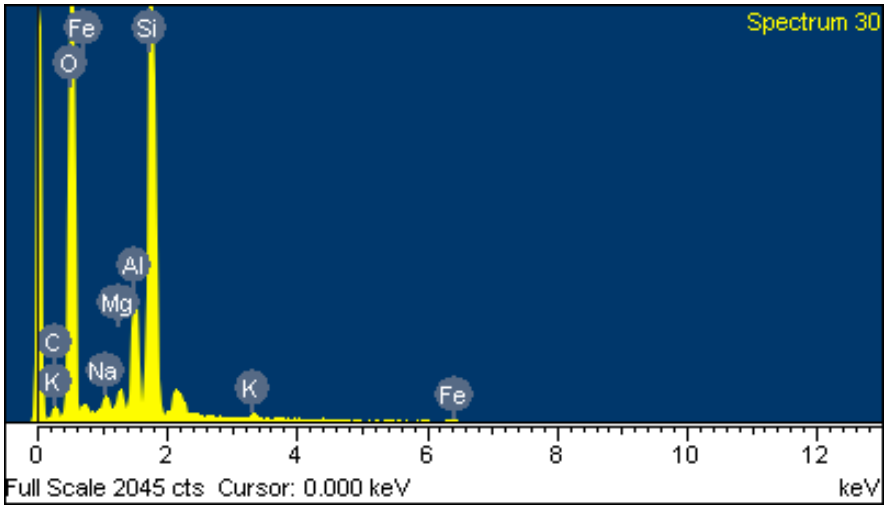

Comment: Sample 4A2: Ferromagnesium silicate minerals, clay minerals, and silica possible in small quantities.

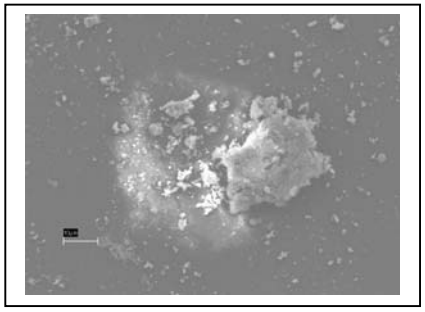

Spectrum processing :
Peak possibly omitted : 2.144 keV

Processing option : All elements analyzed (Normalised)
Number of iterations = 4

Standard :
C CaCO3 1-Jun-1999 12:00 AM
O SiO2 1-Jun-1999 12:00 AM
Na Albite 1-Jun-1999 12:00 AM
Mg MgO 1-Jun-1999 12:00 AM
Al Al2O3 1-Jun-1999 12:00 AM
Si SiO2 1-Jun-1999 12:00 AM
K MAD-10 Feldspar 1-Jun-1999 12:00 AM
Fe Fe 1-Jun-1999 12:00 AM

Element	Weight%	Atomic%
C K	34.87	47.08
O K	38.65	39.18
Na K	0.49	0.35
Mg K	0.92	0.61
Al K	4.35	2.61
Si K	14.14	8.17
K K	0.82	0.34
Fe L	5.75	1.67
Totals	100.00	

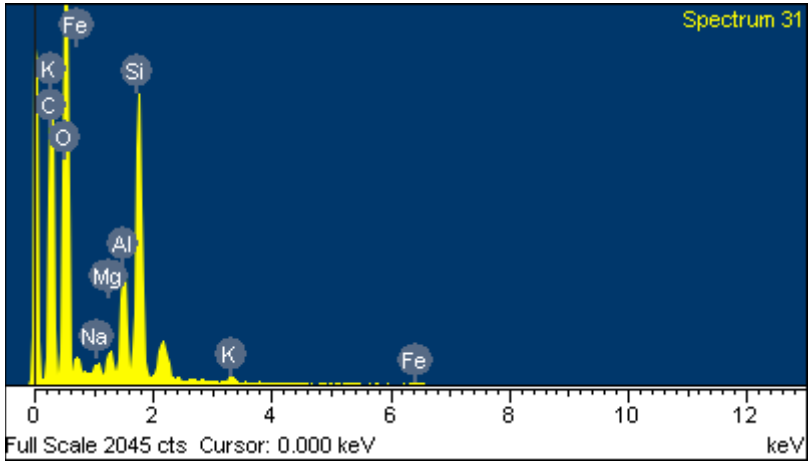

Comment: Sample 4A3, randomly taken, is mainly composed of Ferromagnesium silicates and clay minerasl, although the remains of diatoms can be seen.

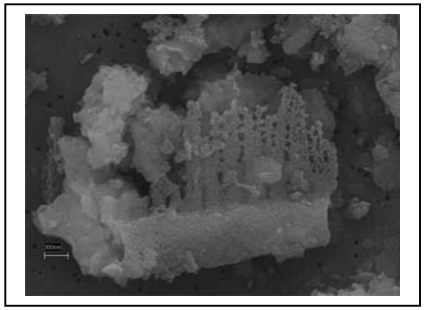

Bodele

17/07/2006 12:01:09

Spectrum processing :
Peak possibly omitted : 2.140 keV

Processing option : All elements analyzed (Normalised)
Number of iterations = 4

Standard :
C CaCO3 1-Jun-1999 12:00 AM
O SiO2 1-Jun-1999 12:00 AM
Al Al2O3 1-Jun-1999 12:00 AM
Si SiO2 1-Jun-1999 12:00 AM
Fe Fe 1-Jun-1999 12:00 AM

Element	Weight%	Atomic%
C K	43.04	54.46
O K	38.39	36.47
Al K	0.63	0.35
Si K	14.25	7.71
Fe L	3.69	1.00
Totals	100.00	

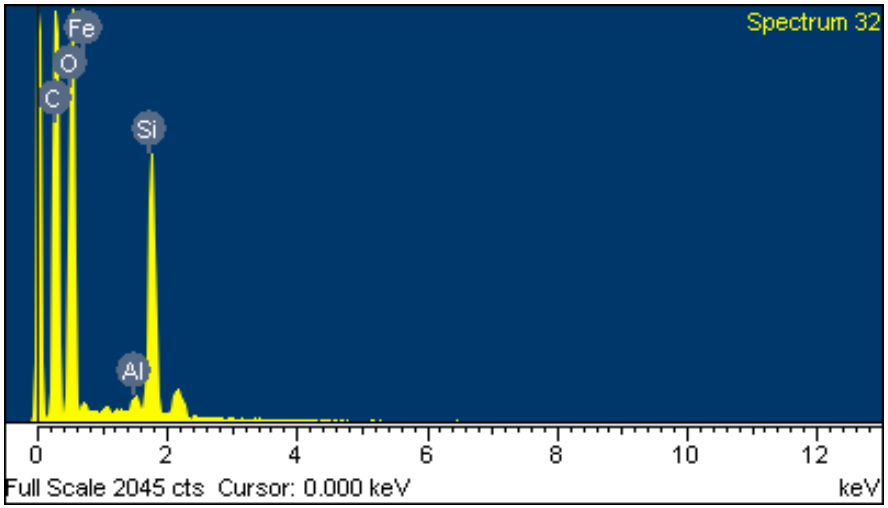

Comment: Sample 4A4 randomized, is primarily iron oxide or clay minerals, and silica.

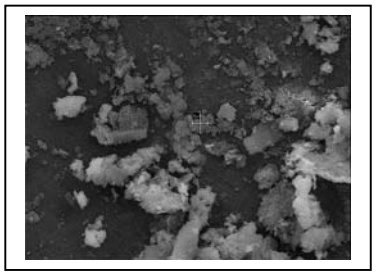

Spectrum processing :
Peak possibly omitted : 2.138 keV

Processing option : All elements analyzed (Normalised)
Number of iterations = 3

Standard :
C CaCO3 1-Jun-1999 12:00 AM
O SiO2 1-Jun-1999 12:00 AM
Na Albite 1-Jun-1999 12:00 AM
Mg MgO 1-Jun-1999 12:00 AM
Al Al2O3 1-Jun-1999 12:00 AM
Si SiO2 1-Jun-1999 12:00 AM
K MAD-10 Feldspar 1-Jun-1999 12:00 AM
Fe Fe 1-Jun-1999 12:00 AM

Element	Weight%	Atomic%
C K	2.02	3.51
O K	49.66	64.57
Na K	1.28	1.16
Mg K	3.17	2.72
Al K	8.35	6.44
Si K	22.18	16.43
K K	1.38	0.73
Fe L	11.95	4.45
Totals	100.00	

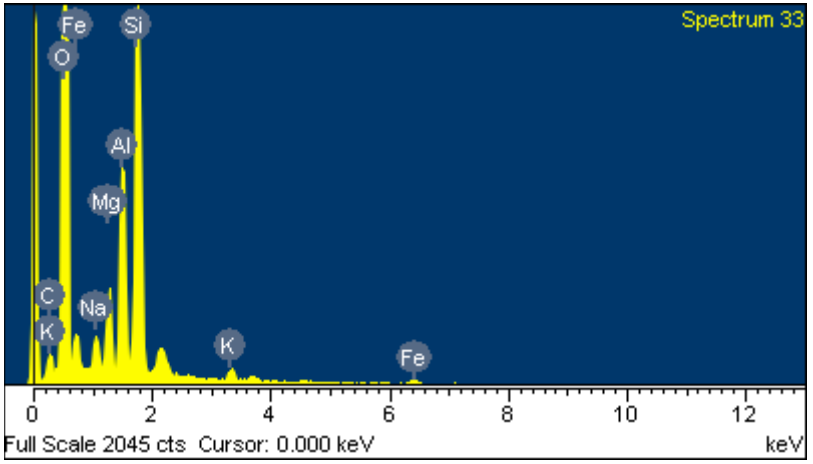

Comment: Sample 4B1: Ferromagnesium silicates and clay minerals with possible iron oxides in the randomized sample.

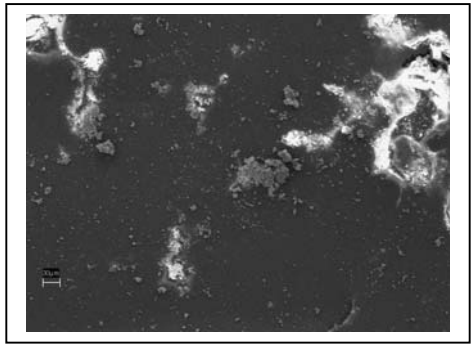

Spectrum processing :
No peaks omitted

Processing option : All elements analyzed (Normalised)
Number of iterations = 2

Standard :
C CaCO3 1-Jun-1999 12:00 AM
O SiO2 1-Jun-1999 12:00 AM
Na Albite 1-Jun-1999 12:00 AM
Mg MgO 1-Jun-1999 12:00 AM
Al Al2O3 1-Jun-1999 12:00 AM
Si SiO2 1-Jun-1999 12:00 AM
K MAD-10 Feldspar 1-Jun-1999 12:00 AM
Fe Fe 1-Jun-1999 12:00 AM
Au Au 1-Jun-1999 12:00 AM

Element	Weight%	Atomic%
C K	3.43	6.26
O K	45.81	62.67
Na K	0.66	0.63
Mg K	2.29	2.06
Al K	9.23	7.49
Si K	21.27	16.57
K K	1.09	0.61
Fe L	6.79	2.66
Au M	9.43	1.05
Totals	100.00	

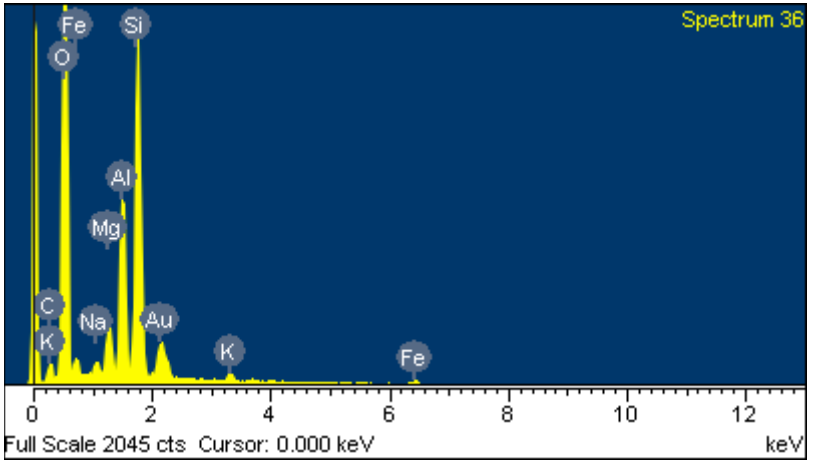

Comment: Sample 4B4: Ferromagnesium silicates, clay minerals, possible iron oxides and some silica. Au backscatter evident.

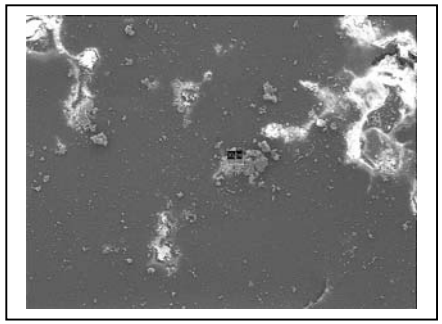

Spectrum processing :
Peak possibly omitted : 2.149 keV

Processing option : All elements analyzed (Normalised)
Number of iterations = 3

Standard :
C CaCO3 1-Jun-1999 12:00 AM
O SiO2 1-Jun-1999 12:00 AM
Na Albite 1-Jun-1999 12:00 AM
Mg MgO 1-Jun-1999 12:00 AM
Al Al2O3 1-Jun-1999 12:00 AM
Si SiO2 1-Jun-1999 12:00 AM
K MAD-10 Feldspar 1-Jun-1999 12:00 AM
Fe Fe 1-Jun-1999 12:00 AM

Element	Weight%	Atomic%
C K	10.28	16.32
O K	48.51	57.83
Na K	0.68	0.57
Mg K	5.68	4.45
Al K	5.24	3.71
Si K	20.49	13.91
K K	0.71	0.35
Fe L	8.41	2.87
Totals	100.00	

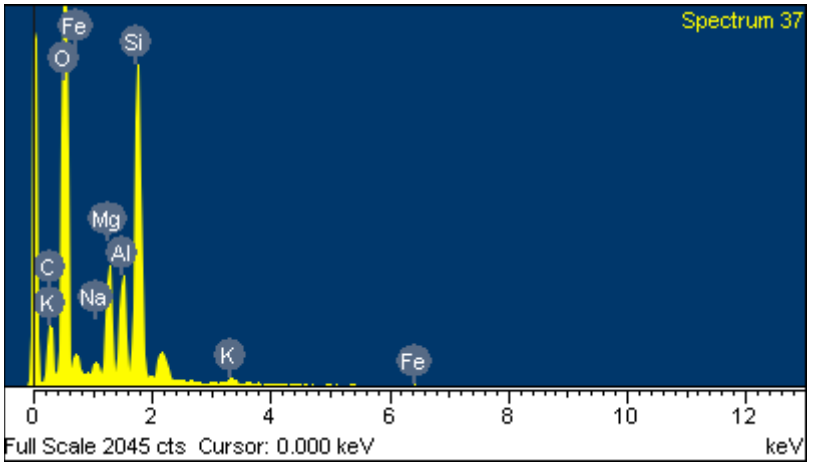

Comment: Sample 4B5: Ferromagnesium silicate minerals, clay minerals, and possible iron oxides and silica.

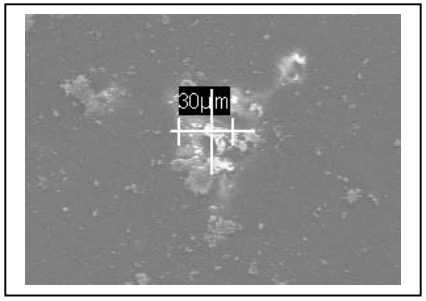

Spectrum processing :
No peaks omitted

Processing option : All elements analyzed (Normalised)
Number of iterations = 3

Standard :
C CaCO3 1-Jun-1999 12:00 AM
O SiO2 1-Jun-1999 12:00 AM
F MgF2 1-Jun-1999 12:00 AM
Na Albite 1-Jun-1999 12:00 AM
Mg MgO 1-Jun-1999 12:00 AM
P GaP 1-Jun-1999 12:00 AM
Ca Wollastonite 1-Jun-1999 12:00 AM

Element	Weight%	Atomic%
C K	5.72	10.00
O K	44.77	58.78
F K	4.59	5.07
Na K	1.28	1.17
Mg K	0.42	0.36
P K	12.73	8.63
Ca K	30.49	15.98
Totals	100.00	

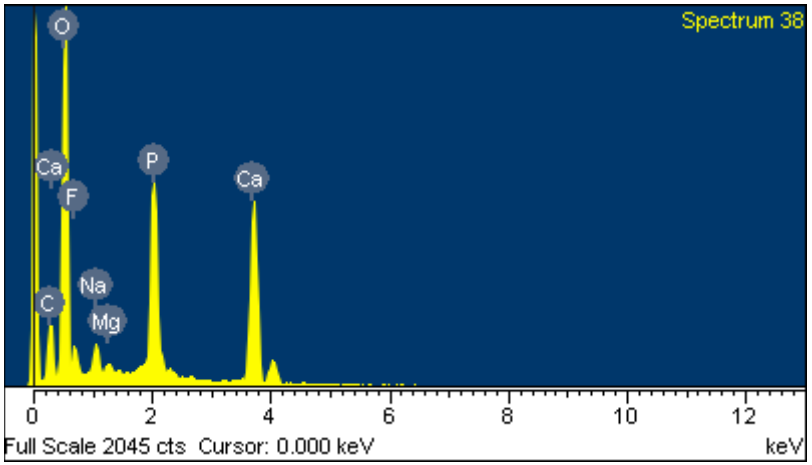

Comment: Sample 4C1: Clay minerals, calcium carbonate, dolomite, and a large amount of the mineral apatite

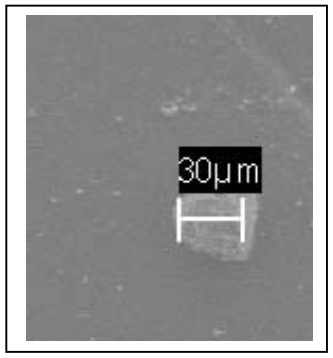

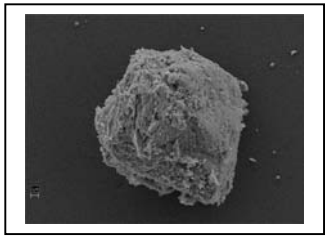

Bodele

17/07/2006 12:02:35

Spectrum processing :
Peak possibly omitted : 2.149 keV

Processing option : All elements analyzed (Normalised)
Number of iterations = 3

Standard :
C CaCO3 1-Jun-1999 12:00 AM
O SiO2 1-Jun-1999 12:00 AM
Mg MgO 1-Jun-1999 12:00 AM
Al Al2O3 1-Jun-1999 12:00 AM
Si SiO2 1-Jun-1999 12:00 AM
K MAD-10 Feldspar 1-Jun-1999 12:00 AM
Ca Wollastonite 1-Jun-1999 12:00 AM
Fe Fe 1-Jun-1999 12:00 AM

Element	Weight%	Atomic%
C K	20.73	33.32
O K	25.21	30.43
Mg K	3.75	2.98
Al K	9.77	6.99
Si K	33.48	23.02
K K	2.22	1.09
Ca K	3.64	1.76
Fe L	1.21	0.42
Totals	100.00	

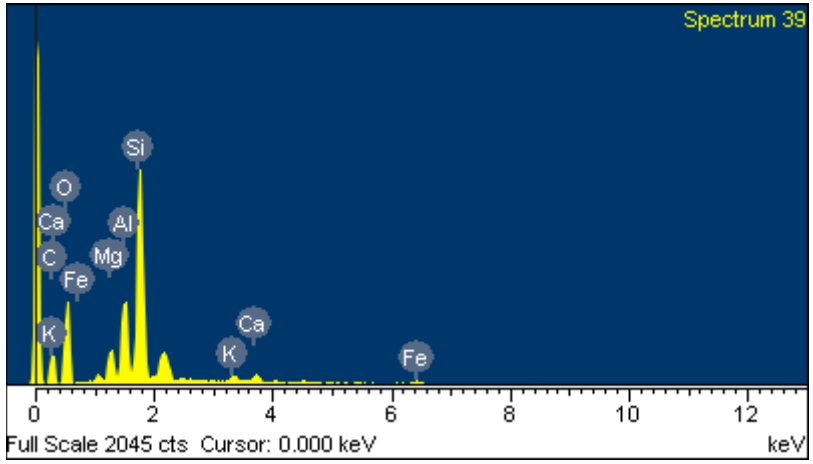

Comment: Sample 4C4: Ferromagnesium silicates, clay minerals, possible iron oxides, and calcium carbonates and/or dolomites.

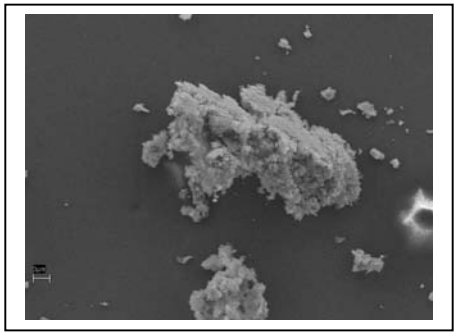

Spectrum processing :
Peak possibly omitted : 2.149 keV

Processing option : All elements analyzed (Normalised)
Number of iterations = 3

Standard :
C CaCO3 1-Jun-1999 12:00 AM
O SiO2 1-Jun-1999 12:00 AM
Mg MgO 1-Jun-1999 12:00 AM
Al Al2O3 1-Jun-1999 12:00 AM
Si SiO2 1-Jun-1999 12:00 AM
K MAD-10 Feldspar 1-Jun-1999 12:00 AM
Ca Wollastonite 1-Jun-1999 12:00 AM
Fe Fe 1-Jun-1999 12:00 AM

Element	Weight%	Atomic%
C K	20.73	33.32
O K	25.21	30.43
Mg K	3.75	2.98
Al K	9.77	6.99
Si K	33.48	23.02
K K	2.22	1.09
Ca K	3.64	1.76
Fe L	1.21	0.42
Totals	100.00	

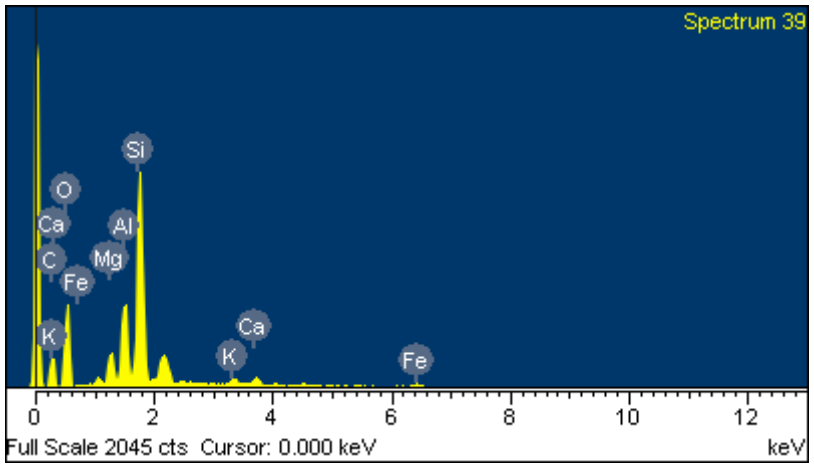

Comment: Sample 4C5: Ferromagnesium silicates, calcium carbonates and/or dolomites.

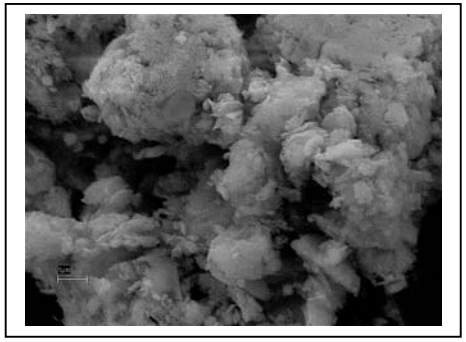

Bodele 17/07/2006 12:02:49

Spectrum processing :
Peak possibly omitted : 2.147 keV

Processing option : All elements analyzed (Normalised)
Number of iterations = 3

Standard :
C CaCO3 1-Jun-1999 12:00 AM
O SiO2 1-Jun-1999 12:00 AM
Na Albite 1-Jun-1999 12:00 AM
Mg MgO 1-Jun-1999 12:00 AM
Al Al2O3 1-Jun-1999 12:00 AM
Si SiO2 1-Jun-1999 12:00 AM
K MAD-10 Feldspar 1-Jun-1999 12:00 AM
Ca Wollastonite 1-Jun-1999 12:00 AM
Fe Fe 1-Jun-1999 12:00 AM

Element	Weight%	Atomic%
C K	17.84	26.73
O K	47.45	53.37
Na K	0.80	0.63
Mg K	1.70	1.26
Al K	5.24	3.49
Si K	17.43	11.17
K K	0.92	0.42
Ca K	1.17	0.53
Fe L	7.45	2.40
Totals	100.00	

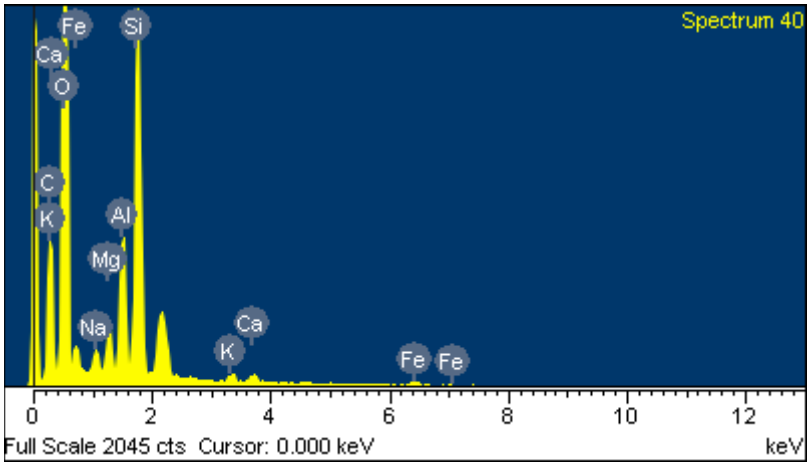

Comment: Sample 4C8: Ferromagnesium silicate minerals, clay minerals, possible iron oxides, and calcium carbonates.

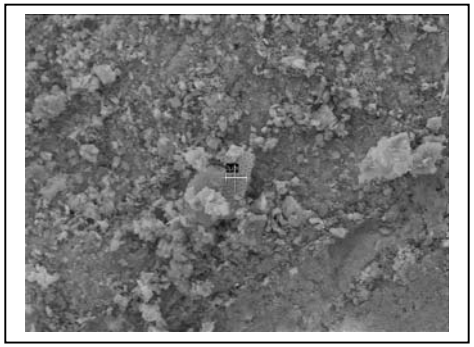

Spectrum processing :
Peak possibly omitted : 2.136 keV

Processing option : All elements analyzed (Normalised)
Number of iterations = 4

Standard :
C CaCO3 1-Jun-1999 12:00 AM
O SiO2 1-Jun-1999 12:00 AM
Mg MgO 1-Jun-1999 12:00 AM
Al Al2O3 1-Jun-1999 12:00 AM
Si SiO2 1-Jun-1999 12:00 AM
K MAD-10 Feldspar 1-Jun-1999 12:00 AM
Ca Wollastonite 1-Jun-1999 12:00 AM
Fe Fe 1-Jun-1999 12:00 AM

Element	Weight%	Atomic%
C K	15.35	23.46
O K	47.60	54.62
Mg K	1.08	0.82
Al K	2.89	1.97
Si K	24.67	16.12
K K	0.74	0.35
Ca K	1.14	0.52
Fe L	6.52	2.14
Totals	100.00	

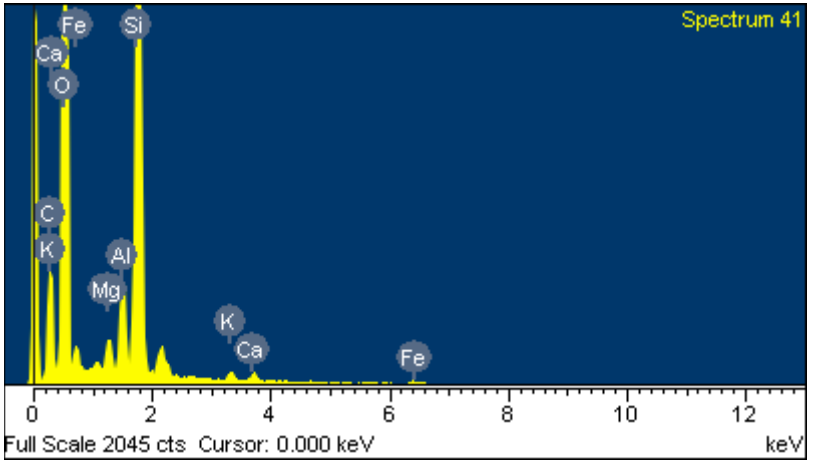

Comment: Sample 4C9: Ferromagnesium silicates, clay minerals, possible iron oxides, and possibly silica .

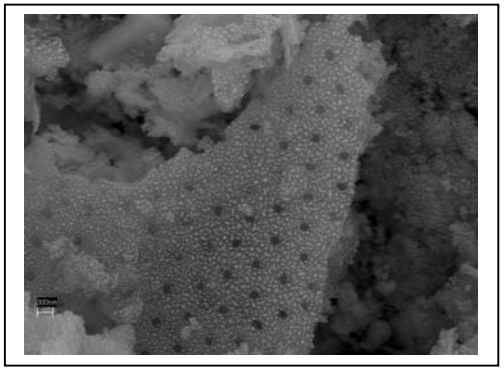

Spectrum processing :
No peaks omitted

Processing option : All elements analyzed (Normalised)
Number of iterations = 3

Standard :
O SiO2 1-Jun-1999 12:00 AM
Na Albite 1-Jun-1999 12:00 AM
Mg MgO 1-Jun-1999 12:00 AM
Al Al2O3 1-Jun-1999 12:00 AM
Si SiO2 1-Jun-1999 12:00 AM
K MAD-10 Feldspar 1-Jun-1999 12:00 AM
Fe Fe 1-Jun-1999 12:00 AM
Au Au 1-Jun-1999 12:00 AM

Element	Weight%	Atomic%
O K	45.29	66.78
Na K	1.18	1.21
Mg K	0.90	0.87
Al K	7.51	6.57
Si K	21.68	18.21
K K	1.26	0.76
Fe L	9.73	4.11
Au M	12.44	1.49
Totals	100.00	

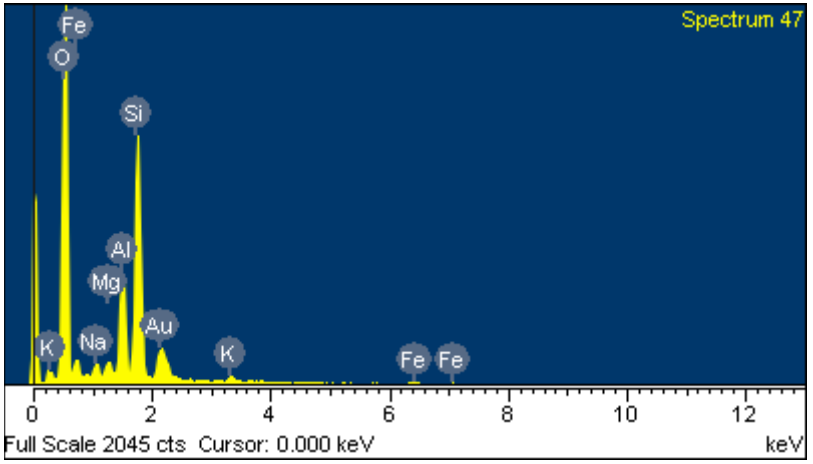

Comment: Sample 4D11: Ferromagnesium silicates, clay minerals, possible iron oxides, and possibly silica. The Au is residual adhesive spray.

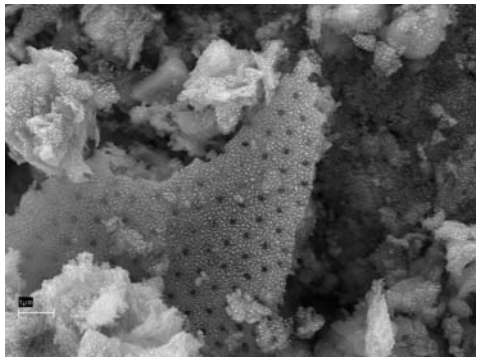

Spectrum processing :
Peak possibly omitted : 2.142 keV

Processing option : All elements analyzed (Normalised)
Number of iterations = 2

Standard :
C CaCO3 1-Jun-1999 12:00 AM
O SiO2 1-Jun-1999 12:00 AM
Na Albite 1-Jun-1999 12:00 AM
Mg MgO 1-Jun-1999 12:00 AM
Al Al2O3 1-Jun-1999 12:00 AM
Si SiO2 1-Jun-1999 12:00 AM

Element	Weight%	Atomic%
C K	3.86	6.68
O K	38.75	50.38
Na K	1.22	1.11
Mg K	0.98	0.84
Al K	4.45	3.43
Si K	50.73	37.57
Totals	100.00	

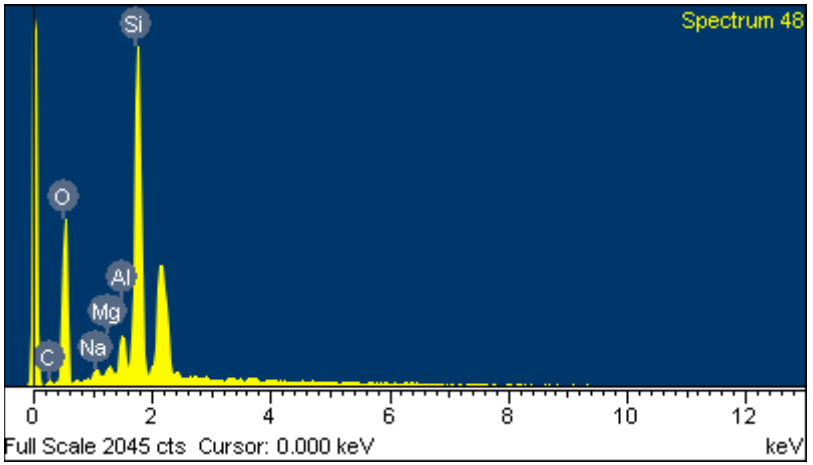

Comment: Sample 4D12 appears to be high in silica, and contain small amounts of aluminum silicate, albite. There is no decision on the high ratio of silicon to oxygen in the sample. This chemical analysis was completed on one of the numerous white ‘spots’ found on the diatom surface seen in 4D11.

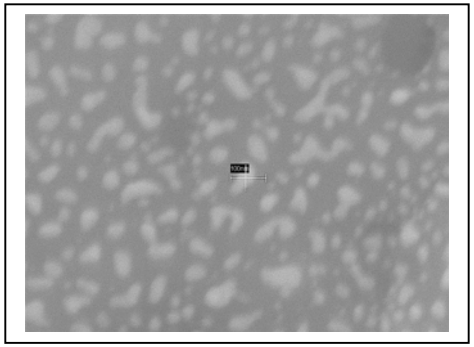

Spectrum processing :
No peaks omitted

Processing option : All elements analyzed (Normalised)
Number of iterations = 3
Standard :
C CaCO3 1-Jun-1999 12:00 AM
O SiO2 1-Jun-1999 12:00 AM
Na Albite 1-Jun-1999 12:00 AM
Mg MgO 1-Jun-1999 12:00 AM
Al Al2O3 1-Jun-1999 12:00 AM
Si SiO2 1-Jun-1999 12:00 AM
S FeS2 1-Jun-1999 12:00 AM
Cl KCl 1-Jun-1999 12:00 AM
K MAD-10 Feldspar 1-Jun-1999 12:00 AM
Ca Wollastonite 1-Jun-1999 12:00 AM
Fe Fe 1-Jun-1999 12:00 AM

Element	Weight %	Atomic%
C K	3.22	5.37
O K	52.82	66.12
Na K	4.19	3.65
Mg K	1.12	0.92
Al K	5.92	4.39
Si K	18.48	13.18
S K	2.08	1.30
Cl K	0.56	0.32
K K	1.01	0.51
Ca K	3.02	1.51
Fe L	7.57	2.71
Totals	100.00	

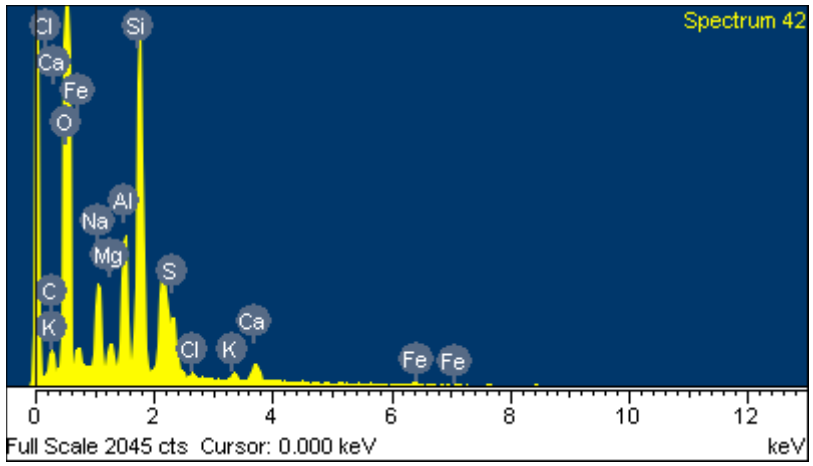

Comment: Sample 4D2: Ferromagnesium silicates, clay minerals, possible iron oxides, calcium carbonate, some silica, and what appears to be residual chlorite from mica (a Ferromagnesium not seen in other samples).

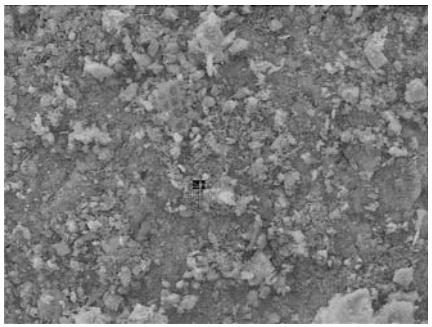

Spectrum processing :
Peak possibly omitted : 2.141 keV

Processing option : All elements analyzed (Normalised)
Number of iterations = 3

Standard :
C CaCO3 1-Jun-1999 12:00 AM
O SiO2 1-Jun-1999 12:00 AM
Al Al2O3 1-Jun-1999 12:00 AM
Si SiO2 1-Jun-1999 12:00 AM
Fe Fe 1-Jun-1999 12:00 AM

Element	Weight%	Atomic%
C K	2.39	4.07
O K	51.15	65.32
Al K	5.21	3.95
Si K	32.03	23.30
Fe L	9.22	3.37
Totals	100.00	

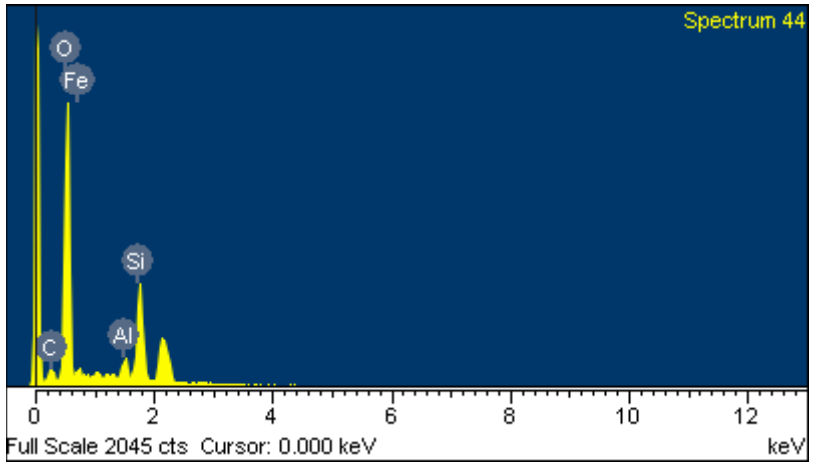

Comment: Sample 4D4 appears to be primarily silica and iron oxides.

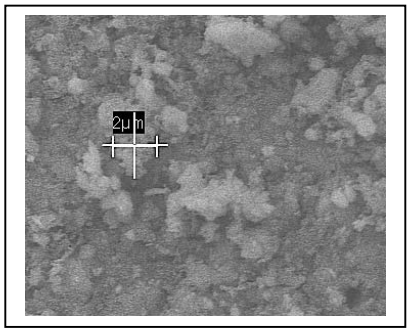

Spectrum processing :
Peak possibly omitted : 2.139 keV

Processing option : All elements analyzed (Normalised)
Number of iterations = 3

Standard :
C CaCO3 1-Jun-1999 12:00 AM
O SiO2 1-Jun-1999 12:00 AM
Na Albite 1-Jun-1999 12:00 AM
Mg MgO 1-Jun-1999 12:00 AM
Al Al2O3 1-Jun-1999 12:00 AM
Si SiO2 1-Jun-1999 12:00 AM
K MAD-10 Feldspar 1-Jun-1999 12:00 AM
Fe Fe 1-Jun-1999 12:00 AM

Element	Weight%	Atomic%
C K	1.16	2.02
O K	48.94	63.89
Na K	1.77	1.61
Mg K	1.35	1.16
Al K	7.73	5.98
Si K	28.36	21.09
K K	1.55	0.83
Fe L	9.14	3.42
Totals	100.00	

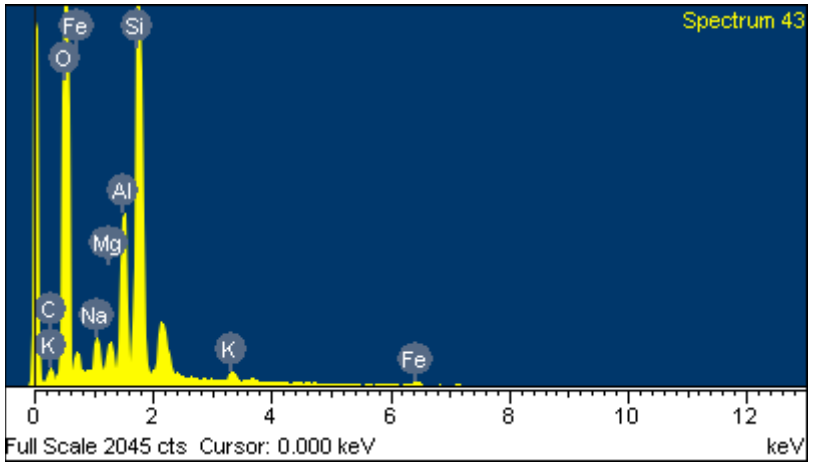

Comment: Sample 4D4: Ferromagnesium silicates, clay minerals, possible iron oxides, and possibly silica.

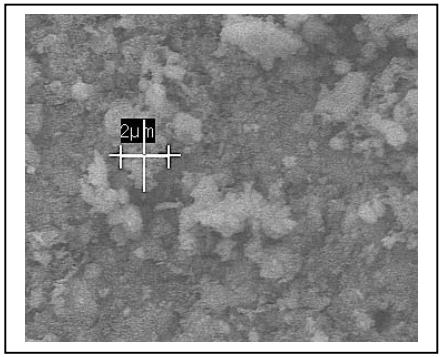

Spectrum processing :
Peak possibly omitted : 2.142 keV

Processing option : All elements analyzed (Normalised)
Number of iterations = 3

Standard :
C CaCO3 1-Jun-1999 12:00 AM
O SiO2 1-Jun-1999 12:00 AM
Na Albite 1-Jun-1999 12:00 AM
Mg MgO 1-Jun-1999 12:00 AM
Al Al2O3 1-Jun-1999 12:00 AM
Si SiO2 1-Jun-1999 12:00 AM
Ca Wollastonite 1-Jun-1999 12:00 AM
Fe Fe 1-Jun-1999 12:00 AM

Element	Weight%	Atomic%
C K	8.60	13.77
O K	52.78	63.43
Na K	1.32	1.10
Mg K	1.97	1.56
Al K	5.04	3.59
Si K	13.85	9.48
Ca K	10.43	5.00
Fe L	6.01	2.07
Totals	100.00	

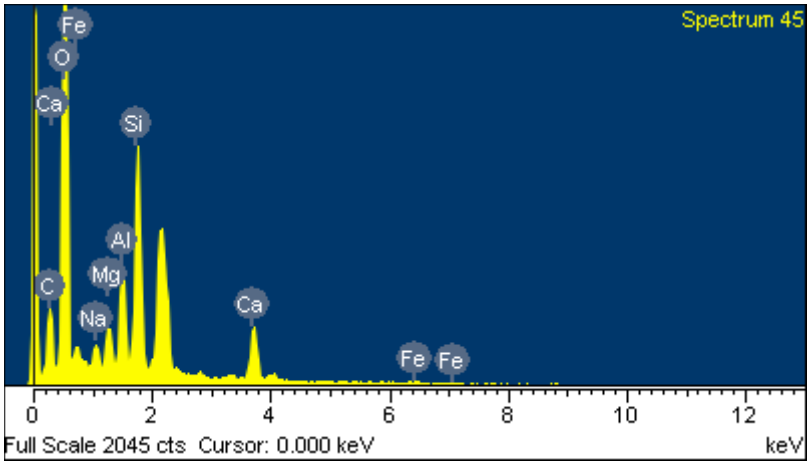

Comment: Sample 4D5: Ferromagnesium silicates, clay minerals, calcium carbonate, and possibly silica.

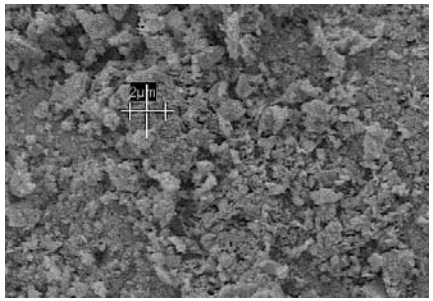

Spectrum processing :
Peaks possibly omitted : 2.149, 3.340, 3.720 keV

Processing option : All elements analyzed (Normalised)
Number of iterations = 2

Standard :
O SiO2 1-Jun-1999 12:00 AM
Na Albite 1-Jun-1999 12:00 AM
Al Al2O3 1-Jun-1999 12:00 AM
Si SiO2 1-Jun-1999 12:00 AM

Element	Weight%	Atomic%
O K	40.52	54.29
Na K	1.19	1.11
Al K	3.31	2.63
Si K	54.98	41.97
Totals	100.00	

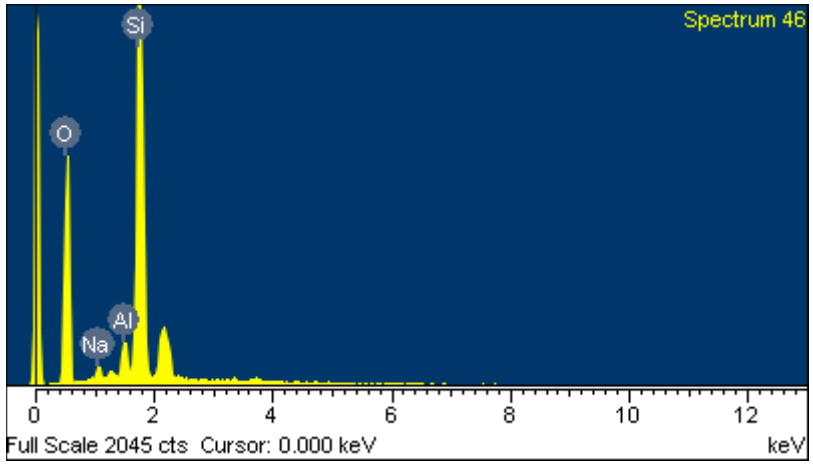

Comment: Sample 4D6 is silica with albite. This may be an indicator to look for other samples with albite.

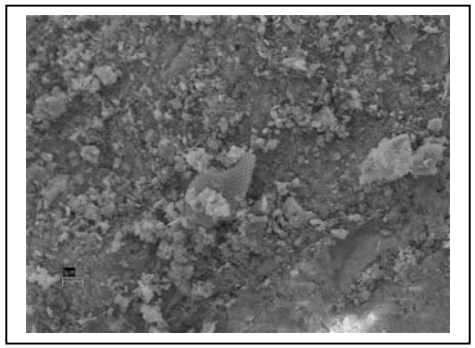

Bodele

17/07/2006 12:04:19

SEM Bulk Chemical Analyses

Element	Weight %	Atomic %	Element	Weight %	Atomic %
Oxygen	48.6	66.36	Silicon	14.43	11.22
Oxygen Total	48.6	66.36	**Silicon Total**	14.43	11.22
	38.46	41.42		18.42	11.3
	48.58	59.41		33.89	23.61
	39.22	38.24		17.15	9.53
	48.34	63.09		28.84	21.44
	48.51	57.83		20.49	13.91
	38.65	39.18		14.14	8.17
	38.39	36.47		14.25	7.71
	49.64	61		31.21	21.85
	52.36	65.99		33.09	23.75
	28.36	28.11		14.94	8.44
	57.72	66.97		10.44	6.9
	53.84	67.48		23.66	16.89
	49.66	64.57		22.18	16.43
	45.81	62.67		21.27	16.57
	39.22	38.24		17.15	9.53
	30.1	27.74		10.12	5.31
	44.77	58.78		33.48	23.02
	25.21	30.43		23.14	16.59
	50.43	63.45		30.84	23.35
	45.81	60.88		33.48	23.02
	25.21	30.43		17.43	11.17
	47.45	53.37		24.67	16.12
	47.6	54.62		21.68	18.21
	45.29	66.78		50.73	37.57
	38.75	50.38		27.53	17.86
	48.66	55.41		35.19	25.51
	49.48	62.97		28.36	21.09
	48.94	63.89		13.85	9.48
	52.78	63.43		54.98	41.97
	40.52	54.69		18.48	13.18
	52.82	66.12		32.03	23.3
	51.15	65.32		15.65	8.74
	37.9	37.15		3.68	2.94
	42.52	59.73		35.57	24.94
	56.4	69.41		30.17	19.13
	42.15	46.93		58.65	39.79
	13.64	16.25		11.24	6.1
	33.81	32.24		26.72	16.33
	57.71	61.91		0.67	0.4
	40.53	56.44		24.84	21.98
	33.29	34.87		24.16	17.78
	43.92	68.21		29.25	22.67
	48.83	63.09	**Grand Total**	1052.14	734.8
	46.29	62.99			
Grand Total	1967.32	2394.94			

SEM Bulk Chemical Analyses

Element	Weight %	Atomic %	Element	Weight %	Atomic %
Aluminum	9.65	7.81	Sodium	1.95	1.77
Aluminum Total	9.65	7.81	**Sodium Total**	1.95	1.77
	0.94	0.6		0.68	0.57
	0.77	0.45		0.49	0.35
	8.93	6.91		0.55	0.47
	5.24	3.71		3.16	2.77
	4.35	2.61		0.9	0.73
	0.63	0.35		1.13	0.99
	4.41	3.22		1.28	1.16
	6.99	5.22		0.66	0.63
	5.44	3.2		1.28	1.17
	2.24	1.54		0.64	0.56
	6.02	4.48		0.55	0.51
	8.35	6.44		0.8	0.63
	9.23	7.49		1.18	1.21
	0.77	0.45		1.22	1.11
	0.67	0.37		0.81	0.72
	9.77	6.99		1.77	1.61
	8.41	6.27		1.32	1.1
	1.35	1.06		1.19	1.11
	9.77	6.99		4.19	3.65
	5.24	3.49		1.2	1.17
	2.89	1.97		0.58	0.5
	7.51	6.57		0.61	0.41
	4.45	3.43		0.83	0.8
	2.67	1.8		0.72	0.52
	5.91	4.46		0.54	0.58
	7.73	5.98		1.21	1.09
	5.04	3.59		1.11	1.05
	3.31	2.63	**Grand Total**	32.55	28.94
	5.92	4.39			
	5.31	3.95			
	0.32	0.18			
	0.88	0.73			
	2.03	1.48			
	2.68	1.77			
	2.42	1.37			
	0.64	0.41			
	3.77	3.47			
	5.93	4.55			
	7.38	5.96			
Grand Total	185.96	138.34			

SEM Bulk Chemical Analyses

Element	Weight %	Atomic %	Element	Weight %	Atomic %
Iron	2.49	0.77	Potasium	1.87	1
Iron Total	2.49	0.77	**Potasium Total**	1.87	1
	3.82	1.07		0.71	0.35
	6.69	2.5		0.82	0.34
	8.41	2.87		0.91	0.46
	5.75	1.67		4.41	2.27
	3.69	1		0.91	0.37
	5.71	2.01		0.79	0.4
	2.38	0.68		1.38	0.73
	8.67	3.11		1.09	0.61
	11.95	4.45		2.22	1.09
	6.79	2.66		0.89	0.46
	3.82	1.07		2.22	1.09
	1.21	0.42		0.92	0.42
	10.53	3.79		0.74	0.35
	3.42	1.3		1.26	0.76
	1.21	0.42		0.9	0.42
	7.45	2.4		0.83	0.43
	6.52	2.14		1.55	0.83
	9.73	4.11		1.01	0.51
	5.2	1.7		0.76	0.35
	4.83	1.76		0.77	0.3
	9.14	3.42		0.86	0.55
	6.01	2.07		1	0.53
	7.57	2.71		2.23	1.24
	9.22	3.37	**Grand Total**	31.05	15.86
	12.3	4.95			
	3.86	1.36			
	3.46	1.1			
	3.82	1.04			
	6.03	2.68			
	13.8	5.11			
	12.3	4.8			
Grand Total	207.78	74.51			

SEM Bulk Chemical Analyses

Element	Weight %	Atomic %	Element	Weight %	Atomic %
Calcium	18.38	8.51	Magnesium	1.12	0.92
			Magnesium Total	1.12	0.92
Calcium Total	18.38	8.51		1.47	0.96
	1.25	0.62		0.77	0.59
	30.49	15.98		2.03	1.68
	3.64	1.76		3.17	2.72
	3.64	1.76		2.29	2.06
	1.17	0.53		0.42	0.36
	1.14	0.52		3.75	2.98
	10.43	5		1.29	1.07
	0.87	0.43		3.75	2.98
	3.38	1.34		1.7	1.26
	3.02	1.51		1.08	0.82
	1.01	0.39		0.9	0.87
	24.45	13.71		0.98	0.84
	1.32	0.5		1.03	0.86
	35.5	19.73		2.96	2.54
	19.83	8.29		5.68	4.45
Grand Total	159.52	80.58		1.35	1.16
				1.97	1.56
				0.92	0.61
				0.47	0.38
				0.31	0.25
				0.39	0.29
				0.62	0.39
				0.99	0.84
				1.44	1.29
			Grand Total	42.85	34.73
			Titanium	25.75	11.74
			Fluorine	4.59	5.07
				2.61	3.06
				1.82	1.61
			Grand Total	9.02	9.74
			Chlorine	0.56	0.32
			Sulfur	2.08	1.3
			Phosphorous	15.96	11.48
				12.73	8.63
				9.85	7.15
				7.73	4.18
			Grand Total	46.27	31.44

APPENDIX D

SEM IMAGES FOR BULK SAMPLES

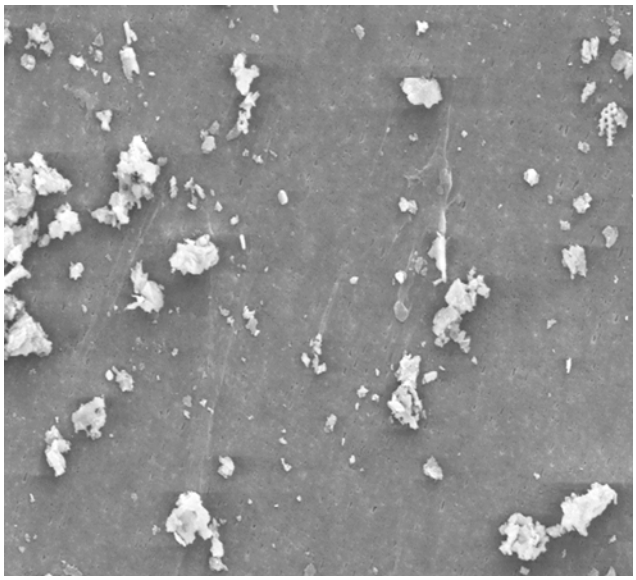

SEM Bodele bulk sample 1A1: Bar scale 300 μm Random scan for chemical analysis

Scanning Electron Microscope: The primary performance specification for the FESEM is resolution. Point-to-point resolution is 1 nm at an accelerating voltage of 30 kV and 4 nm at 1.0 kV.

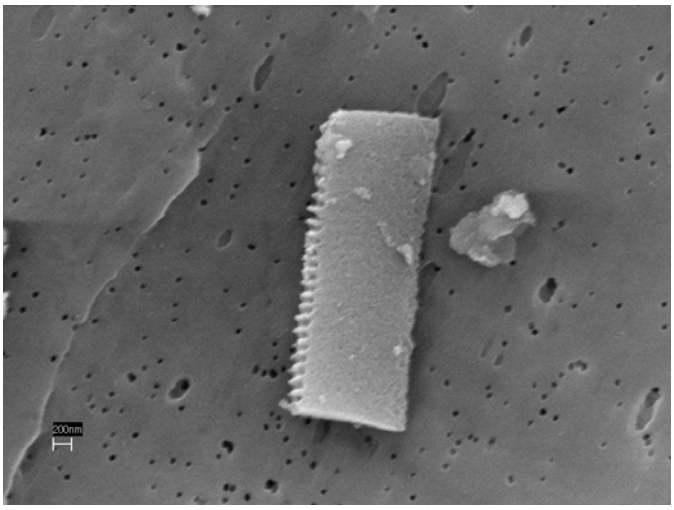

SEM Bodele bulk sample 1A2: Bar scale 200 nm

Scanning Electron Microscope: The primary performance specification for the FESEM is resolution. Point-to-point resolution is 1 nm at an accelerating voltage of 30 kV and 4 nm at 1.0 kV.

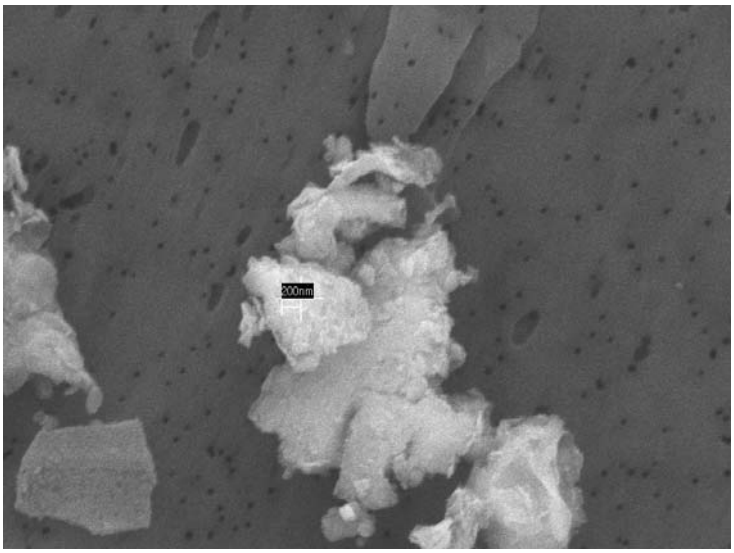

SEM Bodele bulk sample 1A3: Bar scale 200nm

Scanning Electron Microscope: The primary performance specification for the FESEM is resolution. Point-to-point resolution is 1 nm at an accelerating voltage of 30 kV and 4 nm at 1.0 kV.

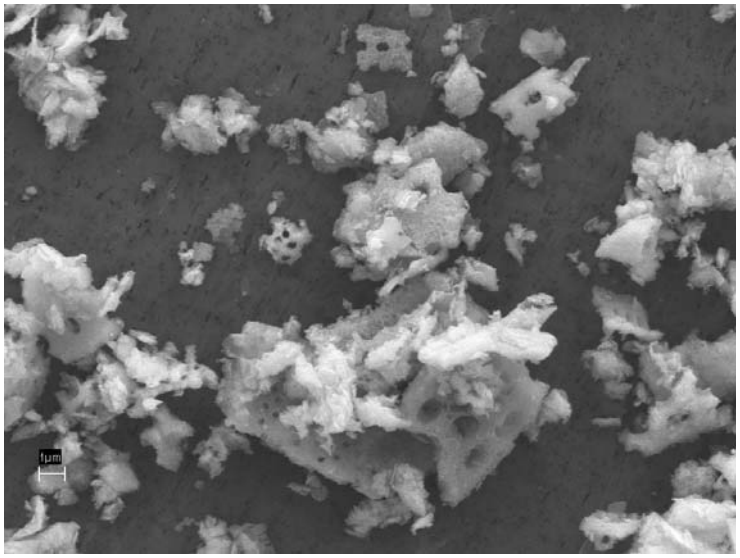

SEM Bodele bulk sample 1A4: Bar scale 1µm

Scanning Electron Microscope: The primary performance specification for the FESEM is resolution. Point-to-point resolution is 1 nm at an accelerating voltage of 30 kV and 4 nm at 1.0 kV.

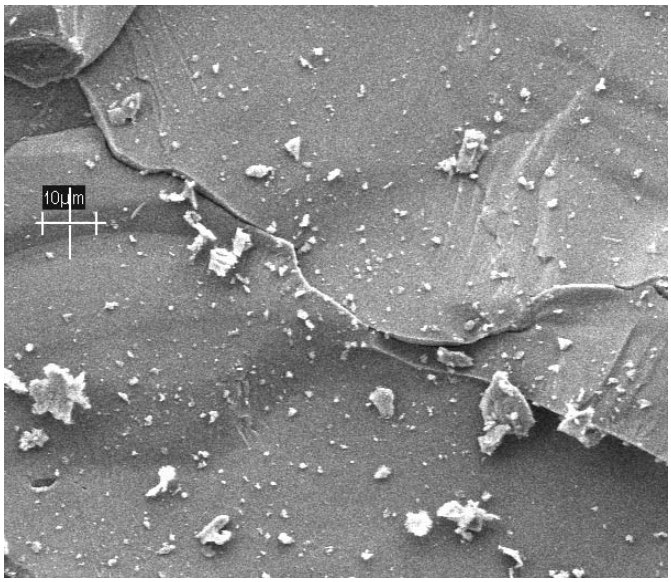

SEM Bodele bulk sample 1B: Bar scale 10 µm

Scanning Electron Microscope: The primary performance specification for the FESEM is resolution. Point-to-point resolution is 1 nm at an accelerating voltage of 30 kV and 4 nm at 1.0 kV.

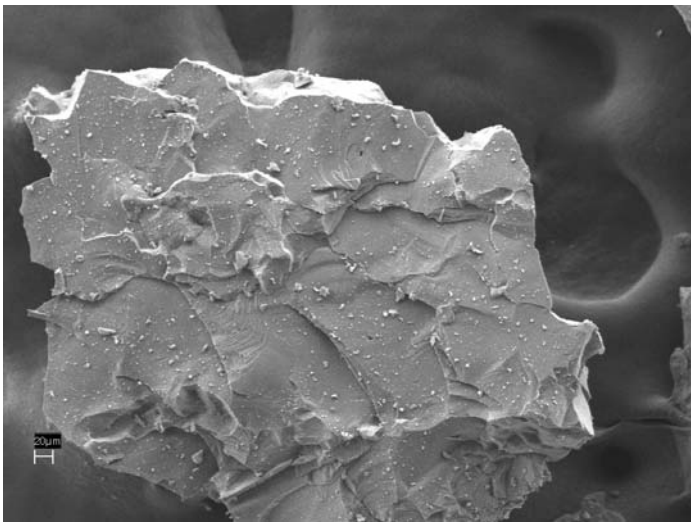

SEM Gross Sample Bodele bulk 1B2: Bar scale 20µm

Scanning Electron Microscope: The primary performance specification for the FESEM is resolution. Point-to-point resolution is 1 nm at an accelerating voltage of 30 kV and 4 nm at 1.0 kV.

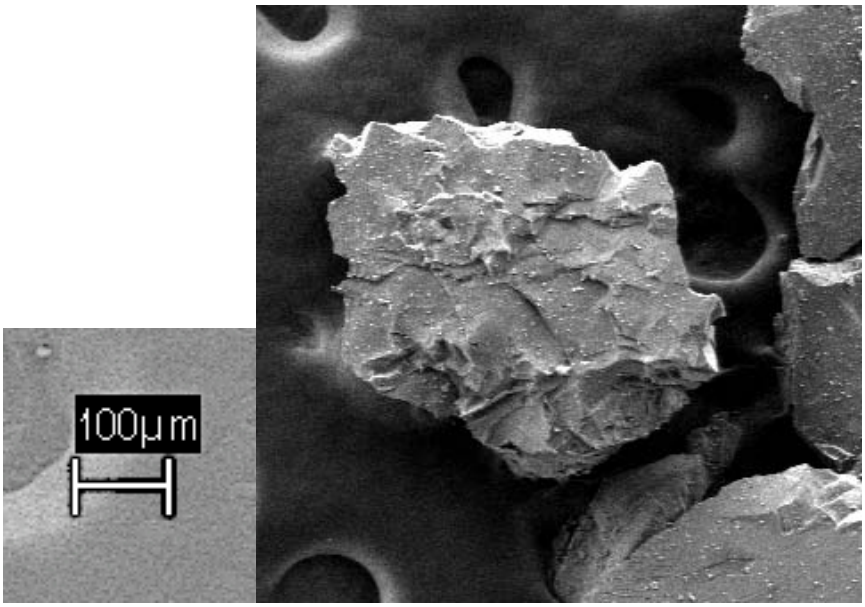

SEM Bodele bulk sample 1B3: Bar scale 100µm

Scanning Electron Microscope: The primary performance specification for the FESEM is resolution. Point-to-point resolution is 1 nm at an accelerating voltage of 30 kV and 4 nm at 1.0 kV.

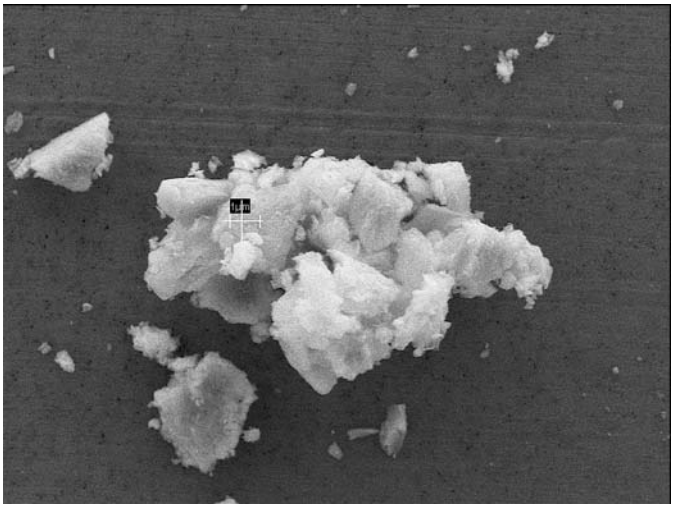

SEM Bodele bulk sample 1C1: Bar scale 1µm

Scanning Electron Microscope: The primary performance specification for the FESEM is resolution. Point-to-point resolution is 1 nm at an accelerating voltage of 30 kV and 4 nm at 1.0 kV.

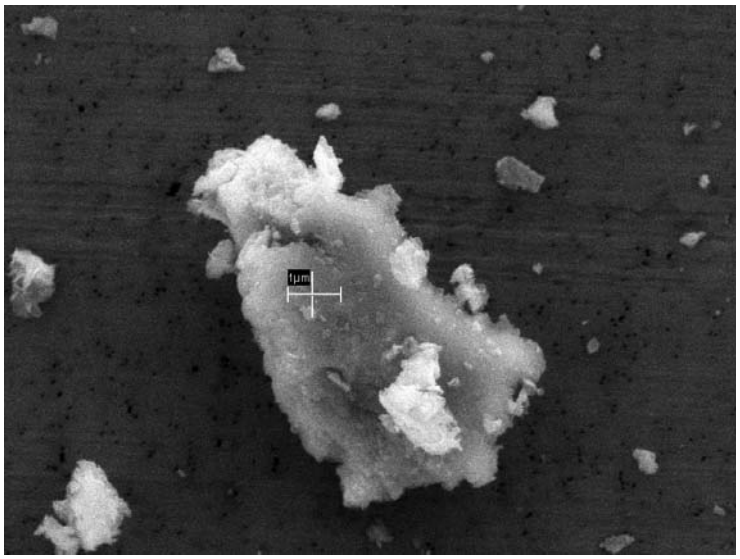

SEM Bodele bulk sample 1C2: Bar scale 1μm

Scanning Electron Microscope: The primary performance specification for the FESEM is resolution. Point-to-point resolution is 1 nm at an accelerating voltage of 30 kV and 4 nm at 1.0 kV.

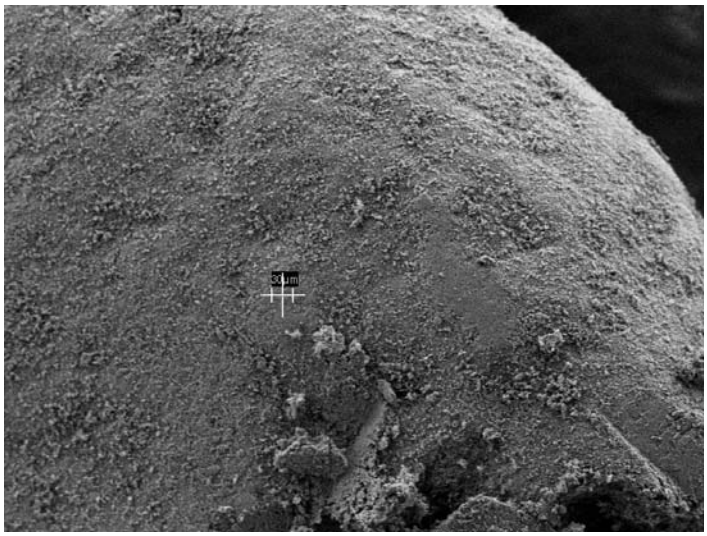

SEM Bodele bulk sample 1D1: Bar scale 30 μm

Scanning Electron Microscope: The primary performance specification for the FESEM is resolution. Point-to-point resolution is 1 nm at an accelerating voltage of 30 kV and 4 nm at 1.0 kV.

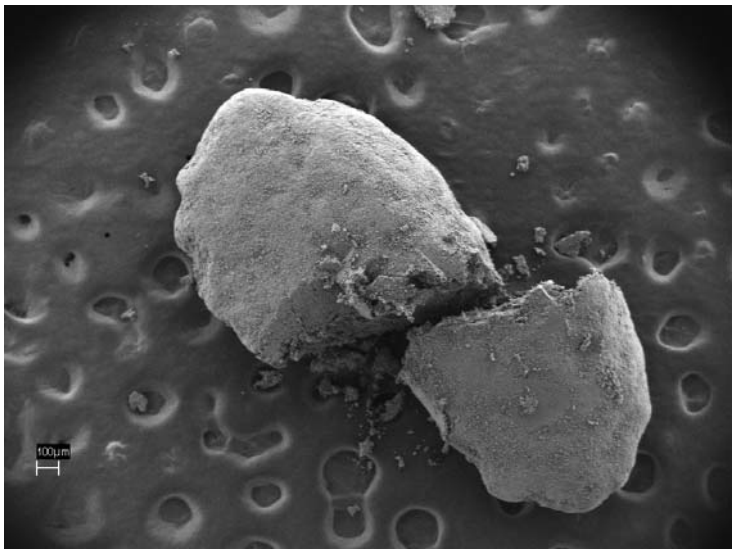

SEM Bodele bulk sample 1D2: Bar scale 100µm

Scanning Electron Microscope: The primary performance specification for the FESEM is resolution. Point-to-point resolution is 1 nm at an accelerating voltage of 30 kV and 4 nm at 1.0 kV.

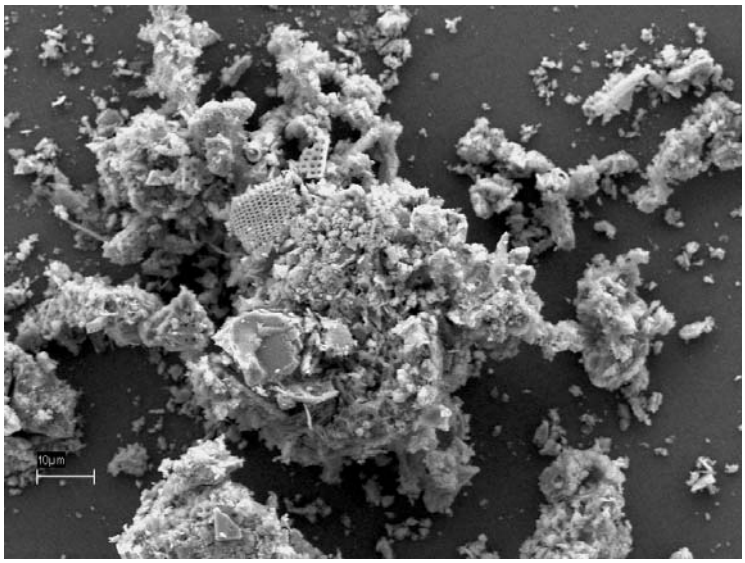

SEM Bodele bulk sample 2A3: Bar scale 10µm

Scanning Electron Microscope: The primary performance specification for the FESEM is resolution. Point-to-point resolution is 1 nm at an accelerating voltage of 30 kV and 4 nm at 1.0 kV.

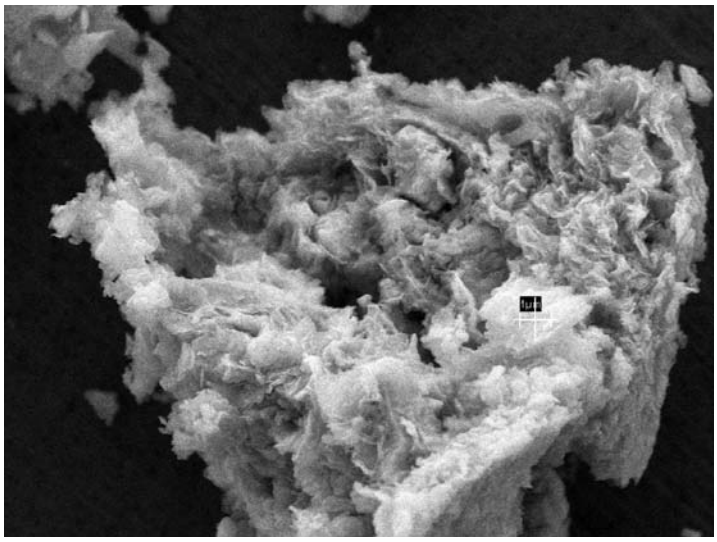

SEM sample Bodele bulk 2B2: Bar scale 1μm

Scanning Electron Microscope: The primary performance specification for the FESEM is resolution. Point-to-point resolution is 1 nm at an accelerating voltage of 30 kV and 4 nm at 1.0 kV.

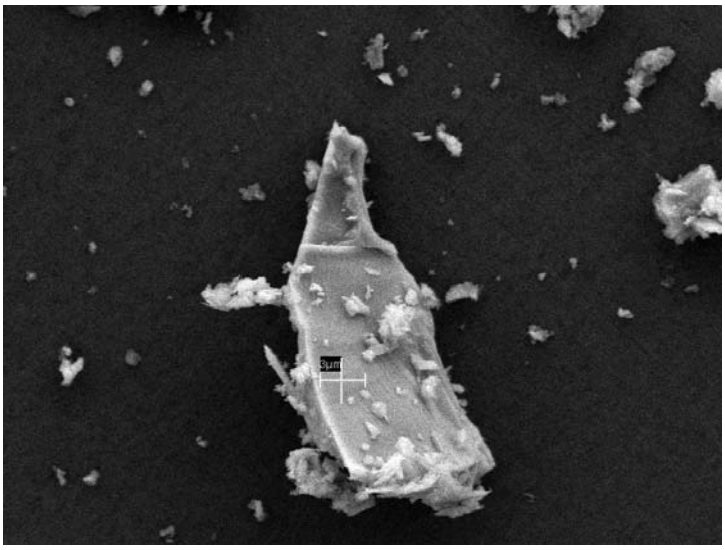

SEM sample Bodele bulk 2B3: Bar scale 3μm: Believed to be cosmic silicon

Scanning Electron Microscope: The primary performance specification for the FESEM is resolution. Point-to-point resolution is 1 nm at an accelerating voltage of 30 kV and 4 nm at 1.0 kV.

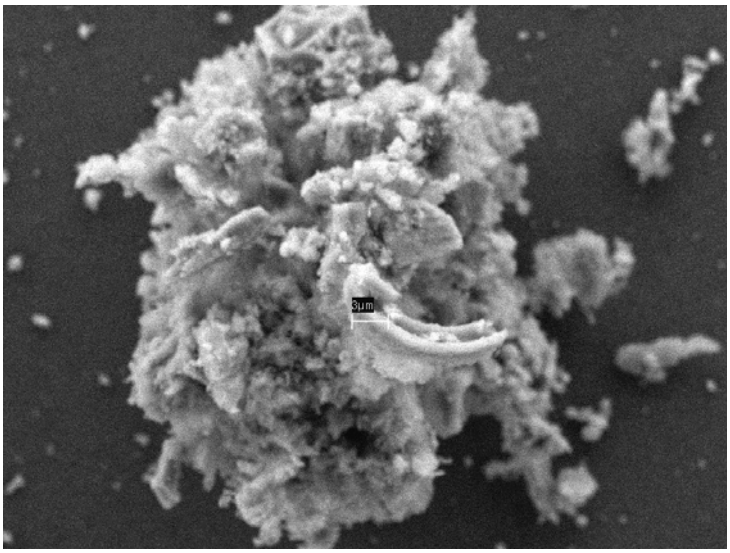

SEM sample Bodele bulk 2C3: Bar scale 3µm

Scanning Electron Microscope: The primary performance specification for the FESEM is resolution. Point-to-point resolution is 1 nm at an accelerating voltage of 30 kV and 4 nm at 1.0 kV.

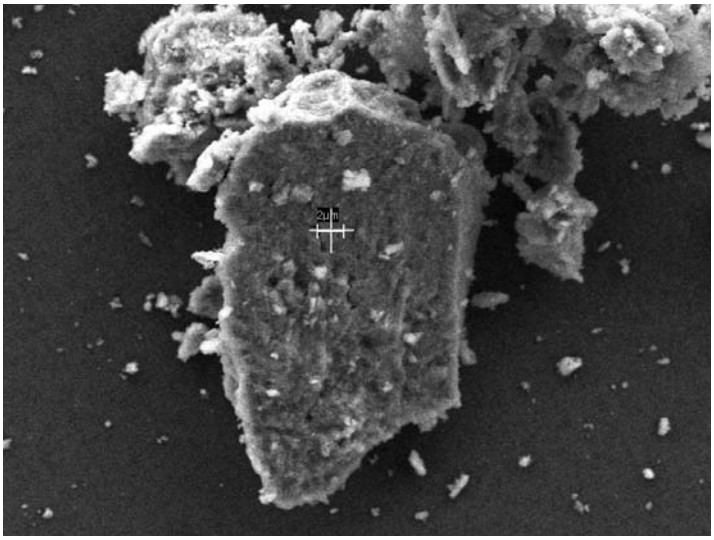

SEM sample Bodele bulk 2C4: Bar scale 2µm

Scanning Electron Microscope: The primary performance specification for the FESEM is resolution. Point-to-point resolution is 1 nm at an accelerating voltage of 30 kV and 4 nm at 1.0 kV.

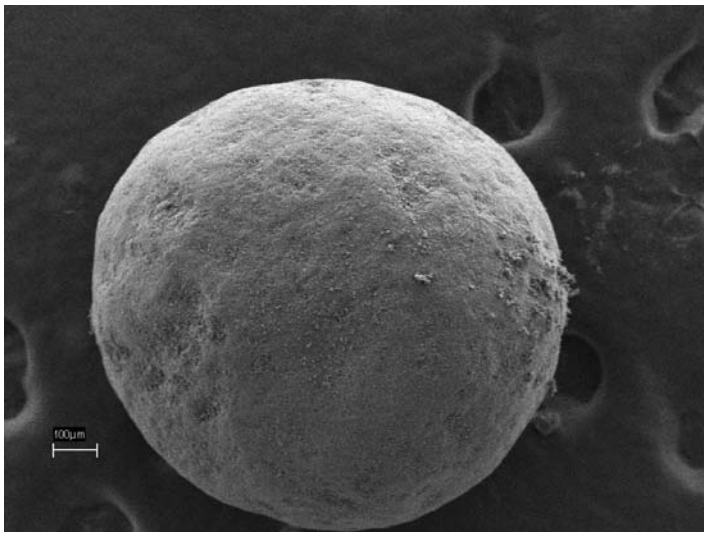

SEM sample Bodele bulk 2D1: Bar scale 100 μm chemical analysis tossed

Scanning Electron Microscope: The primary performance specification for the FESEM is resolution. Point-to-point resolution is 1 nm at an accelerating voltage of 30 kV and 4 nm at 1.0 kV.

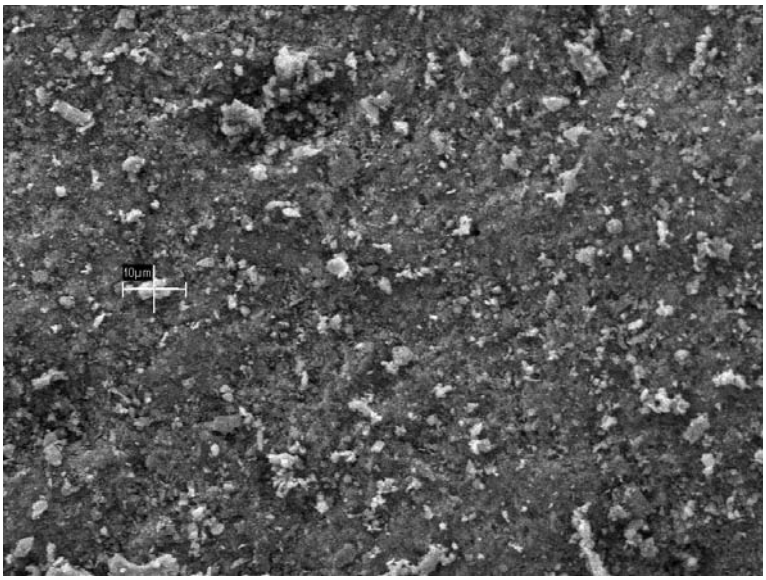

SEM sample Bodele bulk 2D2: Bar scale 10 μm

Scanning Electron Microscope: The primary performance specification for the FESEM is resolution. Point-to-point resolution is 1 nm at an accelerating voltage of 30 kV and 4 nm at 1.0 kV.

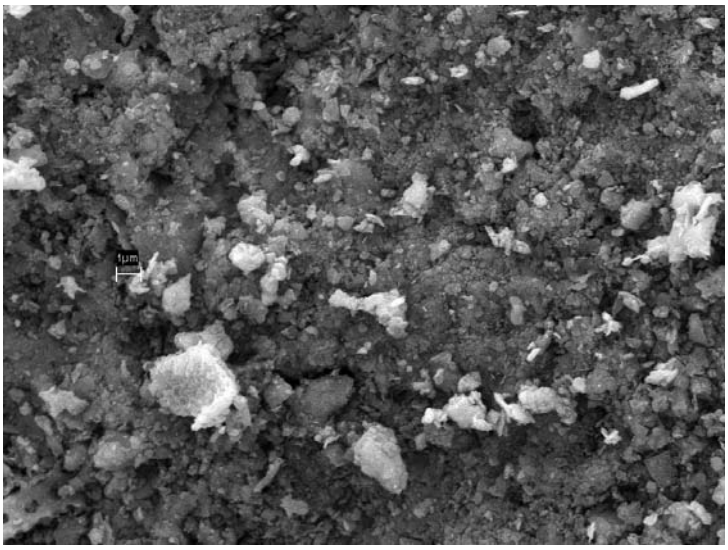

SEM sample Bodele bulk 2D3: Bar scale 1 μm

Scanning Electron Microscope: The primary performance specification for the FESEM is resolution. Point-to-point resolution is 1 nm at an accelerating voltage of 30 kV and 4 nm at 1.0 kV.

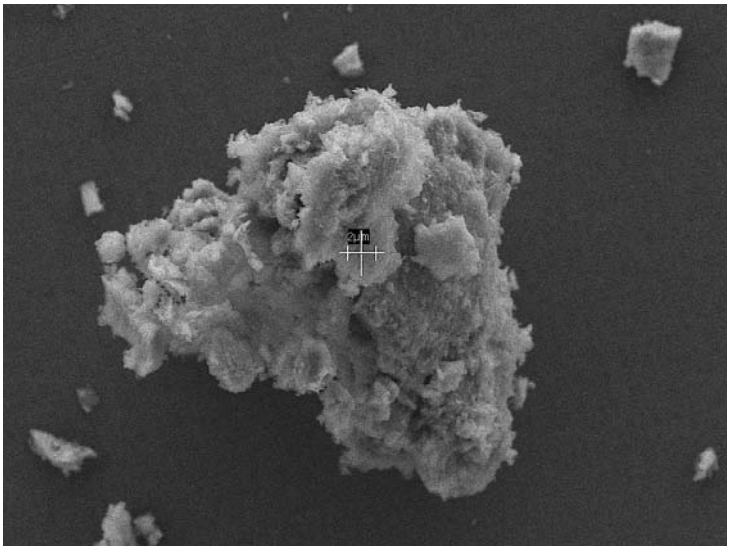

SEM sample Bodele bulk 3A2: Bar scale 2μm

Scanning Electron Microscope: The primary performance specification for the FESEM is resolution. Point-to-point resolution is 1 nm at an accelerating voltage of 30 kV and 4 nm at 1.0 kV.

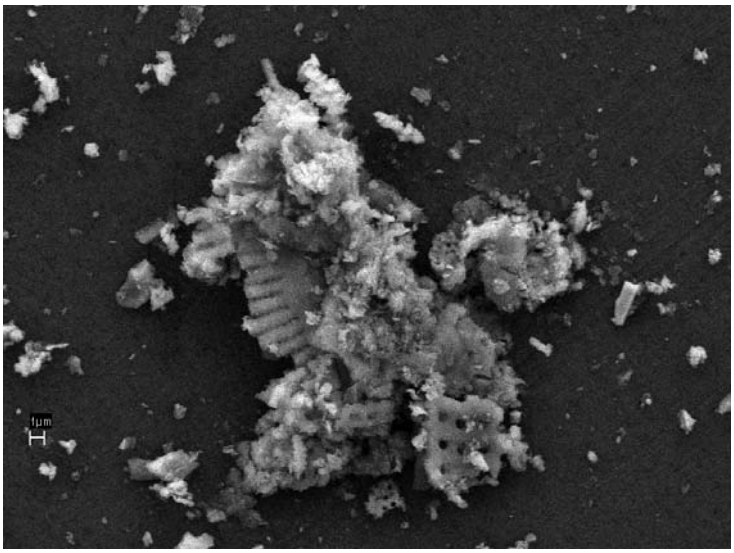

SEM sample Bodele bulk 3B2: Bar scale 1µm

Scanning Electron Microscope: The primary performance specification for the FESEM is resolution. Point-to-point resolution is 1 nm at an accelerating voltage of 30 kV and 4 nm at 1.0 kV.

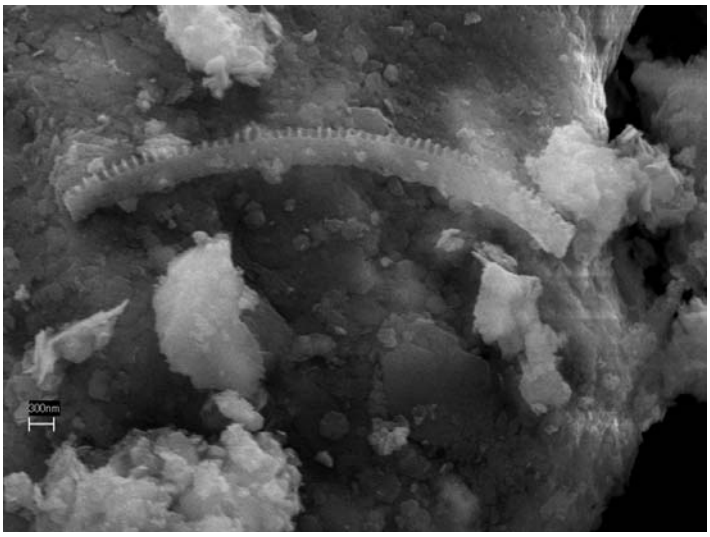

SEM sample Bodele bulk 3B4: Bar scale 300nm

Scanning Electron Microscope: The primary performance specification for the FESEM is resolution. Point-to-point resolution is 1 nm at an accelerating voltage of 30 kV and 4 nm at 1.0 kV.

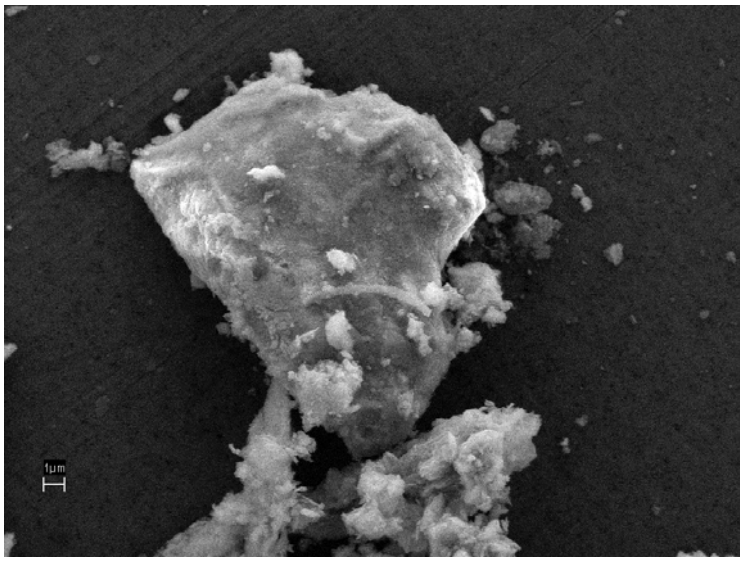

SEM sample Bodele bulk 3B5: Bar scale 1µm

Scanning Electron Microscope: The primary performance specification for the FESEM is resolution. Point-to-point resolution is 1 nm at an accelerating voltage of 30 kV and 4 nm at 1.0 kV.

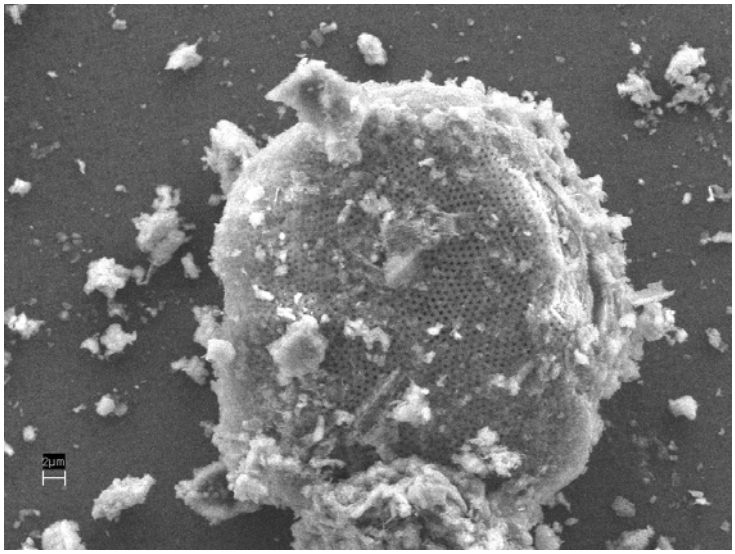

SEM sample Bodele bulk 3C2: Bar scale 2µm

Scanning Electron Microscope: The primary performance specification for the FESEM is resolution. Point-to-point resolution is 1 nm at an accelerating voltage of 30 kV and 4 nm at 1.0 kV.

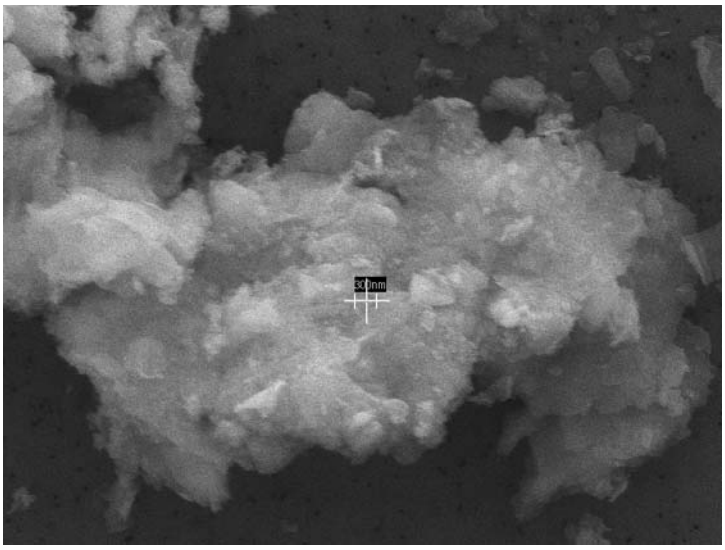

SEM sample Bodele bulk 3C3: Bar scale 300 nm

Scanning Electron Microscope: The primary performance specification for the FESEM is resolution. Point-to-point resolution is 1 nm at an accelerating voltage of 30 kV and 4 nm at 1.0 kV.

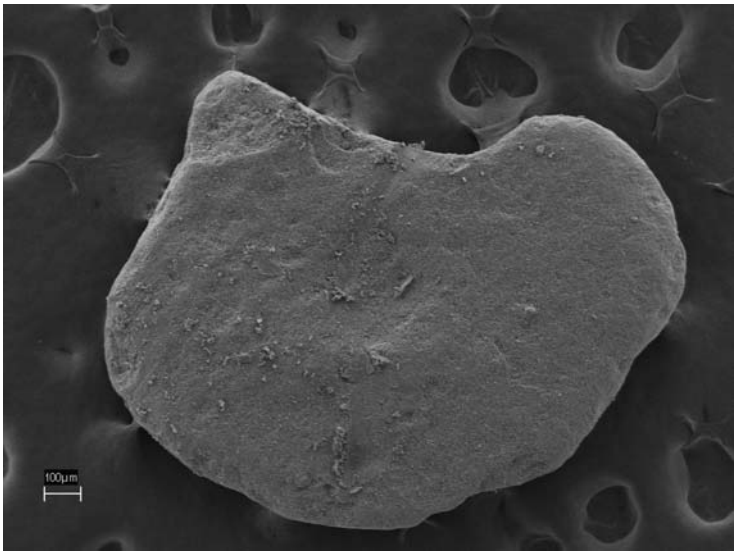

SEM sample Bodele bulk 3D1: Bar scale 100μm

Scanning Electron Microscope: The primary performance specification for the FESEM is resolution. Point-to-point resolution is 1 nm at an accelerating voltage of 30 kV and 4 nm at 1.0 kV.

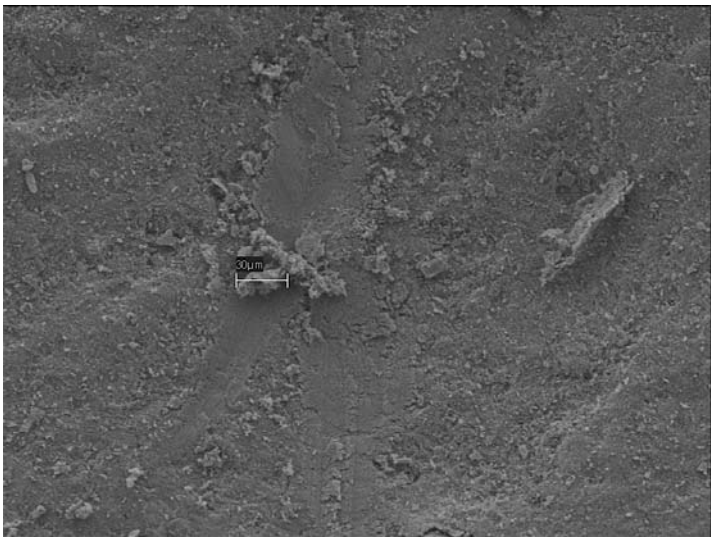

SEM sample Bodele bulk 3D2: Bar scale 30µm

Scanning Electron Microscope: The primary performance specification for the FESEM is resolution. Point-to-point resolution is 1 nm at an accelerating voltage of 30 kV and 4 nm at 1.0 kV.

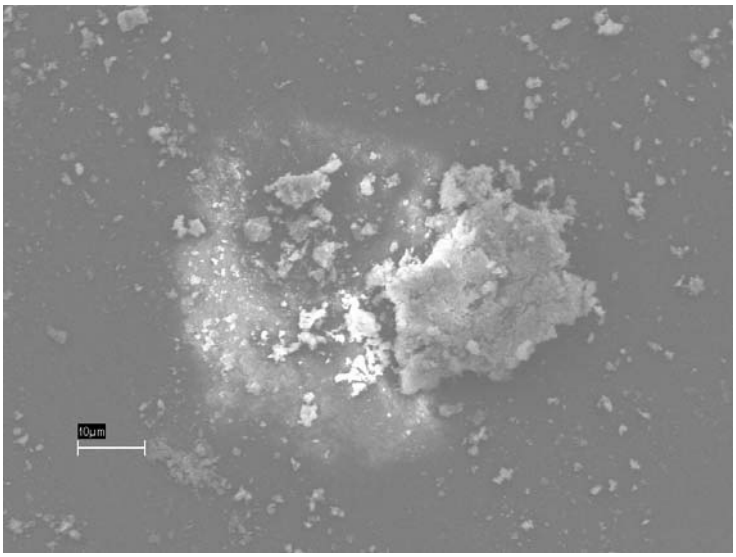

SEM sample Bodele bulk 4A2 and 4A2: Bar scale 10µm

Scanning Electron Microscope: The primary performance specification for the FESEM is resolution. Point-to-point resolution is 1 nm at an accelerating voltage of 30 kV and 4 nm at 1.0 kV.

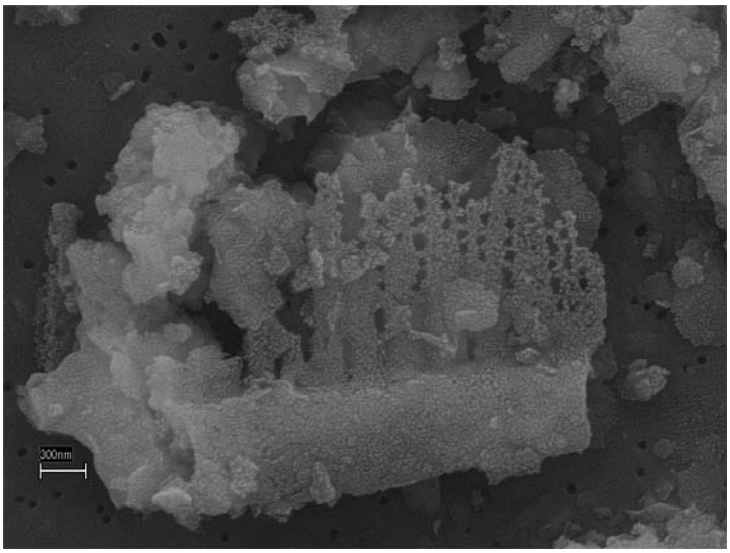

SEM sample Bodele bulk 4A3: Bar scale 300nm

Scanning Electron Microscope: The primary performance specification for the FESEM is resolution. Point-to-point resolution is 1 nm at an accelerating voltage of 30 kV and 4 nm at 1.0 kV.

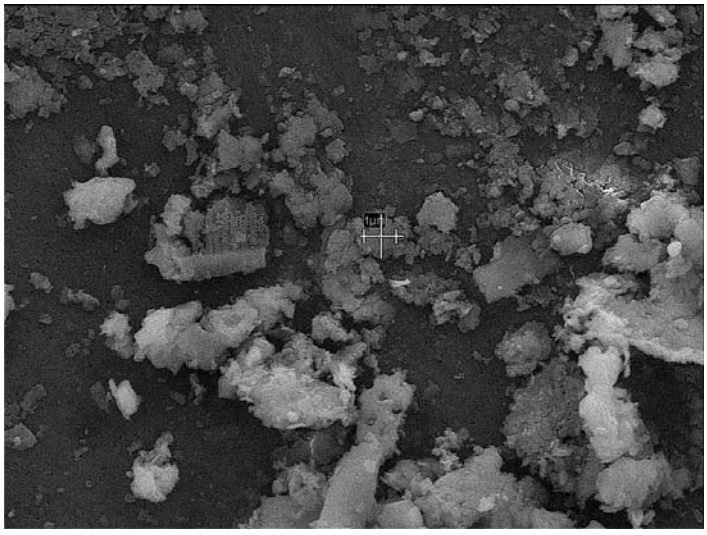

SEM sample Bodele bulk 4A4: Bar scale 1μm

Scanning Electron Microscope: The primary performance specification for the FESEM is resolution. Point-to-point resolution is 1 nm at an accelerating voltage of 30 kV and 4 nm at 1.0 kV.

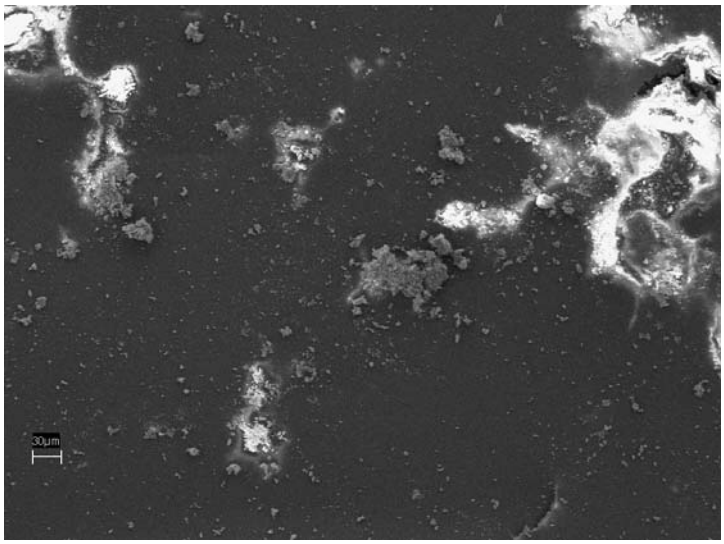

SEM sample Bodele bulk 4B1: Bar scale 30μm Note severe backscatter.

Scanning Electron Microscope: The primary performance specification for the FESEM is resolution. Point-to-point resolution is 1 nm at an accelerating voltage of 30 kV and 4 nm at 1.0 kV.

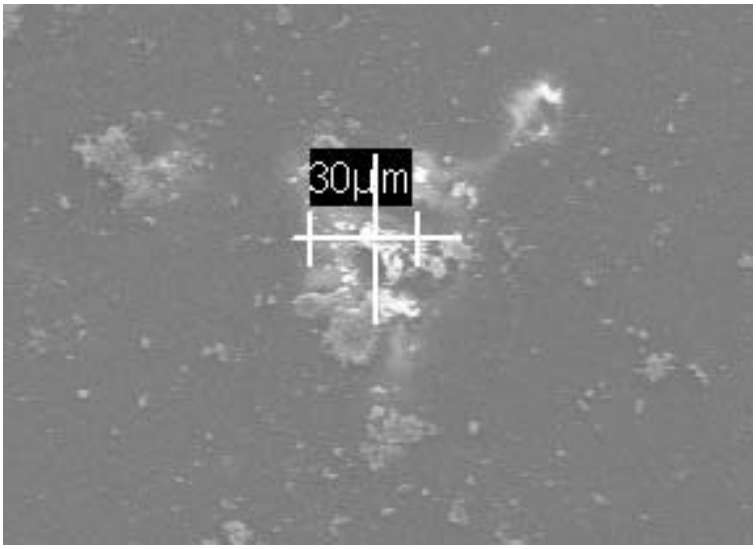

SEM sample Bodele bulk 4B4 and 4B5: Bar scale 30μm Note severe backscatter.

Scanning Electron Microscope: The primary performance specification for the FESEM is resolution. Point-to-point resolution is 1 nm at an accelerating voltage of 30 kV and 4 nm at 1.0 kV.

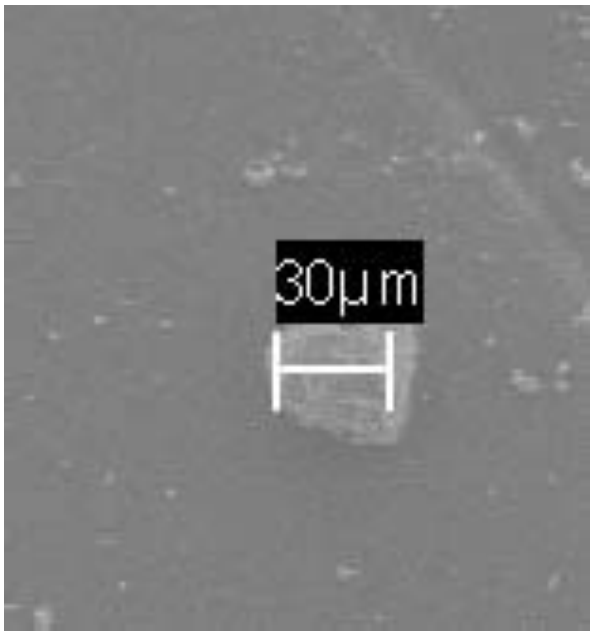

SEM sample Bodele bulk 4C1: Bar scale 30µm

Scanning Electron Microscope: The primary performance specification for the FESEM is resolution. Point-to-point resolution is 1 nm at an accelerating voltage of 30 kV and 4 nm at 1.0 kV.

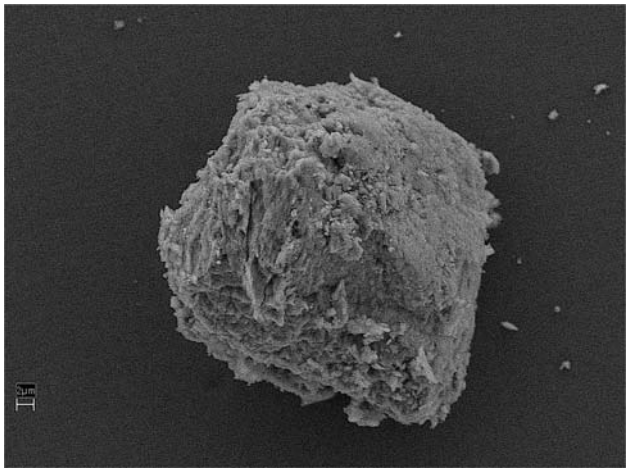

SEM sample Bodele bulk 4C1 and 4C2 (close-up): Bar scale 2µm with randomized scan

Scanning Electron Microscope: The primary performance specification for the FESEM is resolution. Point-to-point resolution is 1 nm at an accelerating voltage of 30 kV and 4 nm at 1.0 kV.

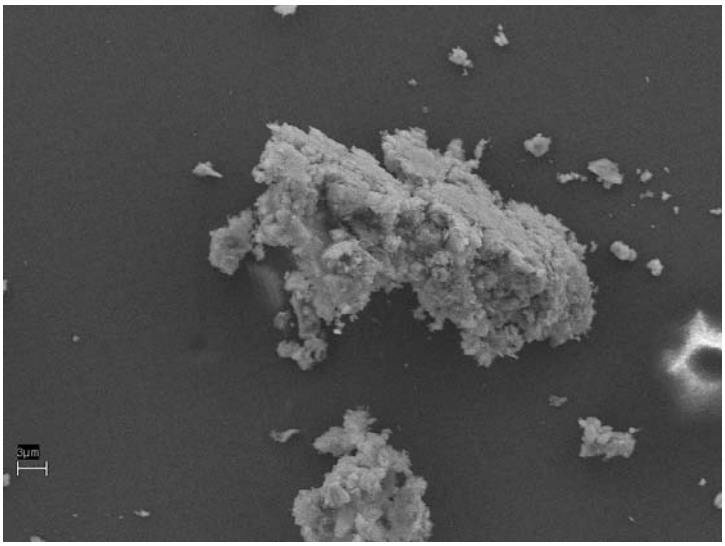

SEM sample Bodele bulk 4C3: Bar scale 3μm

Scanning Electron Microscope: The primary performance specification for the FESEM is resolution. Point-to-point resolution is 1 nm at an accelerating voltage of 30 kV and 4 nm at 1.0 kV.

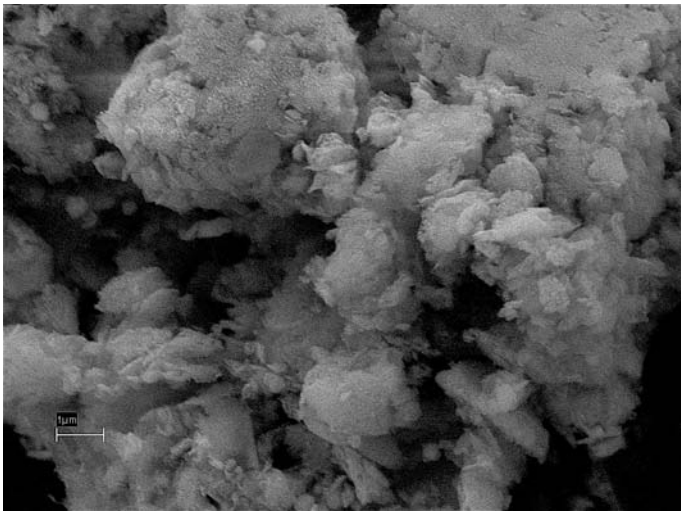

SEM sample Bodele bulk 4C5: Bar scale 1μm

Scanning Electron Microscope: The primary performance specification for the FESEM is resolution. Point-to-point resolution is 1 nm at an accelerating voltage of 30 kV and 4 nm at 1.0 kV.

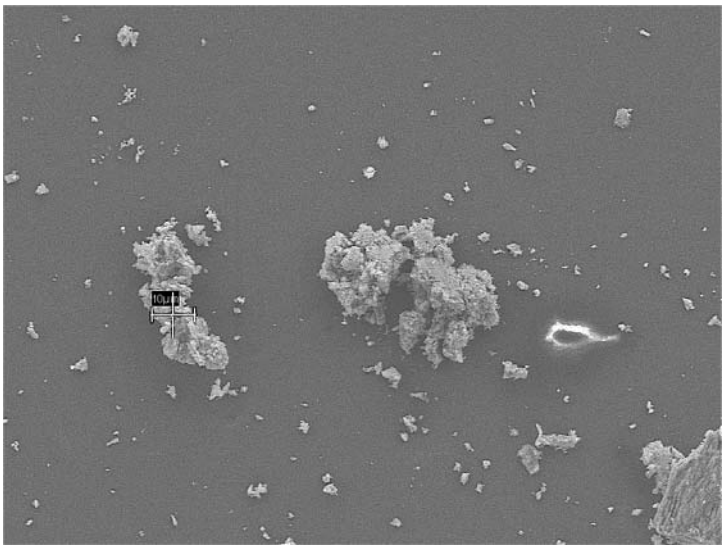

SEM sample Bodele bulk 4C8: Bar scale 10μm Note backscatter.

Scanning Electron Microscope: The primary performance specification for the FESEM is resolution. Point-to-point resolution is 1 nm at an accelerating voltage of 30 kV and 4 nm at 1.0 kV.

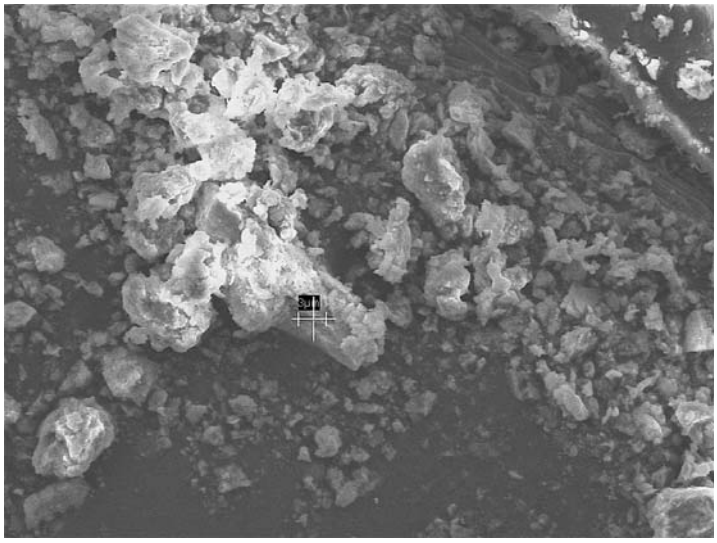

SEM sample Bodele bulk 4C9: Bar scale 3μm Note additional backscatter.

Scanning Electron Microscope: The primary performance specification for the FESEM is resolution. Point-to-point resolution is 1 nm at an accelerating voltage of 30 kV and 4 nm at 1.0 kV.

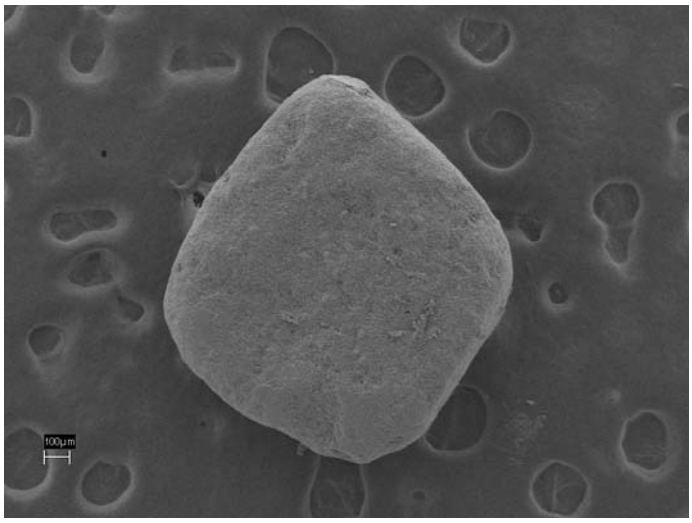

SEM sample Bodele bulk 4D1: Bar scale 100μm

Scanning Electron Microscope: The primary performance specification for the FESEM is resolution. Point-to-point resolution is 1 nm at an accelerating voltage of 30 kV and 4 nm at 1.0 kV.

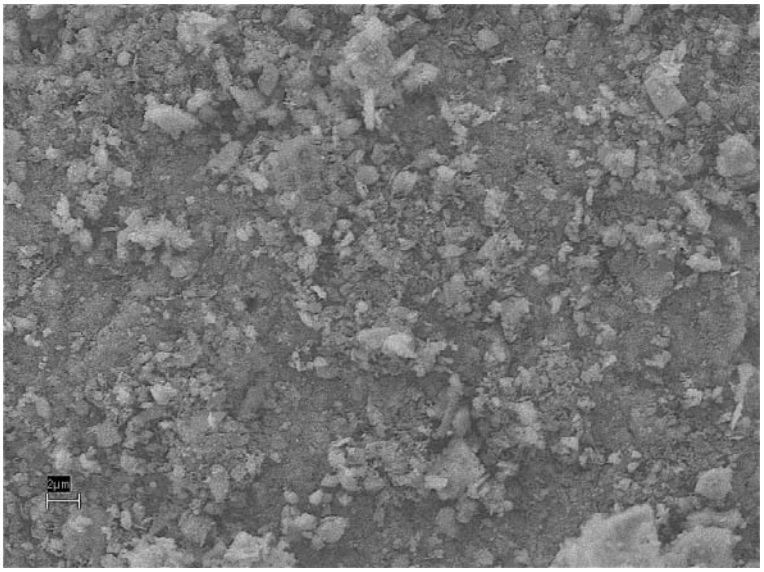

SEM sample Bodele bulk 4D2: Bar scale 2μm

Scanning Electron Microscope: The primary performance specification for the FESEM is resolution. Point-to-point resolution is 1 nm at an accelerating voltage of 30 kV and 4 nm at 1.0 kV.

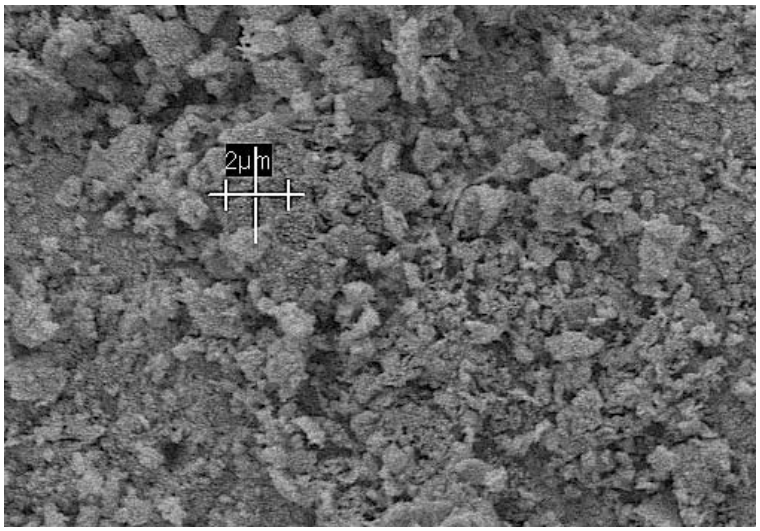

SEM sample Bodele bulk 4D5: Bar scale 2μm

Scanning Electron Microscope: The primary performance specification for the FESEM is resolution. Point-to-point resolution is 1 nm at an accelerating voltage of 30 kV and 4 nm at 1.0 kV.

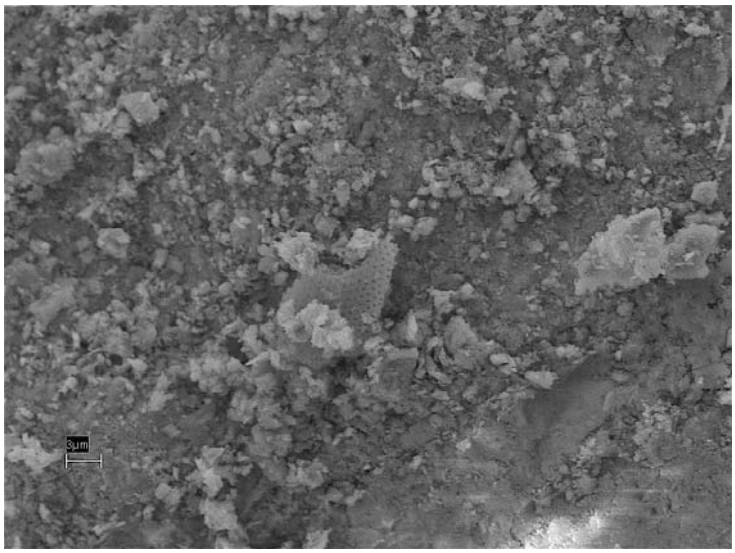

SEM sample Bodele bulk 4D6: Bar scale 3 μm

Scanning Electron Microscope: The primary performance specification for the FESEM is resolution. Point-to-point resolution is 1 nm at an accelerating voltage of 30 kV and 4 nm at 1.0 kV.

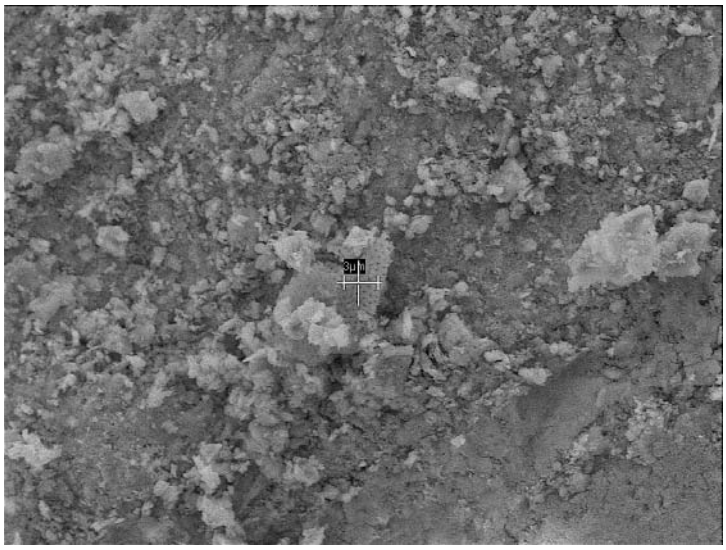

SEM sample Bodele bulk 4D8: Bar scale 3μm centered on visible diatom

Scanning Electron Microscope: The primary performance specification for the FESEM is resolution. Point-to-point resolution is 1 nm at an accelerating voltage of 30 kV and 4 nm at 1.0 kV.

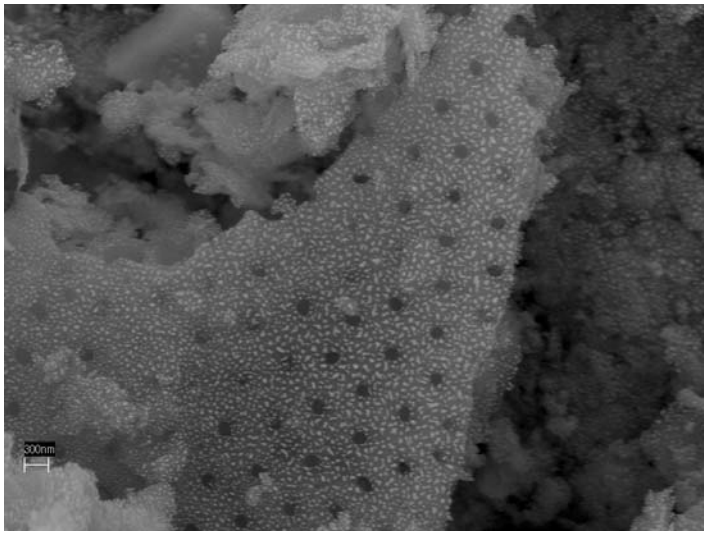

SEM sample Bodele bulk 4D9: Bar scale 300nm: close-up of above SEM image

Scanning Electron Microscope: The primary performance specification for the FESEM is resolution. Point-to-point resolution is 1 nm at an accelerating voltage of 30 kV and 4 nm at 1.0 kV.

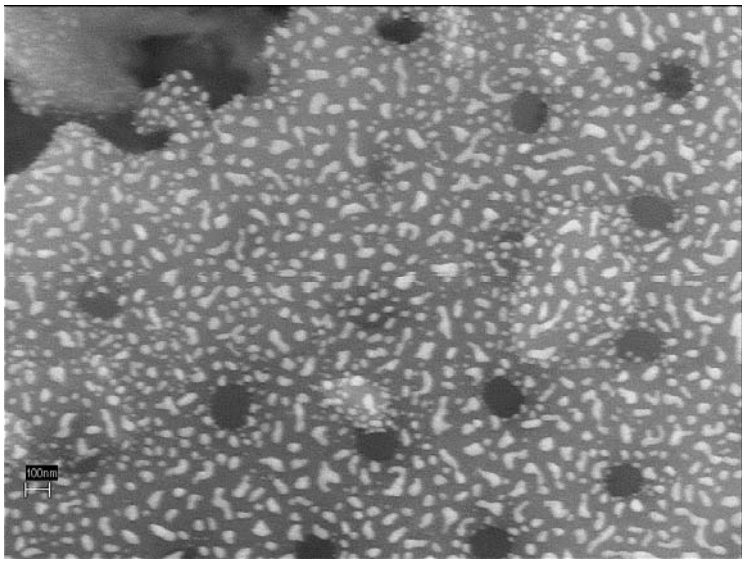

SEM sample Bodele bulk 4D10: Bar scale 100 nm: further close-up of figure 43

Scanning Electron Microscope: The primary performance specification for the FESEM is resolution. Point-to-point resolution is 1 nm at an accelerating voltage of 30 kV and 4 nm at 1.0 kV.

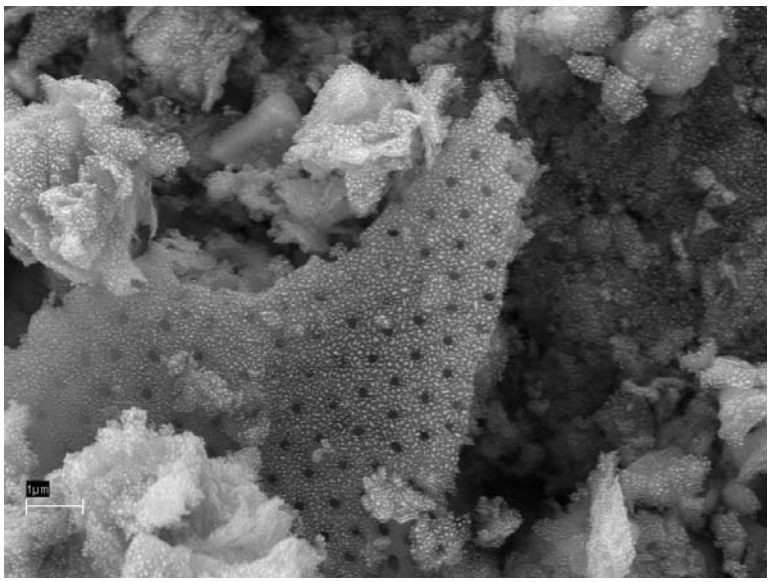

SEM sample Bodele bulk 4D11: Bar scale 1μm

Scanning Electron Microscope: The primary performance specification for the FESEM is resolution. Point-to-point resolution is 1 nm at an accelerating voltage of 30 kV and 4 nm at 1.0 kV.

APPENDIX E

SEM DATA FOR AEROSOL SAMPLES

Spectrum processing :
Peak possibly omitted : 2.135 keV

Processing option : All elements analyzed (Normalised)
Number of iterations = 3

Standard :
C CaCO3 1-Jun-1999 12:00 AM
O SiO2 1-Jun-1999 12:00 AM
Mg MgO 1-Jun-1999 12:00 AM
Al Al2O3 1-Jun-1999 12:00 AM
Si SiO2 1-Jun-1999 12:00 AM
K MAD-10 Feldspar 1-Jun-1999 12:00 AM
Ca Wollastonite 1-Jun-1999 12:00 AM
Fe Fe 1-Jun-1999 12:00 AM

Element	Weight%	Atomic%
C K	15.57	24.47
O K	43.16	50.92
Mg K	1.73	1.34
Al K	7.76	5.43
Si K	19.94	13.40
K K	1.82	0.88
Ca K	1.24	0.59
Fe L	8.78	2.97
Totals	100.00	

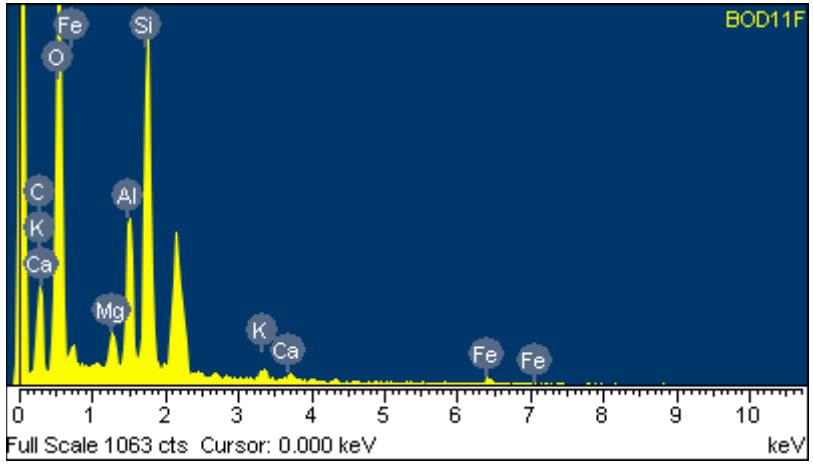

Comment: Sample BOD11F: Ferromagnesium silicates

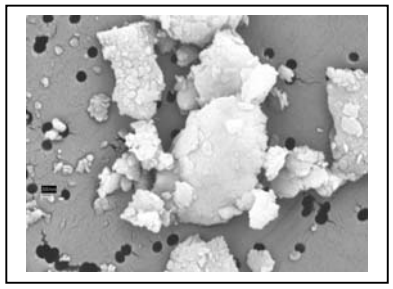

Spectrum processing :
Peak possibly omitted : 2.141 keV

Processing option : All elements analyzed (Normalised)
Number of iterations = 3

Standard :
C CaCO3 1-Jun-1999 12:00 AM
O SiO2 1-Jun-1999 12:00 AM
Al Al2O3 1-Jun-1999 12:00 AM
Si SiO2 1-Jun-1999 12:00 AM

Element	Weight%	Atomic%
C K	25.33	35.33
O K	44.55	46.66
Al K	1.37	0.85
Si K	28.76	17.16
Totals	100.00	

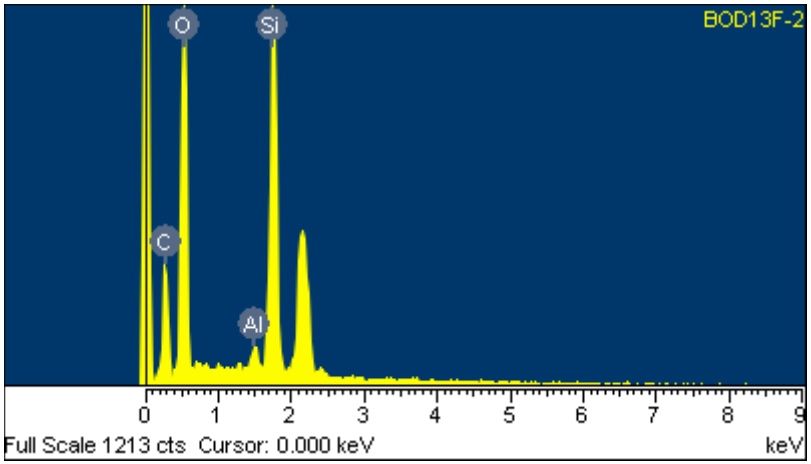

Comment: Sample BOD13F: Mainly silica

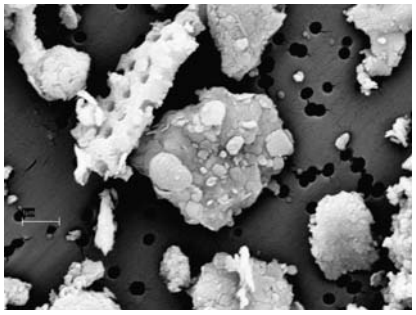

Spectrum processing :
Peaks possibly omitted : 0.700, 2.144 keV

Processing option : All elements analyzed (Normalised)
Number of iterations = 3

Standard :
C CaCO3 1-Jun-1999 12:00 AM
O SiO2 1-Jun-1999 12:00 AM
Mg MgO 1-Jun-1999 12:00 AM
Al Al2O3 1-Jun-1999 12:00 AM
Si SiO2 1-Jun-1999 12:00 AM
K MAD-10 Feldspar 1-Jun-1999 12:00 AM
Ca Wollastonite 1-Jun-1999 12:00 AM

Element	Weight%	Atomic%
C K	16.17	24.30
O K	45.17	50.94
Mg K	1.05	0.78
Al K	11.71	7.83
Si K	23.30	14.97
K K	1.28	0.59
Ca K	1.31	0.59
Totals	100.00	

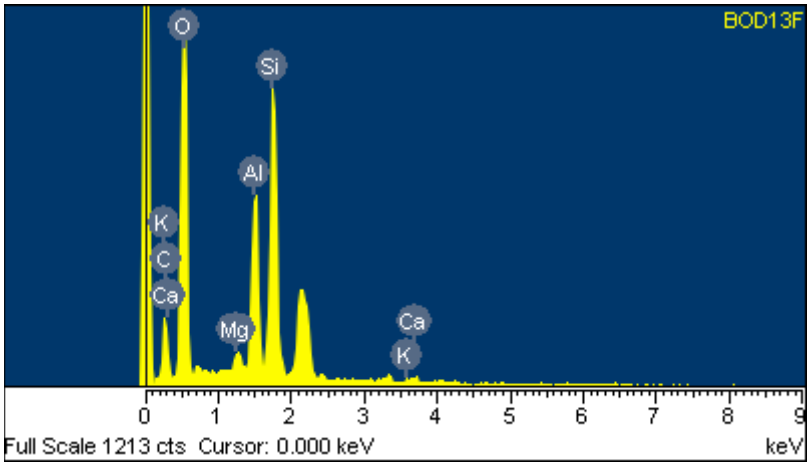

Comment: Sample BOD13F: Silica, clay minerals, carbonates

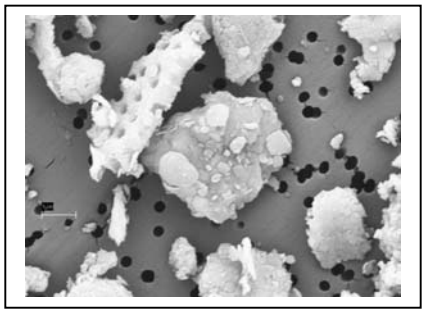

Spectrum processing :
Peaks possibly omitted : 2.140, 3.700 keV

Processing option : All elements analyzed (Normalised)
Number of iterations = 3

Standard :
C CaCO3 1-Jun-1999 12:00 AM
O SiO2 1-Jun-1999 12:00 AM
Al Al2O3 1-Jun-1999 12:00 AM
Si SiO2 1-Jun-1999 12:00 AM

Element	Weight %	Atomi c%
C K	44.62	55.01
O K	39.58	36.63
Al K	1.71	0.94
Si K	14.09	7.43
Totals	100.00	

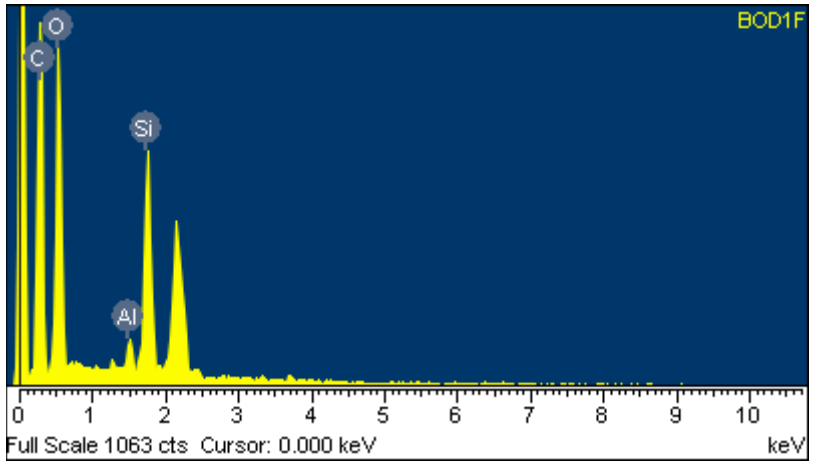

Comment: Sample BOD1F: Silica

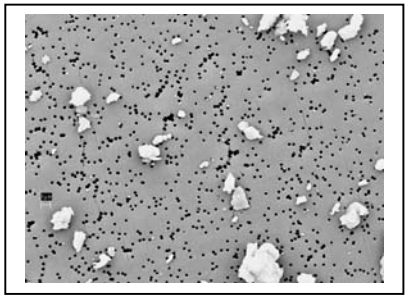

Spectrum processing :
Peak possibly omitted : 2.143 keV

Processing option : All elements analyzed (Normalised)
Number of iterations = 4

Standard :
C CaCO3 1-Jun-1999 12:00 AM
O SiO2 1-Jun-1999 12:00 AM
Al Al2O3 1-Jun-1999 12:00 AM
Si SiO2 1-Jun-1999 12:00 AM
K MAD-10 Feldspar 1-Jun-1999 12:00 AM

Element	Weight%	Atomic%
C K	29.17	39.09
O K	46.91	47.19
Al K	6.35	3.79
Si K	16.76	9.60
K K	0.81	0.33
Totals	100.00	

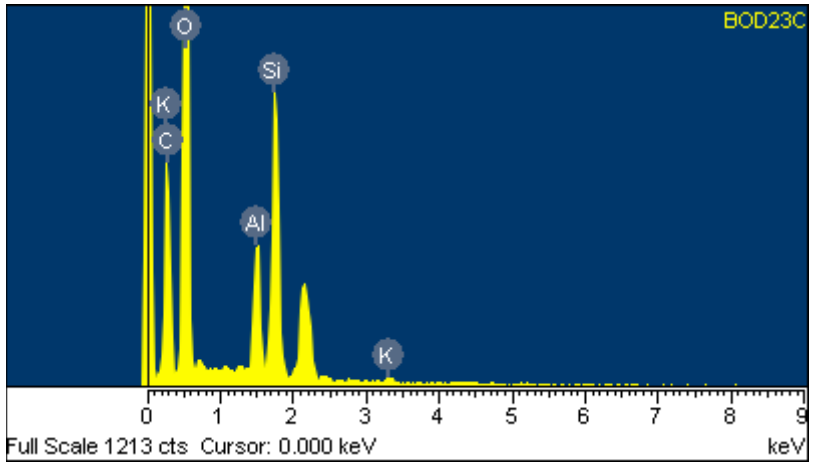

Comment: Sample BOD23C: Clay minerals and silica

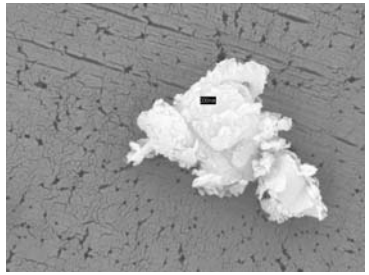

Spectrum processing :
Peak possibly omitted : 2.150 keV

Processing option : All elements analyzed (Normalised)
Number of iterations = 4

Standard :
C CaCO3 1-Jun-1999 12:00 AM
O SiO2 1-Jun-1999 12:00 AM
Al Al2O3 1-Jun-1999 12:00 AM
Si SiO2 1-Jun-1999 12:00 AM

Element	Weight%	Atomic%
C K	41.76	52.55
O K	39.58	37.39
Al K	1.27	0.71
Si K	17.38	9.35
Totals	100.00	

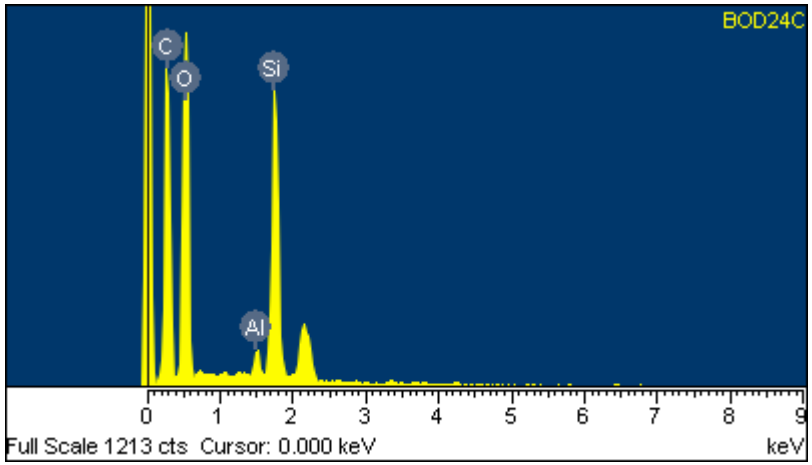

Comment: Mainly silica and/or clay mix

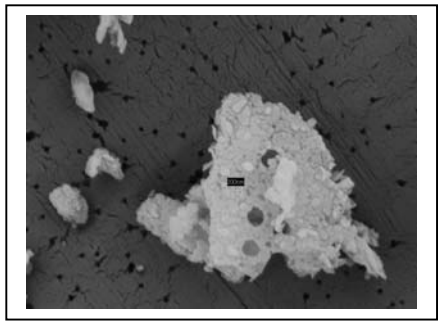

Spectrum processing :
Peak possibly omitted : 2.137 keV

Processing option : All elements analyzed (Normalised)
Number of iterations = 3

Standard :
C CaCO3 1-Jun-1999 12:00 AM
O SiO2 1-Jun-1999 12:00 AM
Mg MgO 1-Jun-1999 12:00 AM
Si SiO2 1-Jun-1999 12:00 AM
Ca Wollastonite 1-Jun-1999 12:00 AM

Element	Weight%	Atomic%
C K	6.68	11.50
O K	45.98	59.45
Mg K	12.65	10.77
Si K	1.67	1.23
Ca K	33.03	17.05
Totals	100.00	

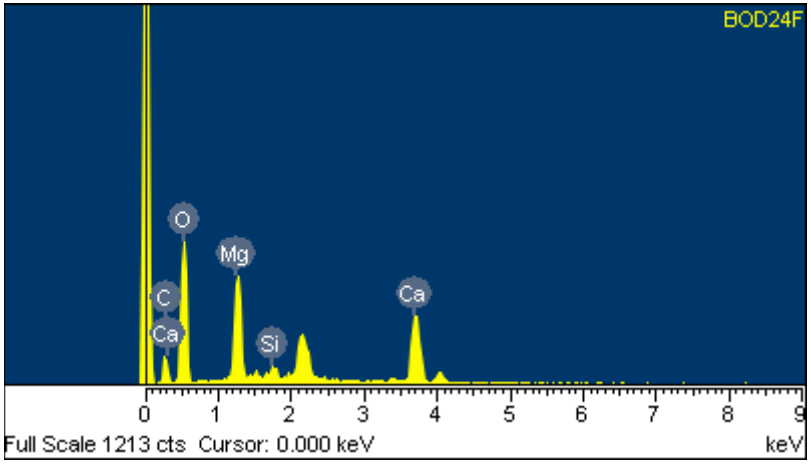

Comment: Sample BOD24F: Dolomite

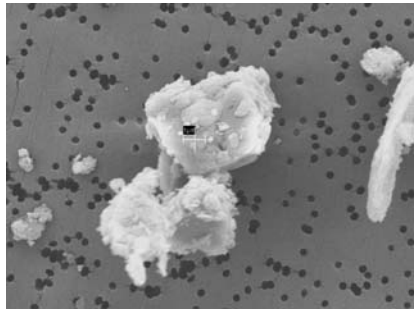

Spectrum processing :
Peak possibly omitted : 2.142 keV

Processing option : All elements analyzed (Normalised)
Number of iterations = 3

Standard :
C CaCO3 1-Jun-1999 12:00 AM
O SiO2 1-Jun-1999 12:00 AM
Mg MgO 1-Jun-1999 12:00 AM
Al Al2O3 1-Jun-1999 12:00 AM
Si SiO2 1-Jun-1999 12:00 AM
Ca Wollastonite 1-Jun-1999 12:00 AM

Element	Weight%	Atomic%
C K	14.55	21.74
O K	50.88	57.08
Mg K	3.10	2.29
Al K	5.42	3.60
Si K	18.93	12.10
Ca K	7.11	3.19
Totals	100.00	

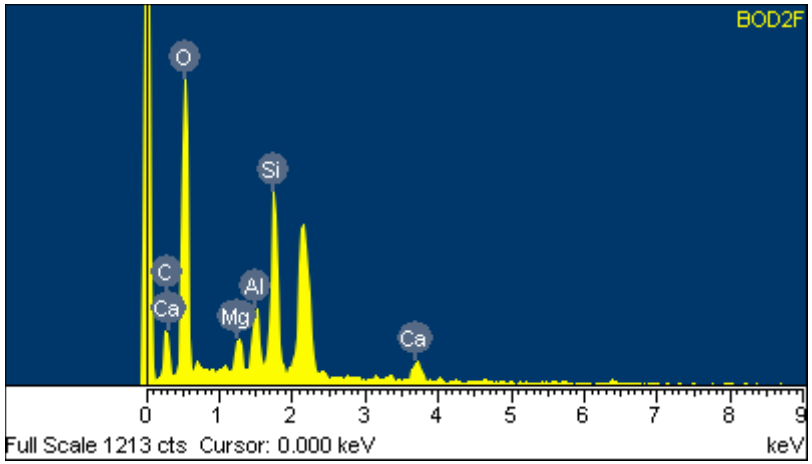

Comment: Sample BOD2F: Calcium carbonates, dolomites, silica

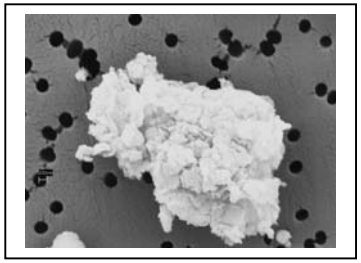

Spectrum processing :
Peak possibly omitted : 2.144 keV

Processing option : All elements analyzed (Normalised)
Number of iterations = 3

Standard :
C CaCO3 1-Jun-1999 12:00 AM
O SiO2 1-Jun-1999 12:00 AM
Si SiO2 1-Jun-1999 12:00 AM

Element	Weight%	Atomic%
C K	53.36	63.90
O K	31.57	28.38
Si K	15.06	7.71
Totals	100.00	

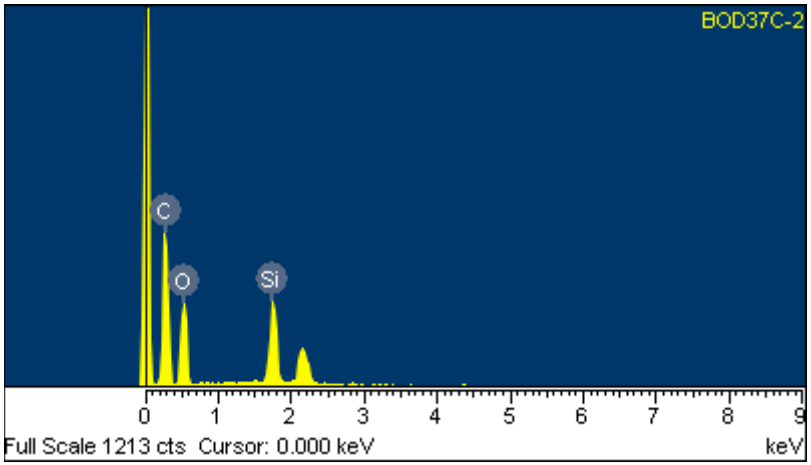

Comment: Sample BOD37C-2: Silica

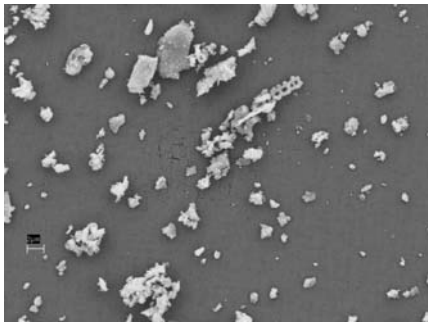

Spectrum processing :
Peaks possibly omitted : 0.720, 2.137 keV

Processing option : All elements analyzed (Normalised)
Number of iterations = 3

Standard :
C CaCO3 1-Jun-1999 12:00 AM
O SiO2 1-Jun-1999 12:00 AM
Na Albite 1-Jun-1999 12:00 AM
Al Al2O3 1-Jun-1999 12:00 AM
Si SiO2 1-Jun-1999 12:00 AM
Ca Wollastonite 1-Jun-1999 12:00 AM

Element	Weight%	Atomic%
C K	15.49	23.03
O K	47.30	52.78
Na K	3.95	3.07
Al K	8.45	5.59
Si K	23.61	15.01
Ca K	1.20	0.53
Totals	100.00	

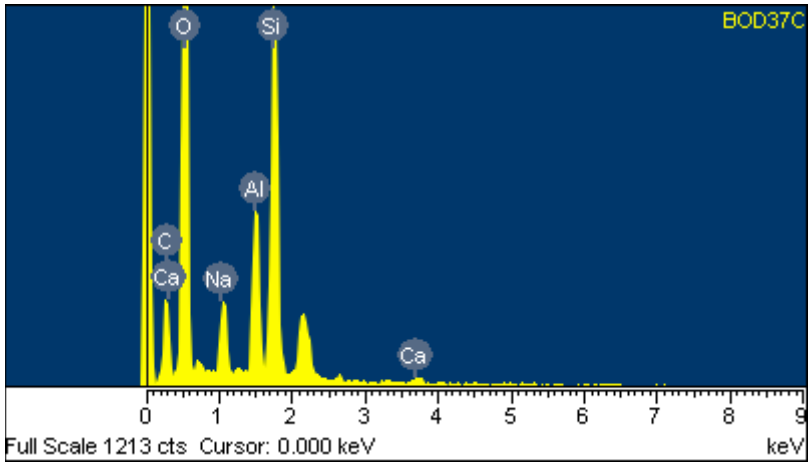

Comment: Sample BOD37C: Aluminum silicates, silica, calcium carbonate

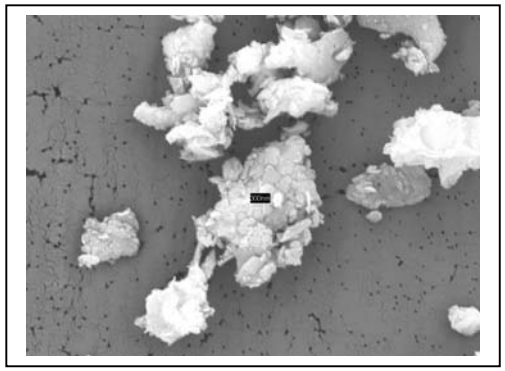

Spectrum processing :
Peak possibly omitted : 2.142 keV

Processing option : All elements analyzed (Normalised)
Number of iterations = 3

Standard :
C CaCO3 1-Jun-1999 12:00 AM
O SiO2 1-Jun-1999 12:00 AM
Mg MgO 1-Jun-1999 12:00 AM
Al Al2O3 1-Jun-1999 12:00 AM
Si SiO2 1-Jun-1999 12:00 AM
Fe Fe 1-Jun-1999 12:00 AM

Element	Weight%	Atomic%
C K	30.45	43.46
O K	38.04	40.76
Mg K	0.92	0.65
Al K	5.70	3.62
Si K	12.77	7.79
Fe L	12.12	3.72
Totals	100.00	

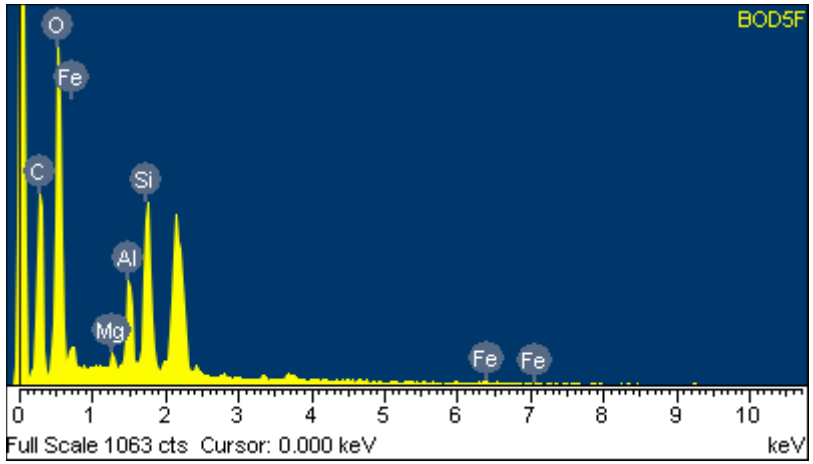

Comment: Sample BOD5F: Ferromagnesium silicates

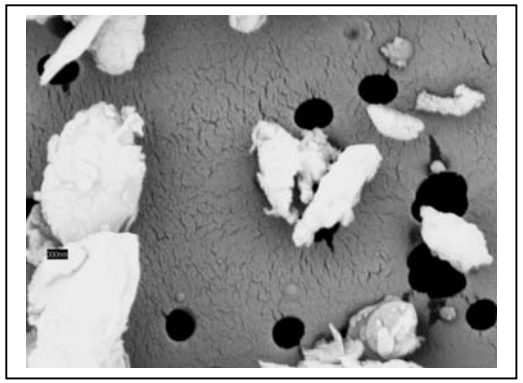

Spectrum processing :
Peaks possibly omitted : 0.700, 2.140 keV

Processing option : All elements analyzed (Normalised)
Number of iterations = 3

Standard :
C CaCO3 1-Jun-1999 12:00 AM
O SiO2 1-Jun-1999 12:00 AM
Mg MgO 1-Jun-1999 12:00 AM
Al Al2O3 1-Jun-1999 12:00 AM
Si SiO2 1-Jun-1999 12:00 AM
K MAD-10 Feldspar 1-Jun-1999 12:00 AM
Ca Wollastonite 1-Jun-1999 12:00 AM

Element	Weight%	Atomic%
C K	22.46	31.83
O K	47.18	50.19
Mg K	2.14	1.50
Al K	7.13	4.50
Si K	16.57	10.04
K K	1.62	0.71
Ca K	2.89	1.23
Totals	100.00	

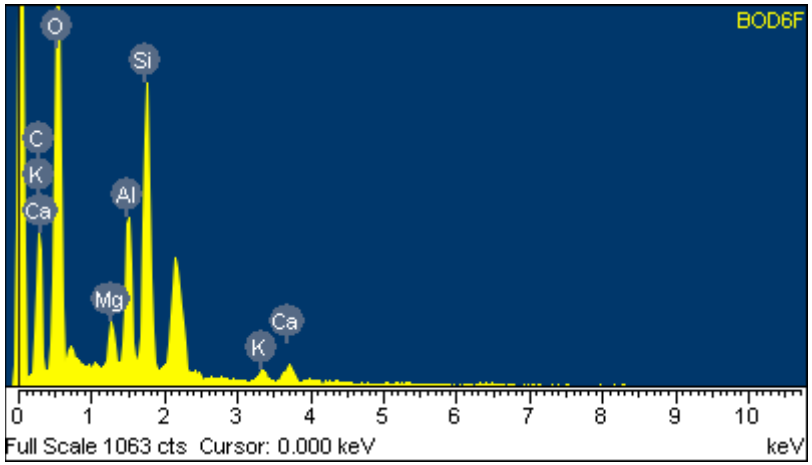

Comment: Sample BOD6F: Clay minerals, calcium carbonate, dolomite, and possible silica

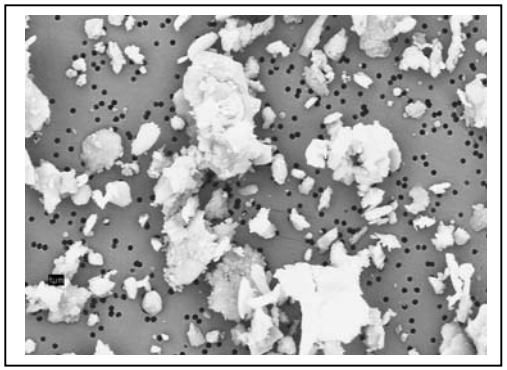

Spectrum processing:
Peak possibly omitted : 2.138 keV

Processing option : All elements analyzed (Normalised)
Number of iterations = 3

Standard :
C CaCO3 1-Jun-1999 12:00 AM
O SiO2 1-Jun-1999 12:00 AM
Mg MgO 1-Jun-1999 12:00 AM
Al Al2O3 1-Jun-1999 12:00 AM
Si SiO2 1-Jun-1999 12:00 AM
K MAD-10 Feldspar 1-Jun-1999 12:00 AM
Ca Wollastonite 1-Jun-1999 12:00 AM
Fe Fe 1-Jun-1999 12:00 AM

Element	Weight%	Atomic%
C K	17.24	26.32
O K	45.78	52.48
Mg K	2.34	1.77
Al K	5.65	3.84
Si K	18.20	11.88
K K	0.58	0.27
Ca K	0.71	0.33
Fe L	9.51	3.12
Totals	100.00	

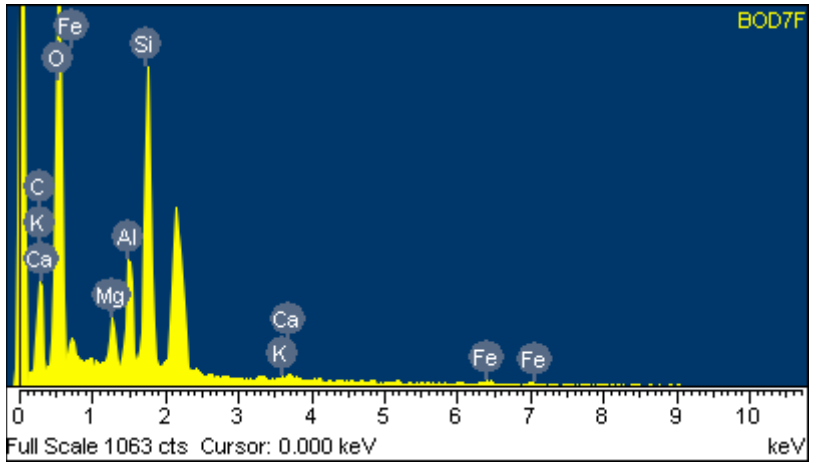

Comment: Sample BOD7F: Ferromagnesium silicate minerals and possible iron oxide

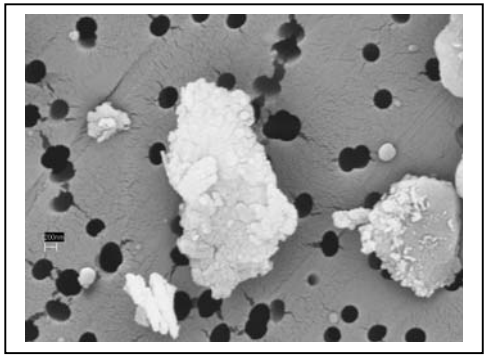

Spectrum processing :
Peak possibly omitted : 2.140 keV

Processing option : All elements analyzed (Normalised)
Number of iterations = 2

Standard :
C CaCO3 1-Jun-1999 12:00 AM
O SiO2 1-Jun-1999 12:00 AM
Na Albite 1-Jun-1999 12:00 AM
Mg MgO 1-Jun-1999 12:00 AM
Al Al2O3 1-Jun-1999 12:00 AM
Si SiO2 1-Jun-1999 12:00 AM
K MAD-10 Feldspar 1-Jun-1999 12:00 AM
Ca Wollastonite 1-Jun-1999 12:00 AM
Fe Fe 1-Jun-1999 12:00 AM

Element	Weight%	Atomic%
C K	7.19	12.18
O K	46.31	58.87
Na K	0.94	0.83
Mg K	1.82	1.52
Al K	6.36	4.80
Si K	21.67	15.69
K K	0.75	0.39
Ca K	1.86	0.95
Fe L	13.10	4.77
Totals	100.00	

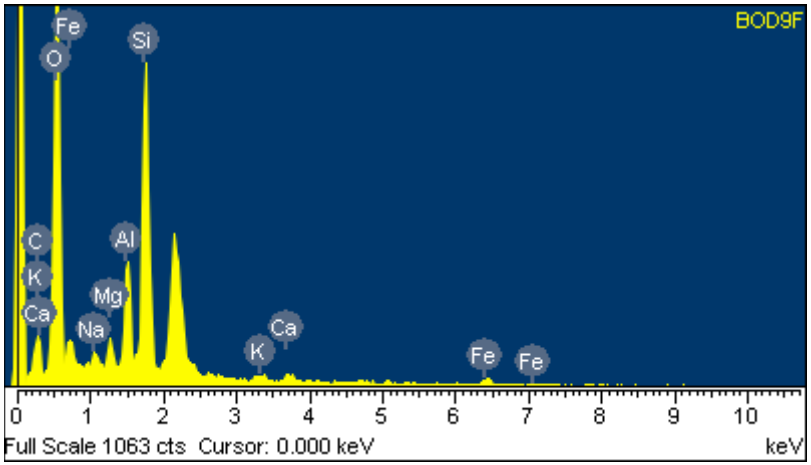

Comment: Sample BOD9F: Ferromagnesium silicate minerals, clay minerals, and possible silica

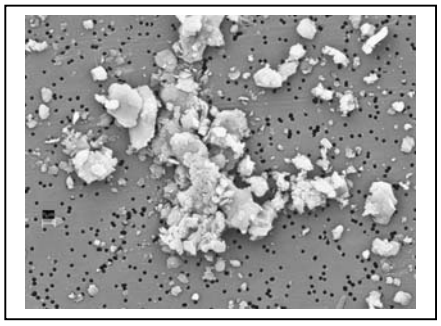

SEM Aerosol Data Chemical Analyses

Element	Weight %	Atomic %	Element	Weight %	Atomoic %
Oxygen	45.17	50.94	Silicon	23.3	14.97
	39.58	36.63		14.09	7.43
	45.98	59.45		1.67	1.23
	39.58	37.39		17.38	9.35
	45.78	52.48		18.2	11.88
	43.16	50.92		19.94	13.4
	46.91	47.19		16.76	9.6
	47.18	50.91		16.57	10.04
	44.55	46.66		28.76	17.16
	38.04	40.76		12.77	7.79
	46.31	58.87		21.67	15.69
	31.57	28.38		15.06	7.71
	47.3	52.78		23.61	15.01
	50.88	57.08		18.93	12.1
Grand Total	611.99	670.44	**Grand Total**	248.71	153.36
Sodium	0.94	0.83			
	3.95	3.07	Aluminum	5.7	3.62
Grand Total	4.89	3.9		6.36	4.8
Iron	9.51	3.12		8.45	5.59
	8.78	2.97		11.71	7.83
	12.12	3.72		1.71	0.94
	13.1	4.77		1.27	0.71
Grand Total	43.51	14.58		5.65	3.84
Potassium	1.28	0.59		7.76	5.43
	0.58	0.27		6.35	3.79
	1.82	0.88		7.13	4.5
	0.81	0.33		1.37	0.85
	1.62	0.71		5.42	3.6
	0.75	0.39	**Grand Total**	68.88	45.5
Grand Total	6.34	3.17			
Magnesium	1.05	0.078	Calcium	7.11	3.19
	12.65	10.77		1.31	0.59
	2.34	1.77		33.03	17.05
	1.73	1.34		0.71	0.33
	2.14	1.5		1.24	0.59
	0.92	0.65		2.89	1.23
	1.82	1.52		1.86	0.95
	3.1	2.29		1.2	0.53
Grand Total	25.75	19.98	**Grand Total**	49.34	24.46

APPENDIX F

SEM IMAGES FOR AEROSOL SAMPLES

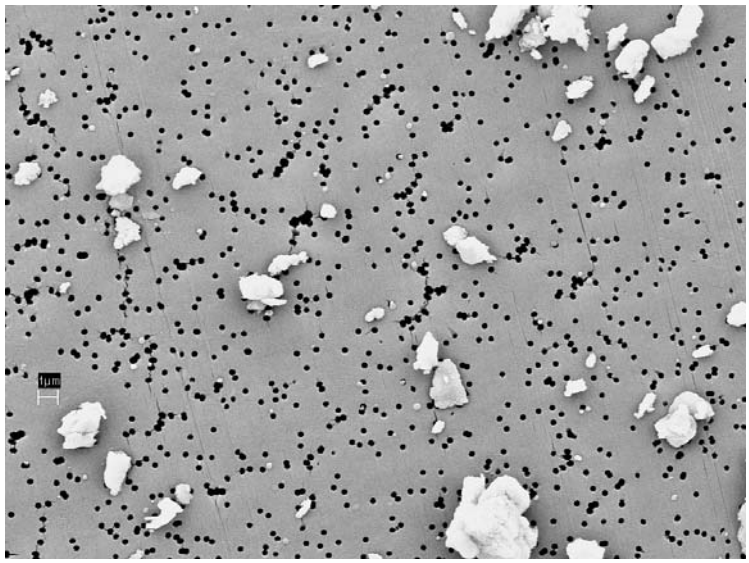

SEM Bodele Aerosol sample BOD1F: Bar scale 1µm

Scanning Electron Microscope: The primary performance specification for the FESEM is resolution. Point-to-point resolution is 1 nm at an accelerating voltage of 30 kV and 4 nm at 1.0 kV.

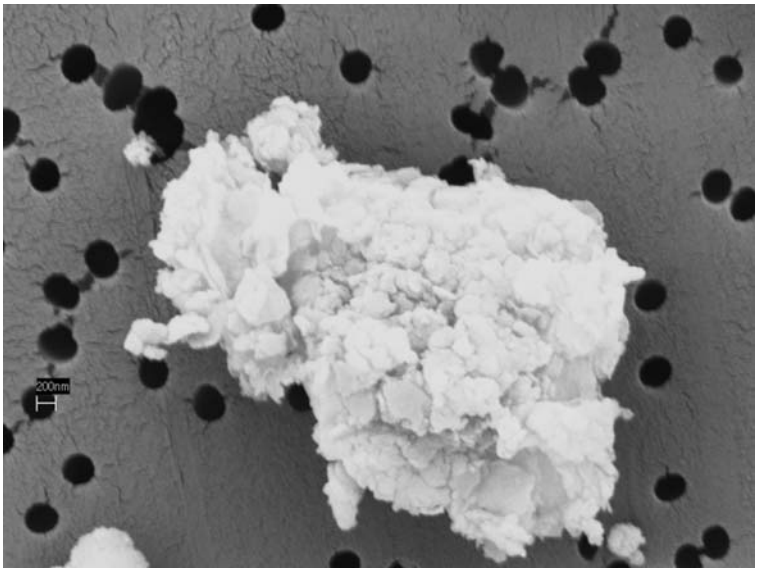

SEM Bodele Aerosol sample BOD2F: Bar scale 200nm

Scanning Electron Microscope: The primary performance specification for the FESEM is resolution. Point-to-point resolution is 1 nm at an accelerating voltage of 30 kV and 4 nm at 1.0 kV.

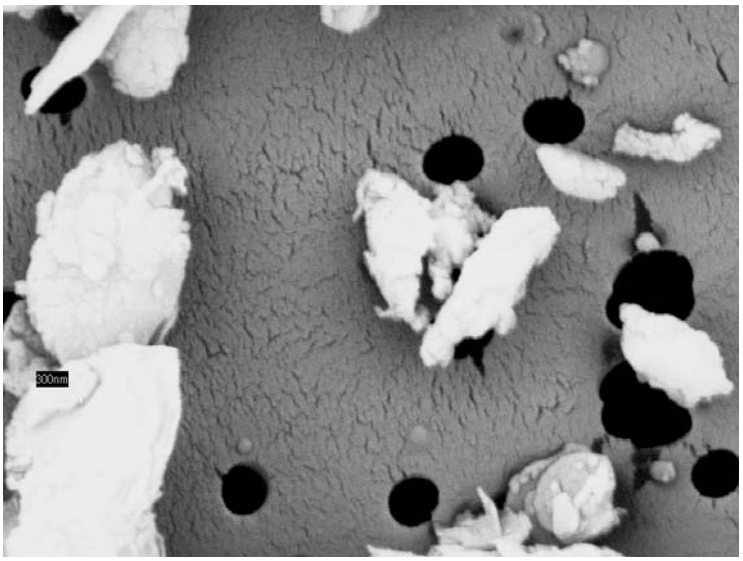

SEM Bodele Aerosol sample BOD5F: Bar scale 300nm

Scanning Electron Microscope: The primary performance specification for the FESEM is resolution. Point-to-point resolution is 1 nm at an accelerating voltage of 30 kV and 4 nm at 1.0 kV.

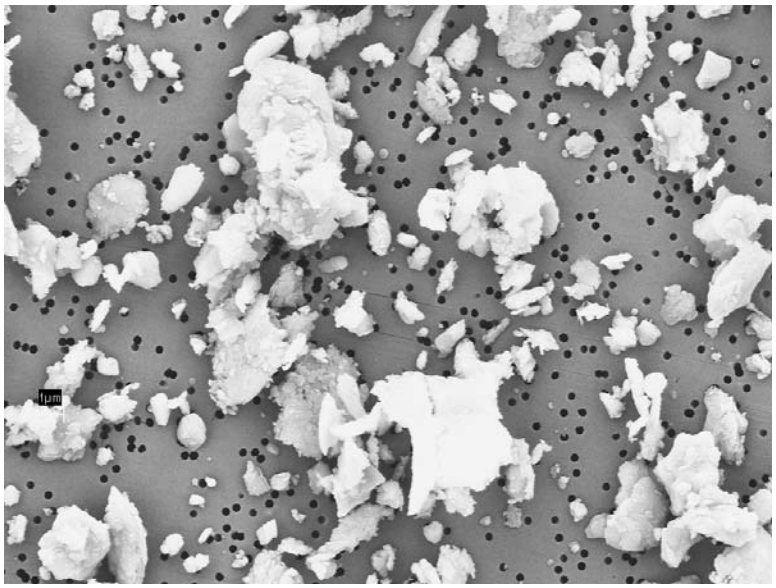

SEM Bodele Aerosol sample BOD6F: Bar scale 1µm

Scanning Electron Microscope: The primary performance specification for the FESEM is resolution. Point-to-point resolution is 1 nm at an accelerating voltage of 30 kV and 4 nm at 1.0 kV.

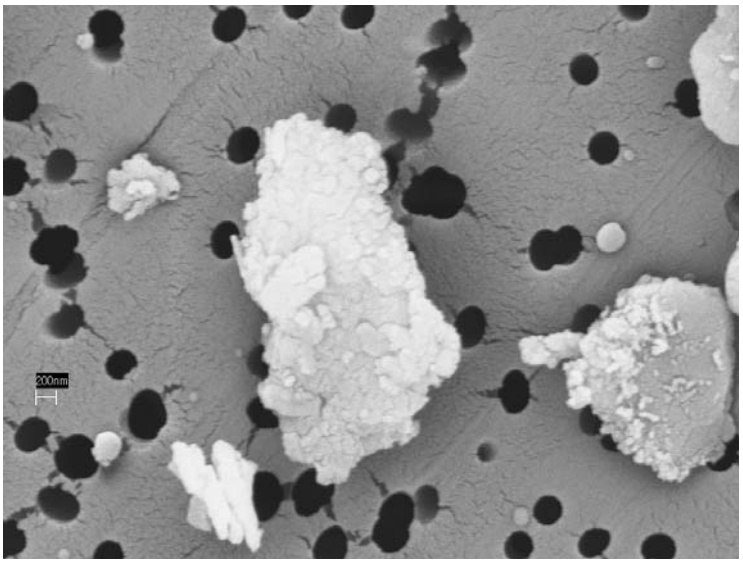

SEM Bodele Aerosol sample BOD7F: Bar scale 200nm

Scanning Electron Microscope: The primary performance specification for the FESEM is resolution. Point-to-point resolution is 1 nm at an accelerating voltage of 30 kV and 4 nm at 1.0 kV.

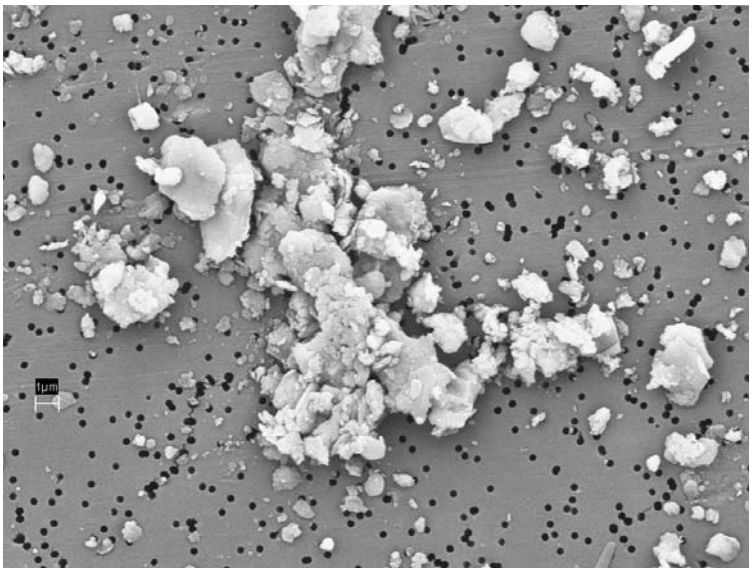

SEM Bodele Aerosol sample BOD9F: Bar scale 1µm

Scanning Electron Microscope: The primary performance specification for the FESEM is resolution. Point-to-point resolution is 1 nm at an accelerating voltage of 30 kV and 4 nm at 1.0 kV.

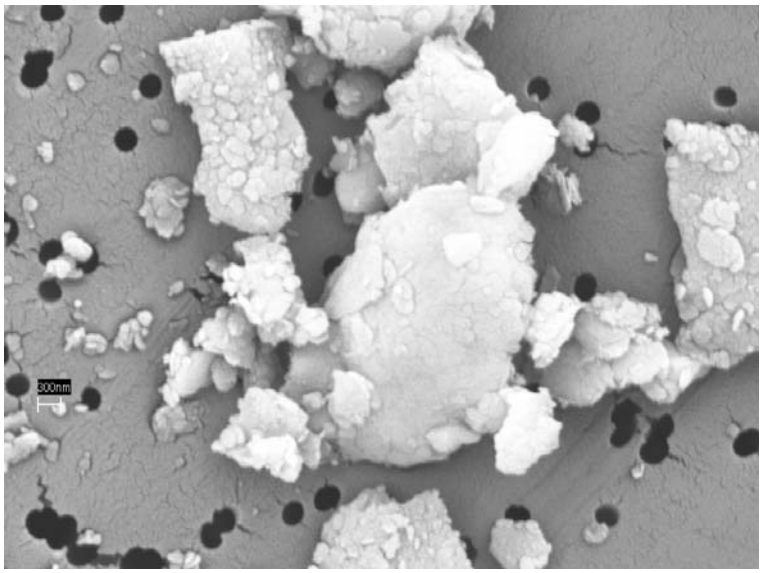

SEM Bodele Aerosol sample BOD11F: Bar scale 300nm

Scanning Electron Microscope: The primary performance specification for the FESEM is resolution. Point-to-point resolution is 1 nm at an accelerating voltage of 30 kV and 4 nm at 1.0 kV.

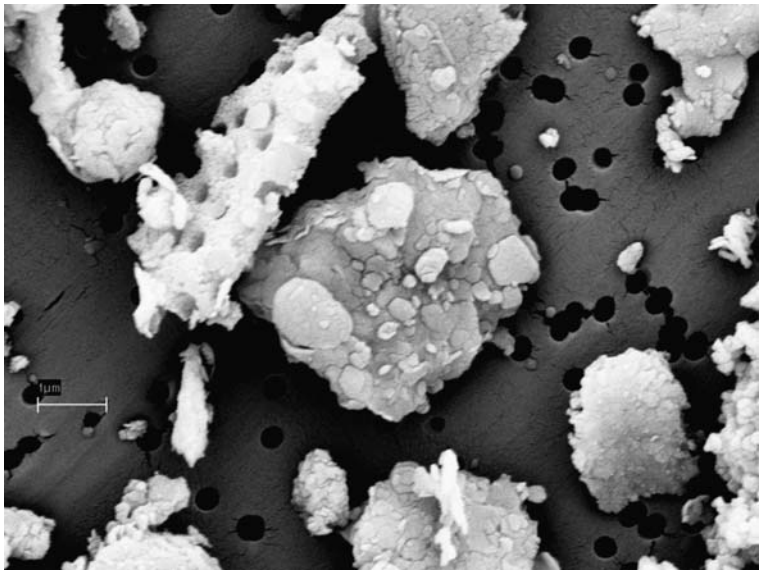

SEM Bodele Aerosol sample BOD13F: Bar scale 1µm

Scanning Electron Microscope: The primary performance specification for the FESEM is resolution. Point-to-point resolution is 1 nm at an accelerating voltage of 30 kV and 4 nm at 1.0 kV.

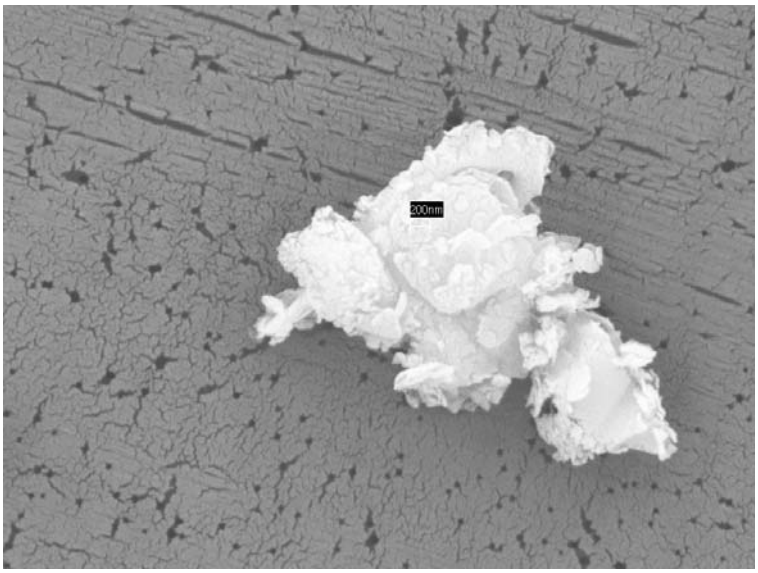

SEM Bodele Aerosol sample BOD 23-C: Bar scale 200nm

Scanning Electron Microscope: The primary performance specification for the FESEM is resolution. Point-to-point resolution is 1 nm at an accelerating voltage of 30 kV and 4 nm at 1.0 kV.

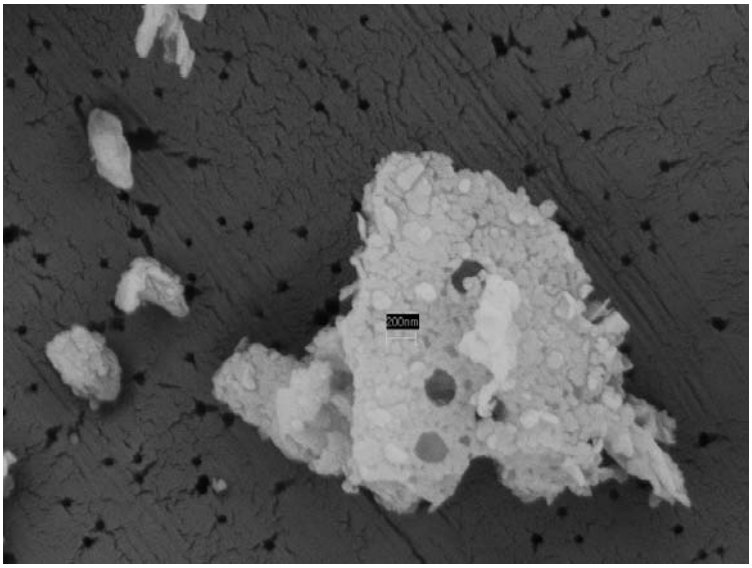

SEM Bodele Aerosol sample BOD24C: Bar scale 200nm

Scanning Electron Microscope: The primary performance specification for the FESEM is resolution. Point-to-point resolution is 1 nm at an accelerating voltage of 30 kV and 4 nm at 1.0 kV.

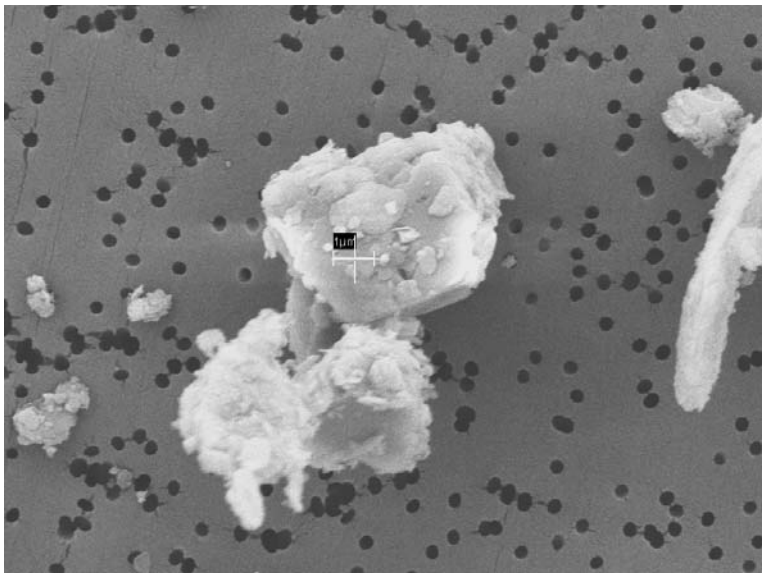

SEM Bodele Aerosol sample BOD24F: Bar scale 1µm

Scanning Electron Microscope: The primary performance specification for the FESEM is resolution. Point-to-point resolution is 1 nm at an accelerating voltage of 30 kV and 4 nm at 1.0 kV.

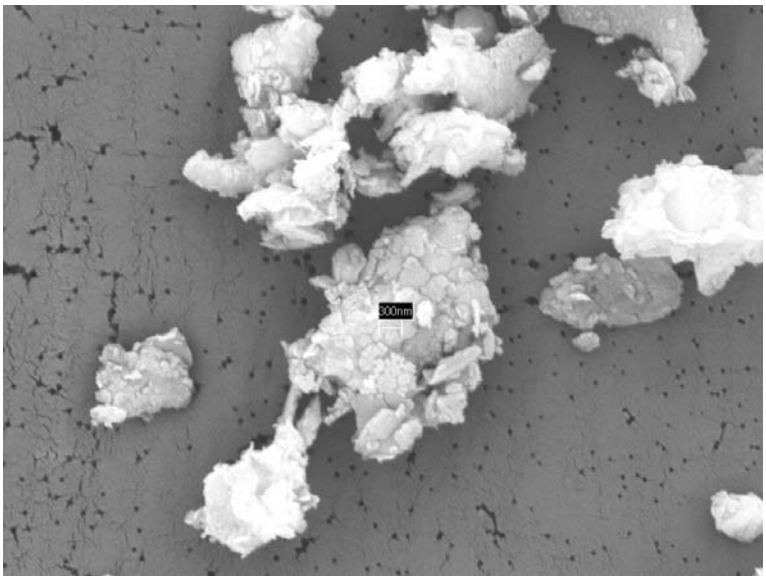

SEM Bodele Aerosol sample BOD37C: Bar scale 300nm

Scanning Electron Microscope: The primary performance specification for the FESEM is resolution. Point-to-point resolution is 1 nm at an accelerating voltage of 30 kV and 4 nm at 1.0 kV.

APPENDIX G

XRD DATA FOR BULK SAMPLE

X-ray diffraction analysis of massive samples from the Bodele indicates the composition of the material to be predominately kaolinite, with smectite, illite, and possibly augite or plagioclase signatures. There is very little evidence for quartz in any of the samples. Although possible for the amorphous material to be quartz, it is highly unlikely given the sparse evidence in XRD and SEM.

Four samples of materials from the surface of the Bodele region in Chad on the continent of Africa have been analyzed to determine the mineralization and source. The samples were prepared separately with sterilized mortar and pestil tools, and run through an XRD for 45 minutes each.

Each run is labeled

The four samples were then mixed with 5% zinc oxide as a baseline, ground to a powder and wet mounted before being sent through the XRD for 45 minutes each. The results are in figure 2.

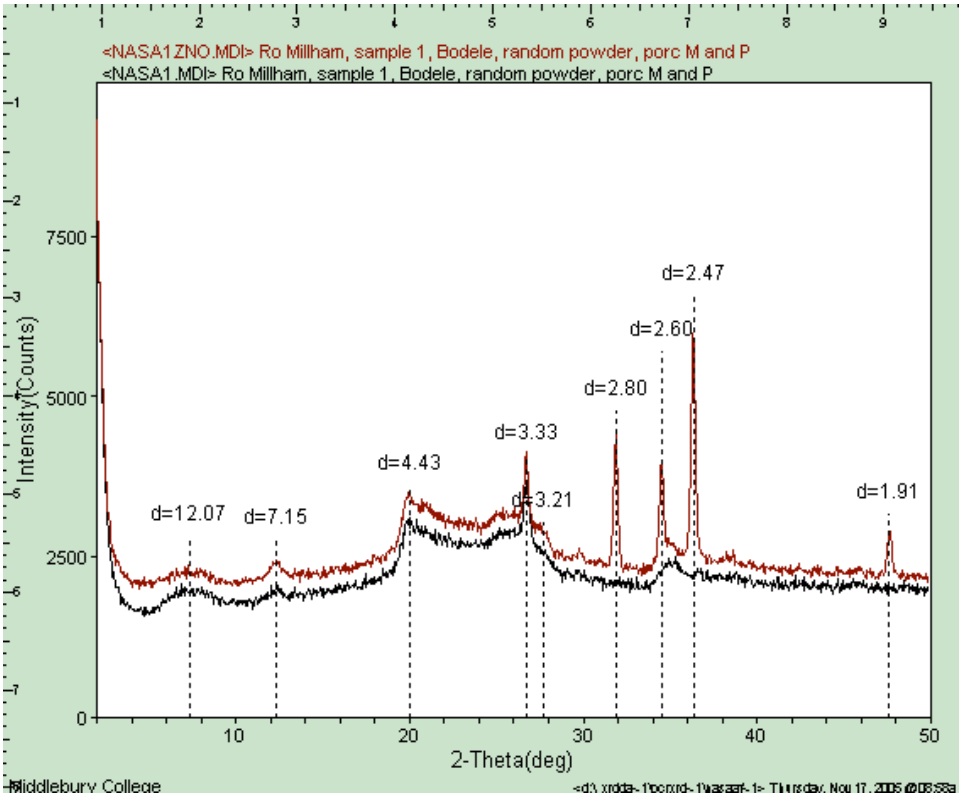

Figure represents ZnO comparison with wet mount runs.

Finally, the four samples were mixed with e-glycol and run, once again though the XRD.

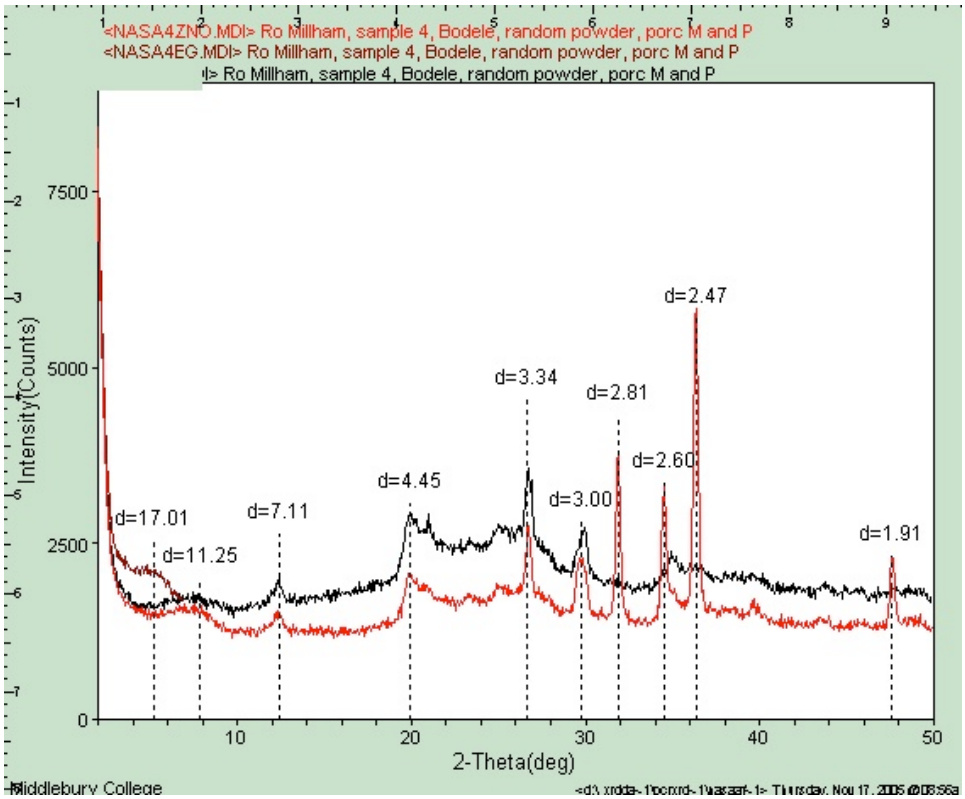

Figure represents ZnO compared with e-glycol runs.

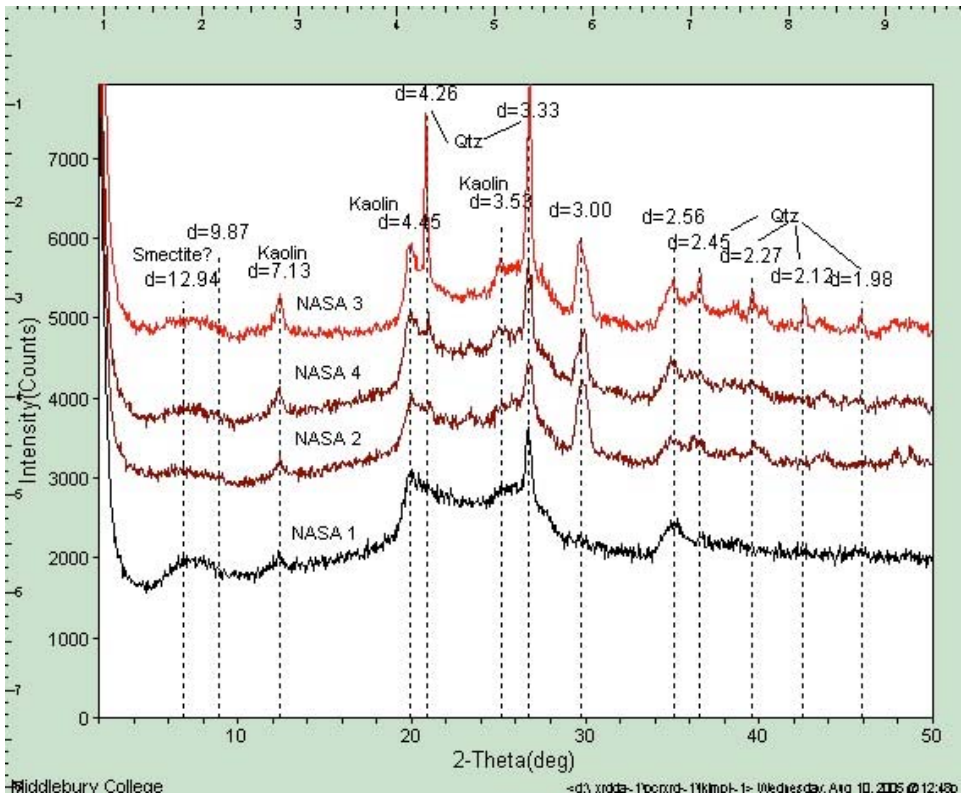

Figure represents all four-bulk samples by comparison.

APPENDIX H

TECHNOLOGY DOCUMENT FOR XRD XRF

GODDARD SPACE FLIGHT CENTER

CCD Based Multi-Wavelength X-ray Diffractometer

Keith Gendreau (GSFC), Zaven Arzoumanian (GSFC), Vanderlei Martins (GSFC), Rosemary Millham (OSU, SP systems), George Ricker (MIT), Peter Ford (MIT), Richard Starr (GSFC), Jack Trombka (GSFC)

Looking to expand

The Concept (for NASA Missions)

- A combination X-ray Diffractometer/ Fluorescence instrument that requires NO sample preparation
- Definitively identifies minerals, including water ice.
- Provides particle/grain sizes, shapes, and orientations -> clues to formation history
- Based on flight proven X-ray CCD technology
- Has option to study aerosol mineral composition

Implementation

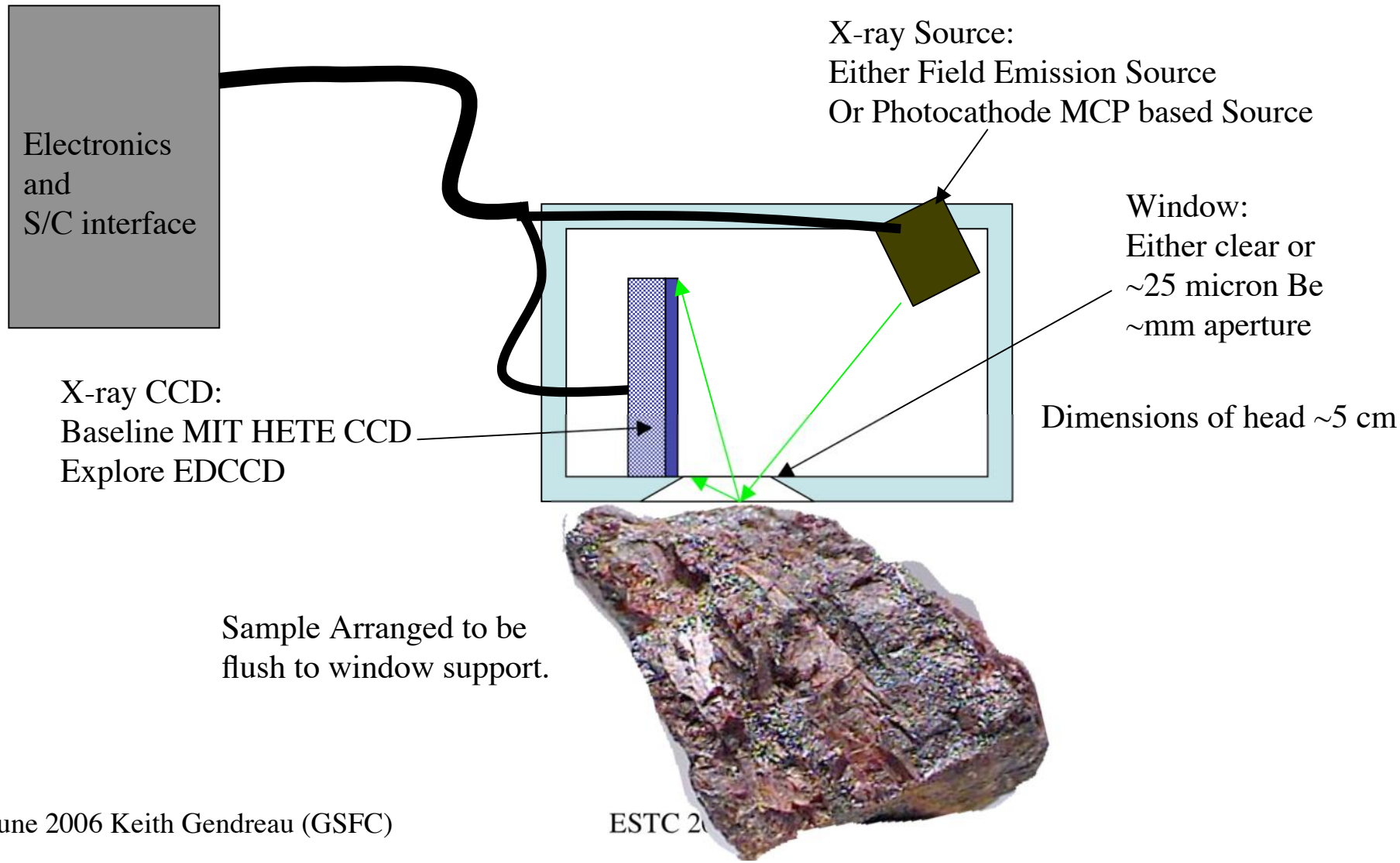

Application to VSE and Lunar Exploration

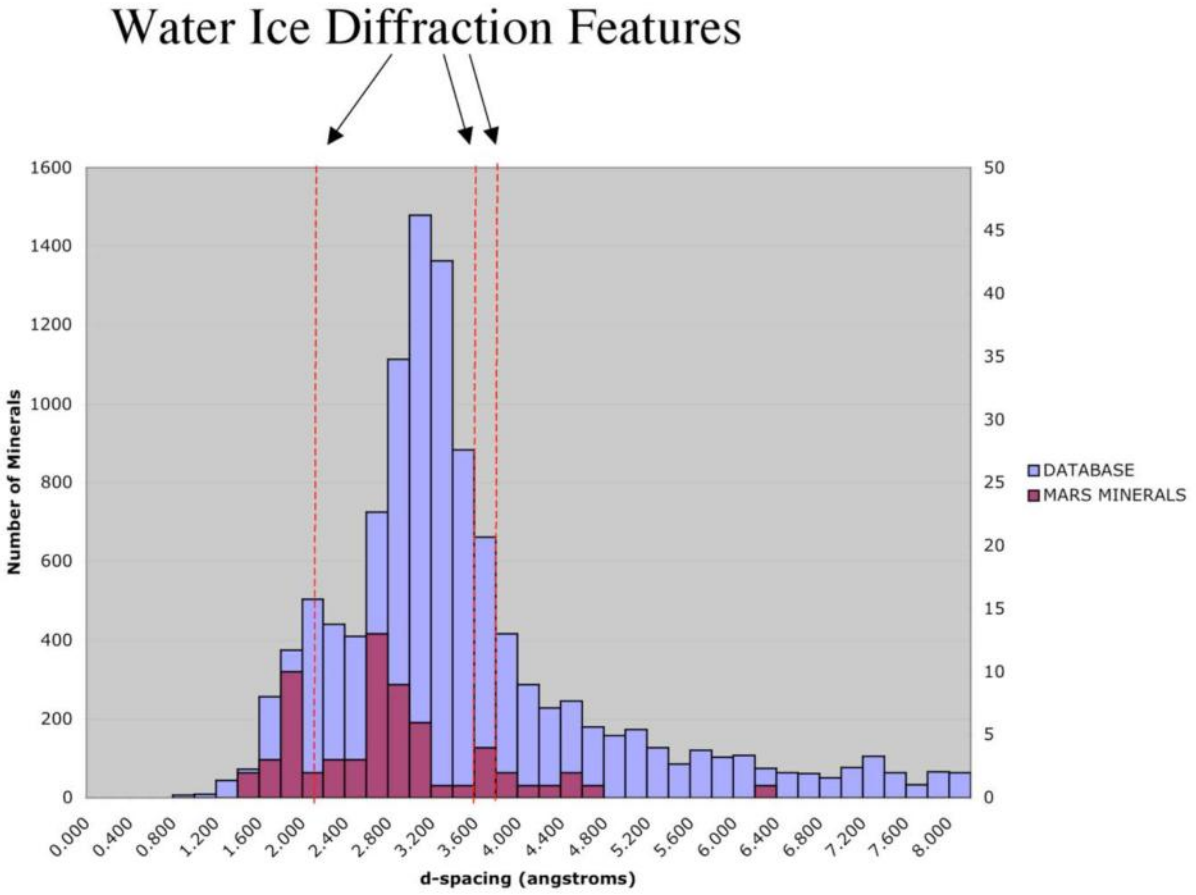

Not the same as CHEMIN

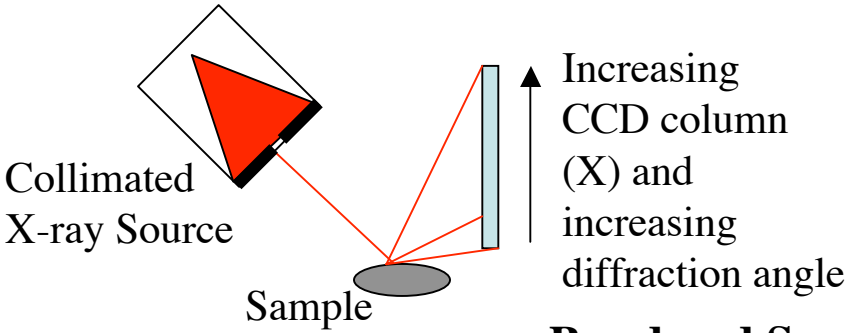

λ=12400 eVÅ/E(eV)
θ=Geometric function(X)
nλ=2d sin(θ)

GODDARD SPACE FLIGHT CENTER

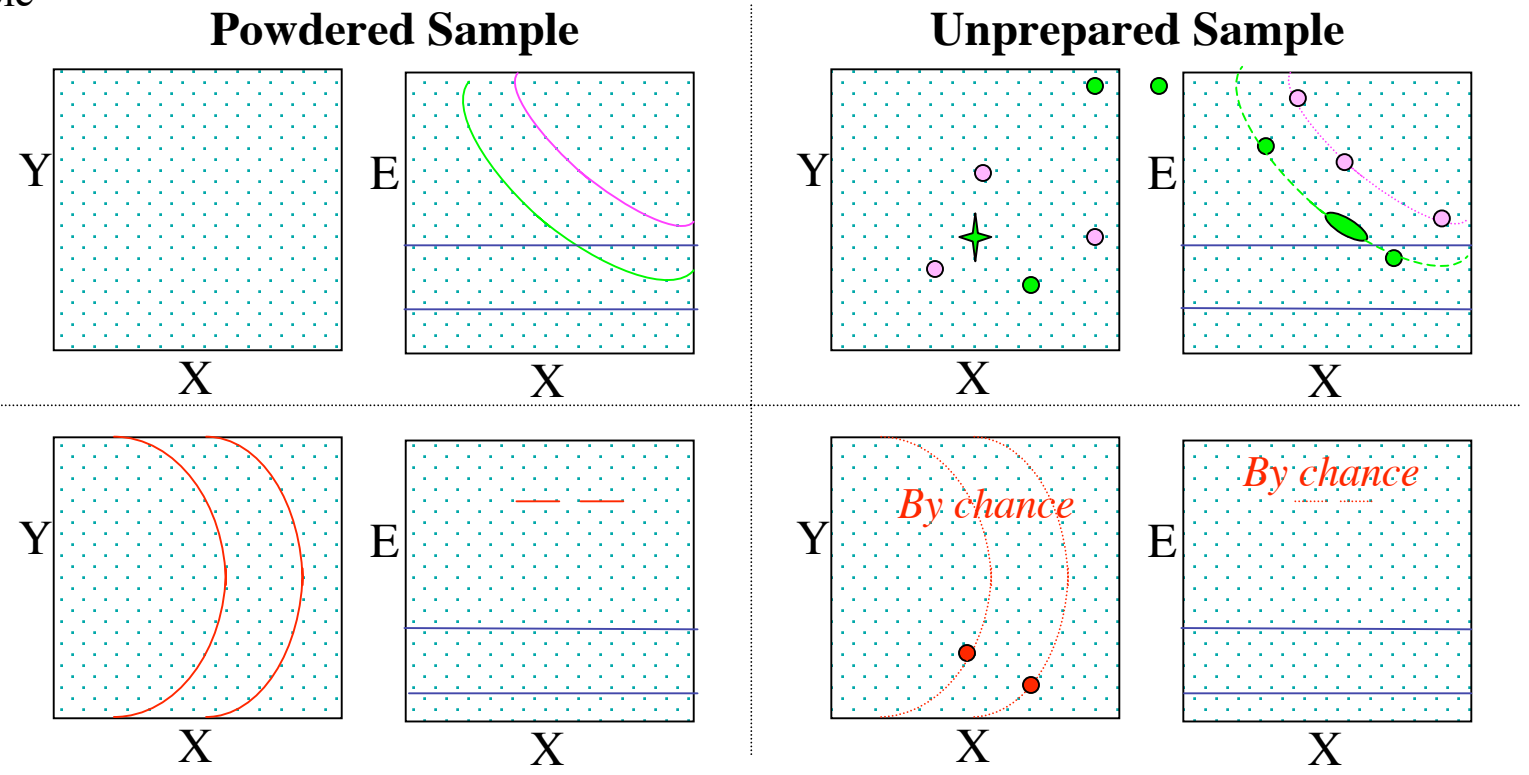

Our new concept expands X-ray diffraction into a new dimension.

Prototype Data (Al 6061)

ODDARD SPA
E FLIGHT CEN
ER

In a plot of energy vs 2Theta we see fluorescence lines as horizontally stretched events. The arcs in this space are due to diffraction and each arc represents a single d-spacing.

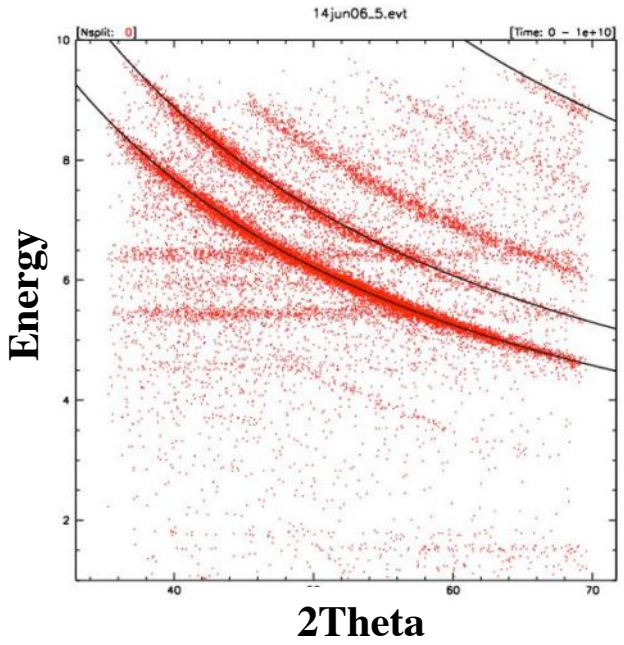

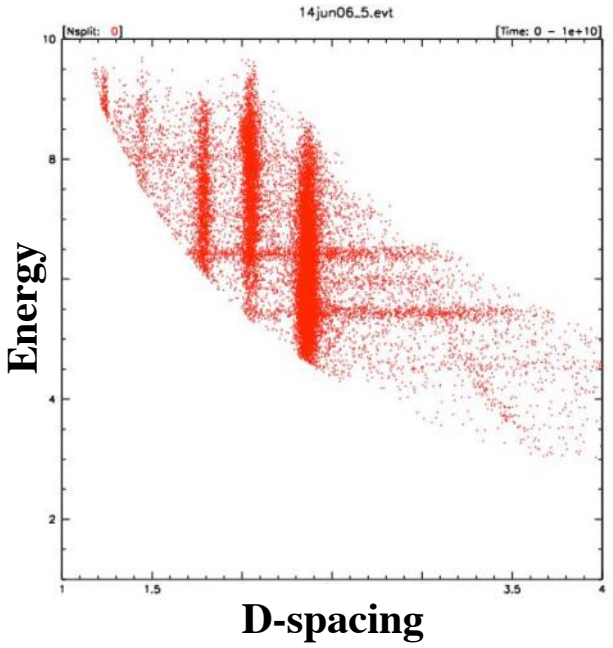

We can convert the energy of each event into a wavelength, take into account the geometry, and convert 2Theta and energy into a d-spacing value for each event using Bragg's Law. Now we can plot an orthogonal space of Energy vs. d-spacing.

The plot directly shows you XRF and XRD information.

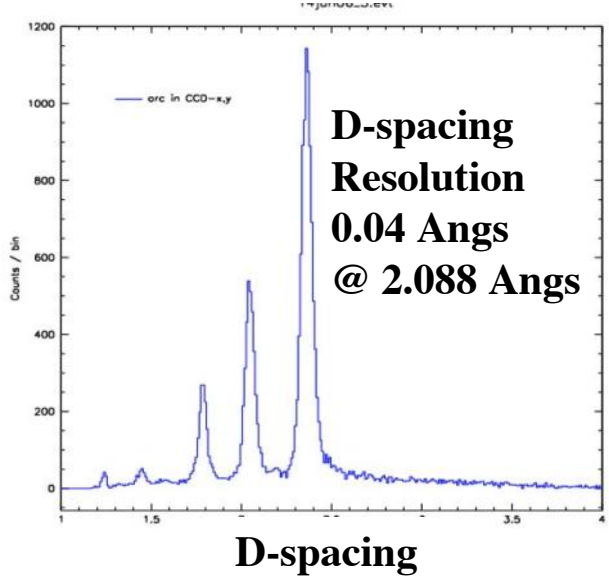

Prototype Data

Random Piece of Quartz Found Around Building 2 at GSFC

Clearly see Si Fluorescence And ~10 XRD Signatures.

Note that the arcs are broken up.

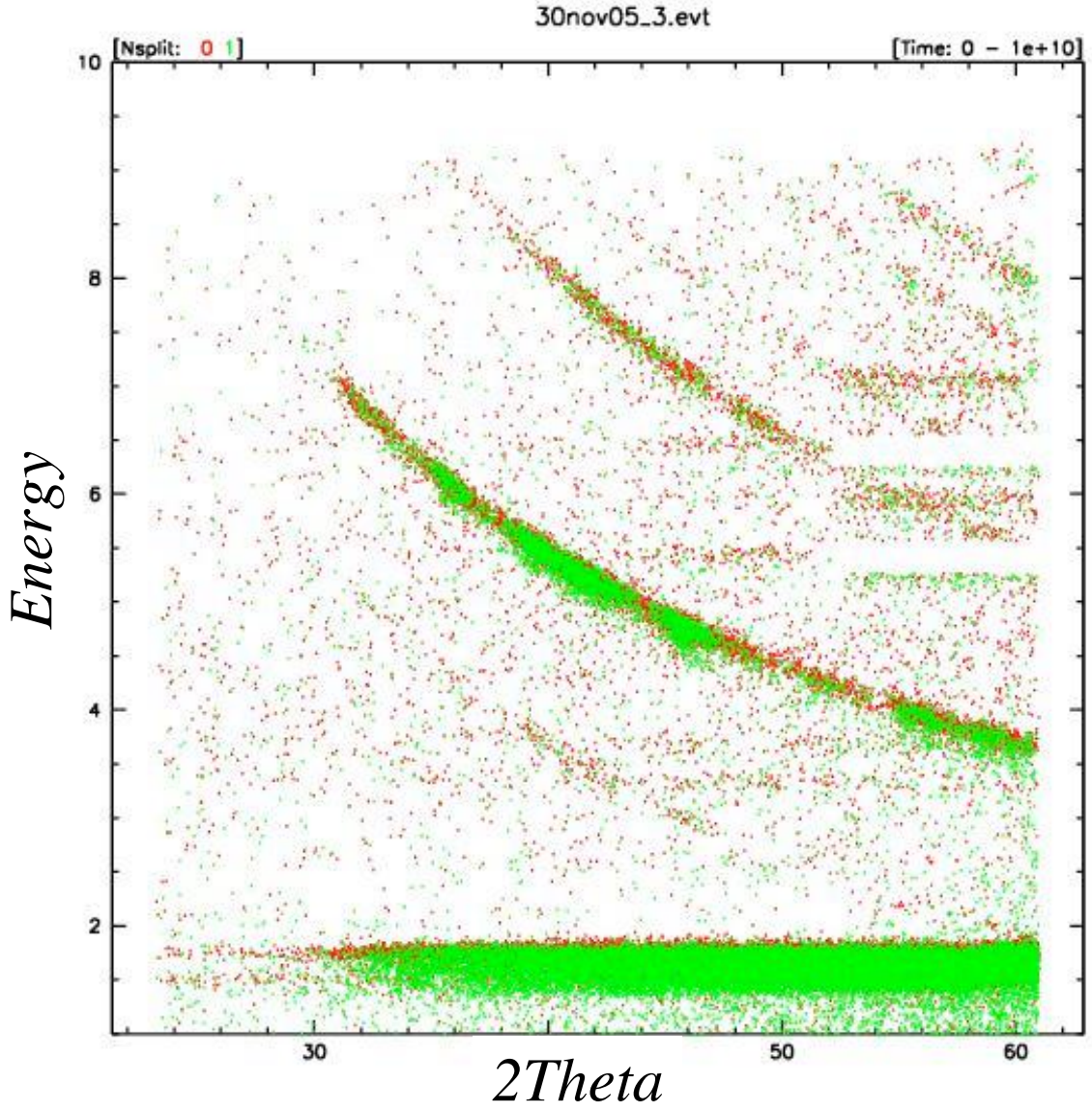

Prototype Data (Quartz Sample)

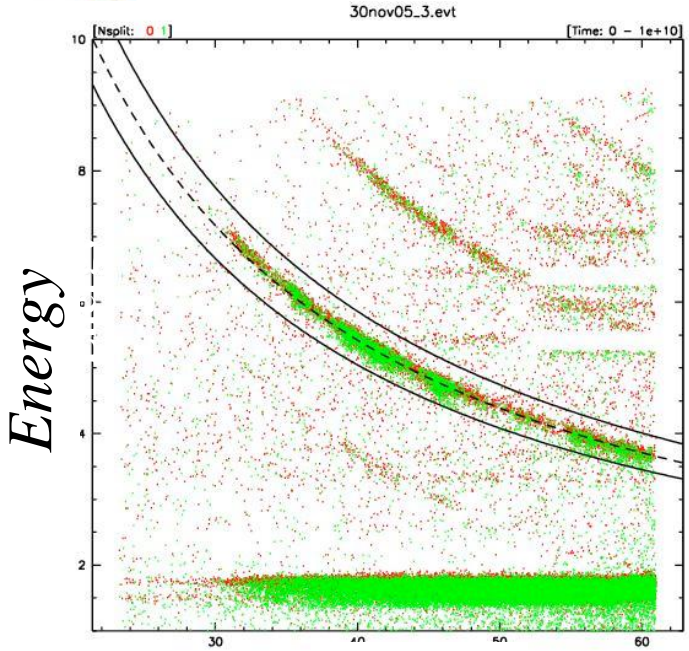

The energy (wavelength) of the events at constant x are the same. As X gets smaller, the energy (wavelength) of the events gets higher (shorter) in accordance with Bragg's Law.

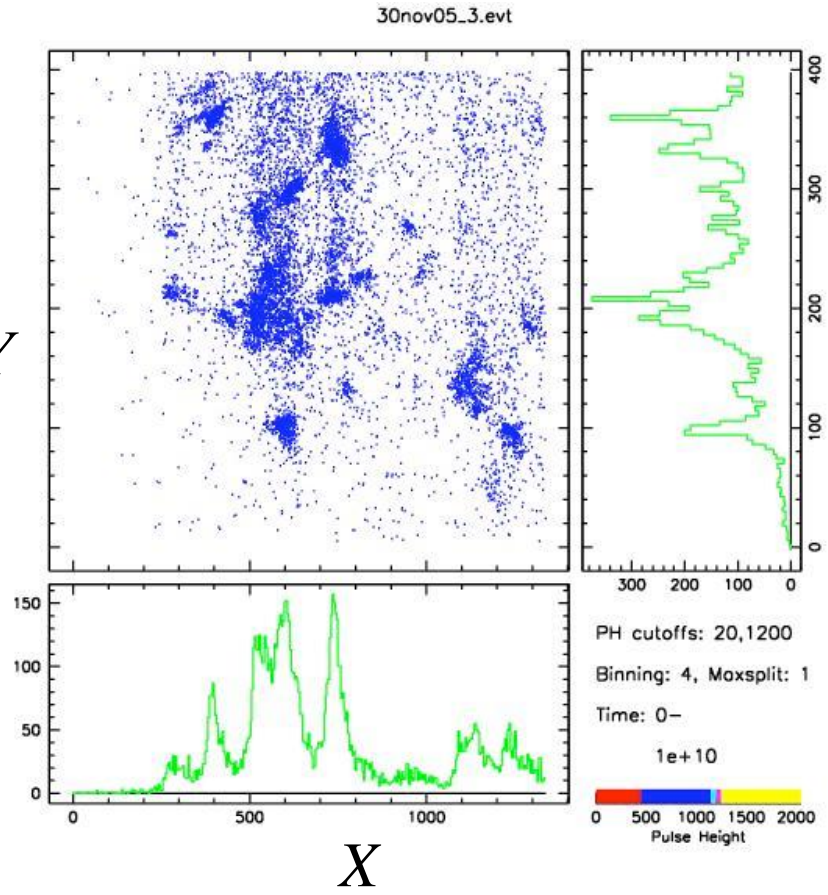

The combination of physical collecting area and broad wavelength coverage with spectroscopy makes the CXRDF insensitive to sample preparation.

Single Crystal of Calcium Carbonate

Here, we took a single crystal of calcium carbonate and oriented it 5 different ways by tipping and tilting at the sample position.

The image to the lower right shows how the diffracted spot moves around the focal plane. As the image is deflected to the left in the image, the energy of the photons diffracted shifts upward.

The image to the upper right shows that all these points line up on a "constant d-spacing arc" in the energy vs X plane.

A traditional XRD using a single wavelength could not do this.

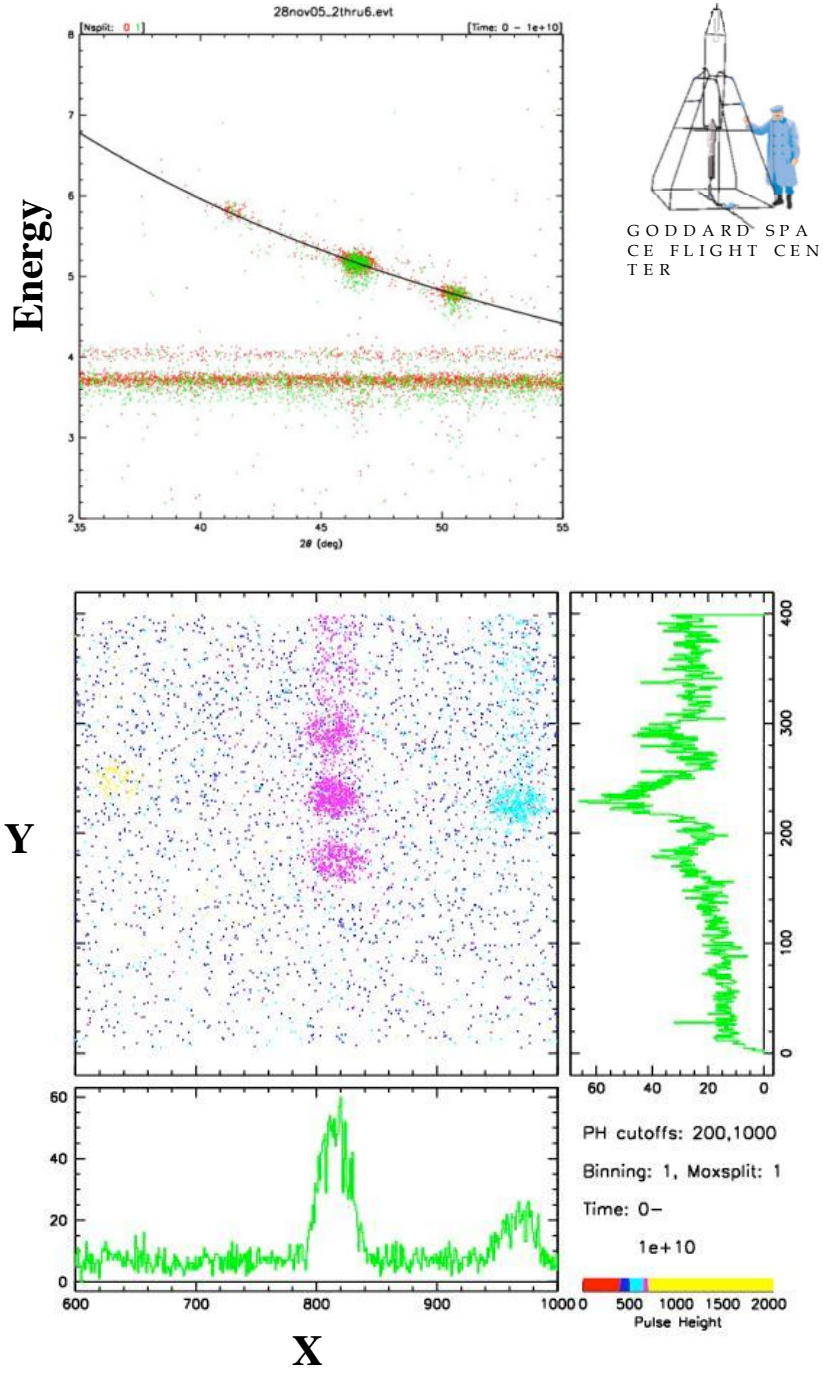

Prototype Data

GODDARD SPACE FLIGHT CENTER

Hematite

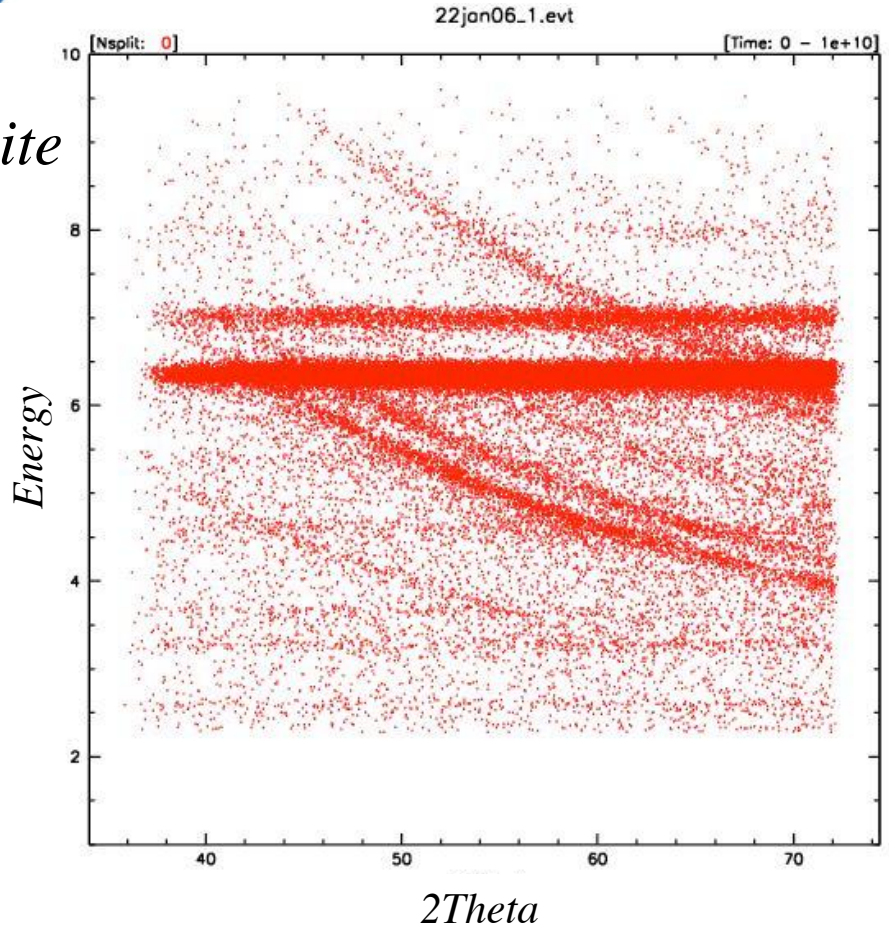

Transform event list

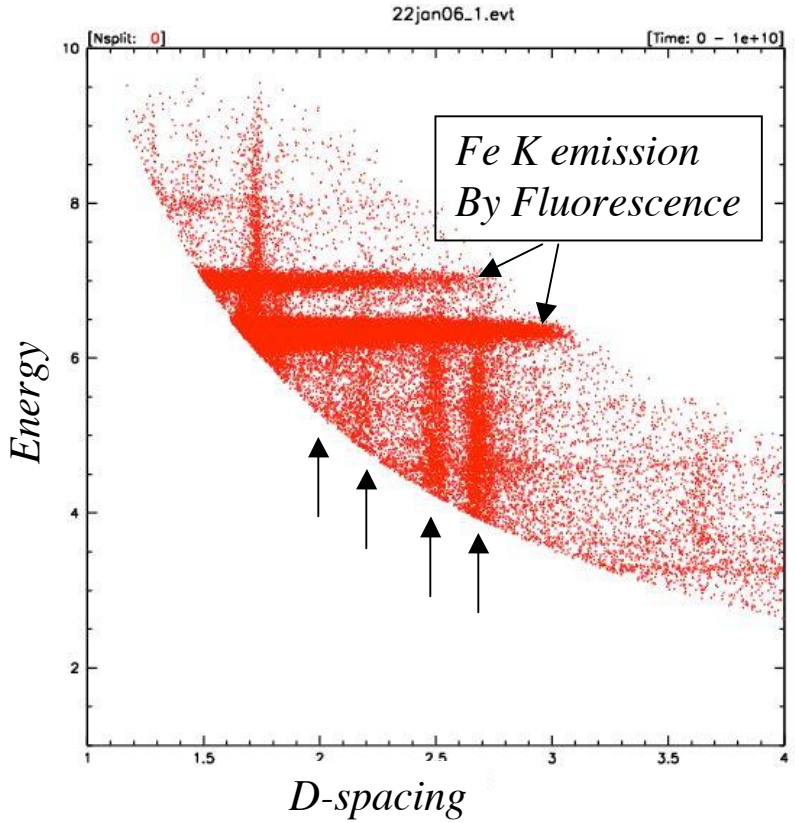

Prototype Data

Water Ice:

1st light water ice with 2nd prototype system

~ 1 minute of data with ice cube pressed up to window

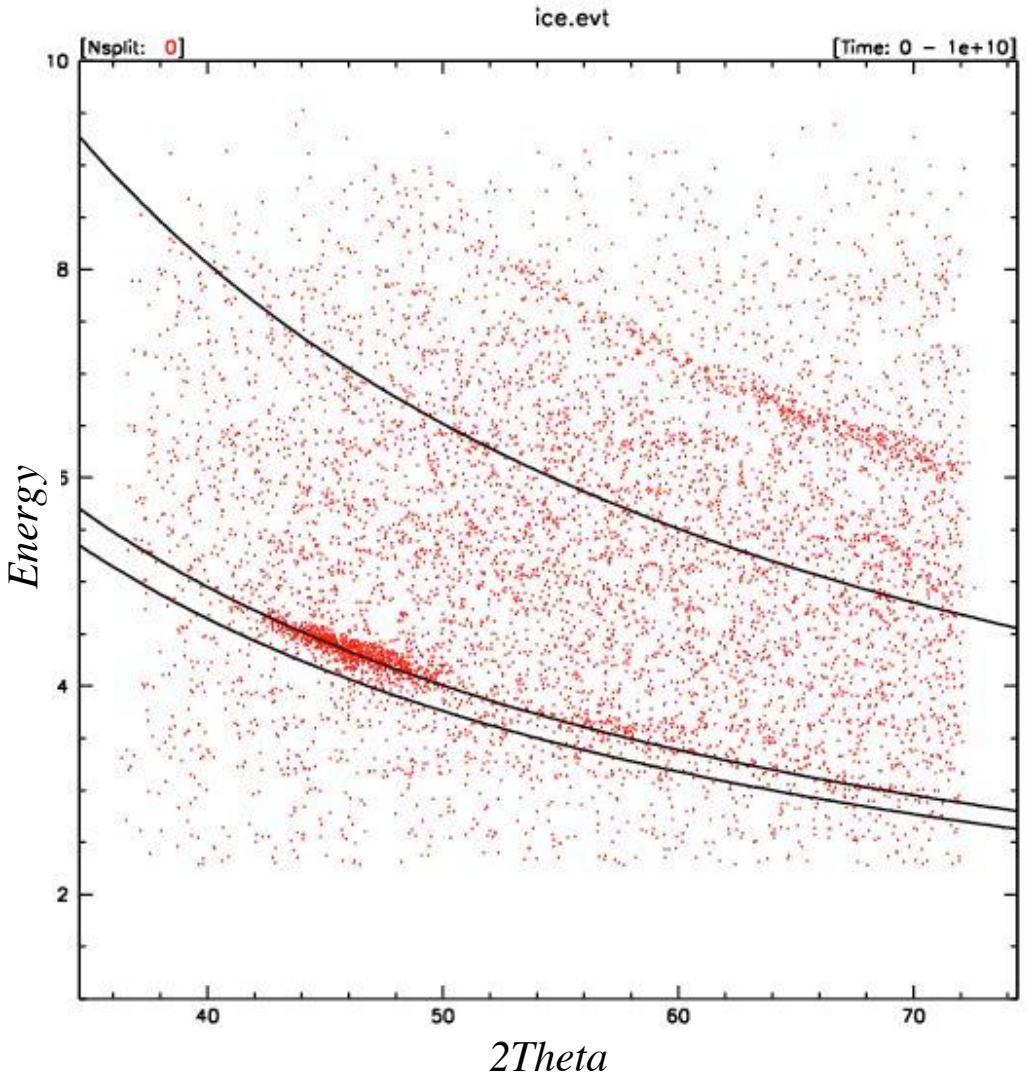

Beryllium Instrument Feature

Expected water ice d-spacing arcs

CRREL Next

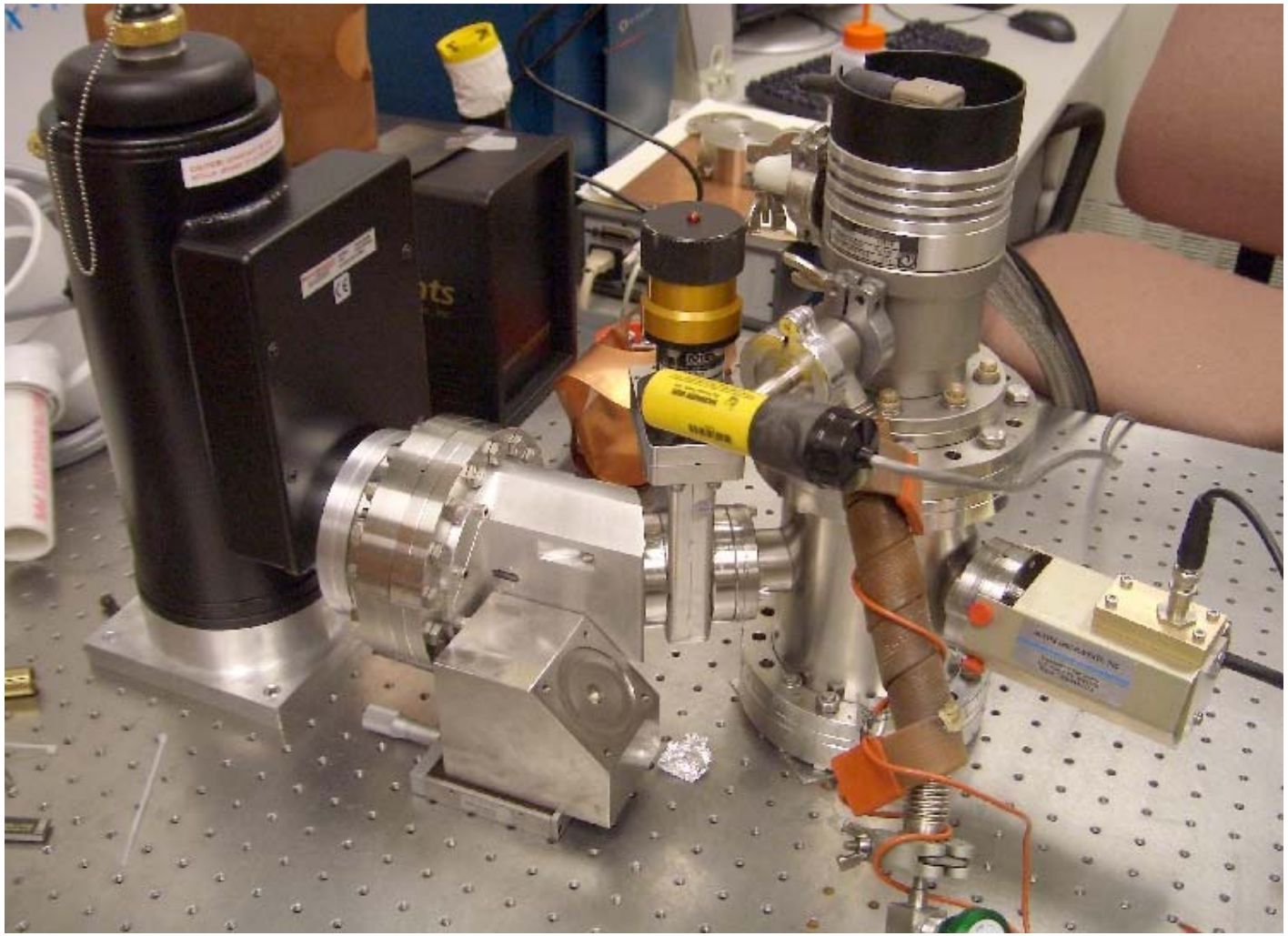

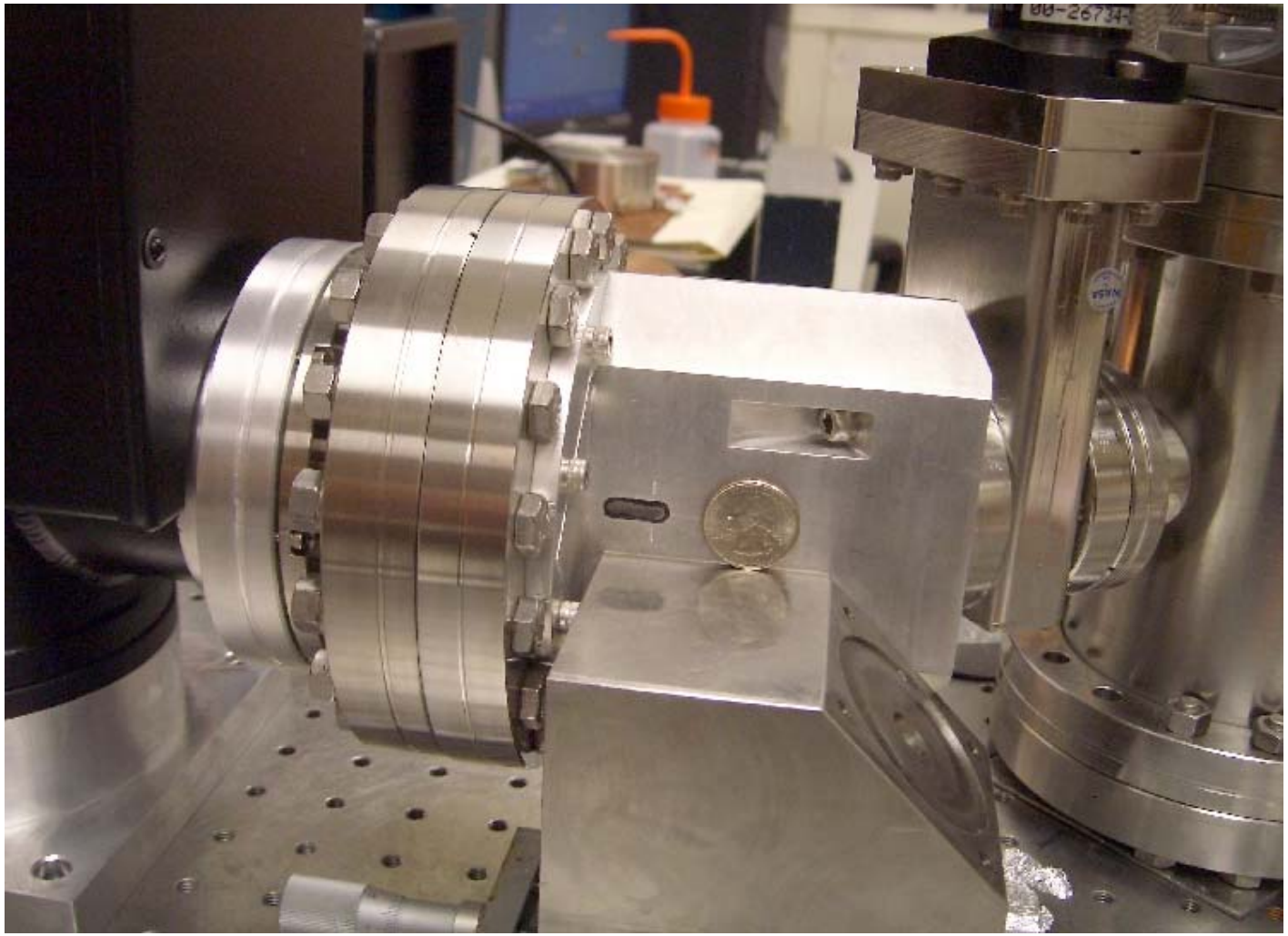

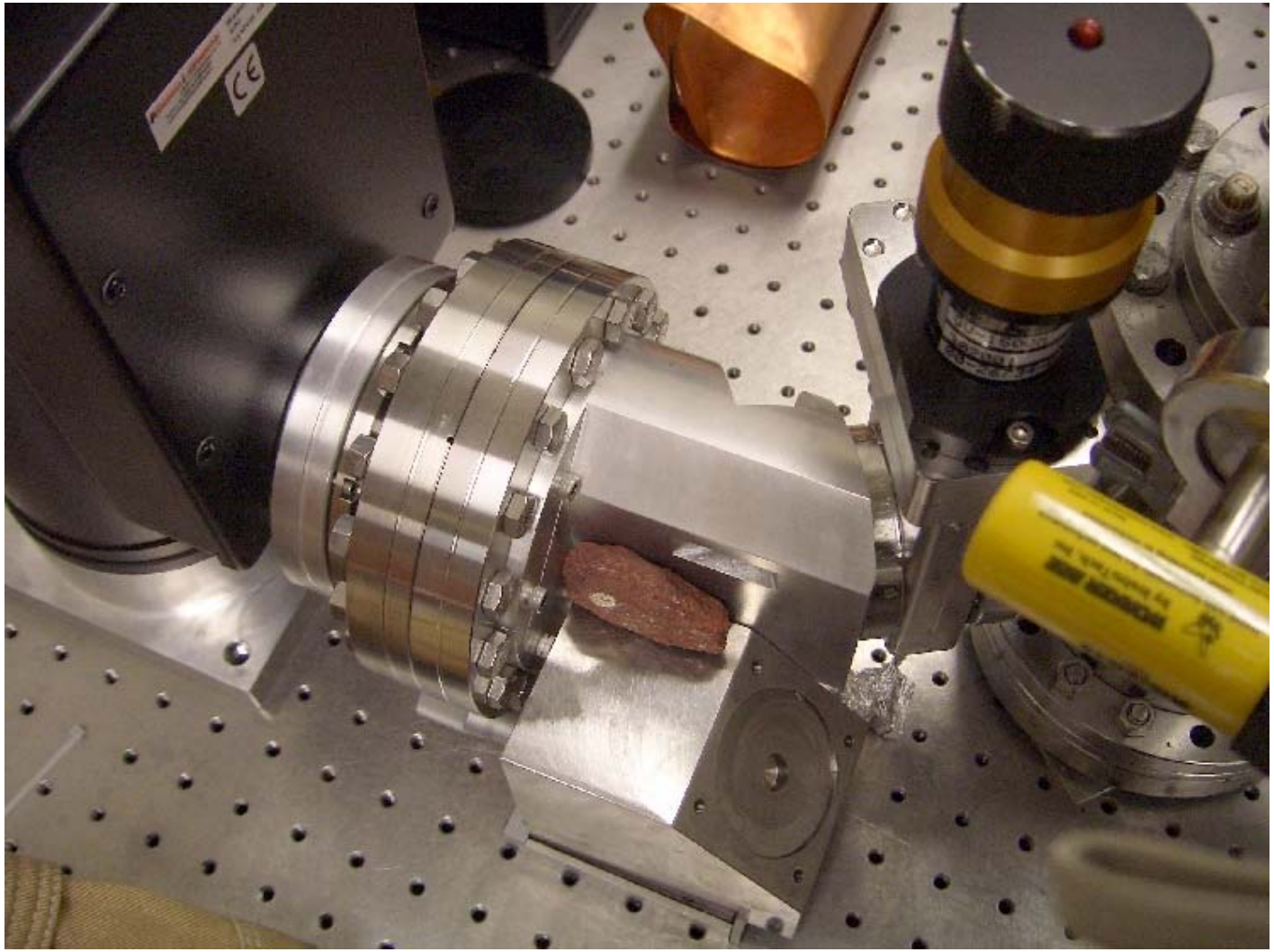

Sensor Head Assembly:
~<5 cm on a side. Shielded

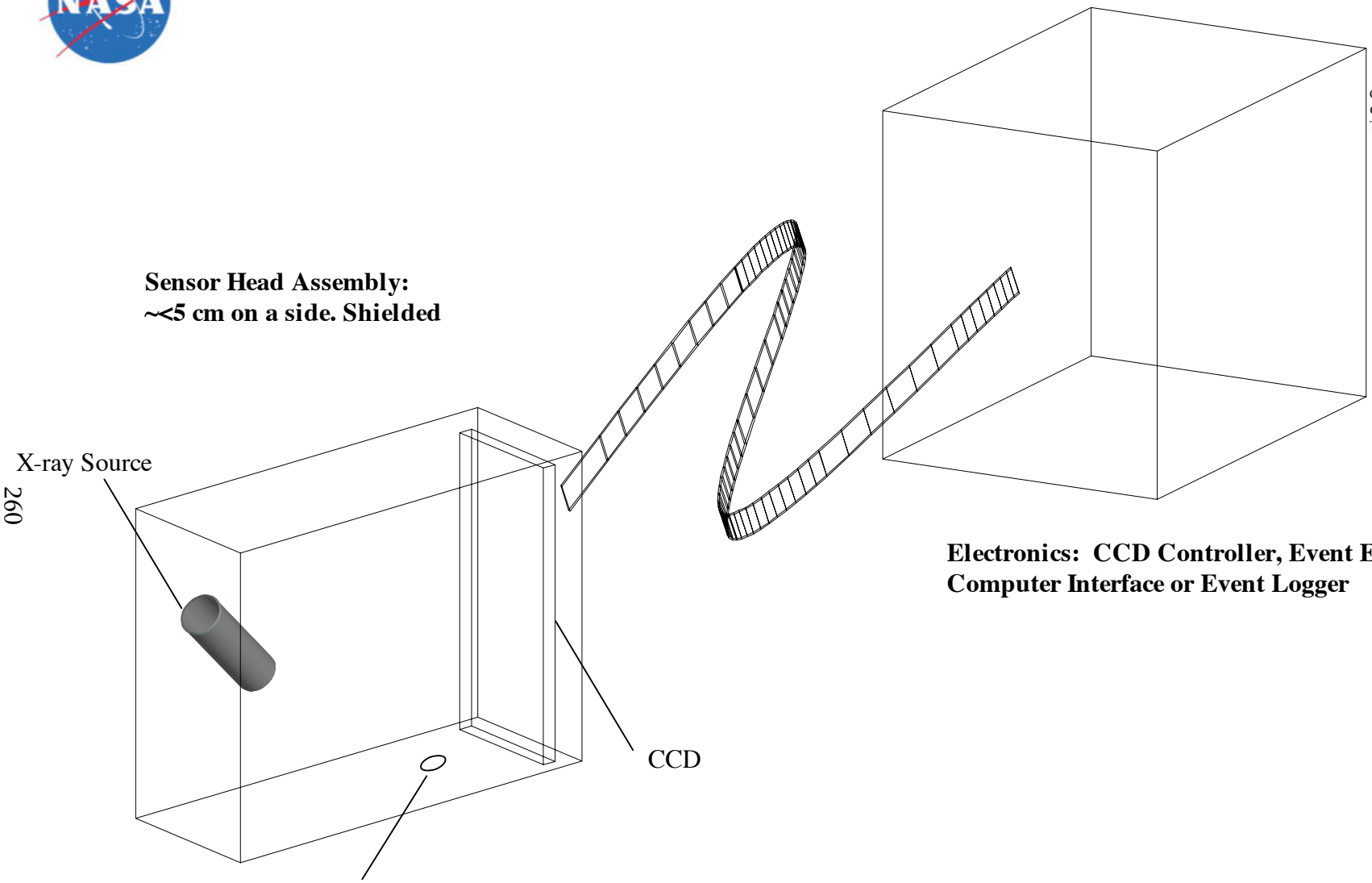

Electronics: CCD Controller, Event Extractor, Computer Interface or Event Logger

260

GODDARD SPACE FLIGHT CENTER

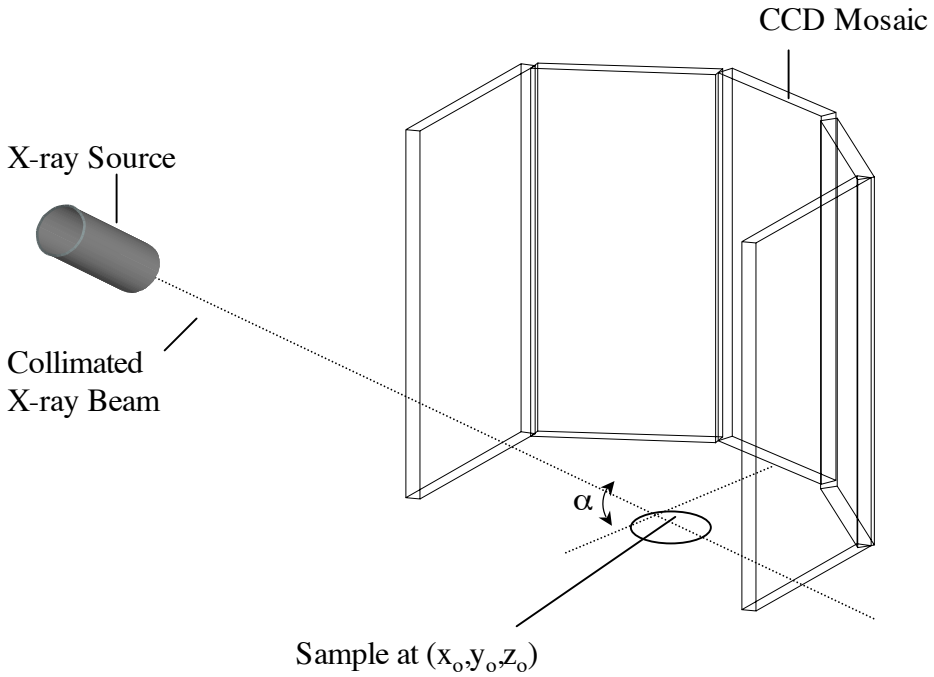

Summary and Status

- A material analysis tool that requires no sample preparation and has potential to identify many minerals including water ice.
- Concept is simple
- No moving parts
- Prototype instruments made from commercial components
- Our MIT collaborators have been flying X-ray CCDs for 13+ years
- Estimated Mass/Power for new flight instrument using latest CCD electronic designs: <2 kg ; <2 watts average

Backup

GODDARD SPACE FLIGHT CENTER

XRD of Crystalline Structures

GODDARD SPACE FLIGHT CENTER

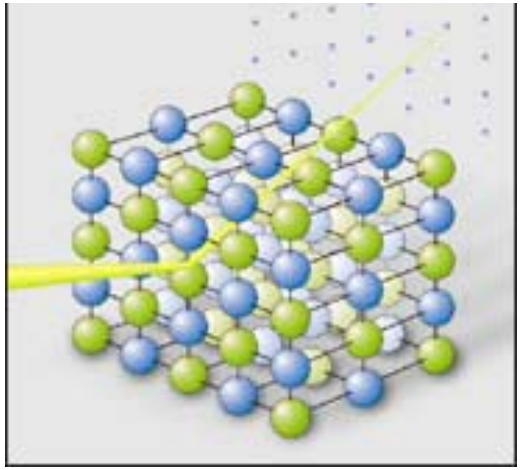

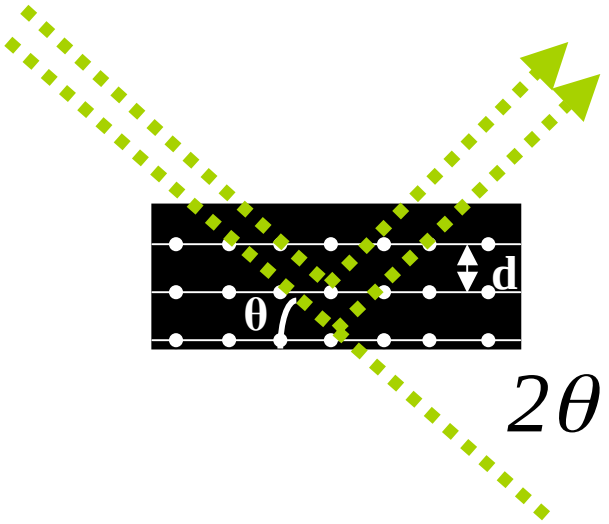

$$n\,\lambda = 2d\sin(\theta)$$

Aerosol Sampling Option

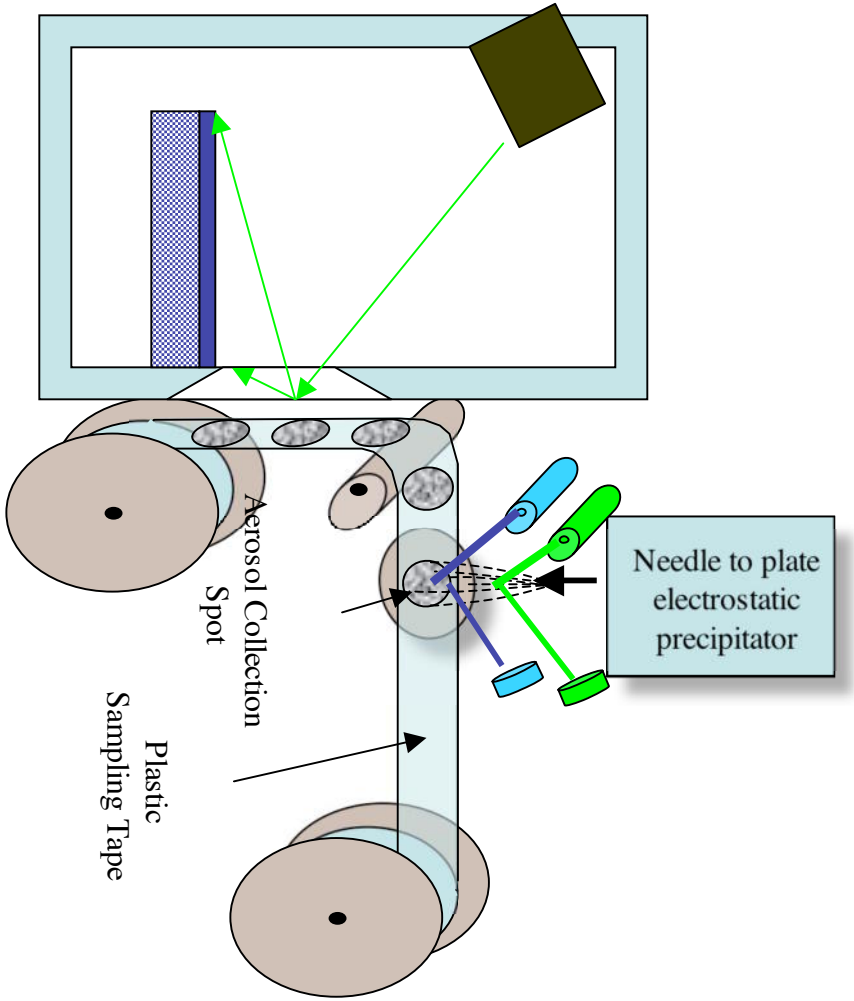

Optical probes for scattering and absorption (provides complementary information on size, refractive indices, etc.)

Instrument Description

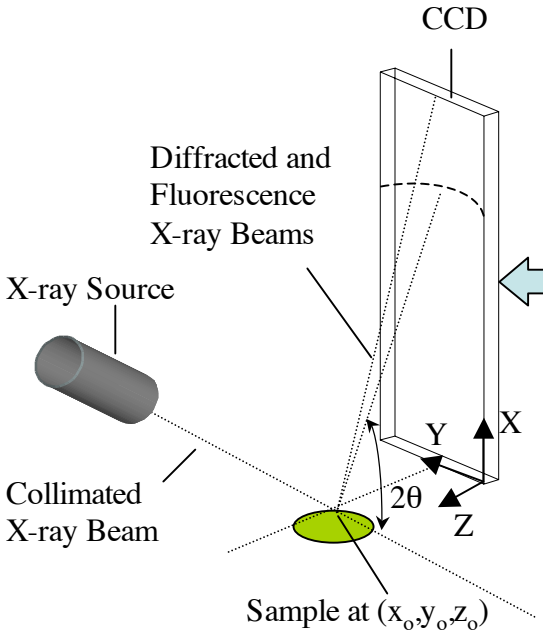

CCD Control and Readout Electronics

Computer Interface with Event Processing

4-Dimensional event list:

Time, X, Y, Energy

For each detected X-ray

Apply Geometry

Time, θ, and λ

For each detected event

Apply Braggs Law
n λ = 2d SIN(θ)

Time, d-spacing and energy

For each detected event

An X-ray Source producing Bremsstrahlung continuum X-rays spanning the 0.1-~10 keV band, sends a collimated beam toward a sample. These X-rays either diffract off the sample or cause characteristic line emission through fluorescence. A photon counting , energy resolving X-ray CCD captures some of these X-rays and produces an event list. This event list can be transformed both fluorescence (elemental composition) and diffraction (mineral atomic-plane spacing) data on an event by event basis.

X-ray Cameras from MIT CCD Group

MIT Center for Space Research has developed and fabricated X-ray cameras and flight electronics optimized for MIT/LL CCDs flown on the ASCA, Chandra, Astro-E, and HETE-2 missions.

ASCA/SIS (1993)

Chandra/ACIS (1999)

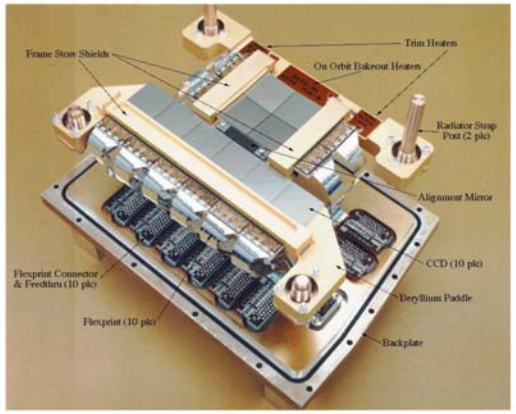

Astro-E/XIS (2000)

HETE SXC (2000)

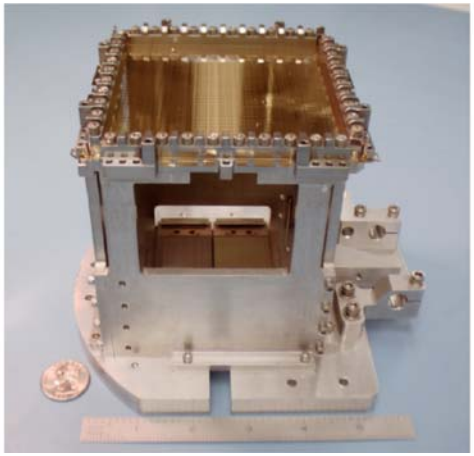

Application to VSE and Lunar Exploration

- Definitive Identification of Minerals
  - Definitive Identification of Water-Ice
- Could Provide Insight into Lunar History via Analysis of structure of the d-spacings and particle/grain size, shape, and orientation distributions

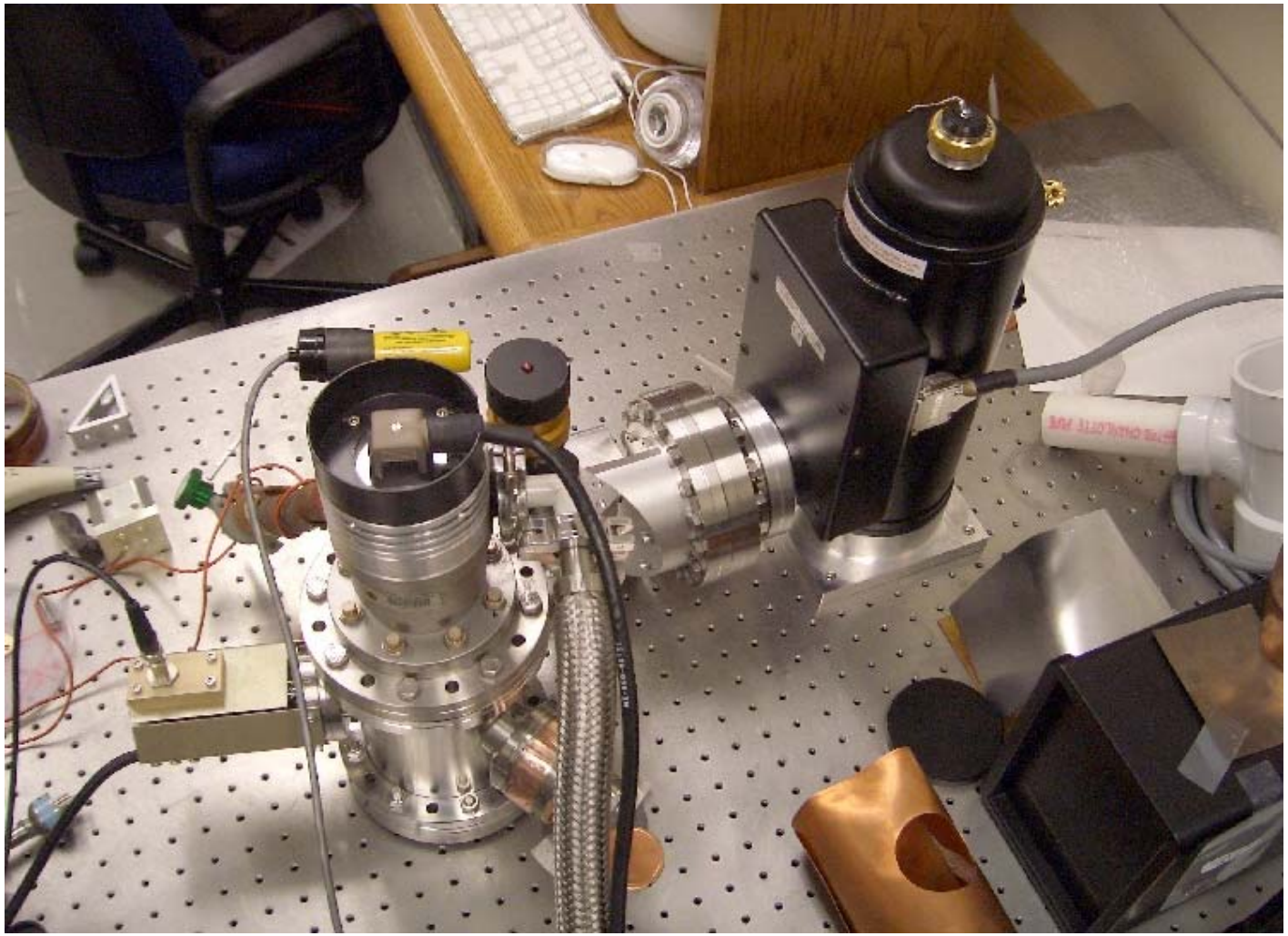

GODDARD SPACE FLIGHT CENTER

Prototype Data

GODDARD SPACE FLIGHT CENTER

Random Piece of Quartz Found Around Building 2 at GSFC

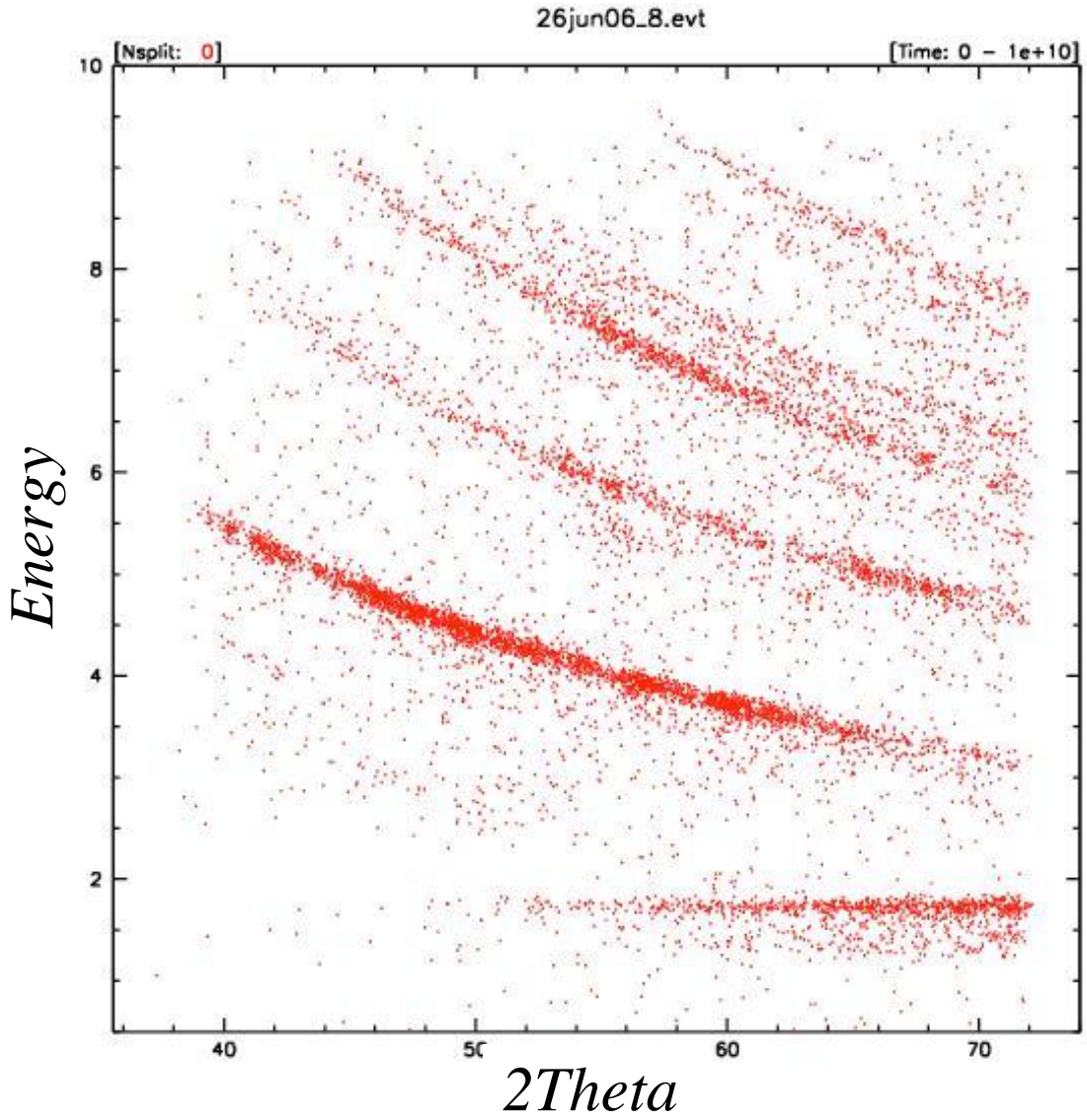

Clearly see Si Fluorescence And ~10 XRD Signatures.

Note that the arcs are broken up.

Prototype Data (Quartz Sample)

GODDARD SPACE FLIGHT CENTER

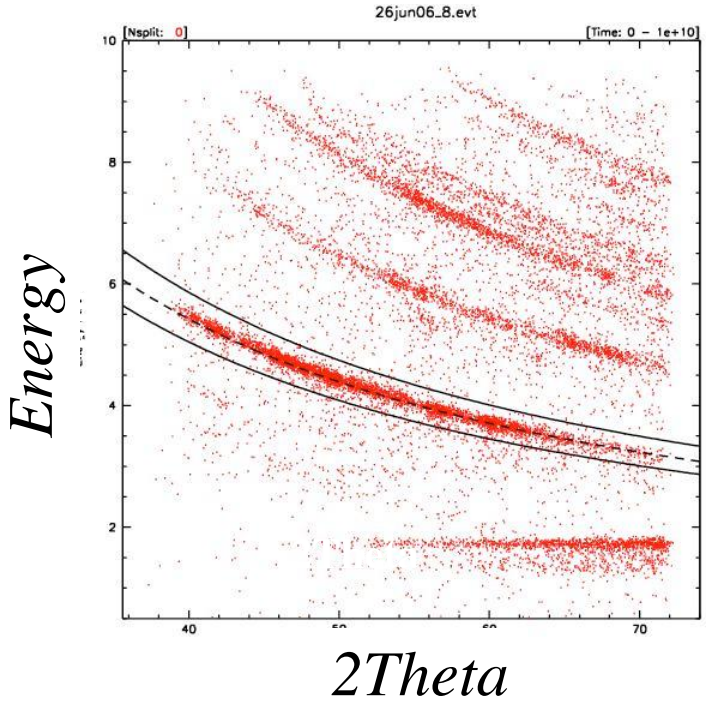

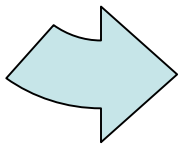

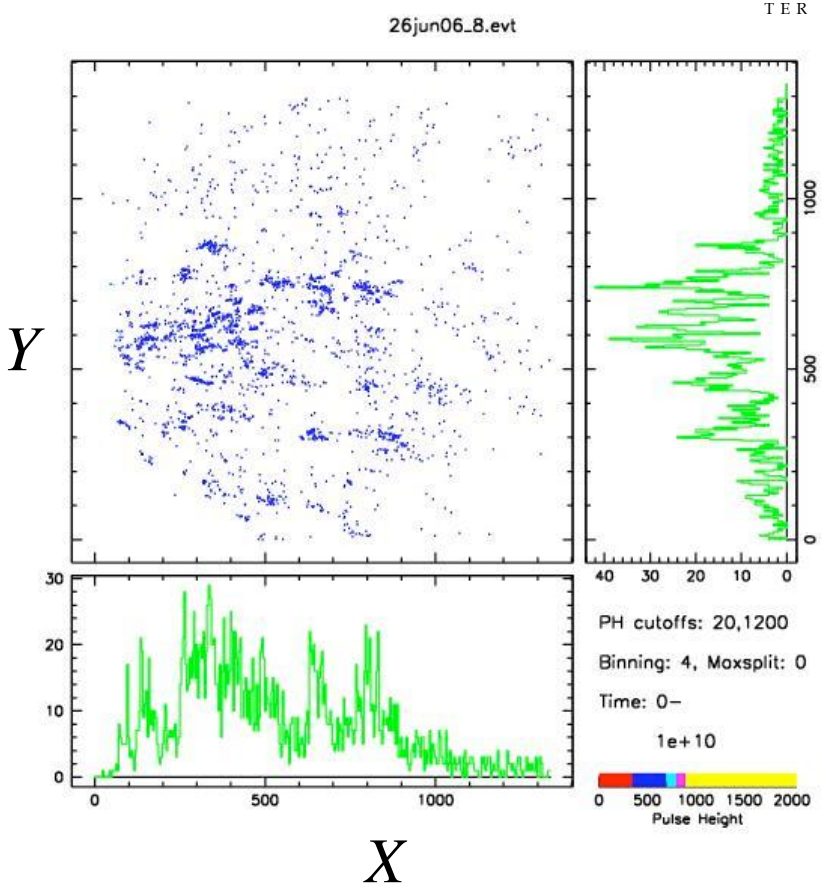

The energy (wavelength) of the events at constant x are the same. As X gets smaller, the energy (wavelength) of the events gets higher (shorter) in accordance with Bragg's Law.

The combination of physical collecting area and broad wavelength coverage with spectroscopy makes the CXRDF insensitive to sample preparation.

VITA

Rosemary Assunta Millham

Candidate for the Degree of

Doctor of Philosophy

Dissertation: MINERALOGY OF DUST EMISSIONS FROM THE BODELE DEPRESSION

Major Field: Environmental Science

Biographical:

Personal Data: Born in Great Barrington, Massachusetts on July 9, 1952, the daughter of Joseph and Florence Spadaccini, married Robert Millham on August 11, 1973.

Education: Graduated from Peru Central High School, in May, 1971; received Bachelor of Science degree in 1983 from State University of New York, at New Paltz, New Paltz, NY; received Master of Science degree in Education from State University of New York at New Paltz, New Paltz, NY in 1987; completed requirements for the Doctor of Philosophy degree at Oklahoma State University in July, 2007.

Professional Experience: Currently an independent consultant in lunar science and education with NASA Headquarters, 2005-2006; Lunar Content Specialist and Project Manager, Lunar Module on NASA's Student Observation Network, 1999-2005; NASA Aerospace Education Specialist, Oklahoma State University, Stillwater, OK: Representative of NASA, 1992-1999; Regents High School Earth Science teacher and Middle School Life Sciences/Physical Science/Earth Sciences teacher, Montgomery, NY, 1994-1999; Adjunct Professor, Mount Saint Mary's College, NY, 1990-1992; Associate Professor, Ulster County Community College, NY, 1987-1990; Elementary Education teacher, grades 1,5,6,7,8 in all Sciences, Language Arts, Social Studies and Mathematics, Highland, NY, 1983-1987; Middle School 6th grade teacher, Language Arts and General Science for two years and 7th and 8th grade Earth and Life Sciences for one year, Valley Central Schools, Montgomery, NY.

Name: Rosemary Assunta Millham Date of Degree: July, 2007

Institution: Oklahoma State University Location: Stillwater, Oklahoma

Title of Study: MINERALOGY OF DUST EMISSIONS FROM THE BODELE DEPRESSION

Pages in Study: 271 Candidate for the Degree of Doctor of Philosophy

Major: Environmental Science

Scope and Method of Study: This study focused on identifying the minerals in the dust emitted from the Bodele Depression in northern Chad in the Saharan Desert. Understanding the mineralogy provides the information needed to assess the effects that mineral dust has on climate and climate change relative to the energy budget and radiative forcings, and cloud characteristics and properties, and assists in providing critical information for assessing amounts of nutrients delivered to oceans and lands. There is a question of health issues related to dust emissions not addressed in this study.

Using a traditional X-Ray diffractometer (XRD), scanning electron microscope (SEM) with chemical analysis capabilities, French geological survey maps, and a new instrument for detecting d-spacings and K-fluorescence in unprepared samples called the XRD XRF (CCDXRD) that couples a CCD with traditional X-Ray diffractometer, mineral identification is possible.

Findings and Conclusions: The samples from the Bodele in situ aerosol and bulk ground materials produce the dust emissions occurring from the region ~40% of the days in a year. The results from literature review, X-Ray diffractometer data, SEM data, geological survey maps, and the CCD XRD data provided concrete identification of the Bodele minerals as typical crustal silicate minerals with small amounts of calcium carbonate, dolomite, silica, desiccated diatoms, and possible iron oxides. The silicate minerals are primarily ferromagnesian and framework silicates typical of low-lying depositional basins and the weathering processes occurring in alternating wet and dry periods. Clays minerals halloysite, kaolinite, and smectites (montmorillite) are the most common.

Exotic materials were detected in two of the bulk samples. A reading of 25.75% titanium in one sample, and elevated isolated silicon data (considered cosmic silicon) provided the only anomalies in the study.

ADVISER'S APPROVAL: Steven Marks